EVALUATION OF DOSIMETRIC UNCERTAINTIES AND TRANSIT DOSIMETRY FEASIBILITY IN PULMONARY STEREOTACTIC BODY RADIOTHERAPY (SBRT)

by

Shu-Hui Hsu

A dissertation submitted in partial fulfillment
of the requirements for the degree of
Doctor of Philosophy
(Nuclear Engineering and Radiological Sciences)
in the University of Michigan
2011

Doctoral Committee:

Associate Professor Jean M. Moran, Co-Chair
Professor Kimberlee J. Kearfott, Co-Chair
Professor Alex F. Bielajew
Professor Mitchell M. Goodsitt
Professor Peter L. Roberson

2011

To my parents

ACKNOWLEDGEMENTS

The success of this dissertation is attributed to the extensive support and assistance I received from a number of people. I am deeply grateful to Dr. Jean Moran, my dissertation advisor in the Department of Radiation Oncology, for her valuable guidance and great encouragement throughout my graduate studies. Under her direction, I have been involved in various research projects, which have greatly strengthened my research abilities and increased my interest in research. I feel extremely privileged to have worked with her, and especially appreciate the amount of time and energy that she put into reading my dissertation chapters and papers. My sincere thanks go to Dr. Peter Roberson, who has helped me tremendously since I entered the department. I feel fortunate to have had active discussions with him on various projects. I greatly appreciate his patient teaching and good advice. I would like to express my deep gratitude to Dr. Kimberlee Kearfott, who is my advisor in the Department of Nuclear Engineering and Radiological Sciences. I am grateful that she gave me the freedom to choose my research projects based on my interests, provided me with constructive comments on my dissertation, and kept me on track. I would like to express my special thanks to my committee members, Dr. Mitchell Goodsitt and Dr. Alex Bielajew. I am very glad to have had excellent discussions with them which have helped me clarify several points in the dissertation.

I would like to thank all the faculty and colleagues of the Department of Radiation Oncology. My special thanks go to Dr. Benedick Fraass and Dr. Eduardo Acosta. Their

TABLE OF CONTENTS

LIST OF FIGURES

x

xi

LIST OF TABLES

ABSTRACT

EVALUATION OF DOSIMETRIC UNCERTAINTIES AND TRANSIT DOSIMETRY FEASIBILITY IN PULMONARY STEREOTACTIC BODY RADIOTHERAPY (SBRT)

by

Shu-Hui Hsu

Co-Chairs: Jean M. Moran and Kimberlee J. Kearfott

The aims of this dissertation were to develop a method with improved accuracy for various heterogeneous geometries and to evaluate the feasibility of using EPID transit dosimetry for error detection. This dissertation examined phantom geometries with an emphasis on a tumor-in-lung geometry that may occur in hypo-fractionated SBRT treatments. For dose investigation in heterogeneous geometries, a multi-planar film measurement system was used with a measurement accuracy (within 3%) by using specific procedures to reduce the film perturbation in a low density medium. Measurements were used to validate a Monte Carlo (MC) method, and the results indicated that this MC method can be used as a reference to validate other calculation algorithms or to evaluate the doses delivered to patients for lung treatment. For developing an error detection method, a commercial electronic portal imaging device (EPID) composed of amorphous silicon was characterized for dosimetry application. A general calibration method was explored to use this device as a water-equivalent dosimeter, allowing for direct comparison to calculated doses from treatment planning systems. The calibration method was validated for a range of situations, field shapes,

and intensities. The EPID transit dosimetry was sensitive to delivery errors, such as variations in treatment field shape, machine output and patient setup. The correlation between in-patient and transit dose variations may be established and used to determine acceptance or rejection criteria when the error is found. This dissertation showed the potential of using EPID dosimetry during treatment for on-line error correction and for estimating the in-patient dose error.

CHAPTER I

INTRODUCTION

I.A. Overview of advances in radiotherapy techniques

In recent years, there have been significant improvements in radiotherapy technology. These improvements have led to a greater complexity in treatment techniques to achieve treatment goals, such as improving patient survival and quality of life. Such treatment goals can be achieved by increasing tumor control rates while reducing complication rates, by delivering higher doses to the target volume[a] and lower doses to normal tissues, respectively. Control over the physical dose distribution involves special treatment techniques, such as intensity modulated radiotherapy (IMRT)[b], stereotactic radiosurgery (SRS)[c] and stereotactic body radiotherapy (SBRT)[d]. These techniques can be used to deliver high doses that conform to tumors while reducing doses to the neighboring critical organs.

Due to the complexities of treatment, concerns regarding the treatment accuracy are growing, particularly with regard to targeting and dose accuracies. Targeting

---

[a] The ICRU report No.62[1] defines gross tumor volume (GTV), clinical target volume (CTV), internal target volume (ITV) and planning target volume (PTV).

[b] It refers to a radiation therapy technique in which non-uniform fluence is delivered to the patient from any given position of the treatment beam to optimize the composite dose distribution. The treatment criteria for plan optimization are specified by the planner and the optimal fluence profiles for a given set of beam directions are determined through inverse planning.

[c] It is a single-fraction radiation therapy procedure for treating intracranial lesions using a combination of a stereotactic apparatus and narrow multiple beams delivered through non-coplanar isocentric arcs.

[d] It is a technique similar to SRS but for small localized tumors outside the cranium. It does not use rigid stereotactic frames to immobilize the body. Instead, the tumor is localized through image guidance systems. The major features that separate SBRT from conventional radiation treatment are the delivery of large doses in a few fractions, increased number of beams, frequent use of non-coplanar beam arrangements, and small or nonexistent beam margins for penumbra.

accuracy has been greatly improved by implementing image-guided systems on the treatment unit to verify patient treatment positions and other techniques to address organ motion. Concerns surrounding dose accuracy have been mainly addressed by controlling the accuracy of calculation algorithms in treatment planning systems (TPSs). Modeling of calculation algorithms has been improved to account for complex beam delivery systems and complex patient geometries. However, there still exist large calculation uncertainties in particular regions, such as interfaces between high and low density tissues, especially when a small field is used. Due to the dependence of calculation accuracy on the patient geometry, the delivered doses may be different from planned doses when the patient geometry changes during the course of treatment. This discrepancy can lead to negative consequences and is more significant for those complex treatment techniques. These techniques deliver high conformal doses to tumors and partially missing the target or delivering incorrect doses degrades the understanding of the dose response of tissues. To reduce this risk, delivered dose verification techniques are being investigated to determine the actual doses delivered to patients. A few institutes have initiated techniques to verify delivered doses in each fraction or to accumulate the as-delivered doses from each fraction of treatment. The delivered dose data can be used to review or adapt the treatment plan (so-called adaptive radiotherapy) and be documented to evaluate dose responses and clinical outcome for tumor and normal tissue. Adaptive therapy considers the change of patient geometry over treatment courses, and ensures that the cumulative doses over the treatment course meet the expected doses. Therefore, on-line images are acquired before treatment for each fraction or off-line images in a period of treatment to monitor the change of patient geometry. The plans may be changed for the new patient geometry and/or the doses may be compensated in the following fractions.

In addition to verifying delivered doses to patients, dose verification techniques can be developed to catch unpredicted errors, which may occur during the treatment but were not discovered before the treatment. These techniques aim to identify such errors before these errors harm patients.

I.B. Sources of delivered dose errors and their impact on the treatment outcome

Delivered dose errors may have an important impact on treatment outcome. Piermattei et al[2] reported a patient with locally recurrent tongue carcinoma, who was treated with concurrent chemotherapy and IMRT. During the third week of radiotherapy, the patient developed grade 3 mucositis. This was due to marked tumor shrinkage and modifications to the critical structures, which resulted in a minimal dose increase in the new target volumes but a marked dose increase to the organs at risk (OAR). Such delivered dose changes as a result of a change in the patient geometry can result in a failure of tumor control or an increase in complication rates. A dose error of 5% may lead to a 10% to 20% change in tumor control probability (TCP) and to an even larger change in normal tissue complication probability (NTCP).[3, 4]

Delivered dose errors are caused by clinical challenges that can be divided into four categories: (1) errors in the functioning of treatment equipment, (2) errors in the data transfer from TPSs to treatment equipment, which causes errors in beam delivery, (3) patient specific errors, and (4) the limitations and uncertainties of calculations in the TPSs.

For the first and second categories, errors in the functioning of treatment equipment include incorrect beam output, energy and field size, while errors in data transfer and beam delivery include incorrect parameter transfer, mechanical inaccuracies (e.g. faulty leaf position and movement), as well as dose over or under

shoot. These two groups of errors can be controlled or avoided by routine quality assurance (QA) of treatment equipment or by performing the patient-specific QA prior to the first treatment to check the fluence map delivered on a geometric phantom.

The third category, patient specific errors, includes setup errors, organ motion, and anatomical changes during the treatment period. Currently, setup errors can be reduced to within 2 mm for some treatment sites through the use of accurate body fixation with adjuvant image-guided techniques.[5-8] Organ or tumor motion from respiratory, cardiac, and gastrointestinal motions for thoracic and abdominal regions can result in discrepancies between the planned and delivered doses. In pelvic treatments, the filling or emptying of the bladder or rectum can also lead to variations in organ positions. Among these factors, respiratory motion is the most significant, challenging and difficult to manage because it is patient-specific and leads to tissue deformation. The amount of organ movement due to breathing can be up to 1 or 2 cm, depending on the treatment site, and leads to artifacts during image acquisition. Many groups have studied organ motion and proposed several solutions to deal with this problem. These include breathing control techniques and incorporation of organ motion into the treatment plan.[9] Studies of the errors due to anatomical changes have shown that after several fractions of treatment, tumor shrinkage can occur, possibly making it necessary to modify the treatment plan to boost the remaining smaller tumor volume.[10, 11] A modified treatment plan could reduce normal tissue complication rates and probably increase tumor control rates although the biological effect of this dose modification is not well understood yet. Optimum treatment will require detailed anatomical information at multiple time points and the development of thresholds for re-planning.

The fourth group of errors, limitations and uncertainties of calculations in TPSs, includes inaccurate modeling of features of the multileaf collimator (MLC) in machines

and inaccurate calculation in electron disequilibrium regions. For calculation uncertainties, the concerns are with respect to with electron disequilibrium in the buildup region, interface regions, and regions receiving doses from beams with small field size. For example in lung tumor treatments, inaccurate dose calculations may lead to dose over-estimation in the region of the tumor close to the lung (under-dosage) or dose under-estimation in a normal lung (over-dosage). To reduce the possibility of treatment failure, improved accuracy in dose calculations is important to ensure that prescribed doses are given to the tumor while acceptable doses are given to neighboring normal tissues. More accurate information can also lead to a better understanding of the dose response of the tumor and normal tissues. To address this issue, the accuracy of calculation algorithms is usually verified with measurements for both simple and challenging conditions before the algorithm can be implemented in the clinic.[12]

I.C. Delivered dose verification methods

Due to those uncertainties described in Section I.B., the implementation of delivered dose verification techniques in clinics will be an important topic of research in the next decade. The verification of delivered dose to the target volume or to the neighboring normal tissue can be performed in several ways: (1) in-vivo dose measurements with implantable dosimeters; (2) dose recalculations using inter-fractional computed tomography (CT) images; or (3) back-projection of transmission doses (transit dosimetry) with planned or inter-fractional CT images to calculate actual doses.

The first method, in-vivo dosimetry, uses pre-calibrated radiation dosimeters, such as miniature metal-oxide-semiconductor field effect transistors (MOSFETs) and/or thermoluminescent dosimeters (TLDs). MOSFETs and TLDs can be placed inside the tissue or on the surface to measure doses delivered to patients. For example, Beyer *et*

al[13] compared the measured dose with the predicted dose using MOSFETs for prostate cancer patients. They found that in some patients, the cumulative dose differed from the planned dose by ≥ 5%, and suggested that an implantable dosimeter could help identify dose discrepancies (random or systematic) and could be used as a daily treatment verification tool. However, this approach has drawbacks because it is invasive and provides limited dose information based on one (or a few) measured point(s).

In the second method, inter-fractional images can be acquired before or after beam delivery using in-room kilovoltage CT (kVCT) or megavoltage CT (MVCT). These images can be either used for treatment position verification or sent back to TPSs for dose recalculation. The recalculated doses based on actual treatment geometry can then be compared with the planned doses.[14-16] However, the information is limited to the change of patient geometry, excluding the actual delivered dose information when the beam is delivered. In addition, in-room CT images suffer from bad image quality, and several corrections may be required particularly for MVCT.

For the third approach, transit doses are acquired during beam delivery, usually using an electronic portal imaging device (EPID) attached to the treatment machine. Transit dosimetry records all information from the beam delivery and patient specific variations without interfering with the treatment. The transmission data can be used to detect errors during treatment or when necessary, to reconstruct the three-dimensional (3D) doses delivered to patients either on planned CT images[17-20] or on inter-fractional CT images[21, 22]. While dose reconstruction using planned images assumes that dose errors mainly come from variations in the radiation beam, dose reconstruction using inter-fractional images considers the variations in both the patient geometry and radiation beam. The latter method may yield the highest quality estimates of the delivered dose for the least effort invested. The optimum frequency of using dose

reconstruction on inter-fractional images to obtain a sufficiently accurate as-delivered dose will depend on patient stability and treatment site considerations. If the total dose delivered to the patient over the entire treatment is monitored, the impact of discrepancies can be determined and minimized in the subsequent fractions. This method can provide both a safety net for advanced treatments involving dose escalation, as well as a full account of the delivered dose to specific volumes, allowing the original treatment plan to be adapted if necessary.

I.D. Lung stereotactic body radiotherapy (SBRT)

Hypo-fractionated SBRT is used to treat small tumors that are generally smaller than 6 cm in diameter.[23-26] This technique uses a small number of fractions and delivers very high doses in each fraction compared to a standard fractionation scheme. For example, 4 to 20 Gy per fraction and 1 to 5 fractions are used for lung SBRT compared to 1.8 to 2 Gy per fraction over 30 or more fractions used for standard fractionation. Due to the high dose delivery and dose sensitivity of normal tissues, this technique requires a high targeting precision (≤ 5 mm error) and many beam angles. To achieve this high precision of treatment, this technique uses a stereotactic coordinate system, body immobilization and image-guidance to ensure treatment position, and methods to limit breathing or to gate treatment when treating tumors in chest and abdominal regions. Figure I.1 shows a general flow chart for SBRT, from initial simulation with patient immobilization to treatment. During the CT simulation stage, images are acquired for treatment planning and for determining if motion management is required. As part of treatment planning, the target and critical organs will be contoured on individual image structures to create 3D volumes. The prescribed dose to the target and dose constraints to critical organs will be specified based on the patients' condition. The beam directions, shaping, and weighting will be specified and doses will be calculated using TPSs. When the plan is approved for

delivery, the treatment position will be confirmed in the treatment room before beginning the beam delivery. A possible final procedure is acquiring delivered dose data during treatment, which will be a possible step in the routine application for radiotherapy.

SIMULATION	Body immobilization Stereotactic coordinate systems

CT	1. 3D image dataset 2. Motion management?

TREATMENT PLANNING	1. Target and organ at risk contouring 2. Dose constraints 3. Beam arrangement 4. Dose calculation

POSITION VERIFICATION	Daily pre-treatment images

TREATMENT	

DELIVERED DOSE VERIFICATION (*Possible*)	1. In-vivo dosimetry 2. Dose recalculation with inter-fractional images 3. Transit dosimetry with planned or inter-fraction images

Figure I.1. A general flow chart for SBRT treatment. The final step, delivered dose verification, will be a possible step in radiotherapy.

Challenges remain for the treatment of lung tumors, such as organ motion primarily due to breathing and less accurate dose calculations at interfaces between the tumor and lung due to the different densities. Particularly for lung SBRT treatment, the

tumors are mostly small, and the ratio of tumor surface to tumor volume increases with decreasing target volume, making the interface problem more significant. These challenges can lead to more significant dose discrepancies between the calculated and delivered doses for SBRT treatment. Because this type of treatment uses fewer fractions, inaccurate tumor or normal tissue doses will not be compensated by inter-fraction random errors, which is likely for conventional conformal radiotherapy.

I.E. Dissertation aims and overview

As described above, it is challenging to deliver and verify that the proper radiation dose to the treatment region. To determine this, a technique must be implemented during treatment that can provide confirmation of how the dose is delivered. As described in Section I.C., several possible techniques have been discussed in the literature. Among these techniques, transit dosimetry with planned or inter-fractional images shows advantages in (1) providing sufficient dose information and (2) reflecting the variations in both the patient geometry and the radiation beam. However, this technique involves complex procedures of reconstructing doses inside the patient, leading to increased uncertainty of the estimated dose. Another limitation of the method is that it may not be suitable for on-line dose verification because the time devoted to the calculation may be too long for clinical use. This is significant since on-line dose verification can enable on-line corrections in the beginning of treatment when a large dose discrepancy is found. Thus, on-line correction is extremely important for the radiotherapy techniques involving a very high dose per fraction (4-20 Gy) with few fractions (1-5 fractions), such as hypo-fractioned SBRT. In such cases, preventing the wrong dose from being delivered to the patient is more important than compensating for incorrect dose delivery in the following fractions, especially since it is not always possible to accomplish this.

In addition to achieving on-line corrections, it is highly desirable to improve the accuracy of the calculated dose so as to prevent the wrong dose from being delivered to the patient. One of the main challenges of methods used to calculate doses in TPSs arises when the dose is calculated for a small radiation field (< 5 x 5 cm^2) and at the interface between low and high density medium (e.g. lung-tumor interface). To improve confidence in the dose accuracy under these conditions, one standard method is to compare calculations with measurements in a phantom geometry and then improve the calculation method. However, dose measurements for small field sizes and at interfaces are also challenging. To address this issue, dose investigations under these conditions are needed for both measurements and calculations. Then the accuracy of the dose delivered to the patient can be improved.

This dissertation is the first phase in a series of studies to develop and implement a novel technique of using EPID transit dosimetry to catch errors during treatment. Unlike the methods of dose reconstruction inside patients, the developed technique is simple and applicable, and enables on-line corrections when the discrepancy is greater than the acceptable criteria. To my knowledge, this technique has not been investigated in the published literature. This dissertation discusses two issues: validating the calculation accuracy and exploring EPID transit dosimetry. Validating the calculation accuracy in a TPS not only improves the accuracy of the dose delivered to the patient, but also ensures that the technique of using EPID transit dosimetry for error detection is feasible, especially when the dose error found on the transmission images is used to interpret the dose error inside the patient. The initial study examines several phantom geometries with the emphasis on a tumor-in-lung geometry representative of hypo-fractionated SBRT, and investigates the feasibility of EPID-based transit dosimetry for on-line error detection. The aims of this dissertation are to (1) develop a method to

measure doses with improved measurement accuracy as a function of heterogeneous geometry and implement it for more thorough evaluation of calculation algorithms, and (2) evaluate the feasibility of using the EPID transit dosimetry for error detection. Chapters III to VII each include an introduction to the problems, the details in the methodology, results, discussion of results and limitations, and a short conclusion.

In Chapter II, the literature review relevant to this dissertation is presented, including the challenges of measurements and calculations in the disequilibrium region and the use of portal dosimetry for pre-treatment QA, treatment verification, and error detection.

Chapter III investigates dosimetric characteristics for lung tumor geometries for a 6 MV photon beam. This chapter presents a robust design of the phantom geometry to provide dose information along the beam axis and lateral direction for simple lung and tumor-in-lung geometries. In addition, the detector perturbation in measurements performed in heterogeneous geometries and the approach used to reduce this perturbation are discussed. This methodology is used to investigate the dose variation as a function of heterogeneous geometry, and then measured doses are used to validate the accuracy of the Monte Carlo DPM (Dose Planning Method)[27] implemented in the TPS as an example.

Chapter IV characterizes an EPID for dosimetric verification. This chapter provides a thorough evaluation of the response characterization of a portal imaging device attached to a linear accelerator, such as linearity, field size dependence and non-uniform backscatter effect. A general calibration method for the EPID is explored and accounts for the issues associated with EPID dosimetry. The calibration method converting EPID responses to doses at 8 mm depth in water allows the use of the EPID

as a water-equivalent dosimeter for pre-treatment and treatment verification. The accuracy of the calibration method for pre-treatment verification (without the phantom in the beam) is evaluated for jaw only (MLC-parked)[e], MLC-shaped[f] and IMRT (intensity modulated radiotherapy) fields.

Chapter V evaluates the accuracy of the calibration method proposed in Chapter IV to convert EPID responses to doses at any specific depth in water (for pre-treatment verification). The evaluation is performed for jaw only, MLC-shaped and IMRT fields. The results will support that the calibration method is general and relevant to clinical situations.

Chapter VI uses the calibration method proposed in Chapter IV in transit dosimetry (with the phantom in the beam) for treatment verification. This chapter evaluates the accuracy of the calibration method in transit dosimetry for homogeneous and heterogeneous geometries, and investigates the effect of scatter from the phantom in the beam as a function of phantom thickness and air gap.

Chapter VII investigates the sensitivity of transit dosimetry in error detection for lung SBRT. Through applying the knowledge learned from Chapters III and VI, the EPID is used to explore the sensitivity as a function of known delivery errors that would affect the delivered dose of lung SBRT treatments. These delivery errors include beam delivery and patient specific errors. This chapter also discusses the dosimetric impact of these delivery errors, the possibility of relating the transit dose variation to the in-patient dose variation for these delivery errors, and finally an approach to implement transit

---

[e] The beam is collimated by one or two pairs of lead or tungsten blocks (jaws) and a multi-leaf collimator (MLC) that provide a rectangular opening from 0 X 0 to the maximum field size (40 X 40 cm or a little less) projected at a standard distance such as 100 cm from the x-ray source (focal spot on the target). The MLC can be parked and only the jaws are used to control the radiation fields (only rectangular fields).

[f] The MLC is used to shape the radiation fields (irregular fields).

dosimetry for error detection in clinics.

In Chapter VIII, a summary of the dissertation work and possible future work are presented.

References

1. International Commission on Radiation Units and Measurements. "Prescribing, recording, and reporting photon beam therapy (supplement to ICRU Report 50)" in ICRU Report No. 62, ICRU, Bethesda, MD (1999).

2. A. Piermattei, S. Cilla, G. D'Onofrio, L. Grimaldi, C. Digesu, G. Macchia, F. Deodato and A. G. Morganti, "Large discrepancies between planned and actually delivered dose in IMRT of head and neck cancer. A case report," Tumori 93, 319-322 (2007).

3. B. A. Fraass, J. Smathers and J. Deye, "Summary and recommendations of a National Cancer Institute workshop on issues limiting the clinical use of Monte Carlo dose calculation algorithms for megavoltage external beam radiation therapy," Med Phys 30, 3206-3216 (2003).

4. N. Papanikolaou, J. J. Battista, A. L. Boyer, C. Kappas, E. Klein, T. R. Mackie, M. Sharpe and J. van Dyk, "AAPM Report No. 85: Tissue inhomogeneity corrections for megavoltage photon beams," in AAPM Report No. 85, Medical Physics, Madison, WI, pp1–135 (2004).

5. A. Bel, P. H. Vos, P. T. Rodrigus, C. L. Creutzberg, A. G. Visser, J. C. Stroom and J. V. Lebesque, "High-precision prostate cancer irradiation by clinical application of an offline patient setup verification procedure, using portal imaging," Int J Radiat Oncol Biol Phys 35, 321-332 (1996).

6. C. L. Creutzberg, V. G. Althof, M. D. de Hoog, A. G. Visser, H. Huizenga, A. Wijnmaalen and P. C. Levendag, "A quality control study of the accuracy of patient positioning in irradiation of pelvic fields," Int J Radiat Oncol Biol Phys 34, 697-708 (1996).

7. J. Hanley, M. A. Lumley, G. S. Mageras, J. Sun, M. J. Zelefsky, S. A. Leibel, Z. Fuks and G. J. Kutcher, "Measurement of patient positioning errors in three-dimensional conformal radiotherapy of the prostate," Int J Radiat Oncol Biol Phys 37, 435-444 (1997).

8. D. Yan, J. Wong, F. Vicini, J. Michalski, C. Pan, A. Frazier, E. Horwitz and A. Martinez, "Adaptive modification of treatment planning to minimize the deleterious effects of treatment setup errors," Int J Radiat Oncol Biol Phys 38, 197-206 (1997).

9. P. J. Keall, G. S. Mageras, J. M. Balter, R. S. Emery, K. M. Forster, S. B. Jiang, J. M. Kapatoes, D. A. Low, M. J. Murphy, B. R. Murray, C. R. Ramsey, M. B. Van Herk, S. S. Vedam, J. W. Wong and E. Yorke, "The management of respiratory motion in radiation oncology report of AAPM Task Group 76," Med Phys 33, 3874-3900 (2006).

10. S. C. Erridge, Y. Seppenwoolde, S. H. Muller, M. van Herk, K. De Jaeger, J. S. Belderbos, L. J. Boersma and J. V. Lebesque, "Portal imaging to assess set-up errors, tumor motion and tumor shrinkage during conformal radiotherapy of non-small cell lung cancer," Radiother Oncol 66, 75-85 (2003).

11. L. N. McDermott, M. Wendling, J. J. Sonke, M. van Herk and B. J. Mijnheer, "Anatomy changes in radiotherapy detected using portal imaging," Radiother Oncol 79, 211-217 (2006).

12. B. Fraass, K. Doppke, M. Hunt, G. Kutcher, G. Starkschall, R. Stern and J. Van Dyke, "American Association of Physicists in Medicine Radiation Therapy Committee Task Group

53: quality assurance for clinical radiotherapy treatment planning," Med Phys 25, 1773-1829 (1998).

13. G. P. Beyer, C. W. Scarantino, B. R. Prestidge, A. G. Sadeghi, M. S. Anscher, M. Miften, T. B. Carrea, M. Sims and R. D. Black, "Technical evaluation of radiation dose delivered in prostate cancer patients as measured by an implantable MOSFET dosimeter," Int J Radiat Oncol Biol Phys 69, 925-935 (2007).

14. O. Morin, J. Chen, M. Aubin, A. Gillis, J. F. Aubry, S. Bose, H. Chen, M. Descovich, P. Xia and J. Pouliot, "Dose calculation using megavoltage cone-beam CT," Int J Radiat Oncol Biol Phys 67, 1201-1210 (2007).

15. H. Guan and H. Dong, "Dose calculation accuracy using cone-beam CT (CBCT) for pelvic adaptive radiotherapy," Phys Med Biol 54, 6239-6250 (2009).

16. Y. Yang, E. Schreibmann, T. Li, C. Wang and L. Xing, "Evaluation of on-board kV cone beam CT (CBCT)-based dose calculation," Phys Med Biol 52, 685-705 (2007).

17. V. N. Hansen, P. M. Evans and W. Swindell, "The application of transit dosimetry to precision radiotherapy," Med Phys 23, 713-721 (1996).

18. T. R. McNutt, T. R. Mackie, P. Reckwerdt and B. R. Paliwal, "Modeling dose distributions from portal dose images using the convolution/superposition method," Med Phys 23, 1381-1392 (1996).

19. R. J. Louwe, E. M. Damen, M. van Herk, A. W. Minken, O. Torzsok and B. J. Mijnheer, "Three-dimensional dose reconstruction of breast cancer treatment using portal imaging," Med Phys 30, 2376-2389 (2003).

20. G. Jarry and F. Verhaegen, "Patient-specific dosimetry of conventional and intensity modulated radiation therapy using a novel full Monte Carlo phase space reconstruction method from electronic portal images," Phys Med Biol 52, 2277-2299 (2007).

21. L. N. McDermott, M. Wendling, J. Nijkamp, A. Mans, J. J. Sonke, B. J. Mijnheer and M. van Herk, "3D in vivo dose verification of entire hypo-fractionated IMRT treatments using an EPID and cone-beam CT," Radiother Oncol 86, 35-42 (2008).

22. M. Partridge, M. Ebert and B. M. Hesse, "IMRT verification by three-dimensional dose reconstruction from portal beam measurements," Med Phys 29, 1847-1858 (2002).

23. S. H. Benedict, K. M. Yenice, D. Followill, J. M. Galvin, W. Hinson, B. Kavanagh, P. Keall, M. Lovelock, S. Meeks, L. Papiez, T. Purdie, R. Sadagopan, M. C. Schell, B. Salter, D. J. Schlesinger, A. S. Shiu, T. Solberg, D. Y. Song, V. Stieber, R. Timmerman, W. A. Tome, D. Verellen, L. Wang and F. F. Yin, "Stereotactic body radiation therapy: the report of AAPM Task Group 101," Med Phys 37, 4078-4101 (2010).

24. B. K. Chang and R. D. Timmerman, "Stereotactic body radiation therapy: a comprehensive review," Am J Clin Oncol 30, 637-644 (2007).

25. J. Y. Chang and J. A. Roth, "Stereotactic body radiation therapy for stage I non-small cell lung cancer," Thorac Surg Clin 17, 251-259 (2007).

26. R. D. Timmerman, C. Park and B. D. Kavanagh, "The North American experience with stereotactic body radiation therapy in non-small cell lung cancer," J Thorac Oncol 2, S101-112 (2007).

27. J. Sempau, S. J. Wilderman and A. F. Bielajew, "DPM, a fast, accurate Monte Carlo code optimized for photon and electron radiotherapy treatment planning dose calculations," Phys Med Biol 45, 2263-2291 (2000).

CHAPTER II

LITERATURE REVIEW

In the introduction section, an overview of issues in advanced radiotherapy, such as the challenges in targeting and dose accuracies, has been provided. This dissertation focuses on dosimetric issues associated with lung stereotactic body radiotherapy (SBRT) techniques. These issues include dose uncertainties when small tumors are embedded in low density lung tissues, dose variations due to breathing motion, and the importance of implementing delivered dose verification techniques because of dose uncertainties in beam delivery and the use of an extremely high dose per fraction (from 4 Gy up to 20 Gy) with small treatment fields. The focus of this chapter is a more detailed review of the relevant literature with respect to dose uncertainties in the disequilibrium region and dose variations due to breathing motion, and the methods used for delivered dose verifications. Finally, a summary of how to address these issues in this dissertation is provided.

II.A. Dose uncertainties in the disequilibrium region

In dosimetry, electronic equilibrium exists when the number of electrons with the same energy entering a cavity equals the number of electrons with the same energy leaving the cavity. The equilibrium will generally exist when a radiation field is uniform (i.e. negligible attenuation), no inhomogeneous electric or magnetic fields are present, the atomic composition of the medium is homogeneous, and the density of the medium is

homogeneous (when the stopping power density effect in the medium is significant) (Figure II.1). For clinical beams and human tissues, the stopping power density effect is small. Thus, based on Fano theorem, the equilibrium still exists for the medium with different densities. For broad radiation beams, the disequilibrium mainly appears in the buildup region and close to the edges of radiation fields. While the field size decreases (e.g. ≤ 5 x 5 cm^2 for 6 MV photons), most regions inside the field are in the lateral-disequilibrium region (Figure II.1). This situation is worse when a low-density medium is present, because the electron range in the low-density medium is greater. The increased range of scattered photons and secondary electrons in a low-density medium causes a significant loss of lateral electronic equilibrium and affects the dose to adjacent tissues. For example, for small fields in a heterogeneous geometry (e.g. water-lung-water), the doses in the lung region are smaller compared to a homogeneous geometry (e.g. water only). This is due to more electrons leaving than those entering the lung region, and then electron equilibrium does not exist in that region. Considering the variation in the electron range, the dose decreases significantly in the lung region for increased energies and decreased field sizes.[1-3]

Under equilibrium conditions, dose calculations are simpler and it is easier to measure the dose accurately. However, patients have a more complex geometry with multiple tissue interfaces and a simple algorithm may not be valid in complex geometries. The weakness of calculation algorithms in this situation is due to approximations made in the modeling of electron transport. Current calculation algorithms in treatment planning systems (TPSs) have been modified to better account for complex treatment geometries. However, the accuracy of calculations in disequilibrium conditions can still be questionable because accurate measurements are

needed to validate calculation algorithms in such complex situations. Finally, inaccuracies in dose calculation result in systematic errors in radiotherapy treatments.

Electron equilibrium conditions:

Photon

e₁

v

e₂

e₃

V

Number of e- entering the volume = Number of e- leaving the volume (same energy)

Equilibrium exists in volume v:

1. **The boundaries of v and V are separated by at least electron range (i.e. the volume v is not in the buildup region).**
2. **Attenuation is negligible.**
3. **No inhomogeneous electric or magnetic fields are present.**
4. **The atomic composition of the medium is homogeneous.**
5. **The density of the medium is homogeneous (which may not be necessary for radiotherapy).**

Small field sizes and heterogeneous geometries:

Low density

High density

Lateral electron disequilibrium: Close to the field edge

Large detector perturbation when doing measurements in the disequilibrium region

A small detector size and medium-medium-equivalent materials are needed.

Figure II.1. An illustration of electron equilibrium and disequilibrium.

II.A.1. Challenges in the measurements

A standard method to verify calculation accuracy is to compare with measurements. However, measurements performed in the disequilibrium region are challenging, with no one standard dosimeter and protocol in use. In the situation of small field sizes less than 5 x 5 cm^2, the main problems are the limitation of detector size and the non-tissue equivalence of the materials. The detector should be considerably smaller than the

beam radius when lateral equilibrium is not established in order to get accurate measurements. Because the field sizes are small, the measurement accuracy is also very sensitive to detector setup. Results of output factors, depth dose curves and profiles as a function of field size have been shown to deviate significantly, depending on the detector, when measurements were performed using Si-diodes and cylindrical ion chambers from 0.007 to 0.6 cm^3.[4] The deviation increases with decreasing field size.

To deal with the challenge of small field measurement, cross-comparisons with various detectors are usually performed and the most reliable data are selected.[5-8] Table I.1 shows common detectors used in measurement for small field dosimetry. Each detector has individual strengths and weaknesses. Corrections may be needed for individual detectors to achieve reliable data. Although point dosimeters are well-developed and could provide one-dimensional (1D) dose information, the information is still not sufficient for validating calculation accuracy. In contrast, three-dimensional (3D) dosimeters, such as gel, can provide the most information but these techniques are still under development. Due to the limitations of point and 3D dosimeters, two-dimensional (2D) dosimeters have several advantages for dose measurements in small field dosimetry. These include lower sensitivity to setup error and more dose information compared to point dosimeters.

Table II.1. Common detectors used in small field dosimetry (summarized based on Das *et al*[4]).

Detector	Size	Dimension	Strengths	Weaknesses	Example
Ion chamber	$10^{-1}\sim10^{-3}$ cm^3	1D	Availability, and independence of energy, dose and dose rate	Low signal to noise for small volume chamber. Fluence perturbation and volume effect for large volume chamber	Spherical, cylindrical and parallel
Semi-conductor diode	$10^{-2}\sim10^{-3}$ cm^3	1D	Quick response (μs), excellent spatial resolution, absence of external bias, and high sensitivity	Temperature, dose rate, energy, and incident angle dependence	SFD and PFD
Diamond	$1\sim6$ mm^3	1D	Large signal, tissue-equivalent materials and no angular dependence	Expensive detector and dose rate dependence (correction is required)	
TLD	$1\sim10$ mm^3	1D	Tissue-equivalent material and ability for in-vivo dosimetry	Limited accuracy, time consuming, and supra-linearity to dose	Rod, chip and powder
MOSFET	0.2×0.2 mm^2	1D	Ability for in-vivo dosimetry and independence of MV beam, dose rate and temperature. Similarity to conventional detectors (reproducibility, linearity and angular responses)	Short life, repeated calibration is required for accurate measurements	
Radiographic film		2D	High spatial resolution	Energy and processing condition dependence	XV and EDR
Radiochromic film		2D	Tissue-equivalent material, high spatial resolution, and light insensitivity	Expensive detector, noise and non-uniformity	EBT
Bang gel		3D	Tissue equivalent material, high spatial resolution and energy independence	Considerable fabrication time and image artifacts	MAGIC gel
Others: Radiophotoluminescent glass plate, Scintillator, Alanine pallets					

Other approaches have been proposed when measuring beam profiles in small fields with large volume detectors. The first method is an extrapolation of measurements to zero detector size,[9-11] and the second is a deconvolution of measurements using a detector dose response kernel.[12-15] Many authors also have proposed Monte Carlo (MC) systems as suitable tools for small beam commissioning.[16] The MC method provides a "gold" standard because it can simulate energy deposition per each radiation particle in a given material. However, MC results should be validated with measurements before being used as the standard, because the accuracy of MC results not only depends on the modeling of physical interactions in the medium but also depends on modeling the configuration of the machine head.

For measurements in a heterogeneous geometry, an ideal detector requires the same characteristics as those required for measurements in small field sizes, namely a minimum sensitive volume and water-equivalence to reduce fluence perturbation when measuring doses in electronic disequilibrium regions. In addition, the dosimeter should provide high spatial resolution of dose information because steep dose gradients appear at penumbras and interfaces. Common detectors used in heterogeneity measurements are similar to those used in small field measurements (Table II.1).

II.A.2. Challenges in the calculations

The accuracy of planned doses on patients depends on the modeling used in calculation algorithms. Papanikolaou *et al*[17] have summarized various calculation correction methods in the presence of tissue heterogeneity. The correction methods can be divided into four categories: (1) 1D TERMA, (2) 3D TERMA, (3) 1D DOSE, and (4) 3D DOSE. TERMA is defined as "total energy released per unit mass" and is given as the product of the total mass attenuation coefficient (μ/ρ) and the energy fluence (ψ) at a point.

KERMA is defined as "kinetic energy release to charged particles only per unit mass", and for monoenergetic photons, is given as the product of mass energy transfer coefficient (μ_{tr}/ρ) and the energy fluence (ψ). DOSE is the collision KERMA, which means the absorbed energy along the charged particle tracks per unit mass, and for monoenergetic photons, is given by the product of mass energy absorption coefficient (μ_{en}/ρ) and the energy fluence (ψ). Therefore, correction methods based on the DOSE concept provide more accurate results but the corrections are more complex and calculation times are longer. Currently, mainly pencil beam (PB, 1D DOSE category) or convolution/superposition (CVSP, 3D DOSE category) are implemented in TPSs for heterogeneity corrections.

Several studies have reported on the accuracy of current treatment planning algorithms: PB and CVSP, and MC methods for heterogeneous and small field conditions.[17-22] Most conventional treatment planning algorithms do not accurately model secondary electron transport. As described previously, the considerable range of secondary electrons is responsible for the loss of electronic equilibrium in narrow high-energy photon beams, an effect that is even more pronounced when the beam passes through low-density regions. Particularly in inhomogeneous media the use of algorithms that do not model electron transport adequately may lead to errors in dose prediction. PB algorithms are less accurate because they use an 1D density correction that does not accurately model the distribution of secondary electrons in media of different density. Doses are scaled according to the radiological depth along a ray line from the radiation source to the calculation point, not accounting for the effects of side and backscattered radiation. In commercial TPSs, CVSP algorithms are the most accurate algorithms for dose calculations in heterogeneities, because they take into account secondary electron transport and energy deposition from scattered photons.[23-25] MC methods[26-28] are

thought most accurate because they simulate all physical interactions leading to dose deposition, but they may be time consuming for clinical use.

Regarding the calculation accuracy for various planning systems, Paelinck *et al*[21] compared lung calculated doses using a MC method and two CVSP algorithms (Pinnacle and Helax-TMS). A deviation of about 3.6% was found beyond the lung region between the MC and Pinnacle CV/SP algorithms. A deviation up to 5.6% was found for small fields in the lung region between the MC and Helax-TMS CVSP algorithms, but the agreement was better at depths beyond the lung region between the two methods. Krieger *et al*[20] evaluated the accuracy of dose predicted in a heterogeneous multi-layer phantom by a MC method, and a PB and collapsed cone CVSP algorithms implemented in Helax-TMS. The PB generated very large errors for the dose in the vicinity of interfaces and within low-density regions. Bragg *et al*[18] investigated the accuracy of photon dose calculations performed by an analytical anisotropic algorithm (AAA), implemented in the Eclipse TPSs, in homogeneous and inhomogeneous media and in simulated treatment plans. The AAA is a type of CVSP model that utilizes pre-calculated treatment-unit specific parameters together with beam data measured on the end user's linear accelerators to model the clinical treatment beams. The inhomogeneity correction is implemented through scaling photon and electron scatter kernels anisotropically, according to the electron density distribution of the treated medium. The algorithm was shown to be more accurate than the PB, particularly in the presence of low density heterogeneities.

II.B. Dose variations due to breathing motion

Another important issue when treating lung tumors is the motion of the tumor and/or critical organs due to the breathing. The motion can be divided into inter-fraction and

intra-fraction motion. The inter-fraction motion is the movement of the tumor or organ movement from day to day for each fraction of treatment, and leads to a shift (for small number of fractions) or blurring (for large number of fractions) of dose distributions. The intra-fraction motion is the movement of the tumor or organ during beam delivery, and leads to a blurring of dose distributions (Figure II.2). The challenge when dealing with the effects of breathing needs to be assessed individually. The moving amplitude, trajectory, frequency and deformation pattern are differ between individuals. For lung SBRT treatment, motion management is usually used to reduce the motion to acceptable magnitude, e.g. 5 mm. However, the question is how the residual movement affects doses delivered to patients. Both organ movement and air volume variations due to breathing will make patient geometries different from what was used in planning processes and result in variations in the delivered dose.

Inter-fraction motion   **Intra-fraction motion**
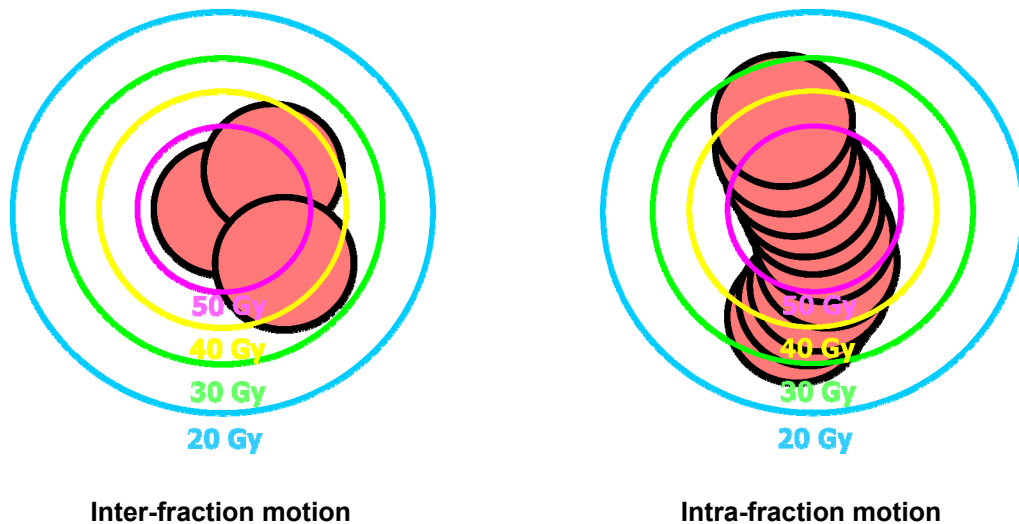
Figure II.2. An illustration of (tumor) dose variations due to inter-faction and intra-fraction motion.

II.C. Electronic portal imaging devices (EPID) for dosimetric verification

As described in Chapter I, treatment uncertainties make it advantageous to implement a dose verification technique in clinics. Among several methods mentioned in Chapter I,

the method using electronic portal imaging devices (EPIDs) can provide sufficient information during beam delivery. This device can be used for both position and dosimetric verification. The interest of EPID dosimetry is increasing because of its desirable characteristics, such as fast image acquisition, high resolution, digital format, and convenience. This section provides an overview of EPID devices and techniques for dosimetric verification.

II.C.1. Electronic portal imaging devices (EPIDs)

Several types of EPIDs have been investigated for dosimetric verification.[29] The most common type of EPID is the amorphous-silicon (a-Si) EPID or flat-panel imager. These flat-panel detectors have been divided into two classifications, direct and indirect configurations. The indirect configuration uses a scintillator screen to convert deposited energy to optical photons, while the direct configuration does not use a scintillator and the photodiode array directly senses the radiation energy.[30] The indirect a-Si EPID is a common configuration with modern linear accelerators (LINACs) because of its great sensitivity, which is preferable for positioning verification and dosimetric applications. However, unlike direct flat-panel detectors, the indirect a-Si EPID does not show a similar response to ion chamber, and such device exhibits a scattering phenomenon, which needs to be corrected.

This general description of indirect a-Si system uses a Varian aS500 EPID (Palo Alto, CA) as an example. A sensitive area of 40×30 cm^2 is divided into 512×384 pixels of 0.784×0.784 mm^2. The system includes (1) an image detection unit (IDU), featuring the detector and accessory electronics, (2) an image acquisition system (IAS3), containing drive and acquisition electronics and interfacing hardware, and (3) a workstation located outside the treatment room.[31] The principle detector components

24

include a 1 mm copper layer, a 0.34 mm scintillating layer ($Gd_2O_2S:Tb$) and 1.1 mm amorphous silicon flat-panel light sensor (including photodiode and thin film transistor) (Figure II.3). The copper layer provides buildup and also absorbs low energy scattered radiation from the machine head and patient. The scintillating layer converts the incident radiation into light photons. The photodiode converts light photons into the electric charge and stores it, and the thin film transistor controls the signal during the readout.[31-33] There are various acquisition modes, depending on the application. Typically, an integrated mode is selected to acquire all dose information during beam delivery.

Protective cover (9 mm)
Cu (1 mm, 0.896 g/cm^2)
$Gd_2O_2S:Tb$ (0.34 mm, 0.134 g/cm^2)
Photodiode on glass substrate (1.1 mm)
Protective cover (9 mm)
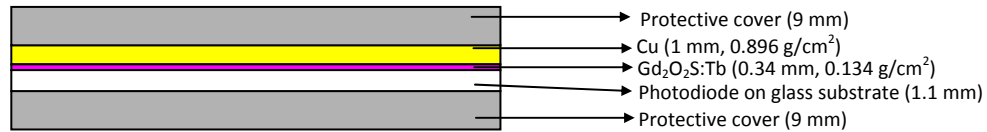
Figure II.3. Varian aS500 detailed detector configuration (re-plotted).[33]

Various dosimetric characteristics of a-Si EPIDs have been reported.[31, 32, 34-42] The dose-response relationship is independent of dose rate and approximately linear with integrated doses.[30, 35] The linearity is good to within 2% for monitor units (MU) larger than 30.[31] However, EPIDs exhibit a relative under-response (4%-10% lower response-to-MU ratio) for low MUs. This under-response is attributed to charge trapping within the photodiode layer, resulting in ghosting effects.[36] The ghosting effect is a gain effect whereby trapped charges change the electric field strength of the bulk and surface layers, lasting minutes and affecting subsequent images.[29] It depends on irradiation time and the dose per frame, not on dose or dose-rate directly.[35, 36] However, it is only detected under extreme conditions, meaning that it may not have an impact on integrated dosed acquired from an entire field exposure. The stability of the detector over the short term (day-to-day) and long term (over one year period) was found to be

within 2%.[31] With respect to energy dependence, the EPID exhibits over-response at low photon energies compared to water due to components with high atomic number.[43] Therefore, the EPID response will depend on the off-axis position (more low-energy photons off-axis than on the central axis), thicknesses of the patient or phantom (beam hardening), field size, and magnitude of leaf transmission (beam hardening).[31, 32, 43-48] Several studies added buildup material on the top of the EPID to attenuate low-energy scattered photons and to ensure measurements are performed beyond the depth of maximum dose. Another characteristic found in EPIDs is the optical photon scatter (known as glare effect). This is possibly due to optical dispersion within the phosphor layer, resulting in significant contribution to the image.[43]

II.C.2. Dosimetric verification methods

There are two primary categories of EPID use for dosimetry: (1) pre-treatment verification and (2) treatment verification, depending on when measurements are performed.[29] Van Elmpt *et al*[29] provided a detailed review of these approaches. The purpose of each approach is different. The approaches relevant to this dissertation are described.

II.C.2.i. Pre-treatment verification

Pre-treatment verification is usually performed to confirm beam delivery parameters by comparing measurements with predicted results. This verification approach has been widely used for IMRT techniques before treatment plans are used for patient delivery. However, ion chambers, films or 2D detector arrays are primary tools for pre-treatment verification. Because of several advantages in EPIDs, some institutions have begun using EPIDs instead of ion chambers or films. The EPID images are acquired for each

field without any phantoms or patients between the source and detector, which is called a non-transmission image.

There are two methods to use these non-transmission images for dosimetric verification. In the first method, the EPID raw (or dose-to-water converted) data are compared with predicted EPID raw responses (or dose-to-water) at the level of the EPID.[31, 33] For example, Van Esch *et al*[31] reported on a method based on a single pencil beam dose calculation algorithm with parameters fitted from measurements with EPIDs rather than ion chamber in water. The predicted portal dose image (PDI) is calculated from convolving the fluence with a point spread function of the detector response and accounting for collimator scattering and off-axis ratio corrections. Then, the predicted portal dose image is compared with the measured portal dose image. In the second method, the EPID data are converted to energy fluence and this energy fluence is used to reconstruct 2D or 3D doses inside patients or phantoms.[49-53] For example, Warkentin *et al*[49] deconvolved EPID responses with a (EPID) dose–glare kernel to get primary energy fluence. 2D dose distributions at a specific depth in phantom were reconstructed by convolving the energy fluence with a phantom scatter kernel. The derived dose distributions are then compared with calculated dose distributions at the same depth using TPSs. This way has an advantage over the first method, that is, the calculation uncertainty of TPSs in the leaf configuration (e.g. tongue-and-groove effect[9]) can be estimated at the same time. In addition to that, Van Elmpt *et al*[50-53] derived the primary energy fluence from the EPID for each beam and recalculated 3D doses in homogeneous or heterogeneous phantoms and patients using a MC method with

---

[9] In order to reduce the inter-leaf leakage between the adjacent leaves, the leaves are designed with one side of the leaf protruding outward ("tongue") and the other recessing inward ("groove") so that the central parts of the adjacent leaves fit like a jigsaw puzzle. This overlap of the leaves reduces the extent of radiation leakage through interleaf gaps, which are necessary for leaf motion relative to each other. This is called a tongue-and-groove effect and it gives rise to higher radiation leakage than that through the middle body of the leaves but less than what it would be if the leaf sides were designed plane-faced.

derived energy fluence. For dose reconstruction in patients, the images can be either planned CT images or images acquired during treatment, which represents actual patient geometry at that time.

II.C.2.ii. Treatment verification

The weakness of the pre-treatment verification method is that the provided information may not represent actual doses delivered to patients. In contrast, EPID responses acquired during beam delivery (called transmission images) include all information, such as beam delivery and patient-specific geometry. If an independent calculation method is used for the EPID dose reconstruction, then the accuracy of TPSs could be also verified. However, the transmission dosimetry is more complicated than the non-transmission dosimetry. The scattering from the patient will increase noise in EPID responses and decrease the accuracy of derived primary energy fluence. The magnitude of scattering will depend on various factors, such as field size, patient geometry, and the air gap between the patient and detector. For the primary energy fluence to be accurate, these factors must be considered. In addition, models based on homogeneous phantoms need to be modified to account for tissue heterogeneities in patients.

There are also two methods for using transmission images. In the first method, the doses can be verified at the EPID level.[54-57] For example, Van Elmpt *et al*[56] adapted the portal dose prediction model proposed by Pasma *et al*.[54] This model used pencil beam scatter kernels and was based on a portal dose image without the patient in the beam in combination with the radiological thickness of the patient to calculate the portal dose image behind the patient. Then the calculated portal dose image can be compared with the measured portal dose to verify actual doses delivered to patients. In the second method, the 2D and 3D doses can be reconstructed in patients.[58-64] The dose

reconstruction procedure involves the conversion of EPID response to dose, the correction of scatter inside the EPID and from the patient, the derivation of entrance energy fluence using attenuation information from planned CT images or CBCT images during treatment, and then dose reconstruction inside patients.

II.C.3. Error detection using EPID dosimetry

Various methods of EPID dosimetry were discussed in Section II.C.2. In addition, as described in Chapter I, there are four types of uncertainties resulting in delivered dose errors: (1) the functioning of treatment equipment, (2) data transfer from TPSs to treatment equipment, (3) patient specific uncertainties, and (4) plan or calculation uncertainties. Pre-treatment verification (non-transmission data) at the EPID level is only able to detect errors related to machine malfunction and data transfer, while dose reconstruction inside the phantom from non-transmission data can provide additional information, that is, calculation accuracy in TPSs (if an independent algorithm is used for EPID dose reconstruction). On the other hand, treatment verification (transmission data) at the EPID level is able to detect errors related to machine malfunction, data transfer and patient-specific uncertainties. Dose reconstruction inside the patient from transmission data can also detect errors from calculation uncertainties (if independent algorithm is used for EPID dose reconstruction).[29]

In-vivo dose reconstruction during treatment can be a powerful technique for delivered dose verification. However, this technique is only for dose verification and relying on it alone to detect or distinguish all types of errors is not necessarily efficient for clinical use. Appropriate steps to improve the accuracy of the dose delivered to the patient are (1) to reduce the calculation uncertainty to within an acceptable level, (2) to use EPIDs or other detectors for pre-treatment verification to detect errors related to

machine and data transfer, (3) to use image guided systems to check the patient's position before the beginning of treatment, and (4) to use delivered dose verification techniques to catch unpredicted errors, because delivering the correct dose to the patient is more important than adapting plans or compensating doses in subsequent fractions. Especially for single or hypo-fractionated treatment techniques, there may be no chance to compensate for errors. However, the use of EPID dosimetry for treatment verification is undoubtedly helpful in radiotherapy. The information from EPID dosimetry during treatment provides evidence of how accurate are the doses delivered to patients and can be used to track unpredictable discrepancies (such as missing the tumor) during treatment. The 2D information at the EPID level during treatment is sufficient. From a quality assurance perspective, the important point is whether or not there has been a change which impacts dose to the patient. For example, this information is used to trigger a review of treatment when the discrepancy is larger than acceptance criteria. Another issue associated with in-vivo dose reconstruction is the procedure involving several corrections in the EPID, conversion of entrance fluence and dose reconstruction algorithms. Due to this complexity, the performance of a dose reconstruction model is more uncertain, and may limit its application for on-line correction.

II.D. Summary

Several issues in current radiotherapy are presented in this chapter, particularly for lung SBRT. To ensure correct doses delivered to patients with lung treatment, the accuracy of the TPS calculation must be validated for electron disequilibrium conditions. Few studies discussed the dose variation in a tumor-in-lung geometry.[2, 65, 66] While Rice *et al*[65] and Yorke *et al*[66] examined the dose variation along the beam axis, Charland *et al*[2] examined the dose variation along the lateral direction. A dose variation along the beam axis and lateral direction has not previously been investigated for different tumor

positions. To address this issue, in this dissertation, dose variations as a function of heterogeneous geometry are investigated for both measurements and calculations (Chapter III).

The second aim of this dissertation is to evaluate the feasibility of using the EPID transit dosimetry for error detection. To achieve this aim, several issues related to EPID transit dosimetry are examined. As mentioned previously, most EPIDs are indirect a-Si EPIDs. This device is composed of high Z materials and responds differently than water. Solutions for using EPIDs for pre-treatment quality assurance (QA) when no patient is present have been provided by several studies. [31, 32, 39-46, 67-69] These studies offered correction methods to the EPID response, but they calculated the predicted EPID response using the fluence and the calculated response was compared with the measured response. This approach cannot provide information on the potential difference between the measured dose and the calculated dose. The use of the device as a water-equivalent dosimeter provides the advantage of a direct comparison to the calculated dose which was obtained using a TPS. For example, Vial *et al*[70] and Sabet *et al*[71] modified the indirect configuration to direct configuration in order to use the EPID as a water-equivalent dosimeter. Alternatively, several calibration methods have been discussed in order to convert the indirect a-Si EPID response into dose in water.[38, 49, 72-74] However, those methods were not simple and general enough to implement in clinics. Therefore, to correct this limitation, this dissertation first explores a general and independent calibration method to use an EPID as a water-equivalent dosimeter. This method can be used for pre-treatment QA (without any patient in the beam) (Chapter IV and V). In a real situation, the EPID response is collected while the patient is treated. Extending the proposed calibration method for transit dosimetry (with the patient in the beam) poses a challenge because the scatter from the patient affects the accuracy of

EPID transit dosimetry. Therefore, this dissertation secondly investigates the scatter from the phantom as a function of phantom thickness and air gap, and determines correction parameters for different geometries (Chapter VI). Finally, a novel and simple technique of using EPID transit dosimetry for error detection is developed. This technique provides potential guidance for assessing the need for on-line corrections to prevent significant errors before they harm patients' lives. To use transit dosimetry for error detection, criteria to determine whether the error is acceptable or not are needed. The criteria likely depend on the sensitivity of transit dosimetry on delivery errors. In addition, the error sensitivity determines if the proposed error detection technique is feasible. Therefore, this dissertation finally investigates the sensitivity of transit dosimetry to various test errors, and discusses a method to relate the transit dose variation (using the developed EPID calibration method) to the in-phantom dose variation (using the validated calculation method) as well as the feasibility of using the proposed EPID transit dosimetry in error detection (Chapter VII).

This dissertation develops a measurement method and designs complex geometries to examine interface and small field dosimetry. This information can evaluate the accuracy of calculation algorithms more thoroughly, and then algorithms can be improved when necessary. In addition to that, this dissertation develops and validates a calibration method for the EPID so that this device can be used as a water-equivalent dosimeter unlike previous models, which provides a direct comparison to calculations from TPSs. The potential of using the EPID as a transit dosimeter for error detection is also discussed. By improving the calculation accuracy and implementing an on-line correction technique, the dose delivered to the patient can be confirmed and the safety of patient treatments can be improved in radiotherapy.

References

1. M. F. Tsiakalos, S. Stathakis, G. A. Plataniotis, C. Kappas and K. Theodorou, "Monte Carlo dosimetric evaluation of high energy vs low energy photon beams in low density tissues," Radiother Oncol 79, 131-138 (2006).

2. P. M. Charland, I. J. Chetty, S. Yokoyama and B. A. Fraass, "Dosimetric comparison of extended dose range film with ionization measurements in water and lung equivalent heterogeneous media exposed to megavoltage photons," J Appl Clin Med Phys 4, 25-39 (2003).

3. M. A. Hunt, G. E. Desobry, B. Fowble and L. R. Coia, "Effect of low-density lateral interfaces on soft-tissue doses," Int J Radiat Oncol Biol Phys 37, 475-482 (1997).

4. I. J. Das, G. X. Ding and A. Ahnesjo, "Small fields: Nonequilibrium radiation dosimetry," Med Phys 35, 206-215 (2008).

5. L. Archambault, A. S. Beddar, L. Gingras, F. Lacroix, R. Roy and L. Beaulieu, "Water-equivalent dosimeter array for small-field external beam radiotherapy," Med Phys 34, 1583-1592 (2007).

6. C. W. Cheng, S. H. Cho, M. Taylor and I. J. Das, "Determination of zero-field size percent depth doses and tissue maximum ratios for stereotactic radiosurgery and IMRT dosimetry: comparison between experimental measurements and Monte Carlo simulation," Med Phys 34, 3149-3157 (2007).

7. G. X. Ding, "An investigation of accelerator head scatter and output factor in air," Med Phys 31, 2527-2533 (2004).

8. O. A. Sauer and J. Wilbert, "Measurement of output factors for small photon beams," Med Phys 34, 1983-1988 (2007).

9. D. J. Dawson, J. M. Harper and A. C. Akinradewo, "Analysis of physical parameters associated with the measurement of high-energy x-ray penumbra," Med Phys 11, 491-497 (1984).

10. D. J. Dawson, N. J. Schroeder and J. D. Hoya, "Penumbral measurements in water for high-energy x rays," Med Phys 13, 101-104 (1986).

11. R. K. Rice, J. L. Hansen, G. K. Svensson and R. L. Siddon, "Measurements of dose distributions in small beams of 6 MV x-rays," Phys Med Biol 32, 1087-1099 (1987).

12. F. Garcia-Vicente, J. M. Delgado and C. Peraza, "Experimental determination of the convolution kernel for the study of the spatial response of a detector," Med Phys 25, 202-207 (1998).

13. P. D. Higgins, C. H. Sibata, L. Siskind and J. W. Sohn, "Deconvolution of detector size effect for small field measurement," Med Phys 22, 1663-1666 (1995).

14. G. Bednarz, M. Saiful Huq and U. F. Rosenow, "Deconvolution of detector size effect for output factor measurement for narrow Gamma Knife radiosurgery beams," Phys Med Biol 47, 3643-3649 (2002).

15. E. Pappas, T. G. Maris, A. Papadakis, F. Zacharopoulou, J. Damilakis, N. Papanikolaou and N. Gourtsoyiannis, "Experimental determination of the effect of detector size on profile measurements in narrow photon beams," Med Phys 33, 3700-3710 (2006).

16. P. Francescon, S. Cora and C. Cavedon, "Total scatter factors of small beams: a multidetector and Monte Carlo study," Med Phys 35, 504-513 (2008).

17. N. Papanikolaou, J. J. Battista, A. L. Boyer, C. Kappas, E. Klein, T. R. Mackie, M. Sharpe and J. van Dyk, "AAPM Report No. 85: Tissue inhomogeneity corrections for megavoltage photon beams," in AAPM Report No. 85, Medical Physics, Madison, WI, pp1–135 (2004).

18. C. M. Bragg and J. Conway, "Dosimetric verification of the anisotropic analytical algorithm for radiotherapy treatment planning," Radiother Oncol 81, 315-323 (2006).

19. B. Vanderstraeten, N. Reynaert, L. Paelinck, I. Madani, C. De Wagter, W. De Gersem, W. De Neve and H. Thierens, "Accuracy of patient dose calculation for lung IMRT: A comparison of Monte Carlo, convolution/superposition, and pencil beam computations," Med Phys 33, 3149-3158 (2006).

20. T. Krieger and O. A. Sauer, "Monte Carlo- versus pencil-beam-/collapsed-cone-dose calculation in a heterogeneous multi-layer phantom," Phys Med Biol 50, 859-868 (2005).

21. L. Paelinck, N. Reynaert, H. Thierens, W. De Neve and C. De Wagter, "Experimental verification of lung dose with radiochromic film: comparison with Monte Carlo simulations and commercially available treatment planning systems," Phys Med Biol 50, 2055-2069 (2005).

22. A. O. Jones and I. J. Das, "Comparison of inhomogeneity correction algorithms in small photon fields," Med Phys 32, 766-776 (2005).

23. T. R. Mackie, J. W. Scrimger and J. J. Battista, "A convolution method of calculating dose for 15-MV x rays," Med Phys 12, 188-196 (1985).

24. A. Ahnesjo, "Collapsed cone convolution of radiant energy for photon dose calculation in heterogeneous media," Med Phys 16, 577-592 (1989).

25. N. Papanikolaou, T. R. Mackie, C. Meger-Wells, M. Gehring and P. Reckwerdt, "Investigation of the convolution method for polyenergetic spectra," Med Phys 20, 1327-1336 (1993).

26. I. J. Chetty, B. Curran, J. E. Cygler, J. J. DeMarco, G. Ezzell, B. A. Faddegon, I. Kawrakow, P. J. Keall, H. Liu, C. M. Ma, D. W. Rogers, J. Seuntjens, D. Sheikh-Bagheri and J. V. Siebers, "Report of the AAPM Task Group No. 105: Issues associated with clinical implementation of Monte Carlo-based photon and electron external beam treatment planning," Med Phys 34, 4818-4853 (2007).

27. D. W. Rogers, B. A. Faddegon, G. X. Ding, C. M. Ma, J. We and T. R. Mackie, "BEAM: a Monte Carlo code to simulate radiotherapy treatment units," Med Phys 22, 503-524 (1995).

28. J. Sempau, S. J. Wilderman and A. F. Bielajew, "DPM, a fast, accurate Monte Carlo code optimized for photon and electron radiotherapy treatment planning dose calculations," Phys Med Biol 45, 2263-2291 (2000).

29. W. van Elmpt, L. McDermott, S. Nijsten, M. Wendling, P. Lambin and B. Mijnheer, "A literature review of electronic portal imaging for radiotherapy dosimetry," Radiother Oncol 88, 289-309 (2008).

30. Y. El-Mohri, L. E. Antonuk, J. Yorkston, K. W. Jee, M. Maolinbay, K. L. Lam and J. H. Siewerdsen, "Relative dosimetry using active matrix flat-panel imager (AMFPI) technology," Med Phys 26, 1530-1541 (1999).

31. A. Van Esch, T. Depuydt and D. P. Huyskens, "The use of an aSi-based EPID for routine absolute dosimetric pre-treatment verification of dynamic IMRT fields," Radiother Oncol 71, 223-234 (2004).

32. C. Kirkby and R. Sloboda, "Consequences of the spectral response of an a-Si EPID and implications for dosimetric calibration," Med Phys 32, 2649-2658 (2005).

33. J. V. Siebers, J. O. Kim, L. Ko, P. J. Keall and R. Mohan, "Monte Carlo computation of dosimetric amorphous silicon electronic portal images," Med Phys 31, 2135-2146 (2004).

34. L. E. Antonuk, Y. El-Mohri, W. Huang, K. W. Jee, J. H. Siewerdsen, M. Maolinbay, V. E. Scarpine, H. Sandler and J. Yorkston, "Initial performance evaluation of an indirect-detection, active matrix flat-panel imager (AMFPI) prototype for megavoltage imaging," Int J Radiat Oncol Biol Phys 42, 437-454 (1998).

35. L. N. McDermott, R. J. Louwe, J. J. Sonke, M. B. van Herk and B. J. Mijnheer, "Dose-response and ghosting effects of an amorphous silicon electronic portal imaging device," Med Phys 31, 285-295 (2004).

36. L. N. McDermott, S. M. Nijsten, J. J. Sonke, M. Partridge, M. van Herk and B. J. Mijnheer, "Comparison of ghosting effects for three commercial a-Si EPIDs," Med Phys 33, 2448-2451 (2006).

37. P. Winkler, A. Hefner and D. Georg, "Dose-response characteristics of an amorphous silicon EPID," Med Phys 32, 3095-3105 (2005).

38. S. M. Nijsten, W. J. van Elmpt, M. Jacobs, B. J. Mijnheer, A. L. Dekker, P. Lambin and A. W. Minken, "A global calibration model for a-Si EPIDs used for transit dosimetry," Med Phys 34, 3872-3884 (2007).

39. C. Kirkby and R. Sloboda, "Comprehensive Monte Carlo calculation of the point spread function for a commercial a-Si EPID," Med Phys 32, 1115-1127 (2005).

40. P. B. Greer, "Correction of pixel sensitivity variation and off-axis response for amorphous silicon EPID dosimetry," Med Phys 32, 3558-3568 (2005).

41. P. B. Greer and C. C. Popescu, "Dosimetric properties of an amorphous silicon electronic portal imaging device for verification of dynamic intensity modulated radiation therapy," Med Phys 30, 1618-1627 (2003).

42. P. B. Greer, P. Vial, L. Oliver and C. Baldock, "Experimental investigation of the response of an amorphous silicon EPID to intensity modulated radiotherapy beams," Med Phys 34, 4389-4398 (2007).

43. B. M. McCurdy, K. Luchka and S. Pistorius, "Dosimetric investigation and portal dose image prediction using an amorphous silicon electronic portal imaging device," Med Phys 28, 911-924 (2001).

44. W. Li, J. V. Siebers and J. A. Moore, "Using fluence separation to account for energy spectra dependence in computing dosimetric a-Si EPID images for IMRT fields," Med Phys 33, 4468-4480 (2006).

45. P. B. Greer, P. Cadman, C. Lee and K. Bzdusek, "An energy fluence-convolution model for amorphous silicon EPID dose prediction," Med Phys 36, 547-555 (2009).

46. P. Vial, P. B. Greer, P. Hunt, L. Oliver and C. Baldock, "The impact of MLC transmitted radiation on EPID dosimetry for dynamic MLC beams," Med Phys 35, 1267-1277 (2008).

47. W. Swindell and P. M. Evans, "Scattered radiation in portal images: a Monte Carlo simulation and a simple physical model," Med Phys 23, 63-73 (1996).

48. S. R. Ozard and E. E. Grein, "Analytical calculation of the portal scatter to primary dose ratio: an EGS4 Monte Carlo and experimental validation at large air gaps," Phys Med Biol 46, 1719-1736 (2001).

49. B. Warkentin, S. Steciw, S. Rathee and B. G. Fallone, "Dosimetric IMRT verification with a flat-panel EPID," Med Phys 30, 3143-3155 (2003).

50. W. van Elmpt, S. Nijsten, B. Mijnheer, A. Dekker and P. Lambin, "The next step in patient-specific QA: 3D dose verification of conformal and intensity-modulated RT based on EPID dosimetry and Monte Carlo dose calculations," Radiother Oncol 86, 86-92 (2008).

51. W. van Elmpt, S. Petit, D. De Ruysscher, P. Lambin and A. Dekker, "3D dose delivery verification using repeated cone-beam imaging and EPID dosimetry for stereotactic body radiotherapy of non-small cell lung cancer," Radiother Oncol 94, 188-194 (2010).

52. W. J. van Elmpt, S. M. Nijsten, A. L. Dekker, B. J. Mijnheer and P. Lambin, "Treatment verification in the presence of inhomogeneities using EPID-based three-dimensional dose reconstruction," Med Phys 34, 2816-2826 (2007).

53. W. J. van Elmpt, S. M. Nijsten, R. F. Schiffeleers, A. L. Dekker, B. J. Mijnheer, P. Lambin and A. W. Minken, "A Monte Carlo based three-dimensional dose reconstruction method derived from portal dose images," Med Phys 33, 2426-2434 (2006).

54. K. L. Pasma, B. J. Heijmen, M. Kroonwijk and A. G. Visser, "Portal dose image (PDI) prediction for dosimetric treatment verification in radiotherapy. I. An algorithm for open beams," Med Phys 25, 830-840 (1998).

55. K. L. Pasma, S. C. Vieira and B. J. Heijmen, "Portal dose image prediction for dosimetric treatment verification in radiotherapy. II. An algorithm for wedged beams," Med Phys 29, 925-931 (2002).

56. W. J. van Elmpt, S. M. Nijsten, B. J. Mijnheer and A. W. Minken, "Experimental verification of a portal dose prediction model," Med Phys 32, 2805-2818 (2005).

57. T. R. McNutt, T. R. Mackie, P. Reckwerdt, N. Papanikolaou and B. R. Paliwal, "Calculation of portal dose using the convolution/superposition method," Med Phys 23, 527-535 (1996).

58. R. Boellaard, M. Essers, M. van Herk and B. J. Mijnheer, "New method to obtain the midplane dose using portal in vivo dosimetry," Int J Radiat Oncol Biol Phys 41, 465-474 (1998).

59. R. Boellaard, M. van Herk and B. J. Mijnheer, "A convolution model to convert transmission dose images to exit dose distributions," Med Phys 24, 189-199 (1997).

60. R. Boellaard, M. van Herk, H. Uiterwaal and B. Mijnheer, "Two-dimensional exit dosimetry using a liquid-filled electronic portal imaging device and a convolution model," Radiother Oncol 44, 149-157 (1997).

61. R. Boellaard, M. van Herk, H. Uiterwaal and B. Mijnheer, "First clinical tests using a liquid-filled electronic portal imaging device and a convolution model for the verification of the midplane dose," Radiother Oncol 47, 303-312 (1998).

62. M. Wendling, R. J. Louwe, L. N. McDermott, J. J. Sonke, M. van Herk and B. J. Mijnheer, "Accurate two-dimensional IMRT verification using a back-projection EPID dosimetry method," Med Phys 33, 259-273 (2006).

63. L. N. McDermott, M. Wendling, B. van Asselen, J. Stroom, J. J. Sonke, M. van Herk and B. J. Mijnheer, "Clinical experience with EPID dosimetry for prostate IMRT pre-treatment dose verification," Med Phys 33, 3921-3930 (2006).

64. L. N. McDermott, M. Wendling, J. J. Sonke, M. van Herk and B. J. Mijnheer, "Replacing pretreatment verification with in vivo EPID dosimetry for prostate IMRT," Int J Radiat Oncol Biol Phys 67, 1568-1577 (2007).

65. R. K. Rice, B. J. Mijnheer and L. M. Chin, "Benchmark measurements for lung dose corrections for X-ray beams," Int J Radiat Oncol Biol Phys 15, 399-409 (1988).

66. E. Yorke, L. Harisiadis, B. Wessels, H. Aghdam and R. Altemus, "Dosimetric considerations in radiation therapy of coin lesions of the lung," Int J Radiat Oncol Biol Phys 34, 481-487 (1996).

67. S. L. Berry, C. S. Polvorosa and C. S. Wuu, "A field size specific backscatter correction algorithm for accurate EPID dosimetry," Med Phys 37, 2425-2434 (2010).

68. P. Rowshanfarzad, B. M. McCurdy, M. Sabet, C. Lee, D. J. O'Connor and P. B. Greer, "Measurement and modeling of the effect of support arm backscatter on dosimetry with a varian EPID," Med Phys 37, 2269-2278 (2010).

69. S. Wang, J. K. Gardner, J. J. Gordon, W. Li, L. Clews, P. B. Greer and J. V. Siebers, "Monte Carlo-based adaptive EPID dose kernel accounting for different field size responses of imagers," Med Phys 36, 3582-3595 (2009).

70. P. Vial, P. B. Greer, L. Oliver and C. Baldock, "Initial evaluation of a commercial EPID modified to a novel direct-detection configuration for radiotherapy dosimetry," Med Phys 35, 4362-4374 (2008).

71. M. Sabet, F. W. Menk and P. B. Greer, "Evaluation of an a-Si EPID in direct detection configuration as a water-equivalent dosimeter for transit dosimetry," Med Phys 37, 1459-1467 (2010).

72. P. Winkler, A. Hefner and D. Georg, "Implementation and validation of portal dosimetry with an amorphous silicon EPID in the energy range from 6 to 25 MV," Phys Med Biol 52, N355-365 (2007).

73. J. Chen, C. F. Chuang, O. Morin, M. Aubin and J. Pouliot, "Calibration of an amorphous-silicon flat panel portal imager for exit-beam dosimetry," Med Phys 33, 584-594 (2006).

74. C. Lee, F. Menk, P. Cadman and P. B. Greer, "A simple approach to using an amorphous silicon EPID to verify IMRT planar dose maps," Med Phys 36, 984-992 (2009).

CHAPTER III

INVESTIGATION OF DOSE DISTRIBUTIONS FOR LUNG TUMOR GEOMETRIES FOR A 6 MV PHOTON BEAM

In Chapters I and II, the introduction and aims of this dissertation were presented. The aims of this dissertation are (1) to develop a method to investigate dose distributions for various heterogeneous geometries in order to quantify the systematic dose errors due to calculation inaccuracy in the disequilibrium conditions, and (2) to evaluate the feasibility of using an EPID as a water-equivalent dosimeter for pre-treatment and treatment dose verification. This dissertation focuses on the geometries and conditions relevant to lung stereotactic body radiotherapy (SBRT). This chapter presents the work to achieve the first aim of this dissertation.

III.A. Introduction

Hypo-fractionated stereotactic body radiation therapy (SBRT) is widely used for the treatment of lung tumors. One of the main challenges in lung SBRT is the dose uncertainty in the region close to an interface between the tumor and neighboring lung tissue. When the tumor (approximately the density of normal tissue) is embedded in lower density lung tissue, there can be a lack of charged particle equilibrium at the tumor-lung interface. In addition, for decreasing tumor size, the ratio of tumor surface to the tumor volume increases, exacerbating the interface problem. For small tumors, the dose accuracy is questionable for both calculations and measurements.

Most conventional treatment planning algorithms do not accurately model the transport of secondary electron arising from primary photon interactions. The considerable range of secondary electrons is responsible for the loss of electronic equilibrium in narrow high-energy photon beams. The effect is more pronounced when a beam with a small field size passes through the low density medium. Many studies have compared algorithms with measurements and reported that convolution-based algorithms and Monte Carlo (MC) methods are more accurate than pencil beam (PB) algorithms.[1-8] The inaccuracy of PB algorithms leads to an over-estimation of the dose to target volume, and can result in insufficient dose to the target for lung treatments.[9-11] While convolution-based algorithms show more accurate results, a range of inaccuracies for these algorithms have been reported.[3, 4, 8, 9] Because MC methods simulate the physical interactions, they are considered to be the most accurate methods. Historically, MC calculations required significantly more time for calculations than other algorithms. With advances in computing, there are now commercially available systems that are slowly being adopted for clinical treatment planning. Instead, MC methods are usually used as a benchmark to verify the accuracy of other calculation algorithms.[9, 11, 12] However, the accuracy of such methods often needs further validation with measurements for specific conditions, e.g. depth doses and lateral dose spreading in low density media for small field sizes for beam axes both parallel and perpendicular to tissue interfaces.[13]

Measurements performed in the disequilibrium region are challenging and complicated by detector perturbation typically due to detector size and non-medium equivalence of detector materials. In addition to the detector perturbation, small field measurements are more sensitive to setup inaccuracy than large field measurements. Investigators have found a range of deviations by using various types of detectors in

small field measurements. Dose accuracy in small fields can be improved with a proper choice of detector and a careful alignment of the detector axis with the beam axis[14], the use of detector corrections[15] or the cross-comparison of multiple detectors[16]. Ion chambers have been shown to be unsuitable for profile measurements for small field dosimetry because of broadening of the penumbra, requiring significant corrections.[17, 18] Among the common detectors used in literature[19], radiochromic films have showed promising advantages.[20, 21] However, attention may be needed to measurements in low-density media when the films are placed parallel to the beam axis.[3]

Dosimetric investigations have been widely performed for a simple geometry, such as a slab phantom with low and high density media. However, few studies discussed dose variations for geometries with a small tumor embedded in lung.[22-24] These previous studies did not investigate the effect of tumor positions on dose variations based on measurements. Sufficient dose information from measurements is necessary to evaluate calculation algorithms thoroughly for both simple heterogeneous and tumor-in-lung geometries. As reported in Chow *et al*[25], the calculation accuracy depends on the heterogeneous geometry (for example, the position and size of the tumor and the dimension, geometry and density of the lung medium). However, in their study, the accuracy of calculation algorithms was evaluated based on a MC method rather than a measurement method. MC methods can provide useful information for complex geometries. However, such methods are more relevant with a thorough validation of the calculation accuracy for different heterogeneous geometries, such as tumor-in-lung.

Considering the literature, the dosimetric investigation for both simple and complex heterogeneous geometries is necessary to validate calculation algorithms. Therefore, the purpose of this study is to investigate dose distributions for various

heterogeneous geometries for a 6 MV photon beam. Measurement data can be used to understand how scatter conditions change with varying heterogeneous geometry, and can be used to evaluate the performance of calculation algorithms, such as MC methods. However, the accuracy of this dose investigation depends on a reliable design of phantom geometries and selection of an appropriate detector, providing sufficient dose information as well as small detector perturbation.

To address these issues, a robust design of phantom geometries with simple lung and tumor-in-lung is developed. The phantom design allows radiographic or radiochromic films to be placed parallel and perpendicular to the beam axis, providing two-dimensional (2D) dose information. To minimize the detector perturbation in the disequilibrium region, the present study uses Gafchromic[TM] EBT film (ISP, Wayne, NJ), because of its water equivalence ($Z_{effective}$ = 6.98) and near independence of energy[26]. This film has other advantages, such as providing 2D dose information with high spatial resolution, self-developing, insensitivity to room light, and water resistance. These characteristics render this film suitable for heterogeneity measurements. When using EBT film for quantitative dosimetry, flatbed scanners are generally used to digitize the film data. These scanners allow the acquisition of transmission scans in up to 48-bit red-green-blue (RGB) mode. Because the absorption spectrum of EBT film exhibits a maximum in the red region of visible spectrum[27, 28], extraction of the red channel from RGB images can improve the sensitivity of flatbed scanners with EBT film. The characteristics of EBT film with flatbed scanners have been thoroughly investigated.[29-34] The uncertainty of EBT film dosimetry can be minimized by (1) applying a dose dependent non-uniformity (due to non-uniform scanner response) correction mainly in the horizontal direction (along the CCD array axis)[35, 36]; (2) subtracting pre-exposure optical density (OD) from post-exposure OD to reduce the influence of film non-

41

uniformities; (3) averaging consecutive scans to reduce scan-to-scan variation; (4) using the same scan orientation for calibration and experimental films[37]; (5) extracting the data in the red channel to maximize readout sensitivity[27]; (6) applying an image filter in the analysis to reduce the film noise; (7) repeating measurements to reduce the influence of film-to-film variation; and (8) scanning the film at least 6 h after irradiation for post-irradiation polymerization[38]. With proper handling, EBT film has been used for absolute dose measurements for a homogeneous geometry with an uncertainty of 1%-2% (one standard deviation, 1σ)[35, 39, 40]. Therefore, to improve the accuracy of dose investigation in this study, EBT film is carefully handled following the suggested procedures.

III.B. Methods and materials

III.B.1. Heterogeneous phantom geometries

The phantom materials used in this study included Solid Water (SW) phantom blocks (Gammex RMI, Middleton, WI) with a density of 1.04 g/cm^3 and lung-equivalent phantom blocks (Gammex RMI, Middleton, WI) with a density of 0.30 g/cm^3. Four heterogeneous geometries were investigated (Figure III.1): tumor-in-lung geometry with tumor and beam axis at 6.5 cm from the outer SW-lung interface (Geometry 1, G1) and at 1.5 cm from the interface (Geometry 2, G2); the lung-only geometry with beam axis at 6.5 cm (Geometry 3, G3) and at 1.5 cm (Geometry 4, G4) from the interface. A SW phantom (3 × 2 × 3 cm^3) to simulate a small lung tumor was embedded in the lung-equivalent material so that the total lung (with tumor) dimension was 12 × 8 × 18 cm^3. The SW phantom was placed around the lung phantom to ensure adequate side scatter and backscatter. In addition, a homogeneous phantom (Geometry 5, G5) was used to verify the accuracy of the measurement system.

(a) 3D view of G1 and G2

(b) Axial view of G1 and G2

(c) BEV of G1

(d) BEV of G2

(e) BEV of G3

(f) BEV of G4
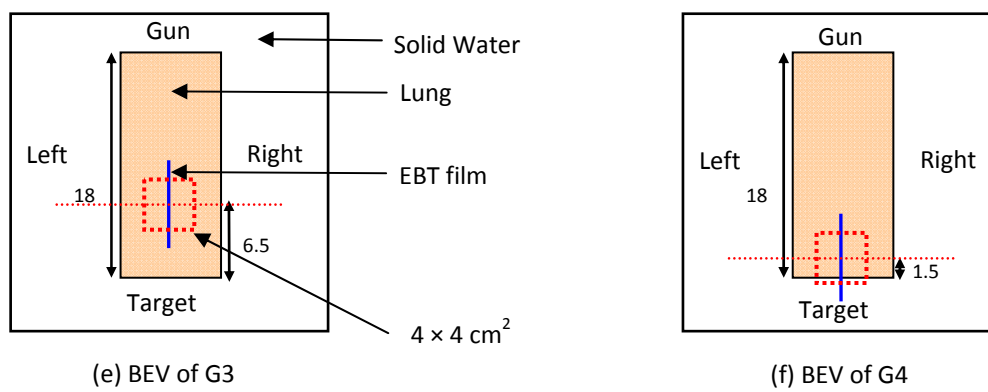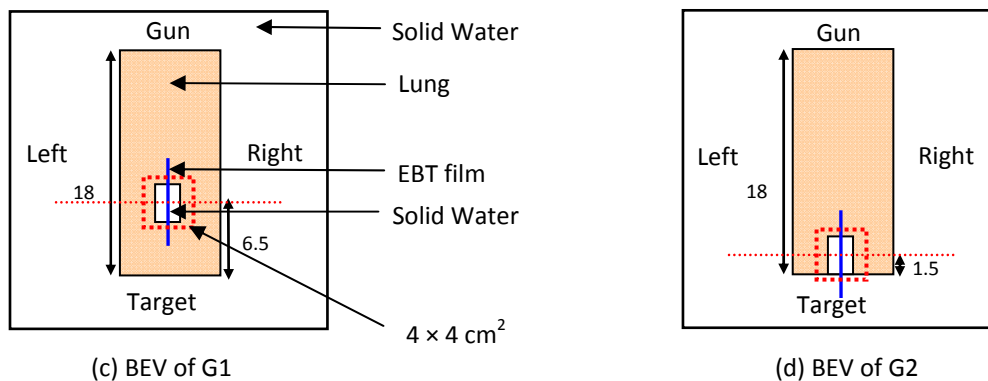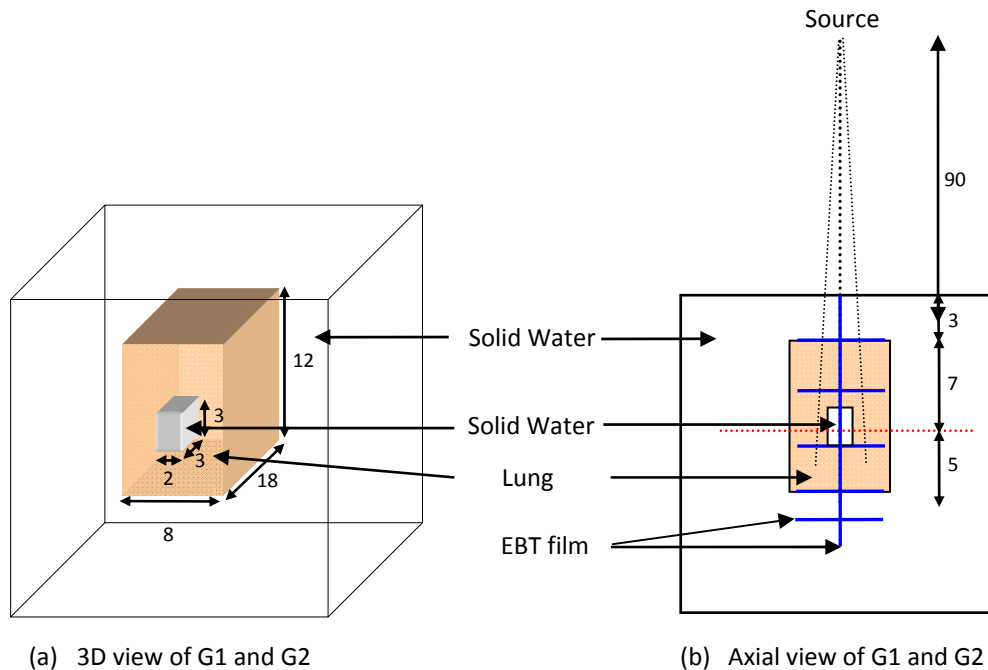
Figure III.1. Illustration of heterogeneous phantom geometries and film locations. (a) Three-dimensional (3D) view of G1 and G2 geometries with the simulated clinical target volume (3 × 2 × 3 cm^3) embedded in the lung-equivalent material (12 × 8 × 18 cm^3). The isocenter is at 10 cm depth (2 cm depth in the simulated tumor). (b) Axial view of G1 and G2 geometries with EBT film

parallel and perpendicular to the beam axis. The films in the perpendicular orientation were placed at 3, 7, 11, 15 and 17 cm depth for heterogeneous geometries. (c) - (f) are beam's eye view (BEV) of G1 – G4 geometries, respectively, with 4 × 4 cm^2 field size in order to cover the simulated tumor for G1 and G2 geometries. The isocenter is at 6.5 cm (G1 and G3) and at 1.5 cm (G2 and G4) from the interface.

III.B.2. Measurement setup

All measurements were performed with a 6 MV photon beam, 600 MU/min dose rate, and 0° collimator from a Varian 21EX accelerator (Varian, Palo Alto, CA) equipped with a Millennium 120 leaf multi-leaf collimator (MLC). The accelerator was calibrated with an output of 0.8 cGy /MU at a depth of 10 cm in water for a 10 × 10 cm^2 field size at 90 cm source-to-surface distance (SSD). Film calibration curves with a dose range of 0-800 cGy were acquired prior to the experiment for 6 MV photons at 10 cm depth and 10 × 10 cm^2 field size in SW. The experimental phantoms were set at 90 cm SSD (Figure III.1). All experiments were performed with a field size of 4 × 4 cm^2 jaw only field, with MLC parked, to cover the simulated tumor. The delivered MU was 570 MU for all measured geometries so that the uncertainty of EBT film with a scanner can be reduced to ~1%.[31] This delivered a dose of ~400 cGy at 10 cm depth in homogeneous water for the 4 × 4 cm^2 field size and 6 MV photon beam.

III.B.2.i. Film perturbation effect in heterogeneous geometries

Previous investigators have reported on challenges of using film placed parallel to the beam axis, such as the presence of air gaps[41] and the attenuation effect[3] due to the higher density when compared to lower-density materials. A small gantry rotation of 1°- 2° or a shift of beam axis from the film position may reduce the film perturbation with film placed parallel to the beam axis.[3, 41, 42] In this work, the film perturbation was measured in the G3 (lung only) heterogeneous geometry (Figure III.1(e)) to quantify the dose

variation when the film was parallel to the beam axis and to determine an appropriate method for correcting film measurements in the parallel orientation. Measurements were performed with EBT films: (1) at 3 and 15 cm depths in the perpendicular orientation for gantry angle of 0°, (2) from 3 to 15 cm depths in the parallel orientation for gantry angle of 0° and 358°. Film data were compared between two orientations for two gantry angles. This experiment was performed once (not repeated) since the investigation was focused on evaluating differences due to film perturbation and the impact of the gantry rotation method in reducing the perturbation.

III.B.2.ii. Verification of EBT film accuracy in SW with an ion chamber in liquid water

To verify the accuracy of the EBT film measurement system, the percentage depth dose (PDD) was compared between the EBT films in homogeneous SW (G5) and ion chamber measurements in water. The ion chamber measurements were performed using a Scanditronix Wellhofer CC13 ion chamber (Radiation Products Design, Inc., Albertville, MN) in a water tank ($68 \times 64 \times 56$ cm^3) for the 4×4 cm^2 field size. For EBT film measurements in the G5 geometry, 2D dose distributions were measured with the films placed parallel and perpendicular to the beam axis. The films in the perpendicular orientation were placed at 3 and 15 cm depths. The EBT film measurements were repeated three times and averaged at each measurement point for better statistical results. The comparison between the ion chamber in water and EBT film in SW was used to determine the total uncertainty caused by the replacement of water with SW material and the accuracy of the EBT film system, including measurements, scanning and analyses.

III.B.2.iii. Dose measurements for various heterogeneous geometries

2D dose distributions in various heterogeneous geometries (G1-G4) were measured with the films placed parallel and perpendicular to the beam axis. The films in the perpendicular orientation were placed at 3, 7, 11, 15 and 17 cm depths (Figure III.1). Measurements in the parallel and perpendicular orientations were used to verify the dose accuracy in two film orientations and to provide 3D dose information for various heterogeneous geometries. For each geometry, measurements were repeated three times.

III.B.3. Film preparation, irradiation and analysis

Basically, the EBT film analysis in this study followed the procedures described in the introduction, except for the handling of the dose dependence correction for the scanner response. The EBT film was cut into small pieces, the scan orientation was marked using a marker pen on the right corner of the film piece ($\sim 7 \times 7$ cm^2 for the films used for calibrations and measurements in the perpendicular orientation, and $\sim 20 \times 7$ cm^2 for the films placed in the parallel orientation), and then films were scanned in portrait position using a flatbed CCD scanner (EPSON V700, Long Beach, CA). Films were placed in the central part of the scanner with a mask to cover the remaining area [35]. To monitor the stability of the scanner, a Kodak XV film (Carestream Health, Inc., Rochester, NY) exposed with multiple OD intensities (from 0.17 to 3) was placed on the scanner and scanned together with the EBT film each time. Each EBT film was scanned before and after irradiation (pre-exposure scan and post-exposure scan). All post-exposure films were scanned at least 6 h after the irradiation to allow for post-irradiation polymerization.

Before analyzing films, the scanner was warmed up with several preview scans. For each film, three consecutive scans were averaged. The software for the device was

used to scan in the professional mode with all imaging adjustment options turned off with a scanning resolution of 200 dpi (0.127 mm/pixel). Transmission images were saved in 48 bit RGB uncompressed TIFF. The transmission values (without any normalization) from the red color channel were extracted, resulting in 16-bit images with pixel values in the range of 0 to 65535 (without any film on the scanner). The film data were analyzed using in-house software written with MATLAB® (The MathWorks, Inc., Natick, MA). The final response images were obtained by subtracting pre-exposure images from post-exposure images after the pixel values were converted to OD using a method described in the literature[33]. A median filter (3 × 3 pixel^2) was applied to reduce the noise and a calibration curve was used to convert OD to dose. Regarding the non-uniformity on the scanner response, the variation of scanning position for small films up to 7 cm width in CCD array direction was estimated to be within 2% based on data in the literature[36, 40] assuming similar behavior for EPSON scanners. Therefore, because of the small field size for this study, the scanner response was not corrected along the CCD array direction. For the calibration curve, the OD in the central region with a radius of 50 pixels was acquired on the calibration films. The calibration curves were fitted with a 5th order polynomial equation resulting in R-squared values between 0.9998 and 1. The inter-day variation of the calibration curve is ~0.4% (1 σ) excluding the background (Figure III.2).

.
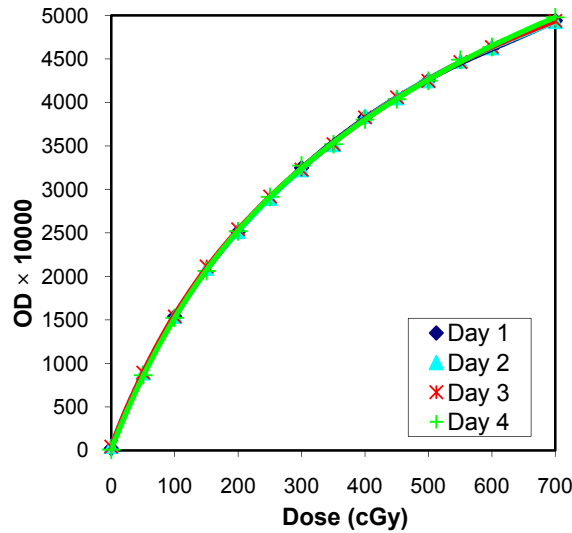
Figure III.2. Calibration curves on four different days.

III.B.4. MC - DPM calculations

Dose calculations were performed using a MC method, a benchmarked Dose Planning Method (DPM)[5, 43-45] code implemented in the University of Michigan treatment planning system (UMPlan) in order to compare measurements for the film perturbation effect and for heterogeneous and homogeneous geometries. For the investigation of the film perturbation effect, a manual lung geometry (the same as G3 geometry in Figure III.1) was created with densities of 1, 1 and 0.25 g/cm^3 for water, film and lung, respectively. The density of 0.25 g/cm^3 for lung phantom was used for simulation based on the average density (density range from 0.2 to 0.3 g/cm^3) of the lung-equivalent media from the CT images. The widths of water, film and lung in the axial view were 16, 0.024 and 8 cm. The doses were calculated and compared for the geometries without and with film at both 0° and 358° gantry angle. The number of histories was 10^{11} under the same measurement condition. The density and calculation voxel sizes were ~0.7 × 0.7 × 0.7 mm^3. The calculation uncertainty was ~1%.

Regarding dose calculations for various geometries, one homogeneous (G5) and four heterogeneous (G1-G4) geometries were CT scanned with 3 mm and 1 mm slices, respectively, and doses were calculated under the same measurement condition. The voxel sizes were $1.2 \times 0.8 \times 1.1$ and $1.7 \times 1.2 \times 1.0$ mm^3 for homogeneous (phantom dimension $30 \times 20 \times 30$ cm^3) and heterogeneous ($43 \times 31 \times 25$ cm^3) geometries, respectively. The number of histories was 10^{12} with an uncertainty (1σ) of ~0.5%. More particles were used in the CT-scanned geometries than in the manual geometry for the film perturbation investigation to reduce the uncertainty for the main data in this study. In addition, calculations in absolute doses were compared with measurements.

For MC calculations, the BEAMnrc code[46] is used to simulate the patient-independent components of a Varian 21 EX linear accelerator, such as the target, primary collimator, flattening filter, transmission chamber, and mirror. The simulation details of the accelerator using BEAMnrc have been reported in Chetty *et al*.[5] The phase space data are read into the DPM code system[43] and used for patient-dependent dose calculations which depend on the MLC, jaw and patient geometries. In order to calculate final values in absolute dose, the energy deposition parameter is multiplied with the total MUs for a particular beam and the calibration factor of 0.8 cGy/ MU (at 10 cm depth for a 10×10 cm^2 field size and 90 cm SSD) for the machine is applied.[45] The DPM calculation has been validated for field sizes from 2×2 to 10×10 cm^2 for homogeneous and simple heterogeneous geometries by comparing diode, ion chamber and film measurements.[5] For the homogeneous geometry, the relative differences between DPM calculations and measurements were within 1% for PDDs and within 1%/1 mm for relative profile doses. For the heterogeneous geometry, the differences were within 1% for PDD comparisons, and 2% in the inner and outer beam regions and

within 1-2 mm distance-to-agreement within the penumbra region for profile comparisons.[5]

III.C. Results

III.C.1. Film perturbation effect in heterogeneous geometries

Figure III.3 shows the film perturbation effect in 12 cm of lung (at depths from 3 to 15 cm) based on measurements and DPM calculations. Both measurements and calculations
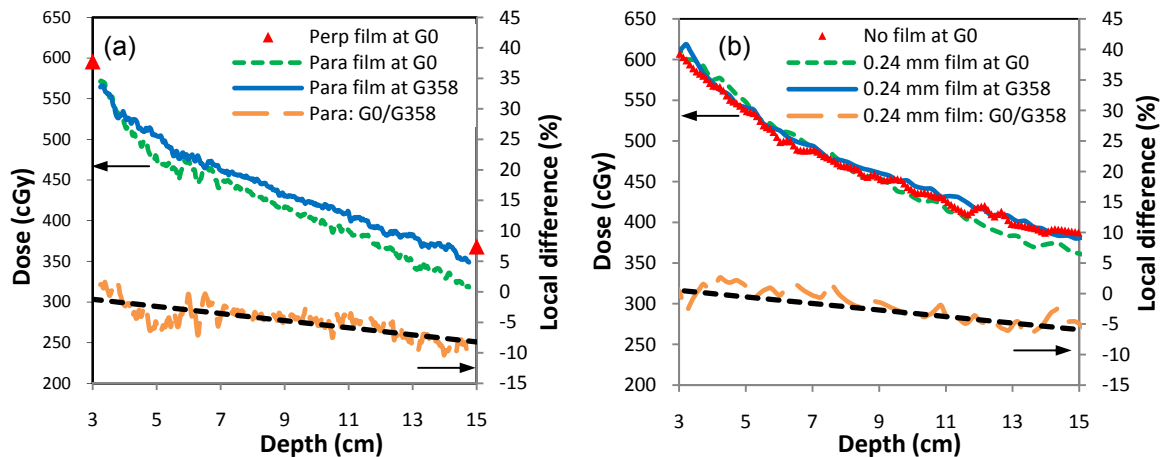
Figure III.3. (a) Measured depth doses in G3 geometry (12 cm lung at depths from 3 to 15 cm) with the film in the perpendicular orientation at 0° incidence (legend: Perp film at G0) and with the film in the parallel orientation at 0° and 358° incidences (legend: Para film at G0 and G358) . (b) Calculated depth doses in the same geometry without film at 0° incidences and with the film in the parallel orientation at 0° and 358° (simulated film thickness: 0.24 mm; actual film thickness: ~0.23 mm). The lower curve shows the difference relative to the local dose in percent and compares doses at 0° and 358° incidences when the film is placed in the parallel orientation.

show the film perturbation when the film is placed parallel to the beam axis, leading to dose under-estimation in the depth dose measurement. The perturbation increases with increasing depth and the reduction is up to ~8% beyond 12 cm of lung (from measurement data). Rotating the gantry by 2° reduces this perturbation and improves the agreement between films in the parallel and perpendicular orientations. The DPM calculations also show a similar reduction in film perturbation when rotating the gantry.

50

Thus, a gantry angle of 358° was used for film measurements in the parallel orientation for all geometries (G1-G5) to reduce the effect of film perturbation. The measurements with the film in the perpendicular orientation were performed with a gantry angle of 0°.

III.C.2. Verification of EBT film accuracy in SW with an ion chamber in liquid water

Figure III.4 shows the comparison between the CC13 ion chamber measurements in water (at 0°) and EBT film in SW with the parallel orientation (at 358°) and perpendicular orientation (at 0°). The CC13 ionization readings were scaled to match doses measured in EBT films at 10 cm depth. The difference was within 2% at d_{max} (the depth of maximum dose) and beyond. Thus, the system of EBT film in SW was shown to be accurate within 2% when compared to ion chamber measurements in water.
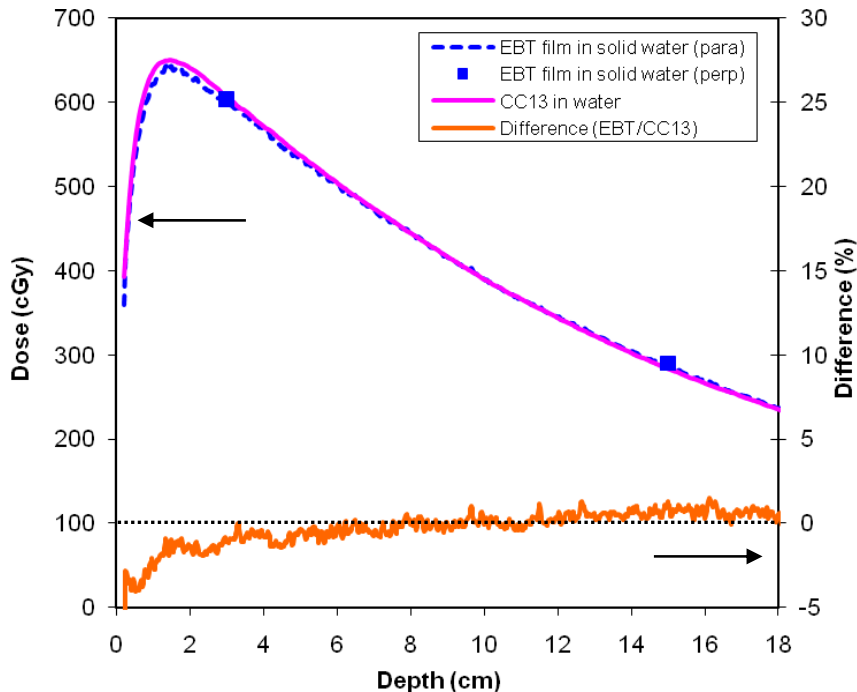
Figure III.4. Comparison between CC13 in water (at 0° gantry angle) and EBT film in SW with parallel orientation (at 358°) and perpendicular orientation (at 0°). The lower curve shows the difference in percent between the ion chamber and film data.

III.C.3. Dose distributions for various heterogeneous geometries

Figure III.5 shows the depth doses from the film in the parallel orientation at the gantry angle of 358° and film in perpendicular orientation at the gantry of 0° for all geometries, and an example of in-plane (target-gun) profiles at 11 cm depth extracted from the film in the parallel orientation. The data shown are the average of three repeated measurements for both parallel and perpendicular orientations. The variation (1σ) was ~1% at d_{max} and deeper for three repeated measurements. In evaluating the depth dose curves (Figure III.5(a)), as expected, the dose decreases when the beam enters the lung and re-builds up when it enters the tumor or SW region. In Figure III.5(b), the dose is reduced near the tumor edge for the G1 geometry (tumor-in-lung, beam axis at 6.5 cm). When comparing the geometries of G1 through G4, the distance of the beam axis from the interface (1.5 cm compared to 6.5 cm) does not show a significant dose difference in the depth dose comparison. The difference relative to the local dose was 0.4% (average) ± 0.9% (1σ) and 0.8% ± 0.7% for G1 vs. G2 (tumor-in-lung) and G3 vs. G4 (lung only), respectively. When evaluating the impact on the profiles, the distance from the interface (1.5 cm vs. 6.5 cm) leads to a sharper penumbra and a significant dose variation with the dose shifting toward the left (target) side in Figure III.5(b), due to more scattering from the side adjacent to the high density material. The difference relative to the local dose at 1.5 cm off-axis was 8.2% ± 2.7% and 7.4% ± 2.4% for G1 vs. G2 and G3 vs. G4, respectively. The left penumbra between 20% and 80% was 6.6, 4.0, 6.4, 3.8 and 3.4 mm at 11 cm depth for G1, G2, G3, G4 and G5, respectively (Figure III.5(b)). The off-axis measurements for different tumor positions can be used to verify the accuracy of the calculation of side-scatter in dose calculation algorithms and to ensure the tumor coverage in radiotherapy.

To reduce the film perturbation effect, a gantry angle of 358° was used when the film was placed parallel to the beam axis. Table III.1 shows the dose comparison at 3, 7, 11, 15 and 17 cm for all geometries between films in the perpendicular orientation at 0° and films in the parallel orientation at 358°. By rotating the gantry angle by 2°, average agreement for measurements in the parallel and perpendicular orientations was 2.6% for heterogeneous geometries. This discrepancy was attributed to the combination of residual film perturbation at 358° and measurement uncertainty. Thus, no depth dependence was found in the discrepancy. The under-dosage for the film in the parallel orientation was on average 0.8% for the G5 homogeneous geometry. These small corrections (2.6% and 0.8%) were applied to the film (in parallel) results for both homogeneous and heterogeneous geometries so that the doses were consistent between two orientations. By analyzing measurements in both parallel and perpendicular orientations, more reliable data can be obtained in various heterogeneous geometries.
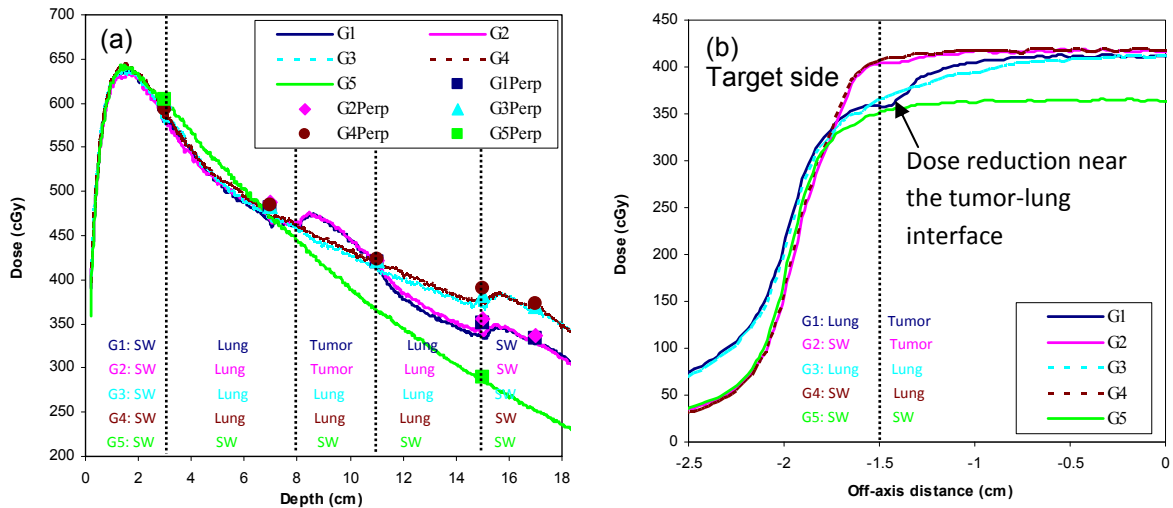
Figure III.5. (a) Depth doses measured with the film in the parallel orientation at 358° incidence (line) and in the perpendicular orientation at 0° (symbol) for all geometries. (b) In-plane profiles at 11 cm depth extracted from films in the parallel orientation. G1 and G2 geometries are tumor-in-lung for beams at 6.5 and 1.5 cm from the interface (Figure III.1(c) and (d)), while G3 and G4 geometries are lung only for beams at 6.5 and 1.5 cm from the interface (Figure III.1(e) and (f)), respectively. G5 geometry is homogeneous SW.

Table III.1. Dose comparison between the film in the perpendicular orientation at 0° incidence and in the parallel orientation at 358° incidence at depths of 3, 7, 11, 15 and 17 cm for all geometries.

Geometry	Depth (cm)	Perpendicular film (cGy)	Parallel film (cGy)	Difference (%)
G1 (Tumor-in-lung, beam at 6.5 cm)	3	598	578	-3.4
	7	481	463	-3.9
	11	420	417	-0.8
	15	351	335	-4.6
	17	333	328	-1.7
G2 (Tumor-in-lung, beam at 1.5 cm)	3	595	580	-2.5
	7	489	466	-4.6
	11	422	421	-0.3
	15	356	340	-4.5
	17	336	329	-2.3
G3 (Lung only, beam at 6.5 cm)	3	602	578	-4.0
	7	483	468	-3.1
	11	422	413	-2.0
	15	382	370	-3.2
	17	369	365	-1.4
G4 (Lung only, beam at 1.5 cm)	3	593	586	-1.2
	7	485	472	-2.6
	11	424	418	-1.4
	15	390	374	-4.1
	17	372	367	-1.4
G5 (Homogeneity)	3	604	600	-0.7
	15	290	287	-1.0

III.C.4. Comparison between measurements and calculations

For film data acquired in the parallel orientation, the small corrections described in the previous section were applied. The corrected film data were shown in Figures III.6, III.7 and III.8 with the comparisons to the calculations. Figure III.6 shows sagittal plane (target-gun direction, along the beam central axis) dose distributions for (corrected) measurements and calculations for all geometries. The overall agreement between

measurements and DPM calculations is good. The main disagreements were at ~3 cm depth, which is the interface between the SW and lung, and the penumbra region of the in-plane profile, where the measurements were sharper than the calculations. This

				cGy
				600
				500
				400
				300
				80

(a) G1   (b) G2   (c) G3   (d) G4   (e) G5
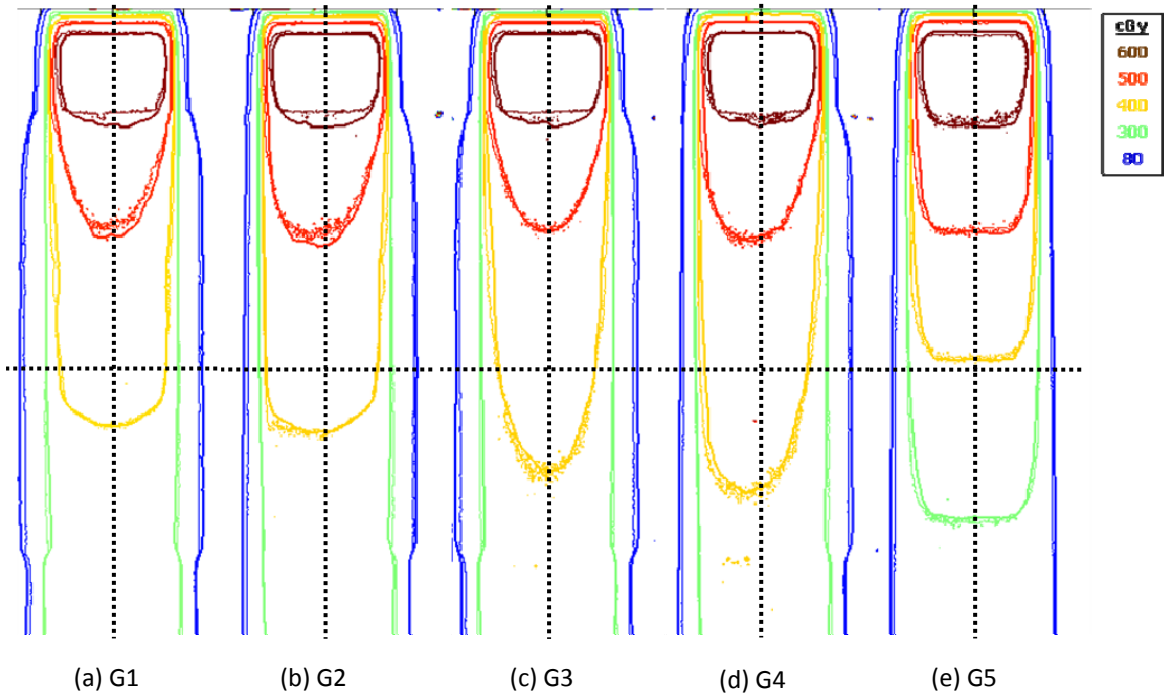
Figure III.6. Sagittal plane (along the central axis) dose distributions for G1-G5 geometries. Left and right sides of each distribution represent target and gun sides, respectively (see Figure III.1). The intersection of dotted lines represents the beam isocenter (at 10 cm depth) for each geometry. The doses shown are 80, 300, 400, 500 and 600 cGy. The thin line with noise and the **thick** line are the corrected film data and **DPM calculations**, respectively.

disagreement can be seen also in Figures III.7, III.8 and III.9, which displays the central axis depth doses, and in-plane and cross-plane profiles at 11 cm depth. Regarding the depth dose comparison (Figure III.7), the difference relative to the local measured dose at d_{max} and deeper depths for all geometries was 0.5% ± 0.4% with a maximum difference of 4.3%. For the calculated in-plane profile at 11 cm depth (Figure III.8), the left (target side) penumbra between 20% and 80% doses was 8.3, 5.2, 8.3, 5.4 and 5.3 mm at 11 cm depth for G1, G2, G3, G4 and G5, respectively. The calculated penumbra

was ~1.6 mm larger than the measured penumbra. However, the calculated penumbra of cross-plane profile (Figure III.9) shows better agreement with the measured penumbra (~0.6 mm difference). For the various heterogeneous geometries in this work, DPM was found to accurately calculate the dose distributions in unit density and lung simulating media as well as at the interfaces between these media.
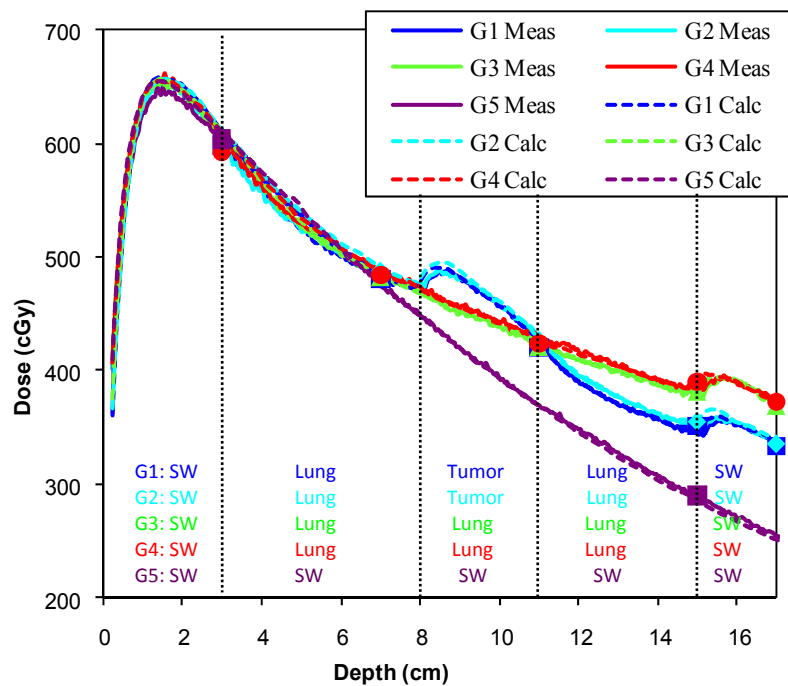
Figure III.7. Corrected measured (Meas) vs. DPM calculated (Calc) depth doses along the central axis, with symbols, solid lines and dash lines which represent film data in the perpendicular orientation, corrected film data in the parallel orientation and DPM calculations, respectively.
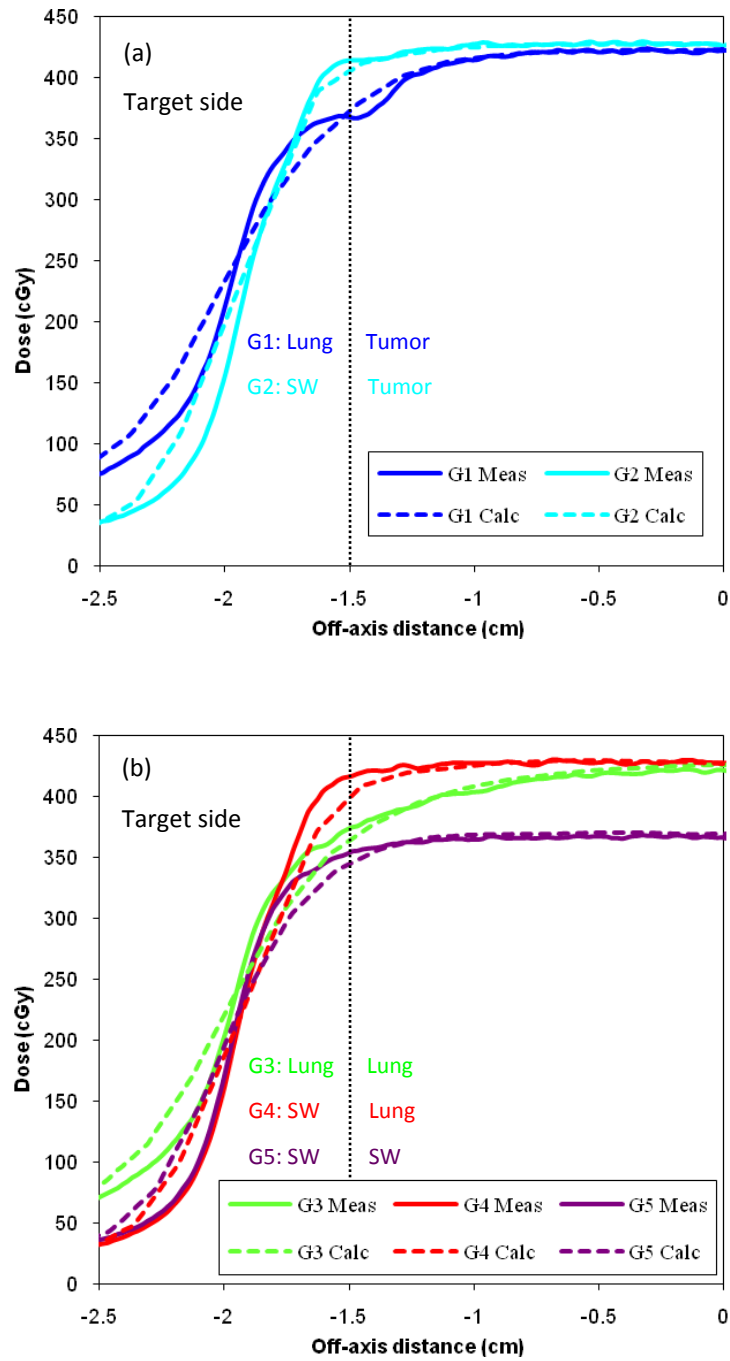
Figure III.8. Corrected measured vs. DPM calculated in-plane profiles at 11 cm depth for (a) G1 and G2 geometries and (b) G3-G5 geometries. The data were extracted from the film (parallel) with corrections.
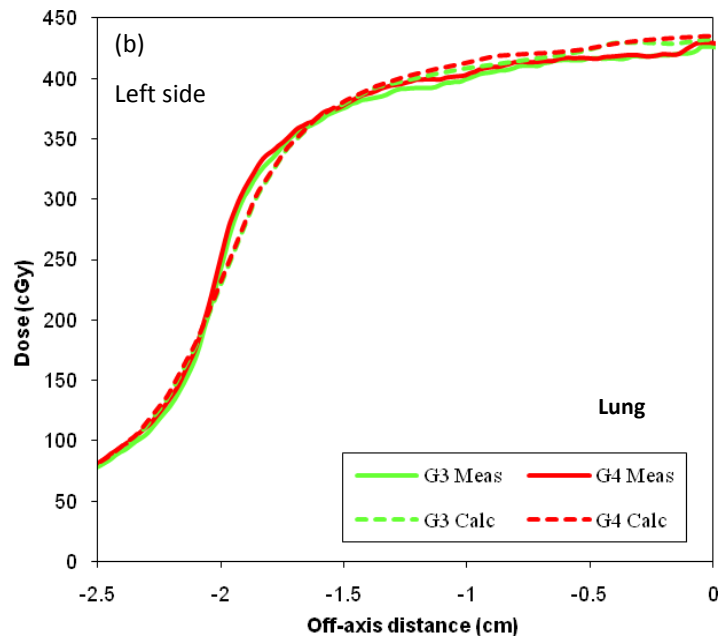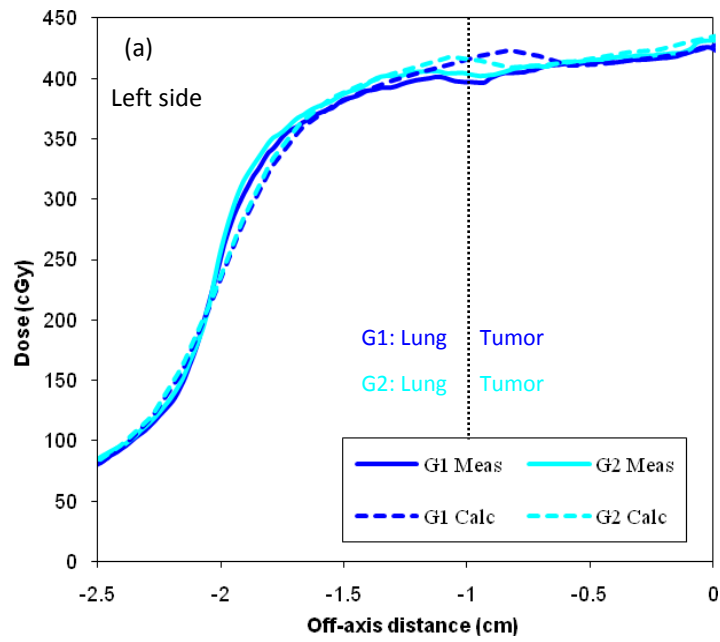
Figure III.9. Measured vs. DPM calculated cross-plane profiles at 11 cm depth for (a) G1 and G2 geometries and (b) G3 and G4 geometries. The data were extracted from the film (perpendicular).

III.D. Discussion

III.D.1. Film perturbation effect in heterogeneous geometries

The effect of film perturbation in a parallel orientation to the beam has been investigated for radiographic film where an increased response of the film was found when compared to film in a perpendicular orientation. This was attributed to the increased forward scattering of electrons in the silver halide for parallel orientation and the reduced attenuation of the beam when a gap appears between film and phantom. A small gantry rotation of 1°-2° typically reduces this perturbation.[3, 41, 42] Suchowerska *et al*[41] found that radiochromic film also over-responded when placed in a parallel orientation for measurements in a tissue-equivalent phantom. They concluded that the over-response was due to the presence of an air gap. Thus, reducing the amount of air gap between film and the media reduces the perturbation in water-equivalent materials due to the presence of the film when placed parallel to the beam. However, when measuring in materials with a density less than water, the use of radiochromic film in a parallel orientation can lead to perturbations in the fluence due to the higher density (~1.1 g/cm^3) of the film. This perturbation is larger for a parallel orientation when compared to the perpendicular orientation. Paelinck *et al*[3] measured doses in a lung heterogeneous geometry using radiochromic films in parallel and perpendicular orientations. They found the film in parallel attenuated the beam and decreased the dose measured behind the cavity. In their work, the under-dosage was avoided by offsetting the film a few centimeters. Their MC simulations also showed the film perturbation in heterogeneous geometries.

Similar to the findings in Paelinck *et al*[3], the DPM calculations in this study show an increasing effect of under-dosage in the film in parallel orientation with increasing depth, with a difference up to ~7% at beyond 12 cm lung cavity, comparing results with

59

and without film present at a 0° gantry. The film perturbation measurements also show the same behavior with a difference up to ~8% beyond 12 cm lung cavity. The measurements are consistent with DPM calculations. However, it should be noted that the accuracy of the calculated film perturbation effect is limited by voxel sizes in phantom density and calculation binning (~0.7 mm), which were larger than the simulated film thickness (0.24 mm). The actual density of voxels in the film region used in the calculations may be smaller than 1 g/cm^3, caused by averaging the density within the voxel. Due to this fact, the film perturbation may be under-estimated in the DPM calculations. In addition, the air gap between the film and phantom was not simulated in the DPM calculation while the air gap may be present in the measurements. While there are uncertainties in the calculations, both measurements and DPM calculations show the film perturbation in the low density media. A slight rotation of ~2° was shown to significantly reduce the film perturbation effects, and to shift the depth dose measurements to more closely resemble film measurements in the perpendicular orientation as well as the calculations without modeling the presence of the film. While the technique of offsetting the film a few centimeters is another method used to reduce the film perturbation, it was considered an inappropriate technique for this work because of the small field size and lung-tumor geometries. DPM was used to calculate depth doses when offsetting the film 5 mm from the beam axis, and results showed no significant reduction of film perturbation for our geometries. Rotating the gantry by ~2° was determined to be a more appropriate approach to minimize the perturbation effects in this study. The other possible method is to apply a depth-dependent correction factor to the doses measured on the film in the parallel orientation.

III.D.2. Verification of EBT film accuracy in SW with an ion chamber in liquid water

The accuracy of the EBT film measurement system was within 2% relative to the local

dose measured with ion chamber in water which is comparable to the accuracy reported

by van Battum *et al*,[40] although the EBT film was placed in water in their study. In the

present study, the difference between the EBT film and ion chamber systems may be

due to the replacement of water with plastic water (i.e. SW), measurement setup error

and uncertainty of EBT film dosimetry. Although the water-equivalent solid phantom has

a similar electron density to water, the mass energy absorption coefficient is different

between a plastic water phantom and water medium, so that there may be a difference

due to the dependence on energy[47, 48]. With respect to the measurement setup error, the

parallel orientation is more sensitive to the setup error when compared to the

perpendicular orientation. The sources of uncertainty in EBT film dosimetry include (1)

inhomogeneity of the film emulsion, (2) energy dependence of film, (3) inherently small

signal-to-noise ratio of film, (4) inhomogeneity, reproducibility and stability of scanner

response, and (5) uncertainties in the nonlinear sensitometric curve. In this study, we

minimized the uncertainty of EBT film dosimetry by averaging three consecutive scans,

subtracting pre-exposure OD from post-exposure OD, averaging three films for each

measurement, and using 14 points (including background) for sensitometric curves. The

total uncertainty of EBT film measurement system in this study was estimated to be 2%

(1 σ) for three repeated measurements, including systematic and random errors, for both

homogenous and heterogeneous geometries.

III.D.3. Dose distributions for various heterogeneous geometries

Due to the loss of electronic equilibrium in low-density tissue for small field sizes,

determining the dose accuracy in the interface and immediately adjacent regions is a

challenging issue which is still under investigation, especially for treatments involving

lung. Dose calculation accuracy in these situations is of significant interest for

determination of the dose delivered to patients for lung SBRT treatments because of the use of small field and hypo-fractionation schemes. However, the anatomy of patients is more complicated than simple lung geometries. In this study, the central axis dose for the simulated tumor next to the SW (G2, tumor-in-lung, beam at 1.5 cm) was not significantly different from the dose for the simulated tumor far from the SW (G1, tumor-in-lung, beam at 6.5 cm). However, the dose difference increases with increasing off-axis distance and is up to ~8% at 1.5 cm off-axis (tumor edge) (Figure III.5(b)). The reason for this negligible difference along the central axis is that the distance from tumor center to tumor edge (1.5 cm) is close to the electron range for 6 MV photons used in this study. When the energy increases to 10 or 16 MV or the tumor size is smaller than 3 cm, the influence of scatter would be more significant, i.e. increasing dose differences along the central axis. Therefore, the lung tumor position, size and photon energy would significantly affect the dose distribution in lung radiotherapy. In these situations, it is important to validate the calculation algorithm in estimating the side-scatter effects and to determine if the discrepancy is acceptable for clinical treatment.

III.D.4. Comparison between measurements and calculations

In Figure III.3, when comparing film measurements at 358° (Figure III.3(a)) and DPM calculations (Figure III.3(b)), the film data were ~5% lower than the calculations while better agreement was found in the G3 geometry in Figure III.7. This inconsistency was attributed to two factors. First, the films (parallel) shown in Figure III.7 were corrected by 2.6%, which was calculated from Table III.1 to correct the residual error in measurements. Second, film (parallel and perpendicular) data shown in Figure III.7 were the average of three repeated measurements, which reduced the film uncertainty, while the film (parallel and perpendicular) data shown in Figure III.3 were from one

measurement since this experiment was designed to determine the appropriate approach for film measurements in the parallel orientation.

The accuracy of several calculation algorithms with inhomogeneity corrections has been discussed by several investigators. A point kernel–based convolution/superposition method is more accurate than the PB algorithm with simple scatter and attenuation corrections. The MC method is a good tool to verify the accuracy of other model-based calculation algorithms if it is validated for specific tests, as suggested by Task Group No. 105.[13] In this study, DPM was evaluated with measurements in simple lung and tumor-in-lung geometries with beam axes near and far from the interface. The DPM calculations agreed well with measurements in the depth dose and cross-plane profiles for various test geometries. Poorer DPM performance was found for in-plane profiles and near the tumor-lung interface. This discrepancy is possibly due to an inaccurate configuration of the machine head rather than the MC simulation method itself. Because of the strong dependence of dosimetric accuracy on the geometry configuration, MC calculations must be validated with measurements. In this study, the jaw only field with MLC parked was used. This simple condition allows distinguishing the inaccuracy in DPM from the inaccuracy in the geometry configuration. Verification of the calculation accuracy of a jaw only field supports further investigations of the dosimetric effect of the MLC, which can include considerations of design factors such as curved leaf ends, tongue and grooves, and inter-leaf vs. intra-leaf leakage.

The 2D dose distributions from films in the parallel and perpendicular orientations provide the 3D dose information to validate the DPM accuracy. Further work could include improving the agreement in the penumbra of in-plane profiles and the dose near the tumor edge, testing for higher energy, smaller field size and smaller tumor size and verifying the accuracy of a full SBRT delivery in an anthropomorphic phantom. A MC

method is a valuable tool in supplementing measurements for validation of other calculation algorithms or estimating more accurate distributions of delivered dose to patients for lung treatment when the MC calculation results are validated.

III.E. Conclusion

To better understand doses in the disequilibrium region, this study constructed a phantom with various heterogeneous geometries, including simple lung and tumor-in-lung with two different tumor positions. This phantom design allowed multi-planar film measurements to investigate dose distributions near, across, and along interfaces thoroughly. Due to the challenges in performing accurate measurements in these geometries, a tissue equivalent dosimeter, EBT film, was chosen. Using the high-density film in a low-density medium suffers a challenge of dose reduction when placed parallel to the beam axis. The approach of 2° gantry rotation, applied to film measurements in the parallel orientation, improved the accuracy of dose measurements for all studied geometries. This result bolsters the confidence of measured dose accuracy in heterogeneous geometries, particularly for tumor-in-lung. Multi-planar measurements provide more reliable dose information for understanding dose distributions in various geometries, which supply additional information to validate current calculation algorithms. DPM was found to calculate doses accurately for studied geometries, indicating this method can be used to verify model-based calculation algorithms for clinically-relevant conditions with decreased measurement effort.

References

1. C. M. Bragg and J. Conway, "Dosimetric verification of the anisotropic analytical algorithm for radiotherapy treatment planning," Radiother Oncol **81**, 315-323 (2006).
2. T. Krieger and O. A. Sauer, "Monte Carlo- versus pencil-beam-/collapsed-cone-dose calculation in a heterogeneous multi-layer phantom," Phys Med Biol **50**, 859-868 (2005).

3. L. Paelinck, N. Reynaert, H. Thierens, W. De Neve and C. De Wagter, "Experimental verification of lung dose with radiochromic film: comparison with Monte Carlo simulations and commercially available treatment planning systems," Phys Med Biol **50**, 2055-2069 (2005).

4. S. E. Davidson, R. A. Popple, G. S. Ibbott and D. S. Followill, "Technical note: Heterogeneity dose calculation accuracy in IMRT: study of five commercial treatment planning systems using an anthropomorphic thorax phantom," Med Phys **35**, 5434-5439 (2008).

5. I. J. Chetty, P. M. Charland, N. Tyagi, D. L. McShan, B. A. Fraass and A. F. Bielajew, "Photon beam relative dose validation of the DPM Monte Carlo code in lung-equivalent media," Med Phys **30**, 563-573 (2003).

6. G. Cranmer-Sargison, W. A. Beckham and I. A. Popescu, "Modelling an extreme water-lung interface using a single pencil beam algorithm and the Monte Carlo method," Phys Med Biol **49**, 1557-1567 (2004).

7. P. Carrasco, N. Jornet, M. A. Duch, L. Weber, M. Ginjaume, T. Eudaldo, D. Jurado, A. Ruiz and M. Ribas, "Comparison of dose calculation algorithms in phantoms with lung equivalent heterogeneities under conditions of lateral electronic disequilibrium," Med Phys **31**, 2899-2911 (2004).

8. H. Schiefer, A. Fogliata, G. Nicolini, L. Cozzi, W. W. Seelentag, E. Born, F. Hasenbalg, J. Roth, B. Schnekenburger, K. Munch-Berndl, V. Vallet, M. Pachoud, B. Reiner, G. Dipasquale, B. Krusche and M. K. Fix, "The Swiss IMRT dosimetry intercomparison using a thorax phantom," Med Phys **37**, 4424-4431 (2010).

9. B. Vanderstraeten, N. Reynaert, L. Paelinck, I. Madani, C. De Wagter, W. De Gersem, W. De Neve and H. Thierens, "Accuracy of patient dose calculation for lung IMRT: A comparison of Monte Carlo, convolution/superposition, and pencil beam computations," Med Phys **33**, 3149-3158 (2006).

10. G. X. Ding, D. M. Duggan, B. Lu, D. E. Hallahan, A. Cmelak, A. Malcolm, J. Newton, M. Deeley and C. W. Coffey, "Impact of inhomogeneity corrections on dose coverage in the treatment of lung cancer using stereotactic body radiation therapy," Med Phys **34**, 2985-2994 (2007).

11. U. Haedinger, T. Krieger, M. Flentje and J. Wulf, "Influence of calculation model on dose distribution in stereotactic radiotherapy for pulmonary targets," Int J Radiat Oncol Biol Phys **61**, 239-249 (2005).

12. A. O. Jones and I. J. Das, "Comparison of inhomogeneity correction algorithms in small photon fields," Med Phys **32**, 766-776 (2005).

13. I. J. Chetty, B. Curran, J. E. Cygler, J. J. DeMarco, G. Ezzell, B. A. Faddegon, I. Kawrakow, P. J. Keall, H. Liu, C. M. Ma, D. W. Rogers, J. Seuntjens, D. Sheikh-Bagheri and J. V. Siebers, "Report of the AAPM Task Group No. 105: Issues associated with clinical implementation of Monte Carlo-based photon and electron external beam treatment planning," Med Phys **34**, 4818-4853 (2007).

14. C. W. Cheng, S. H. Cho, M. Taylor and I. J. Das, "Determination of zero-field size percent depth doses and tissue maximum ratios for stereotactic radiosurgery and IMRT dosimetry: comparison between experimental measurements and Monte Carlo simulation," Med Phys **34**, 3149-3157 (2007).

15. P. Francescon, S. Cora and C. Cavedon, "Total scatter factors of small beams: a multidetector and Monte Carlo study," Med Phys **35**, 504-513 (2008).

16. X. R. Zhu, J. J. Allen, J. Shi and W. E. Simon, "Total scatter factors and tissue maximum ratios for small radiosurgery fields: comparison of diode detectors, a parallel-plate ion chamber, and radiographic film," Med Phys **27**, 472-477 (2000).

17. C. S. Calcina, L. N. de Oliveira, C. E. de Almeida and A. de Almeida, "Dosimetric parameters for small field sizes using Fricke xylenol gel, thermoluminescent and film dosimeters, and an ionization chamber," Phys Med Biol **52**, 1431-1439 (2007).

18. E. Pappas, T. G. Maris, F. Zacharopoulou, A. Papadakis, S. Manolopoulos, S. Green and C. Wojnecki, "Small SRS photon field profile dosimetry performed using a PinPoint air ion chamber, a diamond detector, a novel silicon-diode array (DOSI), and polymer gel dosimetry. Analysis and intercomparison," Med Phys **35**, 4640-4648 (2008).

19. I. J. Das, G. X. Ding and A. Ahnesjo, "Small fields: nonequilibrium radiation dosimetry," Med Phys **35**, 206-215 (2008).

20. E. E. Wilcox and G. M. Daskalov, "Evaluation of GAFCHROMIC EBT film for Cyberknife dosimetry," Med Phys **34**, 1967-1974 (2007).

21. E. E. Wilcox and G. M. Daskalov, "Accuracy of dose measurements and calculations within and beyond heterogeneous tissues for 6 MV photon fields smaller than 4 cm produced by Cyberknife," Med Phys **35**, 2259-2266 (2008).

22. P. M. Charland, I. J. Chetty, S. Yokoyama and B. A. Fraass, "Dosimetric comparison of extended dose range film with ionization measurements in water and lung equivalent heterogeneous media exposed to megavoltage photons," J Appl Clin Med Phys **4**, 25-39 (2003).

23. R. K. Rice, B. J. Mijnheer and L. M. Chin, "Benchmark measurements for lung dose corrections for X-ray beams," Int J Radiat Oncol Biol Phys **15**, 399-409 (1988).

24. E. Yorke, L. Harisiadis, B. Wessels, H. Aghdam and R. Altemus, "Dosimetric considerations in radiation therapy of coin lesions of the lung," Int J Radiat Oncol Biol Phys **34**, 481-487 (1996).

25. J. C. Chow, M. K. Leung and J. Van Dyk, "Variations of lung density and geometry on inhomogeneity correction algorithms: a Monte Carlo dosimetric evaluation," Med Phys **36**, 3619-3630 (2009).

26. A. Rink, I. A. Vitkin and D. A. Jaffray, "Energy dependence (75 kVp to 18 MV) of radiochromic films assessed using a real-time optical dosimeter," Med Phys **34**, 458-463 (2007).

27. S. Devic, N. Tomic, Z. Pang, J. Seuntjens, E. B. Podgorsak and C. G. Soares, "Absorption spectroscopy of EBT model GAFCHROMIC film," Med Phys **34**, 112-118 (2007).

28. M. A. Stevens, J. R. Turner, R. P. Hugtenburg and P. H. Butler, "High-resolution dosimetry using radiochromic film and a document scanner," Phys Med Biol **41**, 2357-2365 (1996).

29. S. Devic, J. Seuntjens, E. Sham, E. B. Podgorsak, C. R. Schmidtlein, A. S. Kirov and C. G. Soares, "Precise radiochromic film dosimetry using a flat-bed document scanner," Med Phys **32**, 2245-2253 (2005).

30. B. C. Ferreira, M. C. Lopes and M. Capela, "Evaluation of an Epson flatbed scanner to read Gafchromic EBT films for radiation dosimetry," Phys Med Biol **54**, 1073-1085 (2009).

31. C. Fiandra, U. Ricardi, R. Ragona, S. Anglesio, F. R. Giglioli, E. Calamia and F. Lucio, "Clinical use of EBT model Gafchromic film in radiotherapy," Med Phys **33**, 4314-4319 (2006).

32. M. Martisikova, B. Ackermann and O. Jakel, "Analysis of uncertainties in Gafchromic EBT film dosimetry of photon beams," Phys Med Biol **53**, 7013-7027 (2008).

33. L. Paelinck, W. De Neve and C. De Wagter, "Precautions and strategies in using a commercial flatbed scanner for radiochromic film dosimetry," Phys Med Biol **52**, 231-242 (2007).

34. E. Wilcox, G. Daskalov and L. Nedialkova, "Comparison of the epson expression 1680 flatbed and the vidar VXR-16 dosimetry PRO film scanners for use in IMRT dosimetry using gafchromic and radiographic film," Med Phys **34**, 41-48 (2007).

35. S. Saur and J. Frengen, "GafChromic EBT film dosimetry with flatbed CCD scanner: a novel background correction method and full dose uncertainty analysis," Med Phys **35**, 3094-3101 (2008).

36. L. Menegotti, A. Delana and A. Martignano, "Radiochromic film dosimetry with flatbed scanners: a fast and accurate method for dose calibration and uniformity correction with single film exposure," Med Phys **35**, 3078-3085 (2008).

37. B. D. Lynch, J. Kozelka, M. K. Ranade, J. G. Li, W. E. Simon and J. F. Dempsey, "Important considerations for radiochromic film dosimetry with flatbed CCD scanners and EBT GAFCHROMIC film," Med Phys **33**, 4551-4556 (2006).

38. T. Cheung, M. J. Butson and P. K. Yu, "Post-irradiation colouration of Gafchromic EBT radiochromic film," Phys Med Biol **50**, N281-285 (2005).

39. H. Bouchard, F. Lacroix, G. Beaudoin, J. F. Carrier and I. Kawrakow, "On the characterization and uncertainty analysis of radiochromic film dosimetry," Med Phys **36**, 1931-1946 (2009).

40. L. J. van Battum, D. Hoffmans, H. Piersma and S. Heukelom, "Accurate dosimetry with GafChromic EBT film of a 6 MV photon beam in water: what level is achievable?," Med Phys **35**, 704-716 (2008).

41. N. Suchowerska, P. Hoban, M. Butson, A. Davison and P. Metcalfe, "Directional dependence in film dosimetry: radiographic and radiochromic film," Phys Med Biol **46**, 1391-1397 (2001).

42. S. Pai, I. J. Das, J. F. Dempsey, K. L. Lam, T. J. Losasso, A. J. Olch, J. R. Palta, L. E. Reinstein, D. Ritt and E. E. Wilcox, "TG-69: radiographic film for megavoltage beam dosimetry," Med Phys **34**, 2228-2258 (2007).

43. J. Sempau, S. J. Wilderman and A. F. Bielajew, "DPM, a fast, accurate Monte Carlo code optimized for photon and electron radiotherapy treatment planning dose calculations," Phys Med Biol **45**, 2263-2291 (2000).

44. N. Tyagi, A. Bose and I. J. Chetty, "Implementation of the DPM Monte Carlo code on a parallel architecture for treatment planning applications," Med Phys **31**, 2721-2725 (2004).

45. N. Tyagi, J. M. Moran, D. W. Litzenberg, A. F. Bielajew, B. A. Fraass and I. J. Chetty, "Experimental verification of a Monte Carlo-based MLC simulation model for IMRT dose calculation," Med Phys **34**, 651-663 (2007).

46. D. W. Rogers, B. A. Faddegon, G. X. Ding, C. M. Ma, J. We and T. R. Mackie, "BEAM: a Monte Carlo code to simulate radiotherapy treatment units," Med Phys **22**, 503-524 (1995).

47. A. Palm and T. LoSasso, "Influence of phantom material and phantom size on radiographic film response in therapy photon beams," Med Phys **32**, 2434-2442 (2005).

48. M. R. McEwen and D. Niven, "Characterization of the phantom material virtual water in high-energy photon and electron beams," Med Phys **33**, 876-887 (2006).

CHAPTER IV

CHARACTERIZATION OF AN ELECTRONIC PORTAL IMAGING DEVICE FOR DOSIMETRIC VERIFICATION

In Chapter III, dose distributions for various heterogeneous geometries were investigated, and the DPM Monte Carlo method was validated in a geometric phantom. In this chapter (and following chapters), the focus is changed from in-phantom dose accuracy to using EPID dosimetry for pre-treatment and treatment verification. In order to use an EPID for dosimetric verification, several issues associated with EPID corrections are discussed in this chapter. The main emphasis of this chapter is to explore a general calibration method for EPID dosimetry to be used for pre-treatment and treatment verification.

IV.A. Introduction

Electronic portal imaging devices (EPIDs) were initially designed to verify the patient position before treatment. EPIDs have fast image acquisition, high resolution, digital format, and stable dose response, which are independent of dose rate and linear with integrated doses.[1, 2] Because of these properties, there has been interest and development in the use of imagers for dosimetric verification, either for pre-treatment quality assurance checks or for verification of dose accuracy during treatment. Currently, a common configuration of EPIDs mounted on linear accelerators is the indirect amorphous-silicon (a-Si) EPID, because of its great sensitivity.[2] This type of EPID includes a copper layer, scintillating layer, and amorphous silicon flat-panel light sensor

with photodiodes and thin film transistors.[2] Due to these components, there are several considerations when investigating the use of a-Si EPIDs for dosimetric verification. First, the EPID response depends on incident photon energies, and it over-responds for low energy photons (< 1 MeV) compared to water due to the pronounced photoelectric effect in the high atomic number (Z) phosphor layer.[3, 4] This effect is related to the mass attenuation coefficient in the medium. The mass attenuation coefficient of the phosphor (gadolinium oxysulfide) is almost constant above 1 MeV, but increases to over 3 orders of magnitude higher at 10 keV.[5] As a result, the dose deposition and scatter phenomenon inside EPIDs are different from that in water.[6, 7] Second, individual pixels in EPIDs may have different sensitivities due to heterogeneity in the detector array or readout electronics. Third, an optical photon scatter (glare) effect was found in phosphor EPIDs, possibly attributable to optical dispersion within the phosphor layer.[4, 8] Fourth, EPIDs are mounted on linear accelerators and moved into position using robotic arms. These arms have metallic parts in their support structures that are not homogenous in composition and geometry, leading to variation in the backscatter as a function of field size and position.[9] Due to these characteristics of EPIDs, several calibration and correction approaches have been investigated to improve their accuracy for dosimetric verification. To do this, most studies correct the predicted EPID response rather than convert the EPID response to dose in water. Specifically, the predicted EPID response is calculated using a known primary fluence with a scatter kernel and then compared with the measured EPID image. The goal of this method is to verify the fluence delivered to patients. The pixel values in EPID images are in arbitrary units rather than the dose units. In conventional pre-treatment verification, the measured doses are compared with the calculated doses in a flat phantom for individual fields and composite fields. The information can be used to verify the accuracy of data transfer and dose calculations, most of which do not consider the multi-leaf collimator (MLC) configuration in the

treatment planning systems (TPSs). This conventional method based on a dose-to-dose comparison scenario provides more information than the EPID method based on an image-to-image comparison scenario, which is in an arbitrary unit. Another drawback of an image-to-image comparison method is that fluence information is needed in order to calculate predicted EPID responses. Therefore, this study aims to develop a general and independent calibration method to convert the EPID responses to doses in water, and to investigate the impact of various corrections on the accuracy of EPID dosimetry. The corrected EPID doses can then be compared with the calculations from TPSs for dose verification before treatment (i.e. pre-treatment verification) or during treatment (i.e. treatment verification).

The first issue regarding EPID corrections is that the high Z material in EPIDs results in a response that differs from water, for example with respect to dose deposition and scatter phenomenon inside the media. This difference can be found in the curves of responses vs. field size changes between EPIDs and water (field size dependence). The field size dependence is caused by the variation in EPID response with the energy spectrum and the different scattering behavior inside EPIDs compared to water. The energy spectrum varies with field shapes and collimation, such as jaw only, MLC-shaped and non-uniform intensity fields (i.e. IMRT fields), and also varies with position, such as the off-axis, inside fields and outside fields. For example, Li et al[10] showed that the mean energy of an MLC-blocked field (or MLC-transmission field)[h] at its center was ~50% higher than that of the corresponding unblocked field (or open field). In addition, the mean energy decreases with increasing radial distance due to less beam hardening caused by the flattening filter for both open and MLC-transmission fields. However,

---

[h] This means that the leaves of the MLC are completely closed. The beam is attenuated by the leaves and only 1-2% radiation will transmit through the leaves. The dose under the leaves is mainly from the transmission radiation.

radial differential beam hardening is more prominent for open fields. In addition to that, Mohan *et al*[11] reported that the mean energy of a 6 MV beam decreases from 1.9 MeV on-axis to 1.5 MeV at 15-20 cm off-axis, while the mean energy of a 15 MV beam decreases from 4.1 to 3 MeV. Several studies have shown the dependence of EPID responses off-axis and for the open and MLC-transmission fields of IMRT beams.[5, 10, 12, 13] For example, Greer *et al*[5] reported that the aS500 EPID had a large off-axis response compared to the response in water, with 13% and 3.5% increases at 15 cm off-axis for 6 and 18 MV photons, respectively. The off-axis over-response is more pronounced for low-energy photons. Therefore, the varying energy spectrum affects the corrections needed for dosimetry with EPIDs. To address the issue of the field size dependence, two general approaches for EPID calibration have been reported. The first approach is an empirical method based on measured field size factors. These factors are used to derive a field-size-dependent relationship between EPID pixel values and the ion chamber (IC) measurements in a water phantom at the center of an open beam.[14] However, away from the central axis, the relationship between EPID pixels and IC measurements is not constant, because of the relative over-response of EPIDs to the softer energies at off-axis positions. Thus, the use of a single correction factor for all points in an entire field is not sufficiently accurate near field edges and for IMRT fields. The second approach is based on the convolution method and scatter kernels. The convolution method is used either to convert a 2-D EPID pixel distribution to a dose distribution in a homogeneous phantom, or to convert a known primary fluence into a portal dose distribution that is compared with the EPID image. These scatter kernels can be derived either by Monte Carlo modeling of the underlying physical scattering processes, or empirically, by adjusting the kernels to obtain the best possible agreement between the EPID doses obtained using the convolution method and measurement by using an IC or film.[4, 6, 7, 15, 16] The second method appears to hold more promise than the first method. To address

the issue of energy dependence for IMRT fields, Li *et al*[10] used Monte Carlo modeling to determine radially-dependent EPID energy-deposition kernels for open and MLC-transmitted radiation spectra. These kernels were convolved with open and MLC-transmitted energy fluence components of the beam. The results from open and MLC-transmitted fields were cumulated to obtain the predicted EPID response. In addition to the study by Li *et al*, Greer *et al*[17] calculated a radially-dependent attenuation coefficient for open and MLC-transmission components.

The second issue regarding EPID correction methods is the variation of EPID pixel sensitivities. Traditionally, the pixel sensitivity variation can be determined by irradiating the EPID with an open uniform field. The resultant image is called a flood field, which is used to correct pixel-to-pixel variations in the sensitivity from the experimental images. However, since there is no real uniform field, the flood field includes information from both pixel sensitivity variation and off-axis differential energy response. As a result, the flood field correction leads to an over-correction of pixel sensitivity and loss of some of the real beam profile information. To address this issue, Greer *et al*[5] proposed a method to measure the off-axis response and pixel sensitivity variation separately to allow corrections of images at any EPID position while retaining beam profile information.

The third issue in relation to EPID corrections is the glare effect in EPIDs. To investigate this effect, Kirkby *et al*[8] used a Monte Carlo method to assess the scattering behavior in EPIDs and then modeled the behavior using exponential functions. They then combined this glare kernel with a dose kernel. This combined kernel can be used either for convolving with the primary energy fluence to calculate predicted portal images[17] or for deconvolving with measured portal images to acquire primary fluence[8]. The correction of the glare effect can improve the accuracy of EPID dosimetry.

The fourth issue is the non-uniform backscatter effect on the EPID response, the magnitude of which depends on field size and pixel position. This non-uniform backscatter for large fields can be corrected using the flood field calibration procedure, which is performed to correct the variation of pixel sensitivity (and off-axis differential energy response) over the entire detector. However, this calibration procedure neglects the variation of backscatter as a function of field size. As a result, non-uniform backscatter was found in portal images with 5%-6.5% asymmetries in the detected signal.[9, 17] To remove this backscatter effect, Ko *et al*[9] suggested using ~5 mm of lead between the detector and the mechanical support structure. However, this method increases the weight of the EPID and may affect the position uncertainty of the device. A different method by Rowshanfarzad *et al*[18] incorporated a backscatter kernel into the EPID dose deposition model to predict the effect of arm backscatter, while Berry *et al*[19] acquired correction matrices to correct backscatter artifacts as a function of field size and detector position.

Considering the influence of these issues on EPID dosimetry, the approach in this study incorporates the corrections, including the non-uniform backscatter, field size dependence, off-axis dependence and glare effect. The present work explores a general calibration method to convert the EPID response to dose in water, providing an advantage of dose-to-dose comparison to the calculation, unlike most studies providing no comparison to the calculation. All parameters needed in the calibration method are acquired from measurements. Finally, the accuracy of the calibration method and parameters are verified with IC and film measurements for jaw only, MLC-shaped and IMRT fields. The comparison between the EPID doses and calculated doses from a TPS is also reported.

IV.B. Methods and materials

IV.B.1. Electronic portal imaging device (EPID)

A commercial amorphous silicon EPID (aS500) (Varian Medical Systems, Palo Alto, CA) with a sensitive area of 40 × 30 cm^2 divided into 512 × 384 pixels of 0.784 × 0.784 mm^2 using the image acquisition system (IAS3) was used in this study. Various acquisition modes can be selected based on the users' purposes. For dosimetric applications, all images were acquired using the integrated operation mode where the image is read out once after the full beam has been delivered. The principle detector components include 1 mm copper layer, 0.34 mm scintillating layer (Gd_2O_2S:Tb) and 1.1 mm amorphous silicon flat-panel light sensor (including photodiode and thin film transistor). The copper layer provides buildup and also absorbs low energy scattered radiation from the machine head and the patient. The scintillating layer converts the incident radiation into light photons. The photodiode converts light photons into electric charge and stores it, and the thin film transistor controls the signal during the readout.[20] Based on the literature, a simplified representation of the a-Si configuration is shown in Figure IV.1. A detailed configuration of the a-Si EPID is shown by Siebers *et al.*[20] The water-equivalent thickness is ~8 mm upstream of the photodiode surface[7] and the water-equivalent backscatter thickness is ~2.5 cm.[8]

Protective cover (9 mm) and screen housing
Cu (1 mm, 0.896 g/cm^2)
Gd_2O_2S:Tb (0.34 mm, 0.134 g/cm^2)
Photodiode on glass substrate (1.1 mm)
Protective cover (9 mm), screen housing and supporting hardware

8 mm water-equivalent buildup
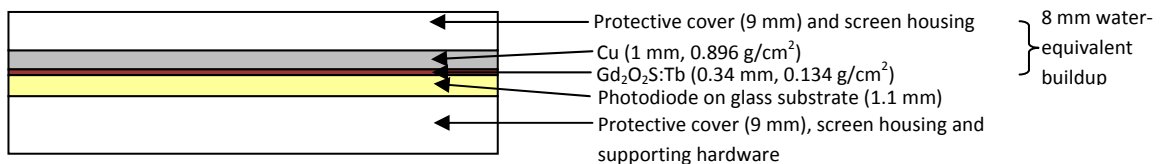
Figure IV.1. Simplified schematic illustration of the a-Si EPID (aS500). [7, 8, 20]

IV.B.2. EPID standard calibration

All measurements were performed with a dose rate of 600 MU/min, 0° collimator angle, and photon energies of 6 and 16 MV using a Varian 21EX accelerator equipped with a 120-leaf Millennium MLC. The square or rectangular fields in this study refer to a field that is shaped only by the jaws with the MLC leaves parked at the most open setting. The accelerator was calibrated with an output of 0.8 cGy/MU at a depth of 10 cm in water for a 10 × 10 cm^2 field size at 90 cm source-to-surface distance (SSD).

Following the recommended protocol by the manufacturer, corrections of dark and flood fields, dose normalization and correction using a default diagonal profile were performed. All calibrations were performed at a source-to-detector distance (SDD) of 150 cm in this study. The dark field image was acquired by averaging 30 frames during the beam off in order to measure the background electronic noise which needs to be removed from the resultant signal. The flood field image was obtained by irradiating the EPID with a 24 × 18 cm^2 field size (defined at 100 cm (isocenter)) so that the projected field on the EPID was 36 × 27 cm^2, which is smaller than the active area of the detector to avoid damage to the imager electronics. The flood field correction was determined by averaging 200 frames. Corrected images are calculated by the following equation,

$$I(x, y) = \left(\frac{I_{raw}(x, y) - DF(x, y)}{FF(x, y) - DF(x, y)}\right)(FF(x, y) - DF(x, y))_{mean} \qquad \textbf{(Equation IV.1)}$$

where x and y are the pixel coordinates on the imager, FF is the flood field integrated image, DF is the dark field integrated image, I is the corrected EPID image data, and I_{raw} is the raw EPID response caused by incident particles.[21]

In the flood field correction, the beam profile is assumed to be flat which introduces errors in the dosimetric images. For example, there is an error in ignoring

beam over-flattening at shallow depths (horn effect) in the profile. The default diagonal profile was measured at 100 cm source-to-surface (SSD), 40 × 40 cm^2 and specific depth (1.7 cm for 6 MV) and then used to correct EPID measured response to retain the profile information. The normalization factor was used to convert the detector response to the calibration unit (CU) or dose to water (cGy) in this study. This normalization factor (EPID response/cGy) was determined by delivering 200 MU at 10 × 10 cm^2 field size on the EPID. The delivered dose at the detector (150 cm SDD and ~8 mm water-equivalent depth) was 0.4363 and 0.3296 cGy per MU delivery for 6 and 16 MV photon beam, respectively. These two values were calculated based on IC measurements at 8 mm depth in water for 100 cm SDD with a simple inverse square law correction to 150 cm.

Portal dose images were exported in DICOM format and analyzed using a program developed in-house using MATLAB$^®$ (The MathWorks, Inc., Natick, MA). Figure IV.2 shows the dark fields, flood fields and final corrected images for 10 × 10 cm^2 for 6 and 16 MV photon beams, which illustrate the need for EPID calibration before starting to use the device for dosimetric verification.
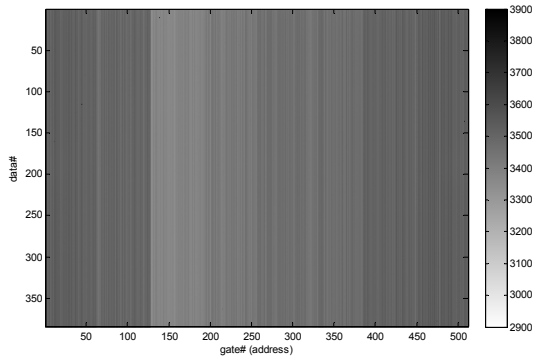
(a) 6 MV
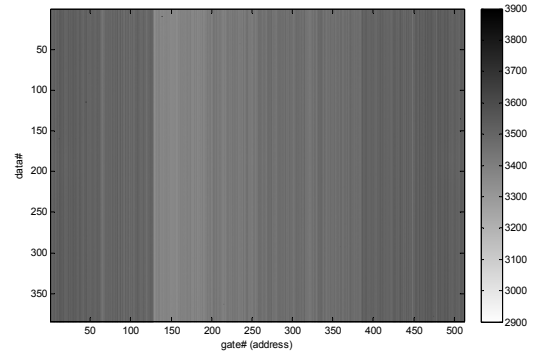
(b) 16 MV
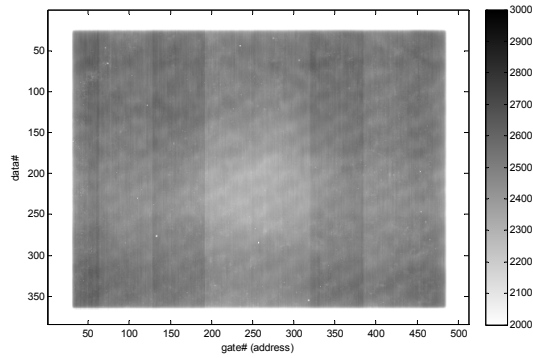
(c) 6 MV
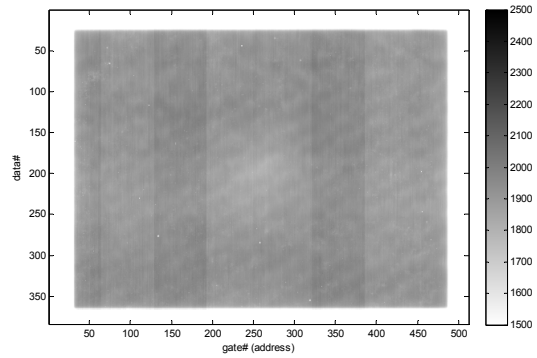
(d) 16 MV
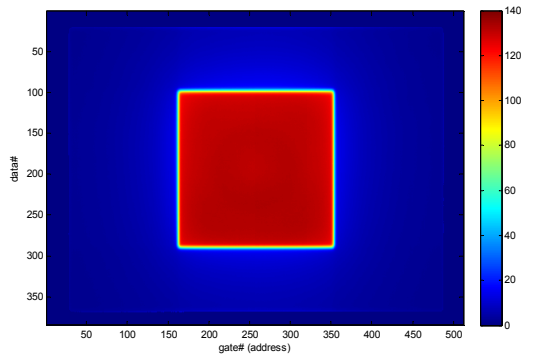
(e) 6 MV
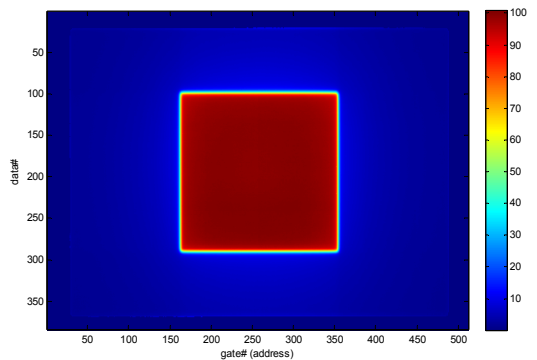
(f) 16 MV

Figure IV.2. (a) and (b) are dark current images (average of 30 frames at 150 cm SDD) for 6 and 16 MV photon beams. (c) and (d) are flood field images (average of 200 frames at 150 cm SDD) for 6 and 16 MV. (e) and (f) are corrected images for 10 × 10 cm^2 (300 MU delivery at 150 cm SDD) for 6 and 16 MV.

IV.B.3. EPID response to dose in water

Figure IV.3 describes the process of converting the response to dose in water at 0.8 cm depth. For jaw only and MLC-shaped fields, the measured EPID responses are

```
                                                        ┌──────────────────────┐
                                                        │  Read MLC sequence   │
                                                        │        file          │
                                                        └──────────┬───────────┘
                                                                   │
                                                                   ▼
  ┌──────────────────────┐                              ┌──────────────────────┐
  │   Measured EPID       │                              │   Calculate MLC      │
  │     response          │                              │   transmission       │
  └──────────┬───────────┘◄┈┈┈┈┈┈ Backscatter           │    fraction          │
             │               artifact correction         └──────────┬───────────┘
             ▼                                                       │
  ┌──────────────────────┐     Separate open and MLC               │
  │   Corrected EPID      │     transmission components             │
  │     response          │◄┈┈  Deconvolve with EPID kernel         │
  └──────────┬───────────┘     Convolve with water kernel   ◄┈┈┈┈┈┘
             │                 Off-axis correction
             ▼
  ┌──────────────────────┐
  │  Conversion to dose   │
  │      to water         │
  └──────────┬───────────┘◄┈┈┈┈┈ Compare
             ▼
  ┌──────────────────────┐
  │  Calculated dose      │
  │   map from TPSs       │
  └──────────────────────┘
```
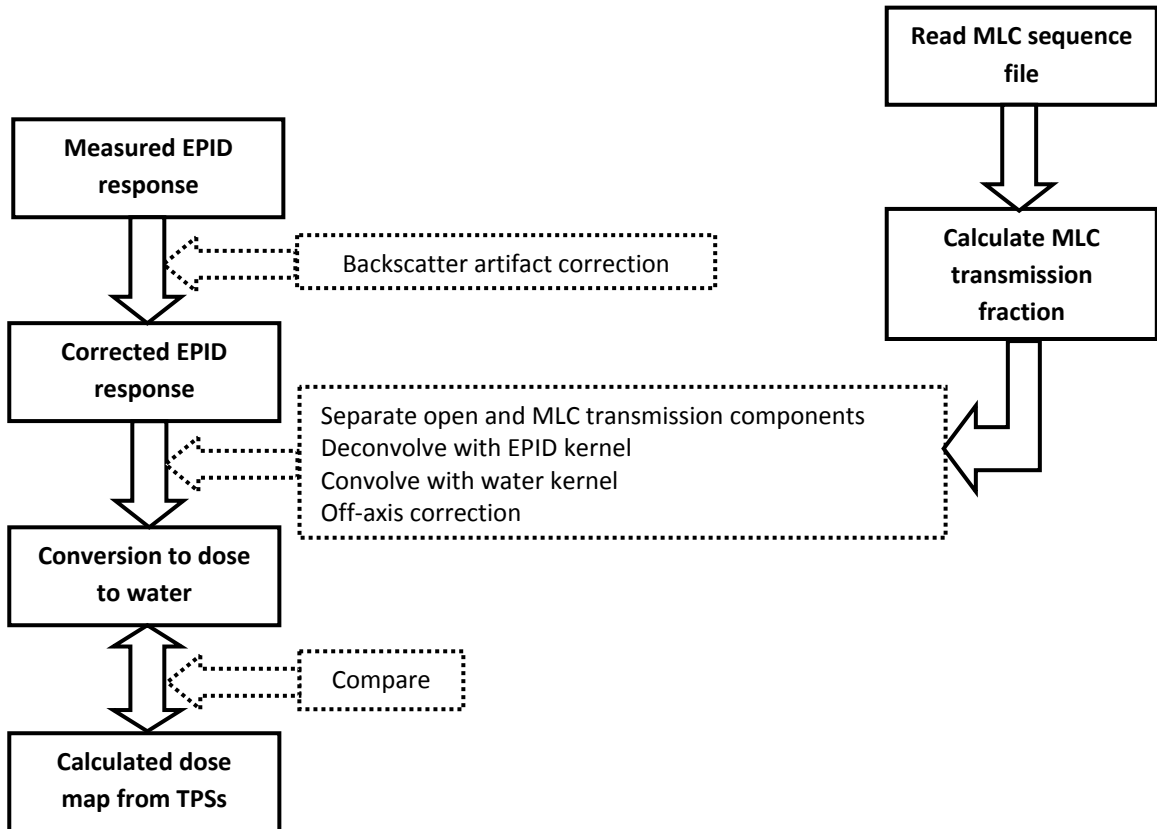
Figure IV.3. EPID corrections, conversion of EPID response to dose to water and comparison to calculated dose map from TPSs.

corrected for the non-uniform backscatter, and the corrected responses are converted to doses in water by deconvolution of an EPID scatter kernel and convolution of the water kernel followed by an off-axis correction. The EPID doses are compared with calculated doses from TPSs. For IMRT fields, an additional step is included. The MLC leaf sequence file for an individual IMRT field is exported and used to calculate the fraction of the response due to MLC transmission. This information is used to separate the

78

responses from the open field and MLC transmission. The individual responses are corrected with individual kernel sets of EPID and water. The following paragraphs describe the derivation of equations which are used to correct EPID responses and convert the responses to doses in water.

In this work, the EPID was calibrated under standard conditions, i.e. 10 × 10 cm^2 jaw only field, so that the EPID readout for these conditions exactly represents the dose to water. However, due to different scattering in the EPID compared to water, the EPID response differs from that of water as a function of field size. A simple correction method is to apply a correction factor as a function of field size to the EPID response, similar to the method reported by Chang *et al*[14]. This correction could work for simple conditions but may not be general enough to deal with the differences in response due to scattering. Therefore, this study uses another method which applies the scatter kernels (i.e. dose deposition kernels) to the measured EPID response. The EPID response (R_E) is due to energy deposited inside EPID, which is equal to *TERMA$_E$* (total energy released per unit mass inside EPID) convolved with the dose deposition kernel (K_E). *TERMA$_E$* is given as the product of the total mass attenuation coefficient ($(\mu/\rho)_E$) and the energy fluence (ψ) at a point. Similarly, the dose to water (D_w) is equal to *TERMA$_w$* convolved with the dose deposition kernel (K_w). The factor (M) of converting *TERMA$_w$* to *TERMA$_E$* is dependent on the mass attenuation coefficient ratio of EPID to water. The equations are shown below,

$$R_E = TERMA_E \otimes K_E = M \cdot TERMA_w \otimes K_E \qquad \textbf{(Equation IV.2)}$$

$$D_w = TERMA_w \otimes K_w \qquad \textbf{(Equation IV.3)}$$

Then, the EPID response can be converted to dose to water by the following equation,

$$D_w = M^{-1}R_E \otimes^{-1} K_E \otimes K_w = CF \cdot R_E \otimes^{-1} K_E \otimes K_w \qquad \textbf{(Equation IV.4)}$$

The *CF* (i.e. *1/M*) is a calibration factor, used to convert *TERMA$_E$* into *TERMA$_w$*. This factor is related to the mass attenuation coefficient ratio of water to that of EPID $((\mu/\rho)_w/(\mu/\rho)_E)$. For calibration of the EPID response for a 10 × 10 cm^2 jaw only field, *CF* is equal to 1 for that jaw only field (i.e. no additional correction will be needed for exported EPID images). Since the mass attenuation ratio of water to EPID is not constant for a range of energies (Figure IV.4), a single calibration factor from the standard condition may not be valid for other conditions, such as off-axis positions and IMRT fields. Therefore, the *CF* should vary with irradiation condition. Using Equation IV.4, the EPID response can be converted into dose to water as a function of field size.
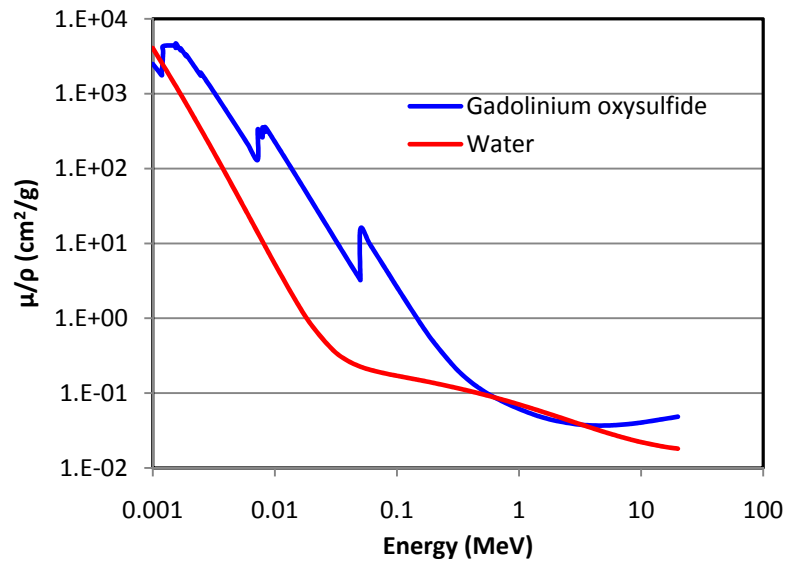
Figure IV.4. Mass attenuation coefficients of gadolinium oxysulfide (phosphor in the EPID) and water (from NIST data).

Given the EPID dependence on the energy spectrum, the use of Equation IV.4 for IMRT fields should require a modification with parameters accounting for IMRT fields

and the softer beam at off-axis positions. Fields for IMRT are typically composed of many small segments. Doses in most regions for IMRT fields have contributions from both open and MLC-transmission fields. Studies have shown that the mean energy is higher for MLC-transmission fields (beam hardening). Because the energy spectrum changes, the factor converting EPID response to dose in water, acquired from an open field, may not apply for IMRT fields. In order to account for energy fluence variations between open and MLC-transmission fields for IMRT, the EPID response ($R_E(x,y)$) is separated into two components: response from the open field ($R_{op}(x,y)$) and response from MLC-transmission ($R_{tr}(x,y)$) (Equation IV.5) using the transmission fraction. The transmission fraction ($TF(x,y)$) is a ratio of the fluence from MLC transmission to total fluence, and is calculated from the MLC sequence file, which includes all of the MLC movement information. Here, to simplify the equation, the $TF(x,y)$ is used to separate the EPID responses into responses from open fields and MLC-transmission.

$$R_E(x,y) = R_{op}(x,y) + R_{tr}(x,y)$$

$$= (1 - TF(x,y)) \cdot R_E(x,y) + TF(x,y) \cdot R_E(x,y) \qquad \textbf{(Equation IV.5)}$$

Then, Equation IV.4 is adapted to,

$$D_w(x,y) = CF_{op}(x,y) \cdot R_{op}(x,y) \otimes^{-1} K_{E_{op}}(x,y) \otimes K_{w_{op}}(x,y)$$

$$+ CF_{tr}(x,y) \cdot R_{tr}(x,y) \otimes^{-1} K_{E_{tr}}(x,y) \otimes K_{w_{tr}}(x,y) \qquad \textbf{(Equation IV.6)}$$

where $CF_{op}(x,y)$ is the calibration factor for the open field and $CF_{tr}(x,y)$ is the calibration factor for the MLC-transmission field. These two factors can correct for the difference in response between open and MLC-transmission fields. In addition to that, the $CF_{op}(x,y)$ and $CF_{tr}(x,y)$ varies with the distance from the central axis to account for the off-axis energy dependence. If the energy is lower than that in the standard calibration condition

(e.g. 10 × 10 cm^2 field size in this study), the *CF* is smaller than 1; otherwise, the *CF* is larger than 1. Similarly, K_{Eop} and K_{Etr} are dose deposition kernels inside the EPID for open and MLC-transmission fields, respectively, while K_{wop} and K_{wtr} are dose deposition kernels in water for open and MLC-transmission fields. Equation IV.6 can then be used to convert the EPID responses to doses in water for most irradiation conditions, such as open and IMRT fields. However, first, two sets of parameters for open ({CF_{op}, K_{Eop}, K_{wop}}) and MLC-transmission fields ({CF_{tr}, K_{Etr}, K_{wtr}}) need to be obtained.

In order to acquire these parameters, several measurements using the EPID only and IC in phantom were performed. In addition to these parameters, the correction matrix for the backscatter effect was also acquired to further improve the accuracy of the EPID dosimetry method (Figure IV.3). All measurements using the IC in phantom (if applicable) were performed at 0.8 cm depth, which is the depth used in the EPID calibration (Section IV.B.2). This means that the EPID responses were converted to the dose at 8 mm depth in water in this study. This study focuses on the 6 MV photon beams, but some measurements were also done with 16 MV photon beams for comparison with 6 MV photon beams. In addition, all results presented in the following sections were acquired at 100 cm SDD.

IV.B.4. Characterization and corrections for EPID dosimetry

IV.B.4.i. Dose response linearity

To check the linearity of the EPID response, MUs from 5 to 600 were delivered for a 10 × 10 cm^2 field size for both energies (6 and 16 MV) at a SDD of 100 cm. The pixel average over ~0.6 cm^2 (10 × 10 pixels) region of interest (ROI) at the field center were acquired.

IV.B.4.ii. Non-uniform backscatter correction

The EPID response is affected by a backscatter artifact which varies with field size. Although the flood field correction is part of the EPID calibration, the backscatter artifact correction is specific for the field used for the flood field correction. To correct for this backscatter artifact, the method proposed by Berry *et al*[19] was used in this study. To use their method, EPID images for field sizes of 2 × 2, 3 × 3, 4 × 4, 5 × 5, 10 × 10, 15 × 15, 20 × 20 cm^2 were analyzed. The backscatter artifact appears in the in-plane direction close to the target (couch) side (Figure IV.5). With the assumption of symmetry in
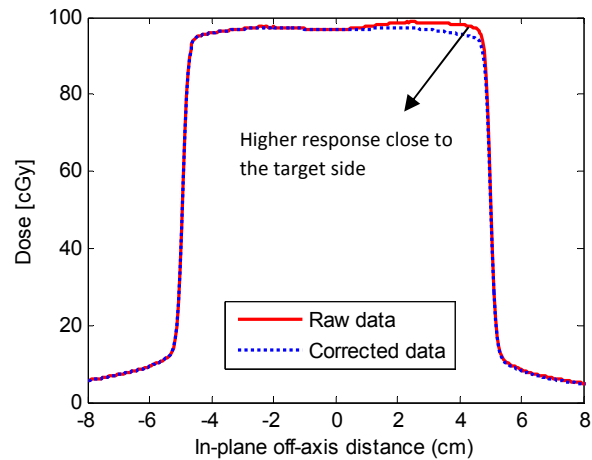
Figure IV.5. An example of in-plane profiles for EPID raw data and backscatter corrected data for 10 × 10 cm^2 field size and 6 MV photons.

profiles, a correction factor as a function of position can be calculated and the profile can be corrected (Figure IV.5). Figure IV.6 shows an example of the correction as a function of distance from the center for 10 × 10 cm^2 field size. The correction was up to 2% at 4 cm off-axis for this field. Since the slope of the correction depends on field size, correction matrices were created based on correction equations as a function of field size. These correction matrices can be applied for the EPID backscatter corrections.
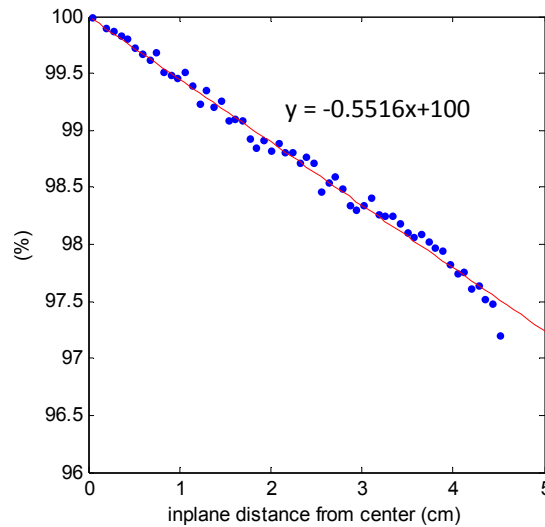
Figure IV.6. An example of the correction as a function of distance from the EPID center for 10 × 10 cm^2 field size and 6 MV photons.

IV.B.4.iii. Scatter kernels in EPID and water for open fields

As noted earlier, the EPID is constructed of materials with higher Z compared to water, leading to different scattering and dose deposition in the EPID than in water. The dose deposition in the EPID can be acquired by convolving the primary energy fluence with a dose-deposition kernel, which can be acquired using a Monte Carlo simulation with a pencil beam geometry. In addition to the dosimetric difference of the EPID from that of water, the problem of optical photon scatter in the EPID (which is known as glare effect) also increases the difficulty of using the EPID for dosimetric applications. An empirical kernel is deconvolved with the measured EPID, removing the influence of the glare effect. For example, Kirkby *et al*[8] used a triple exponential approximation to the kernel which incorporates both dosimetric scattering and light scattering effects. Alternatively, this study measured phantom scatter factors (S_p) in the EPID and water, and these factors were used to derive a combined kernel which includes the dosimetric scattering and light scattering kernels for the EPID, and a dosimetric scattering kernel in water.

The field size factor (S_{cp}) includes collimator scatter (S_c) and phantom scatter (S_p) components. The S_c and S_p factors represent the magnitude of scatter coming from the machine collimation system and phantom medium (such as the EPID and water), respectively. The S_p factor can be used to derive the scattering kernel inside the medium. Since the S_p factor cannot be measured directly, the S_{cp} and S_c factors should be measured and used to derive the S_p factor. The S_{cp} factors were measured with 300 MU for field sizes from 3 × 3 to 20 × 20 cm^2 at 0.8 cm depth and 100 cm SDD for both 6 and 16 MV in EPID and water. The S_c factors were measured for the same fields and SDD with an IC10 ion chamber (0.13 cm^3, Scanditronix Wellhöfer North America, Bartlett, TN) in a CIRS mini-phantom (4 cm in diameter, Computerized Imaging Reference System, Inc., Norfolk, VA). Then, the S_p factor was calculated by dividing the S_{cp} factor by S_c factor. The measurement setup for S_{cp} in water and S_c measurements using the mini-phantom is shown in Figure IV.7.

(a)   (b)
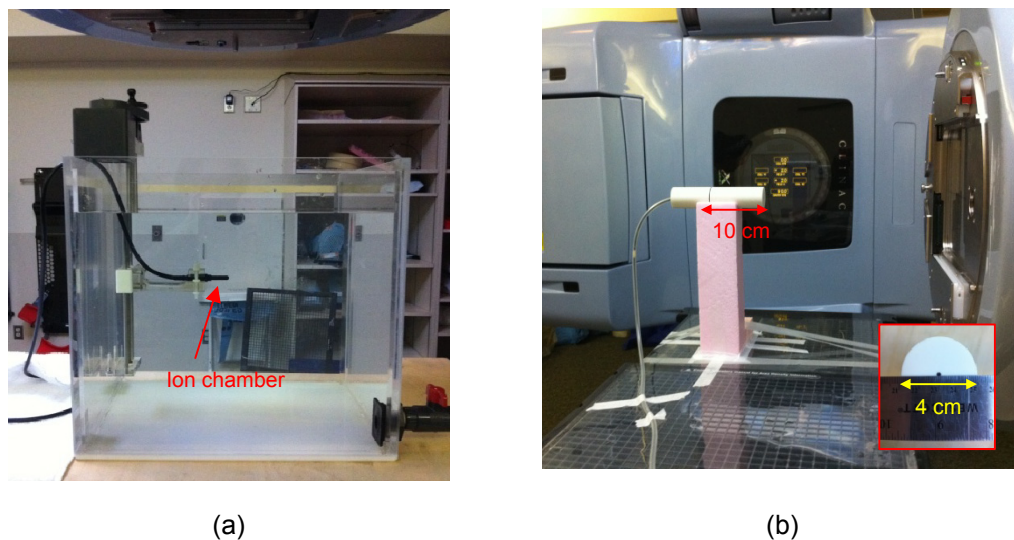
Figure IV.7. An example of measurement setup for (a) S_{cp} in water and (b) S_c using the IC in a mini-phantom for the gantry angle of 90° to reduce the backscatter effect from the floor.

Based on the method proposed by Storchi *et al*[22], a numerical approximation was used to get the kernel with S_p factors in EPID and water. A scatter kernel (K_s) can be expressed as discrete functions with values defined at $R_n=n\delta$, where $n \geq 0$ is an integer and δ is a bin size (0.25 cm in this study). The computed kernel value at r_n will be the value of the kernel over the ring centered at r_n and thickness δ. Figure IV.8 illustrates the concept of computing the scatter kernel. The first approximation of the scatter kernel is calculated by numerical differentiation of $D(R_n)$ at the radial points $R_n=n\delta$ (Equations IV.7 and IV.8). In addition, square fields (X^2) were converted to circular fields with the same area (Equation IV.9). After the K_s was acquired, the difference between calculated and measured S_p values were determined. A correction was made to the kernel based on this difference due to the approximation of square fields which were used to derive the scatter kernel.

$$K_s(R_0) = \frac{D(R_0)}{\pi(0.5\delta)^2} \qquad n = 0 \qquad \text{(Equation IV.7)}$$

$$K_s(R_n) = \frac{D(R_n)-D(R_{n-1})}{2\pi n\delta^2} \qquad n > 0 \qquad \text{(Equation IV.8)}$$

$$R = \frac{X}{\sqrt{\pi}} \qquad\qquad\qquad \text{(Equation IV.9)}$$
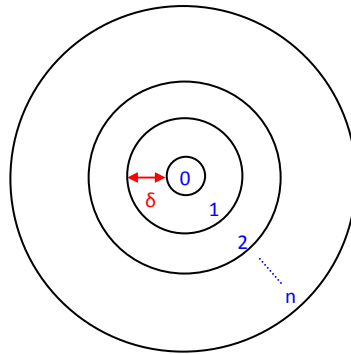
Figure IV.8. Illustration of the geometry for calculating the scatter kernel from the measured doses. δ is 0.25 cm in this study.

IV.B.4.iv. Effect of MLC-transmission fields

Due to beam hardening for MLC-transmission fields, the parameters used in open fields will not be correct for MLC-transmission fields. To acquire the appropriate parameters (CF_{tr}, K_{Etr} and K_{wtr}) in Equation IV.6 for MLC-transmission fields, the EPID responses as a function of field size (3 × 3, 4 × 4, 5 × 5, 10 × 10, 15 × 15, 15 × 25 cm^2 jaw fields) for 6 MV photons were measured for MLC-transmission fields (Figure IV.9) and compared
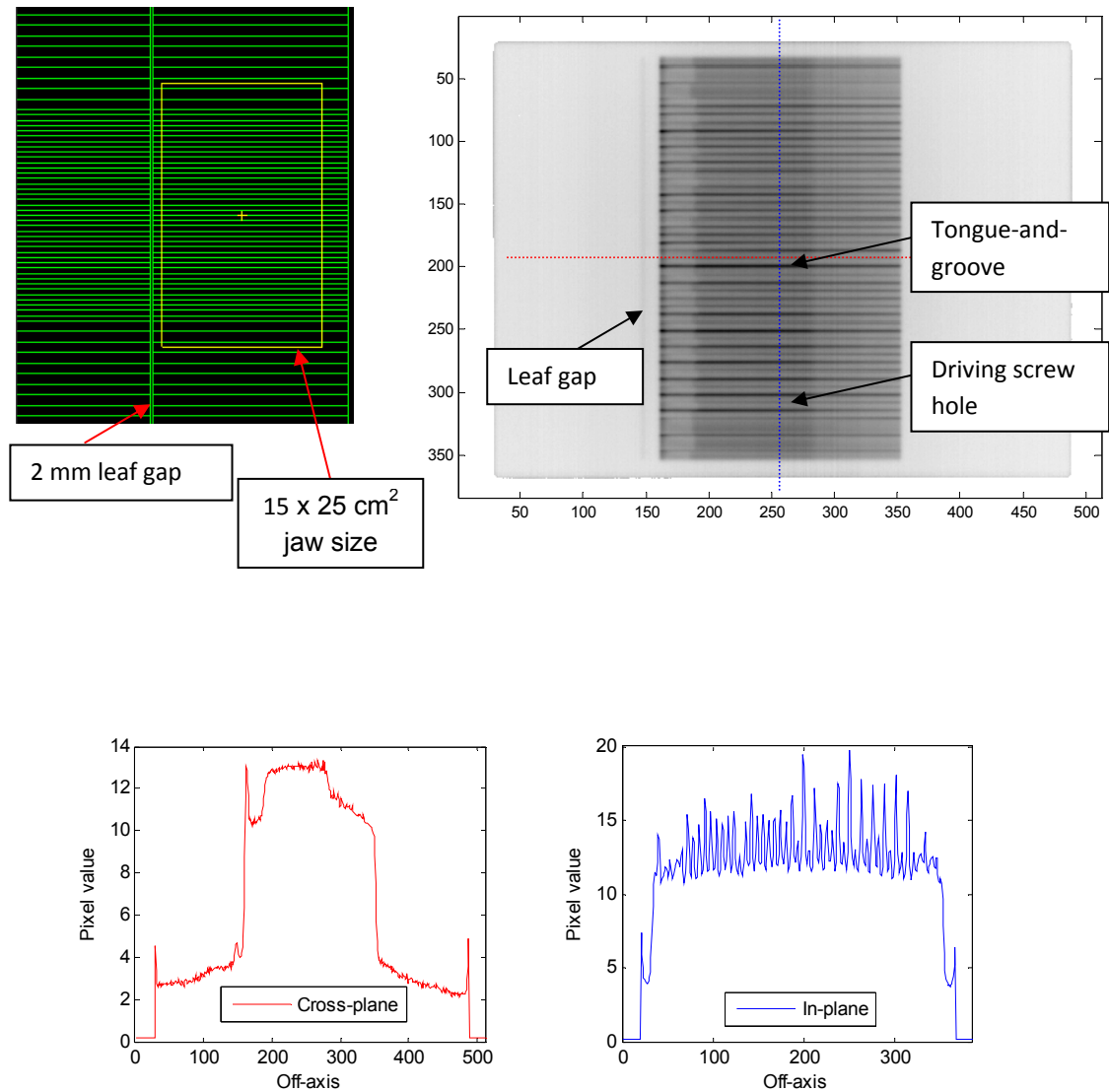
Figure IV.9. An example measurement for the MLC leaves closed at the left side of the field with a jaw opening of 15 × 25 cm^2. The profiles cross the detector center are extracted to illustrate the variation in the MLC-transmission field.

with IC measurements (A12 Exradin Farmer-Type Chamber with an Inovision Therapy Dosimeter Model 35040) in a water tank (Med-Tec Inc., Orange City, IA). In addition to S_{cp} measurements for MLC-transmission fields, the S_c factors were measured with an IC10 and CIRS mini-phantom. The MUs were 800 and 600 for the EPID and IC measurements, respectively. Then, the kernels for MLC-transmission fields in the EPID and water were calculated using the method described in Section IV.B.4.iii.

IV.B.4.v. Off-axis correction

Open field beams are not flat because of the flattening filter. The beam off-axis is softer than at central axis. As a result, the EPID over-responds at off-axis positions. Here, we assume the off-axis dependence only affects calibration factors (CF_{op} and CF_{tr} in Equation IV.6) without affecting the relationship of scatter kernels between the EPID and water for both open field and MLC-transmission terms. Because of the off-axis over-response, the EPID calibration factors decrease with increasing distance from the central axis. In order to get calibration factors at the off-axis positions, the EPID responses (after the scatter kernel correction) for a 20 × 20 cm^2 field size were compared with IC measurements in water. Then the correction matrix was determined and applied to EPID data.

IV.B.5. Experimental verification for jaw only, MLC-shaped and IMRT fields

The parameters and correction factors acquired in Section IV.B.4 were applied to EPID raw data, and the EPID responses were converted to the doses at 8 mm depth in water. In order to verify the accuracy of the proposed method, the corrected EPID doses were compared with IC measurements in water and film measurements in Solid Water. The central axis doses using the IC and the 2D dose distributions using the film were measured at 8 mm depth for jaw only field, MLC-shaped, and IMRT fields for 6 MV

photon beams. The jaw only fields were 3 × 3, 4 × 4, 5 × 5, 10 × 10, 15 × 15 and 20 × 20 cm^2 field sizes. Measurements for MLC-shaped fields used irregular field shapes (Figure IV.10) that were developed at the University of Michigan (and documented in TG53[23]). IMRT fields were randomly selected from a head-and-neck plan, and are shown in Figure IV.11 with the number of segments and MU information for each field.

Film measurements used Kodak EDR2 films (Carestream Health, Inc., Rochester, NY) with Solid Water phantom slabs (Gammex RMI Model 457, Middleton, WI). The lateral dimensions of the phantom slabs were 40 × 40 cm^2 with thicknesses of 3 mm to 5 cm. The buildup thickness was 0.8 cm and the backscatter thickness was 10 cm. Films were placed at 100 cm SDD. A calibration curve was acquired with a dose range from 0 to 400 cGy. All films were developed using a Kodak X-OMAT 3000RA Processor (Eastman Kodak, Rochester, NY), digitized with a VXR-16 Dosimetry PRO^{TM} scanner (VIDAR systems corporation, Herndon, VA) and analyzed using an in-house program. The film resolution was 0.179 × 0.179 mm^2.

To quantify the agreement between EPID and EDR2 film measurements for IMRT fields, the dose-gradient compensation (C) index[24, 25] was calculated with criteria of 2%/1 mm and 5%/1 mm (dose difference tolerance of maximum dose (%) and distance parameter (mm) for the gradient compensation). For comparison, the γ index[26] was calculated with criteria of 2%/2 mm and 3%/3 mm (dose difference tolerance of maximum dose (%) and distance-to-agreement (mm)). The percentage of points in agreement (|C| or |γ| ≤1) was calculated for the region where the dose was higher than 10% of maximum measured film dose (i.e. region of interest (ROI) is the dose >10% of maximum film measured dose). The C index with minimal gradient compensation (distance parameter of 1 mm) was chosen to focus the analysis on dose level discrepancies.

(a)   (b)   (c)
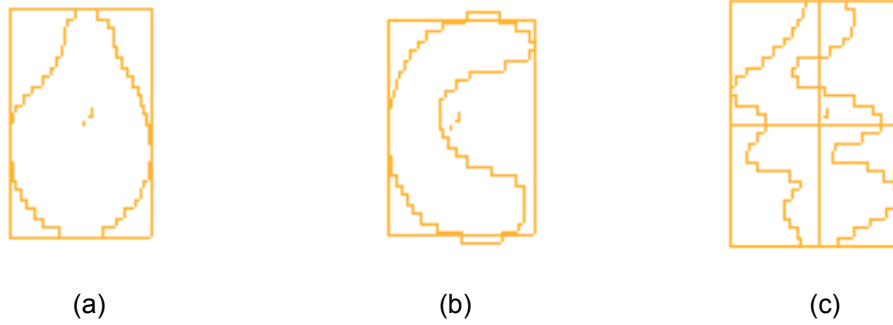
Figure IV.10. MLC-shaped fields of (a) oval, (b) C and (c) squiggle shapes suggested in TG53.[23] Jaw sizes were (a) 18 (X) × 24 (Y), (b) 18 × 22, and (c) 20 × 26 cm^2.

(a) LPO   (b) LLAT   (c) AP

(d) RLAT   (e) RPO
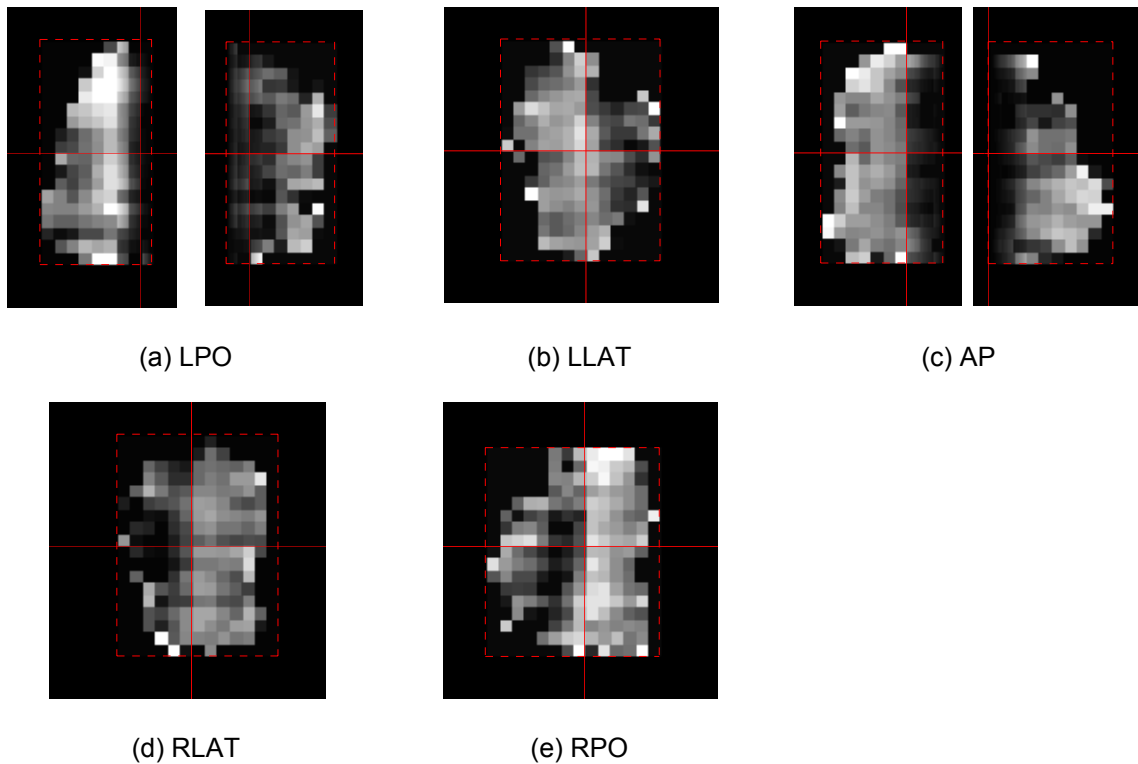
Figure IV.11. IMRT intensity maps (1 cm x 1 cm beamlets) reconstructed from MLC delivery files with 2% MLC transmission. (a) and (c) are split fields with total number of segments of 322 and 284, respectively. (b), (d) and (e) have192, 152 and 237 segments. Total MUs were (a) 278, (b) 168, (c) 243, (d) 134 and (e) 206. Whiter color represents higher intensity.

IV.B.6. Measurements vs. calculations

The final goal for this study is to compare the corrected EPID doses (to water) with calculated dose in TPSs for pre-treatment verification (or treatment verification). Therefore, corrected EPID dose were also compared with calculations using convolution/superposition (CVSP) implemented in the University of Michigan treatment planning system (UMPlan) for jaw only, MLC-shaped and IMRT fields for 6 MV photon beams. Dose calculations were performed in a manual geometry with a density of 1 g/cm^3 and dimension of 30 × 30 × 10.8 cm^3, and SDD of 100 cm. Coronal plane doses at 0.8 cm depth were extracted. Absolute doses were compared with EPID measurements in this study. In addition, for IMRT fields, the C and γ indices were compared.

IV.C. Results

IV.C.1. Characterization and corrections for EPID dosimetry

IV.C.1.i. Dose response linearity

Figure IV.12 shows the linearity for 6 and 16 MV photons at 100 cm SDD. The linearity was good for delivery of MUs larger than 100. The EPID response was 10% lower for 5 MUs compared to MUs larger than 100. Comparing measurements on different days (within 2 months), differences were within 0.6%, except for 10 MU (where up to 1.7% variation was observed).
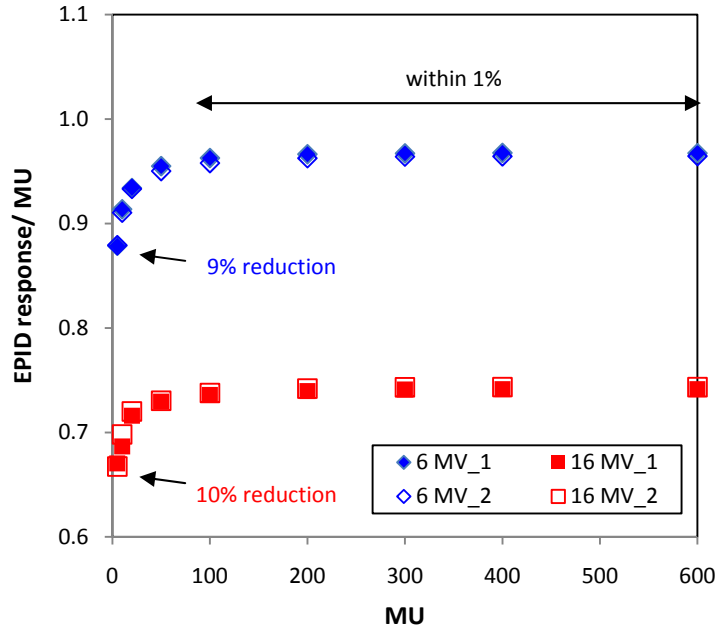
Figure IV.12 EPID response linearity (EPID response per MU vs. MU) at SDD of 100 cm for 6 and 16 MV photon beams.

IV.C.1.ii. Non-uniform backscatter correction

Figure IV.13 shows the slope of the correction equations as a function of field size for 6 MV. Using this information, for pixels from the center to the target side, the corrections (Cor_{BS}) in percentage can be acquired through Equation IV.10.

$$Cor_{BS}(Y_{Jaw}, d) = 100 - 2.809 \cdot e^{-0.1528 \cdot Y_{Jaw}} \cdot d \qquad \textbf{(Equation IV.10)}$$

where Y_{Jaw} and d represent jaw sizes in the in-plane direction and distances from the center to the target side, respectively. For pixels from the center to the gun side, no correction is needed, that is,

$$Cor_{BS} = 100 \qquad \textbf{(Equation IV.11)}$$

The EPID raw data were then multiplied by an individual correction matrix, depending on

the in-plane jaw size (Figure IV.14).

$$y = -2.809e^{-0.1528x}$$
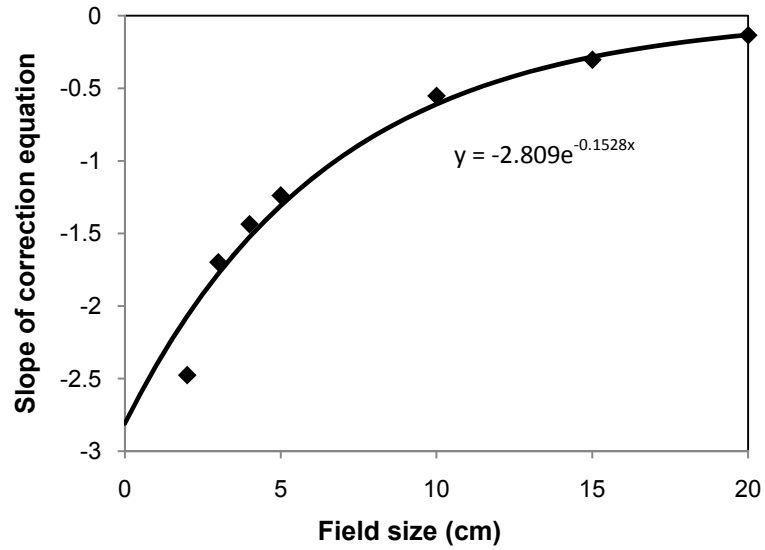
Figure IV.13 The slope of correction equation as a function of field sizes
for 6 MV.
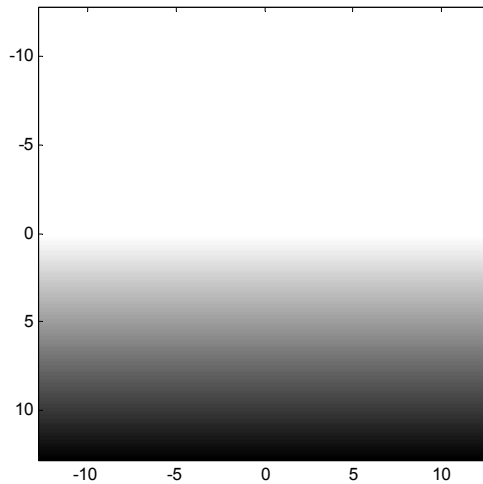
Figure IV.14 An example of the correction matrix for 10 × 10 cm^2 field
size for 6 MV photons. The white color represents no correction.

IV.C.1.iii. Scatter kernels in EPID and water for open fields

Figure IV.15 shows the S_p factors in water and EPID for both energies. The S_p factor dependence on field size was different between water and EPID, indicating that the scattering behavior inside the EPID is different from that in water. The difference for the studied fields was within 3.5% and 11.5% for 6 and 16 MV, respectively. In addition, the behavior of the S_p difference was reversed between 6 and 16 MV. The S_p value as a function of field size was used to derive the scatter kernels in the EPID and water (Figure IV.16). The EPID scatter kernels for both energies were similar but the water kernels were significantly different between two energies. These kernels can then be used to convert the EPID responses to doses in water.

(a)   (b)
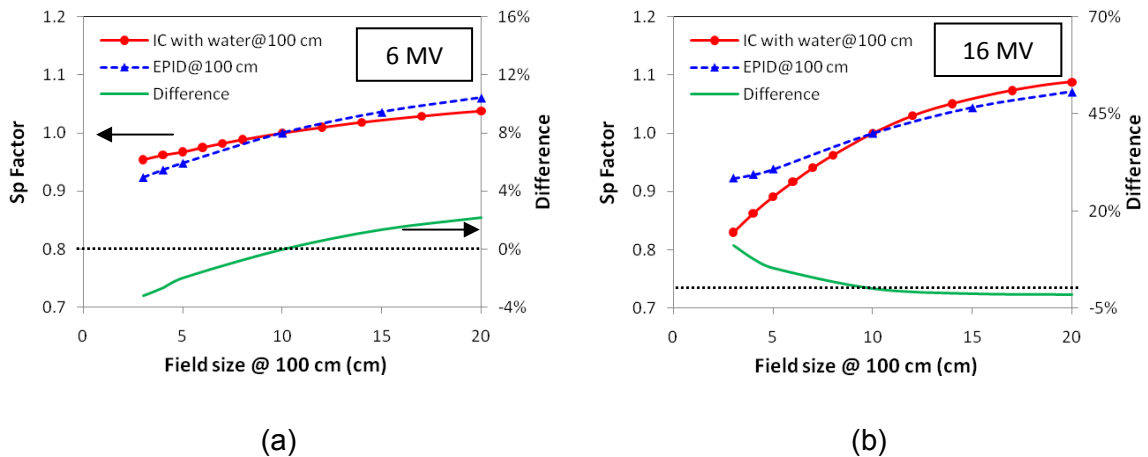
Figure IV.15. S_p factors in water and EPID for (a) 6 MV and (b) 16 MV. Also shown are the S_p differences relative to the value from IC measurements in water.
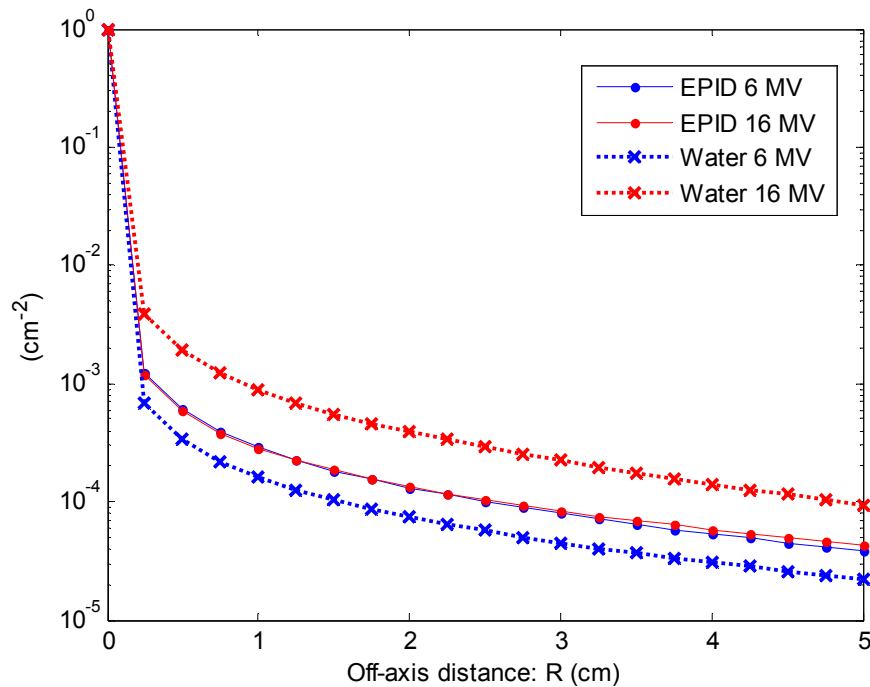
Figure IV.16. Scatter kernels of the EPID and water for 6 and 16 MV photon beams. The bin size used to acquire the kernels is 0.25 cm (δ in Figure IV.8). The data shown here are normalized to the value at R = 0 cm for each curve.

IV.C.1.iv. Effect of MLC-transmission fields

Figure IV.17 shows the S_{cp}, S_c and S_p factors of open and MLC-transmission fields for 6 MV photons measured in water and the EPID. When the fields were fully blocked by the MLC, S_{cp} factors were significantly different from open fields for both water and EPID. The slope of the S_{cp} factor as a function of field sizes was larger for MLC-transmission fields than for open fields. However, the slope was even larger in water than in the EPID (Figure IV.18). Similarly, the S_c slope was larger for MLC-transmission fields. The interesting finding is that the S_p slope slightly increased for MLC-transmission fields in water but it decreased in the EPID. The S_p factor difference between MLC-transmission and open fields was within 1.3% and 3.0% in water and the EPID, respectively, for field sizes from 4 × 4 to 15 × 25 (18.75 × 18.75) cm². These results indicated that the scatter

95

kernels in water for open and MLC-transmission fields are similar (i.e. $K_{wop} \approx K_{wtr}$ in Equation IV.6), while the kernels inside the EPID for open and MLC-transmission fields are different (i.e. $K_{Eop} \neq K_{Etr}$ in Equation IV.6). Figure IV.19 shows the 6 MV scatter kernels of the EPID and water for open and MLC-transmission fields. The scatter kernel of the EPID for MLC-transmission fields was different from that for open fields, and the behavior in the EPID was similar to the behavior in water for MLC-transmission fields.

In this study, the MLC transmission was determined with the range of 1.6% (3×3 cm^2) to 1.9% (18.75×18.75 cm^2) from in-air measurements. The average MLC transmission was 1.7%, and this value was used to derive TF value in Equation IV.5 with MLC leaf sequence files. The CF_{op} and CF_{tr} values at the central axis in Equation IV.6 were determined to be 1.014 and 1.133, respectively.

(a)   (b)
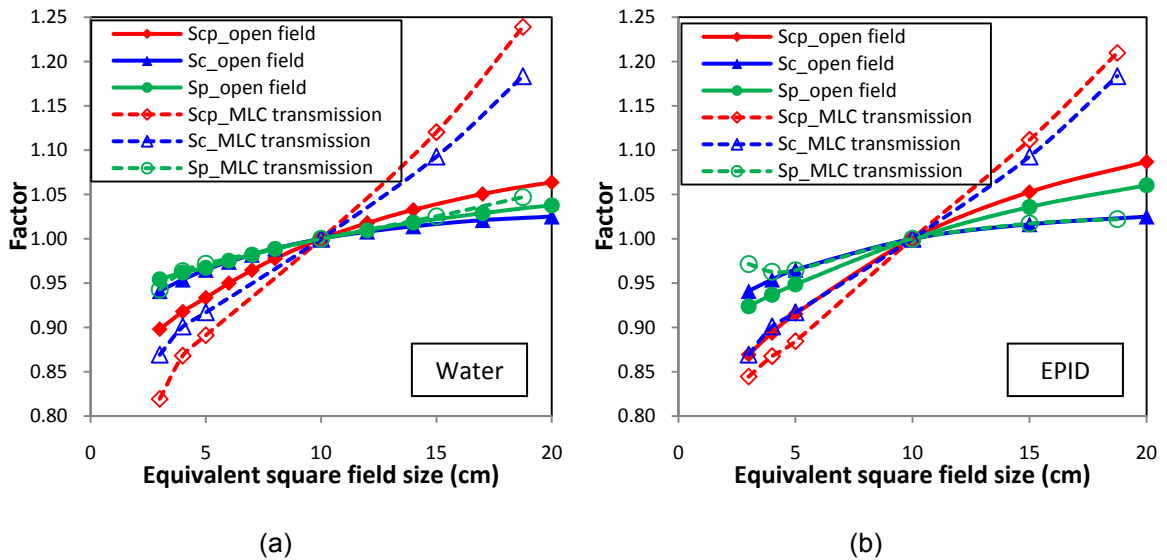
Figure IV.17. S_{cp}, S_c and S_p factors of open and MLC-transmission fields for 6 MV photons measured in (a) water and (b) the EPID. The rectangular field of 15×25 cm^2 (MLC-transmission field) is equivalent to 18.75×18.75 cm^2 shown in the figure. The S_c factors in (a) are the same as that in (b) because this factor is assumed independent of the detector.

(a)   (b)
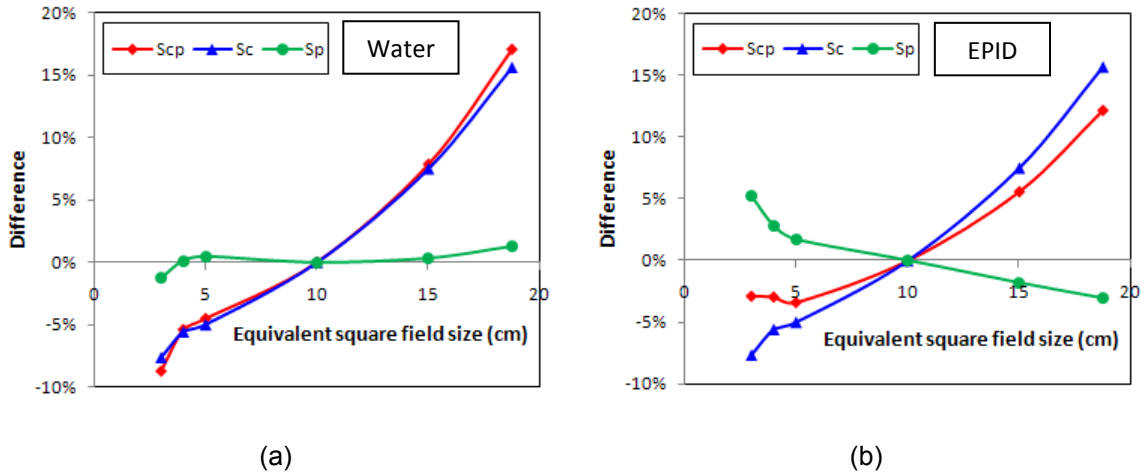
Figure IV.18. S_{cp}, S_c and S_p differences between MLC-transmission and open fields for (a) water and (b) the EPID. The S_c difference in (a) is the same as that in (b) because this factor is independent of the detector.
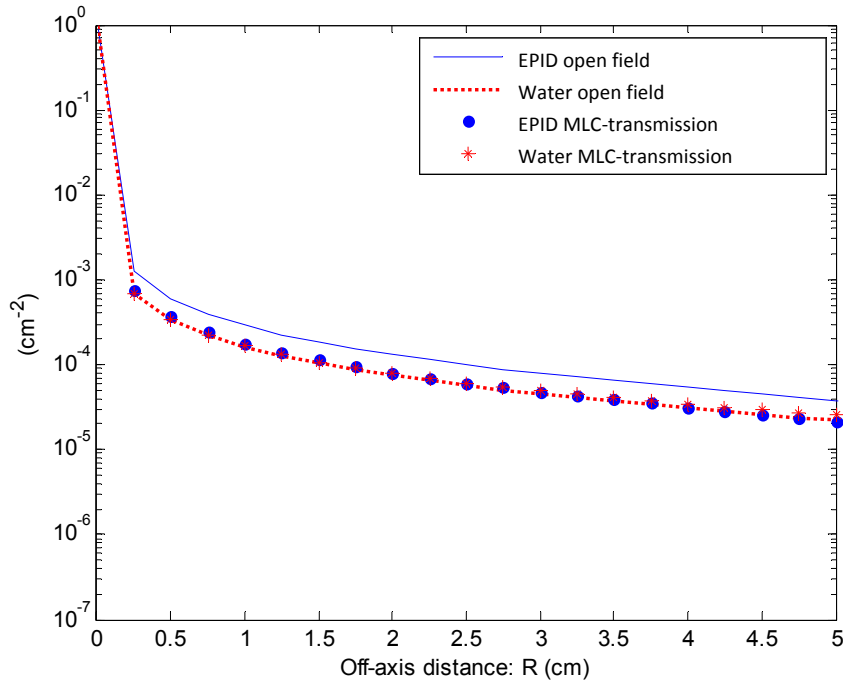
Figure IV.19. 6 MV scatter kernels of EPID and water for open and MLC-transmission fields. The bin size to acquire the kernels is 0.25 cm (δ in Figure IV.8). The data shown here are normalized to the value at R = 0 cm for each individual curve.

IV.C.1.v. Off-axis correction

Measured profiles with an IC in water and for the EPID (with the kernel corrections) are shown in Figure IV.20. There are clear differences at the off-axis positions. The ratio of
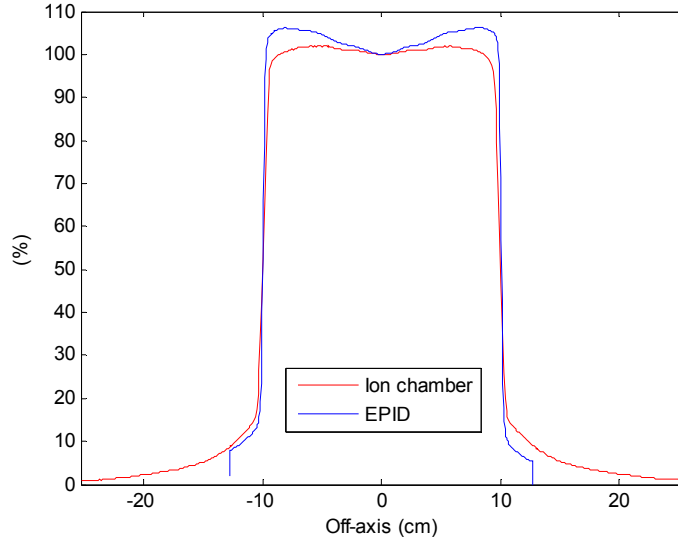
Figure IV.20. Measured profiles of the IC and the EPID (with the kernel correction) for a 20 × 20 cm^2 field size. The data shown here are normalized to the central axis for each curve.

the IC data to EPID data inside the field (80% field range) was fitted with a Gaussian function. The fitting equation is shown below,

$$f(x) = f_0 + \frac{A}{\sqrt{2\pi\sigma^2}} e^{-\frac{(x-x_0)^2}{2\sigma^2}} \qquad \text{with } x_0 = 0 \qquad \textbf{(Equation IV. 12)}$$

where f_0, A and σ are fitting parameters. This function (Figure IV.21) was used to create a 2D correction matrix and applied to CF_{op} and CF_{tr} to correct the energy dependence of the EPID at off-axis positions. Here, we assume the scatter behavior is the same over the entire field, and the off-axis energy dependence only affects the calibration factors for open and MLC-transmission fields. In addition, we assume the behavior of off-axis dependence is the same for open and MLC-transmission fields. Thus, the same off-axis correction matrix was used for open and MLC-transmission fields but the magnitude was

98

different, with the maximum value at the central axis of 1.014 (CF_{op} *(0,0)*) and 1.033 (CF_{tr} *(0,0)*) for open and MLC-transmission fields, respectively.
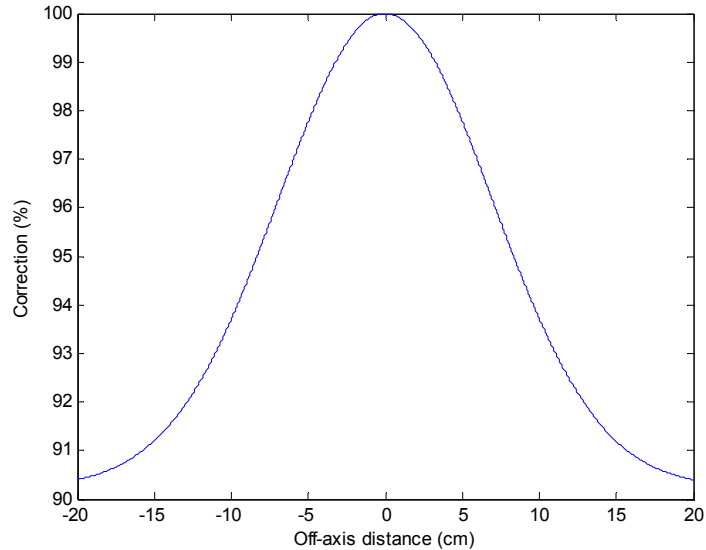
Figure IV.21. Corrections as a function of distance from the central axis.

IV.C.2. Experimental verification for jaw only, MLC-shaped and IMRT fields

The backscatter correction matrix, two sets of parameters for open ({$CF_{op}(0,0)$, K_{Eop}, K_{wop}}) and MLC-transmission fields ({$CF_{tr}(0,0)$, K_{Etr}, K_{wtr}}), and the off-axis correction matrix acquired from Section IV.C.1 were applied to the EPID raw data. The EPID responses were converted to doses at 0.8 cm depth in water. In this section, the corrected EPID responses for jaw only and MLC-shaped fields were compared with the IC measurements at 8 mm depth in water and uncorrected (raw) EPID responses (Table IV.1). The difference between the EPID and IC data reduced from 3.1% to 0.7% for uncorrected and corrected EPID data, respectively, except for the C-shape field. The large difference for the C-shape field was because the central axis for the C-shape field was blocked by the MLC (Figure IV.10(b)). The dose under the block field was relatively

small. In addition, the correction of the MLC-transmission effect was not included for MLC-shaped fields. When the MLC transmission effect was included (i.e. using different calibration factors and kernels for open and MLC-transmission fields), the relative dose varied from 0.078 to 0.099 and the difference reduced from 18.3% to 3.9% for the C-shape field (not shown). Generally, the corrections improved the agreement between the EPID and IC data inside the radiation field.

Table IV.1. Relative doses at the center for jaw only and MLC-shaped fields for IC at 8 mm depth in water, uncorrected EPID responses, corrected EPID doses (with backscatter, scatter kernel and off-axis corrections). Differences were calculated relative to IC data.

Field size (cm^2)	IC in water	Uncorrected EPID		Corrected EPID	
	Relative dose	Relative dose	Difference	Relative dose	Difference
3 × 3	0.898	0.870	-3.1%	0.899	0.1%
4 × 4	0.918	0.894	-2.6%	0.918	0.1%
5 × 5	0.934	0.916	-1.9%	0.935	0.2%
10 × 10	**1.000**	**1.000**	**0.0%**	**1.000**	**0.0%**
15 × 15	1.039	1.053	1.4%	1.038	-0.1%
20 × 20	1.064	1.087	2.2%	1.062	-0.2%
Oval	1.065	1.075	1.0%	1.057	-0.7%
C*	0.095	0.108	14.2%	0.078	-18.3%
Squiggle	1.046	1.056	0.9%	1.046	0.0%

*The dose was measured outside the field (under the MLC) to verify the accuracy of transmission dose.

In addition to the verification using IC measurements, the film measurements were also performed for jaw only, MLC-shaped and IMRT fields. For jaw only fields, Table IV.2 shows the differences between EDR2 film and EPID data without any corrections and with the backscatter correction only and all corrections (backscatter, kernel and off-axis) for 3 × 3, 5 × 5, 10 × 10 and 15 × 15 cm^2 field sizes. The relative difference was calculated as a ratio of dose difference relative to the maximum dose on EDR2 film data for ROI > 10% of maximum dose. The difference decreased when all

corrections were applied to the EPID responses. The average difference decreased from within 2.5% to within 0.8% for all studied fields. The main difference between the film and EPID data can be seen in Figure IV.22. This figure shows the in-plane profiles cross the isocenter for the four field sizes. As expected, the backscatter correction on the EPID response improved the flatness of profiles, but did not affect the dose at the center. The use of all corrections on the EPID response improved the agreement at the center and outside of field. The main difference between the film and EPID data was in the region close to the field edge.

Table IV.2. Differences (average and one standard deviation (1σ)) between the film and EPID data relative to maximum film doses for EPID raw data (no correction), EPID with the backscatter correction (BS), and EPID with the backscatter, kernel and off-axis corrections (BS+Ks+OAR) for ROI > 10% maximum film dose.

Field	Correction	Relative difference to maximum dose
3 x 3	No	-2.25%± 2.86%
	BS	-2.76%± 2.48%
	BS+Ks+OAR	0.45%± 3.66%
5 x 5	No	-1.14%± 2.45%
	BS	-1.80%± 2.05%
	BS+Ks+OAR	0.73%± 2.87%
10 x 10	No	0.65%± 2.25%
	BS	-0.01%± 1.86%
	BS+Ks+OAR	0.36%± 2.30%
15 x 15	No	2.50%± 1.97%
	BS	2.02%± 1.82%
	BS+Ks+OAR	0.14%± 2.07%
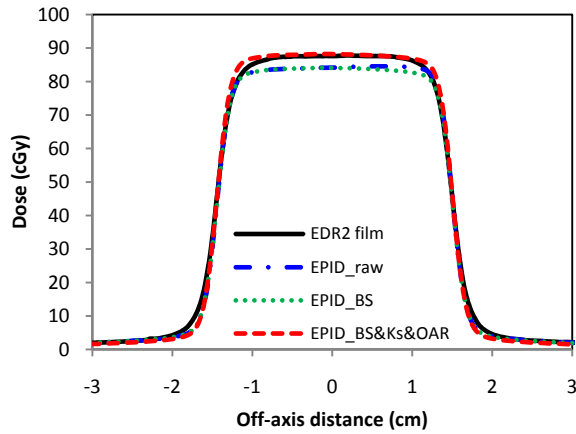
(a) Profiles at x=0 for 3 × 3 cm^2
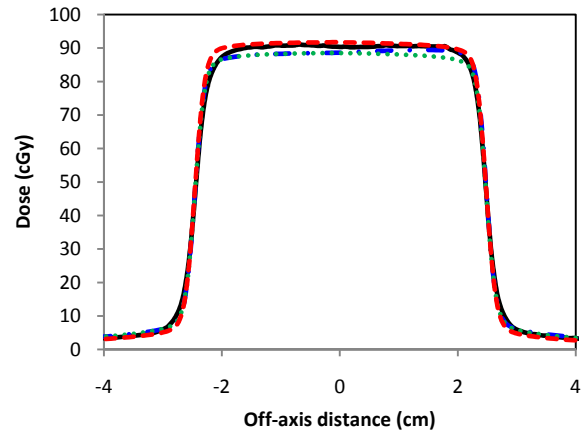
(b) Profiles at x=0 for 5 × 5 cm^2
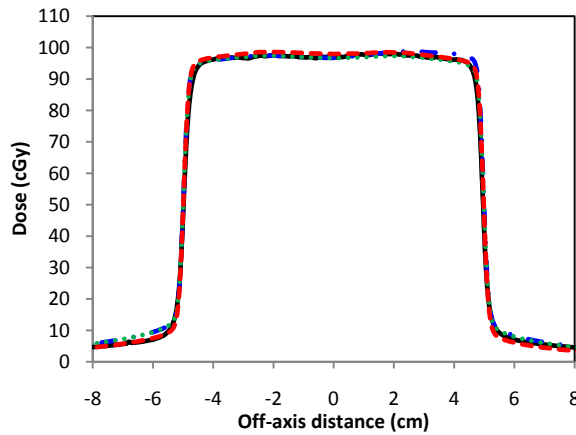
(c) Profiles at x=0 for 10 × 10 cm^2
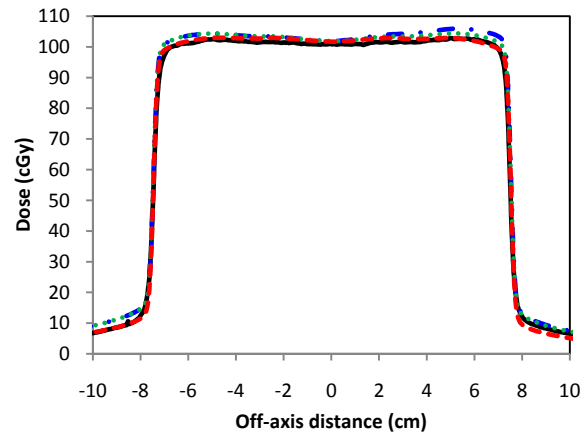
(d) Profiles at x=0 for 15 × 15 cm^2

Figure IV.22. In-plane profiles along the central axis for (a) 3 × 3, (b) 5 × 5, (c) 10 × 10 and (d) 15 × 15 cm^2 field sizes for EDR film data, EPID raw data (EPID_raw), EPID with the backscatter correction (EPID_BS) and EPID with the backscatter, kernel and off-axis corrections (EPID_BS&Ks&OAR).

For MLC-shaped fields, Table IV.3 shows the differences between the film and EPID data without any corrections and with the backscatter correction only and all corrections (backscatter, kernel and off-axis) for the oval, C and squiggle shapes. The average difference decreased from within 1.9% to within 1.4% for all studied fields. Figure IV.23 shows the isodose contour comparison between the film data and EPID

data with all corrections and the dose difference between the film data and the EPID data without any corrections and with all corrections. Inside the field, the difference was uniform for the EPID data with all corrections. Close to the field edge, the difference increased, especially in the in-plane direction. Based on the dose contours at 20%, 50% and 90% of the maximum dose, the EPID data with all corrections agreed well with film data. Figure IV.24 shows the cross-plane and in-plane profiles crossing the isocenter. The corrections mainly improved the agreement in the region close to the field edge when all corrections were applied, especially in the in-plane direction. However, in the low dose region, where the doses primarily come from the MLC transmission, disagreement was found. As stated in the beginning of this section, the difference could be decreased when the individual set of parameters for MLC transmission component was applied. Here, to simplify the algorithm, the correction of the MLC component was not included for MLC-shaped fields.

Table IV.3. Differences (average and 1σ) between the film and EPID data relative to maximum film doses for EPID raw data (no correction), EPID with the backscatter correction (BS), and EPID with the backscatter, kernel and off-axis corrections (BS+Ks+OAR) for ROI > 10% maximum film dose.

Field	Correction	Difference/maximum dose
Oval	No	1.79%± 3.03%
	BS	1.60%± 2.80%
	BS+Ks+OAR	-0.77%± 2.29%
C	No	1.91%± 3.04%
	BS	1.65%± 2.75%
	BS+Ks+OAR	-0.57%± 2.41%
Squiggle	No	1.16%± 3.65%
	BS	1.02%± 3.45%
	BS+Ks+OAR	-1.40%± 2.83%
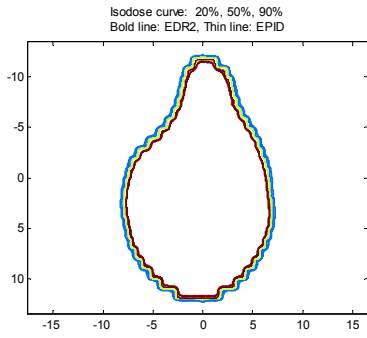
(a) BS+Kop+Offaxis corrected data vs. film
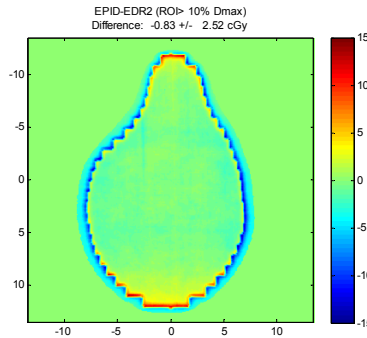
(b) BS+Kop+Offaxis corrected data vs. film
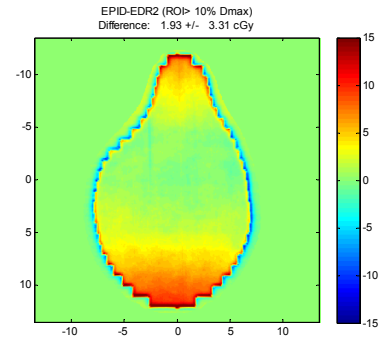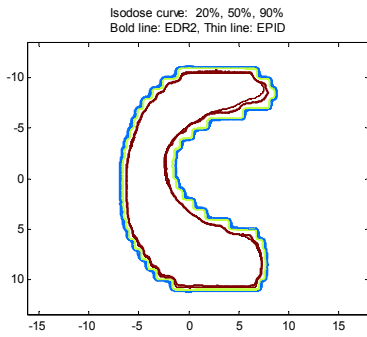
(c) Raw data vs. film

(d) BS+Kop+Offaxis corrected data vs. film
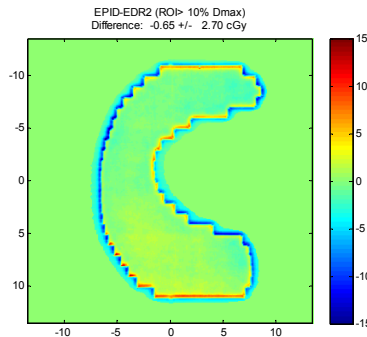
(e) BS+Kop+Offaxis corrected data vs. film
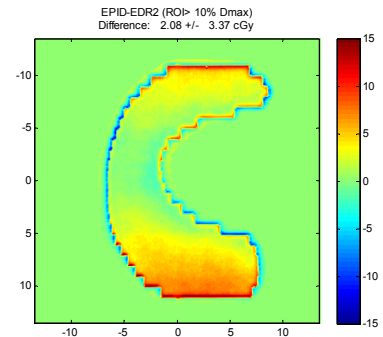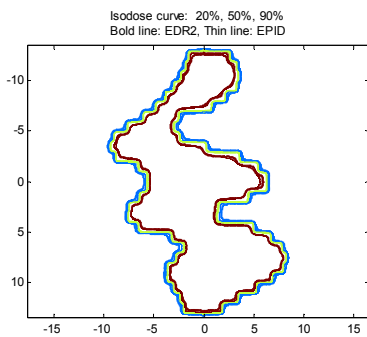
(f) Raw data vs. film

(g) BS+Kop+Offaxis corrected data vs. film
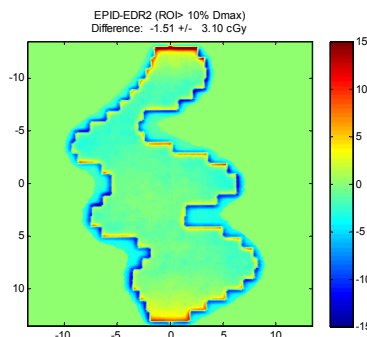
(h) BS+Kop+Offaxis corrected data vs. film
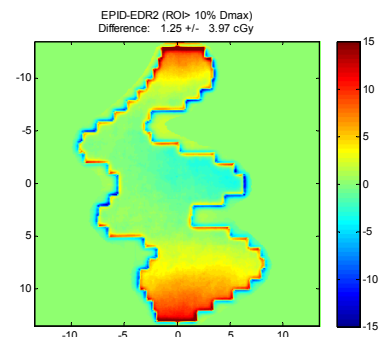
(i) Raw data vs. film

Figure IV.23. Dose contours (a, d, g) and difference maps (b-c, e-f, h-i) between EPID and film results for MLC-shaped fields: oval (a-c), C (d-f) and squiggle (g-i).
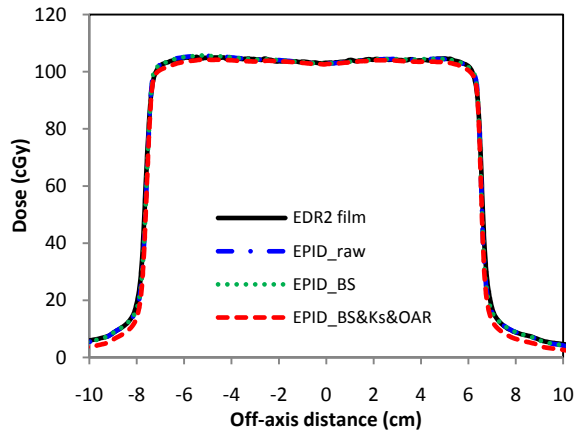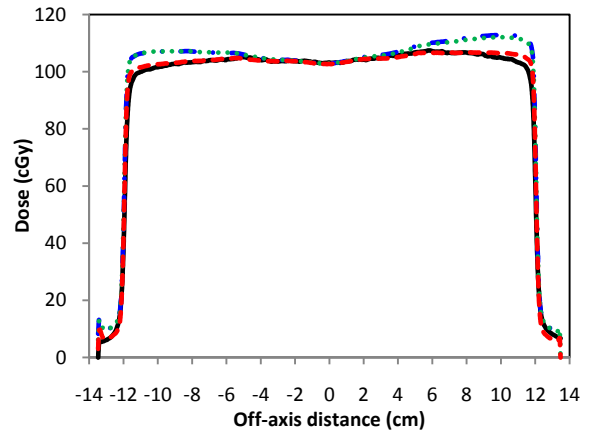
(a) Profiles at y=0 for oval shape

(b) Profiles at x=0 for oval shape
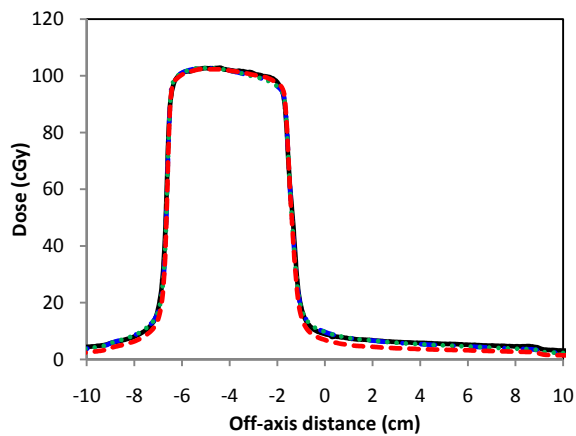
(c) Profiles at y=0 for C shape
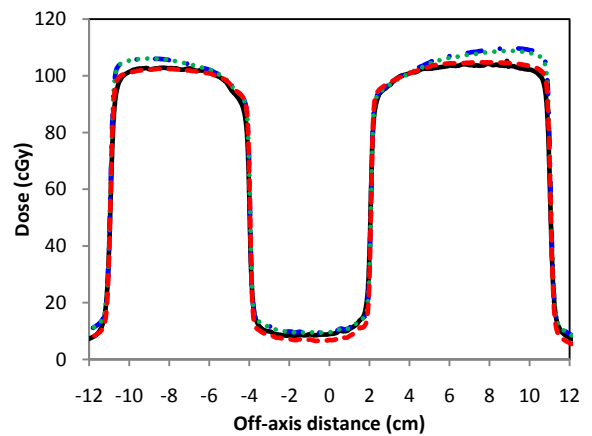
(d) Profiles at x=0 for C shape
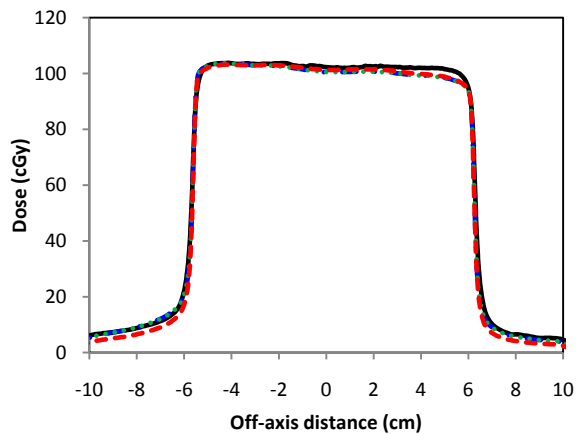
(e) Profiles at y=0 for squiggle shape

(f) Profiles at x=0 for squiggle shape

Figure IV.24. Cross-plane (a,c,e) and in-plane (b,d,f) profiles along the central axis for oval (a-b), C (c-d) and squiggle shapes (e-f) for film and EPID data.

For IMRT fields, Figure IV.25 shows the isodose contour comparison between the film data and EPID data with all corrections and the dose difference between the film data and the EPID data without any corrections and with all corrections. Here, the all corrected data include the backscatter, kernels for open and MLC fields, and off-axis corrections. From the dose difference maps, no significant improvement was found when all corrections were applied. Based on the dose contours at 20%, 50% and 80% of the maximum dose, the EPID data with all corrections agreed with film data. Figure IV.26 shows the cross-plane and in-plane profiles cross the individual point for each field. Interestingly, the EPID data without any correction also agreed with the film data. Any corrections on the EPID response did not significantly improve the agreement. In addition, the effect of accounting for the MLC transmission on the agreement was also small and may be ignored. In order to quantify the agreement for IMRT fields, Table IV.4 shows the γ (2%/ 2 mm and 3%/ 3 mm) and C (2%/ 1 mm and 5%/ 1 mm) indices for the EPID data without and with corrections. This table shows no significant change on the indices between no correction and any corrections. More than 95% points satisfied the criteria of both γ index in 2%/ 2 mm and the C index in 2%/ 1 mm when all corrections were included, except one field. These results indicated that the EPID data with no correction or corrections agree with film data. No significant improvement when accounting for the MLC transmission effect is likely due to small dose contribution from MLC transmission. This can be seen in Figure IV.27, which shows the cross-plane and in-plane profiles of fluence contributed by open field and MLC transmission for an example IMRT field (RPO).
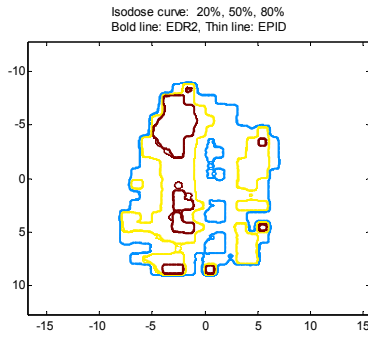
(a) BS+Kop+Ktr+Offaxis
corrected data vs. film
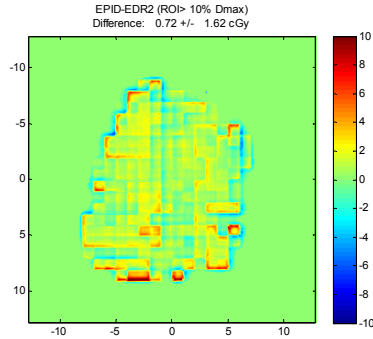
(b) BS+Kop+Ktr+Offaxis
corrected data vs. film
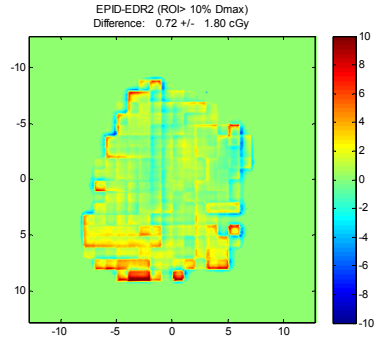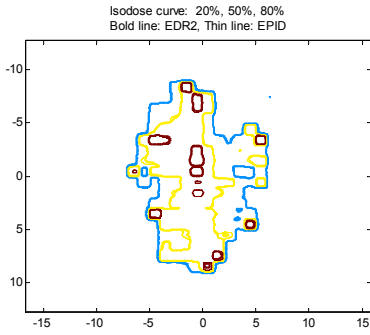
(c) Raw data vs. film

(d) BS+Kop+Ktr+Offaxis
corrected data vs. film
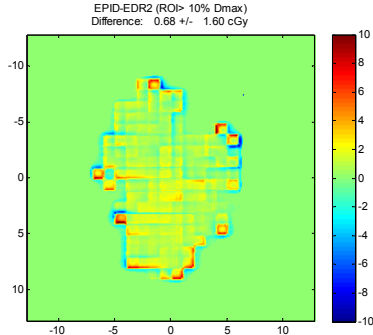
(e) BS+Kop+Ktr+Offaxis
corrected data vs. film
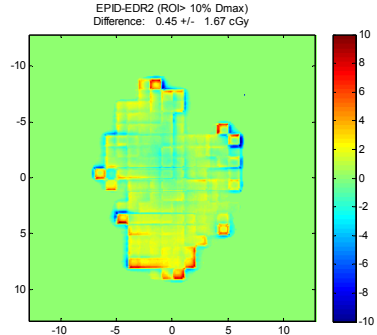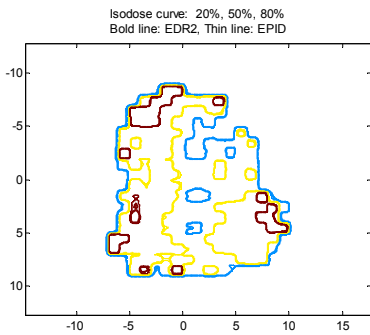
(f) Raw data vs. film

(g) BS+Kop+Ktr+Offaxis
corrected data vs. film

(h) BS+Kop+Ktr+Offaxis
corrected data vs. film

(i) Raw data vs. film

Isodose curve: 20%, 50%, 80%
Bold line: EDR2, Thin line: EPID

EPID-EDR2 (ROI> 10% Dmax)
Difference: 1.36 +/- 1.43 cGy

EPID-EDR2 (ROI> 10% Dmax)
Difference: 1.27 +/- 1.51 cGy
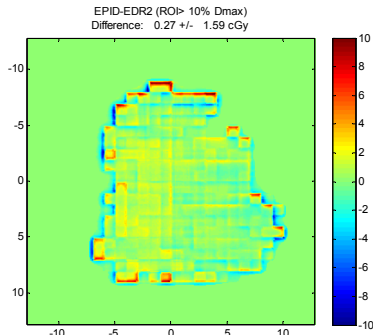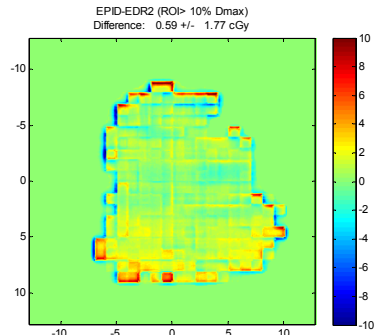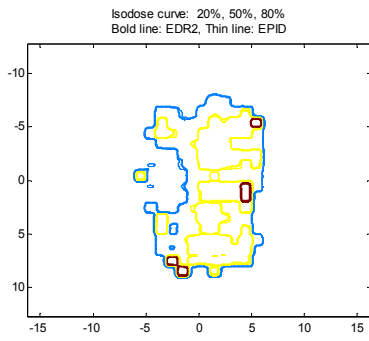
(j) BS+Kop+Ktr+Offaxis
corrected data vs. film
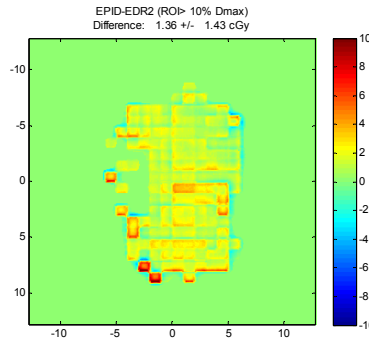
(k) BS+Kop+Ktr+Offaxis
corrected data vs. film

(l) Raw data vs. film

Isodose curve: 20%, 50%, 80%
Bold line: EDR2, Thin line: EPID

EPID-EDR2 (ROI> 10% Dmax)
Difference: 1.05 +/- 1.51 cGy

EPID-EDR2 (ROI> 10% Dmax)
Difference: 1.00 +/- 1.68 cGy
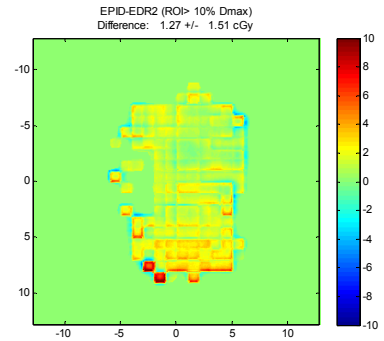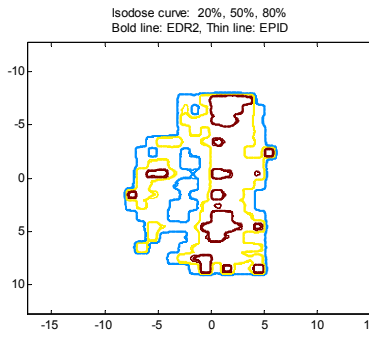
(m) BS+Kop+Ktr+Offaxis
corrected data vs. film
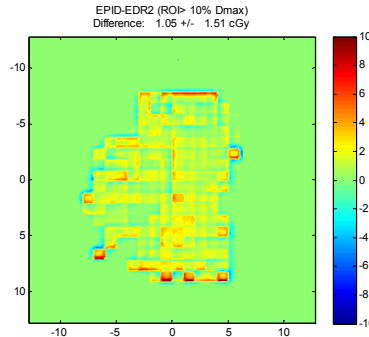
(n) BS+Kop+Ktr+Offaxis
corrected data vs. film
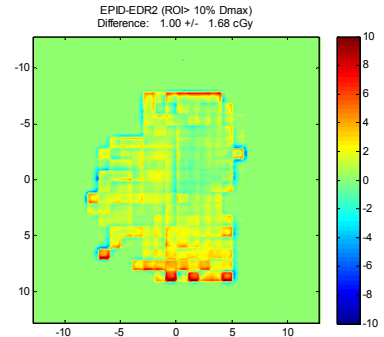
(o) Raw data vs. film

Figure IV.25. Dose contours (a, d, g, j, m) and difference maps (b-c, e-f, h-i, k-l, n-o) between EPID and film results for IMRT fields: LPO (a-c), LLAT (d-f), AP (g-i), RLAT (j-l) and RPO (m-o).
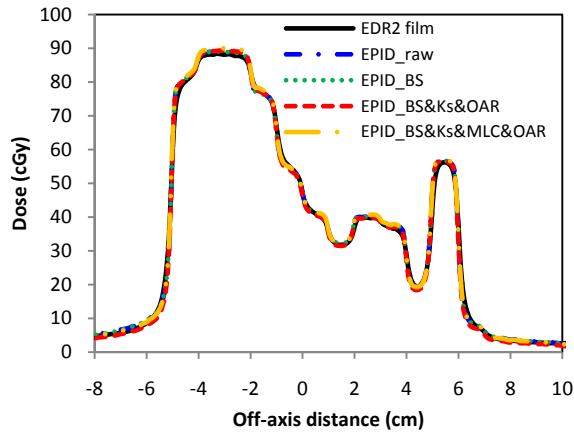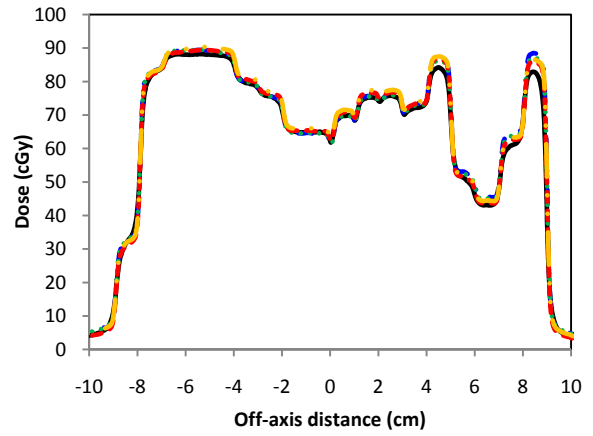
(a) Profiles at y=-4.5
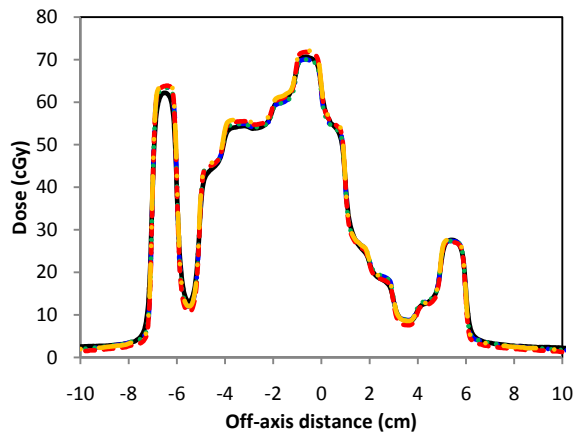
(b) Profiles at x=-2.5
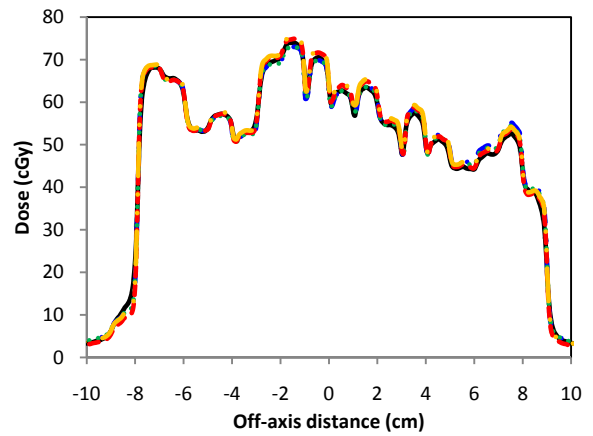
(c) Profiles at y=-0.5
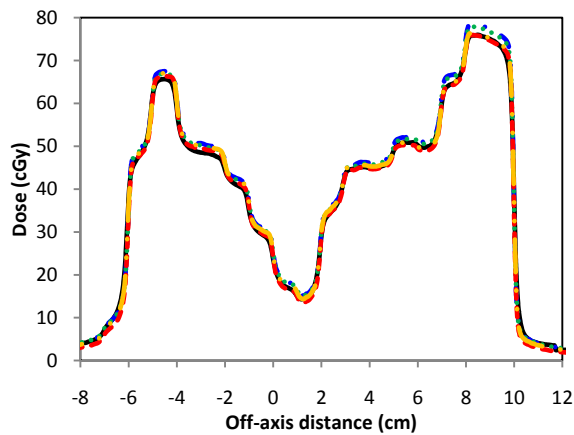
(d) Profiles at x=-0.5
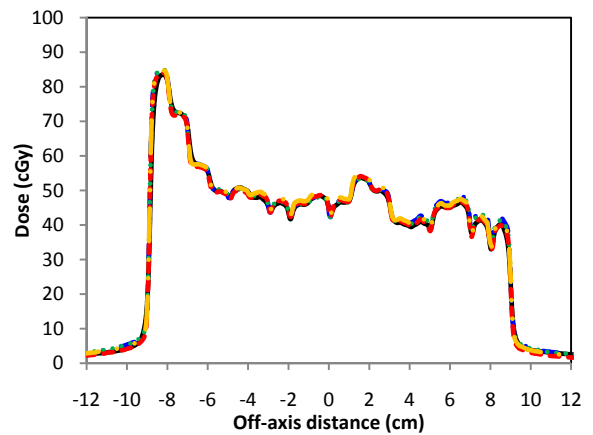
(e) Profiles at y=4.5
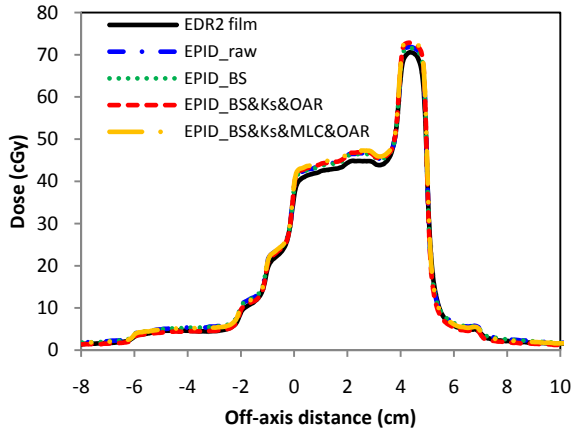
(f) Profiles at x=-1.5
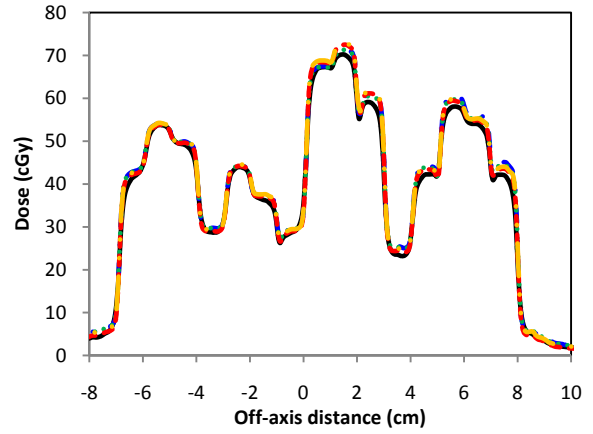
(g) Profiles at y=1.5
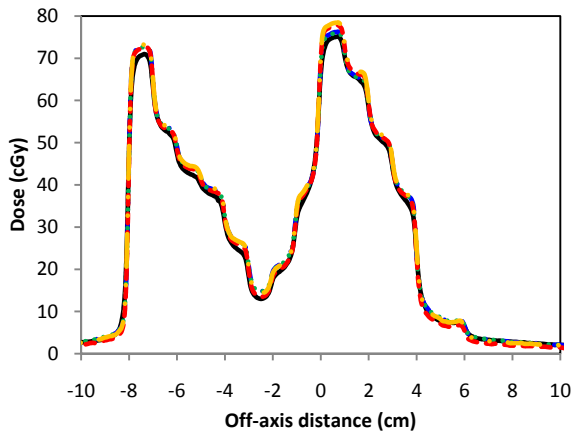
(h) Profiles at x=4.5
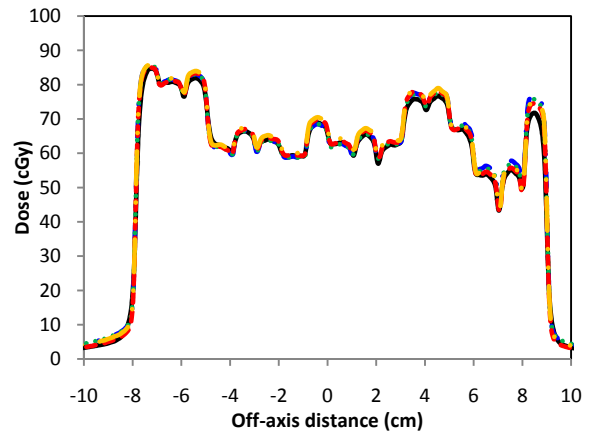
(i) Profiles at y=1.5

(j) Profiles at x=1.5

Figure IV.26. Cross-plane (a,c,e,g,i) and in-plane (b,d,f,h,j) profiles along the central axis for IMRT fields: LPO (a-b), LLAT (c-d), AP (e-f), RLAT (g-h) and RPO (i-j) for film data, EPID raw data (EPID_raw), EPID with the backscatter correction (EPID_BS), EPID with the backscatter, kernel and off-axis corrections (EPID_BS&Ks&OAR), and EPID with the backscatter, kernel, MLC and off-axis corrections (EPID_BS&Ks&MLC&OAR).

Table IV.4. The γ (2%/2 mm and 3%/3 mm) and C (2%/1 mm and 5%/1 mm) indices to quantify the discrepancy between film and EPID data for IMRT fields for EPID raw data (no correction), EPID with the backscatter correction (BS), EPID with the backscatter, kernel and off-axis corrections (BS+Ks+OAR), and EPID with the backscatter, kernel, MLC and off-axis corrections (BS+Ks+MLC+OAR) for ROI > 10% maximum film dose.

Field	Segments	Correction	r		C	
			2%/2 mm	3%/3 mm	2%/1 mm	5%/1 mm
LPO	132+190	No	94.9%	99.0%	98.3%	99.8%
		BS	96.9%	99.4%	99.4%	100.0%
		BS+Ks+OAR	97.4%	99.4%	99.7%	100.0%
		BS+Ks+MLC+OAR	96.4%	99.4%	99.2%	100.0%
LLAT	192	No	95.6%	99.3%	99.2%	100.0%
		BS	97.5%	99.4%	100.0%	100.0%
		BS+Ks+OAR	97.2%	99.3%	99.9%	100.0%
		BS+Ks+MLC+OAR	96.7%	99.3%	99.7%	100.0%
AP	183+101	No	94.7%	99.1%	98.5%	100.0%
		BS	97.1%	99.3%	99.7%	100.0%
		BS+Ks+OAR	97.4%	99.2%	100.0%	100.0%
		BS+Ks+MLC+OAR	97.4%	99.3%	99.9%	100.0%
RLAT	152	No	89.9%	98.9%	94.9%	99.8%
		BS	93.7%	99.5%	98.0%	100.0%
		BS+Ks+OAR	94.7%	99.5%	98.4%	100.0%
		BS+Ks+MLC+OAR	90.4%	99.2%	95.0%	100.0%
RPO	237	No	94.1%	99.0%	97.5%	99.9%
		BS	96.5%	99.3%	99.3%	100.0%
		BS+Ks+OAR	97.2%	99.3%	99.7%	100.0%
		BS+Ks+MLC+OAR	95.5%	99.2%	98.9%	100.0%
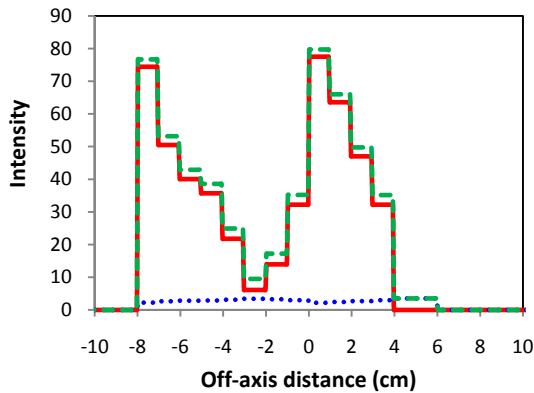
(a) Profiles at y=1.5
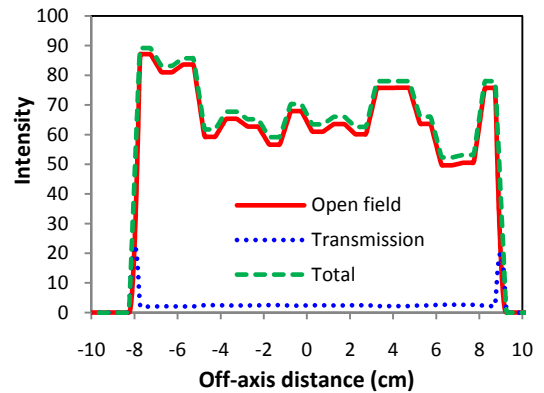
(b) Profiles at x=1.5

Figure IV.27. Cross-plane and in-plane intensity profiles extracted from the MLC sequence file of the RPO field.

IV.C.3. Measurements vs. calculations

The film data and EPID data were compared with CVSP calculations for various fields. For jaw only and MLC-shaped fields, the CVSP calculations agreed with the film and EPID data, except in the penumbra region (Figure IV.28 and IV.29). The penumbra was slightly larger for the CVSP compared to film and EPID images. The resolution of the CVSP algorithm is affected by several grids, such as density, convolution and calculation grids which can affect the calculated penumbra. For IMRT fields, since the TPS does not model the leaf configuration (such as tongue-and-groove effect) and has a lower resolution with the calculation compared to the film or EPID data, the CVSP results disagreed with the film or EPID data in the peak and valley regions. This difference can be seen in the in-plane profiles, which were extracted in the direction perpendicular to the leaf movement (Figure IV.30). Table IV.5 shows the γ (2%/ 2 mm and 3%/ 3 mm) and C (2%/ 1 mm and 5%/ 1 mm) indices for the EPID data without and with corrections. More than 95% points satisfied the criteria of the γ index in 3%/3 mm and the C index in 5%/1 mm.

(a) Profiles at x=0 for 3 × 3 cm^2 (b) Profiles at x=0 for 10 × 10 cm^2
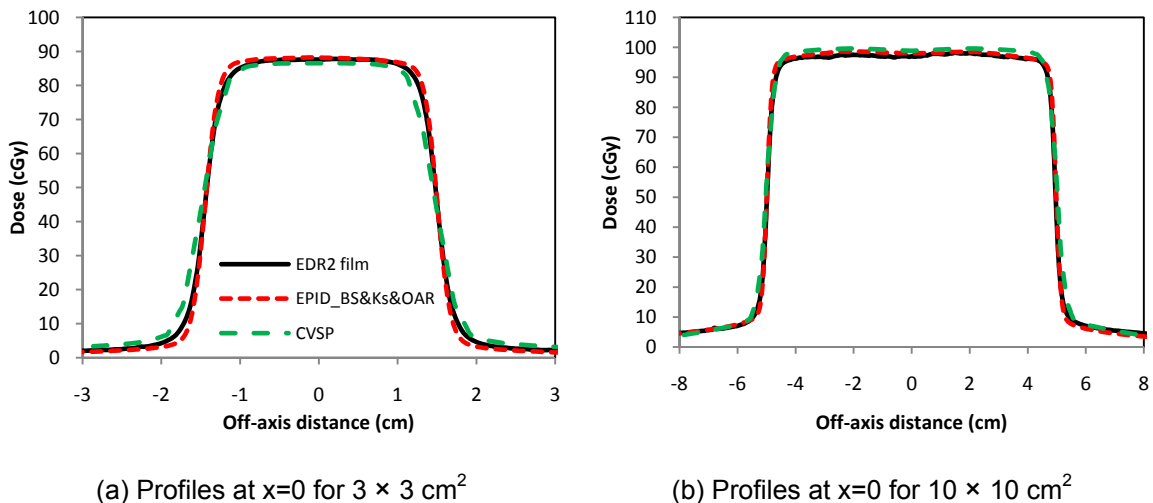
Figure IV.28. In-plane profiles along the central axis for (a) 3 × 3 and (b) 10 × 10 cm^2 field sizes for film, EPID and CVSP calculations.
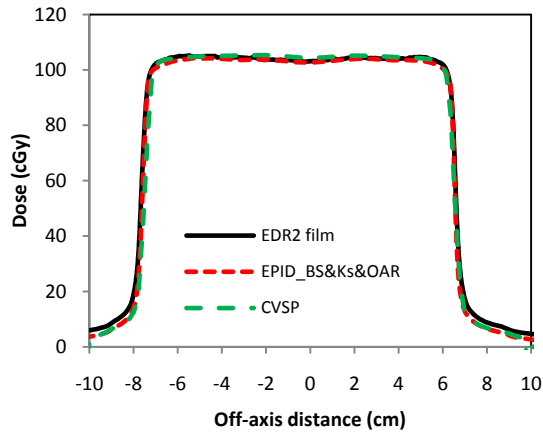
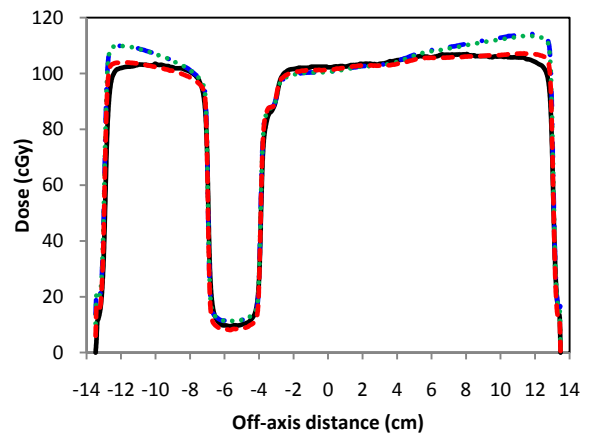(a) Profiles at y=0 for oval shape
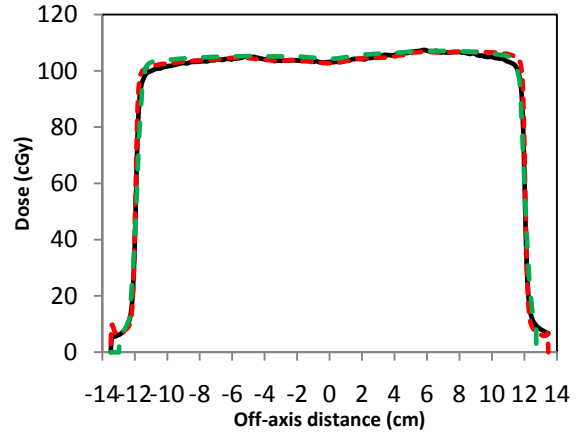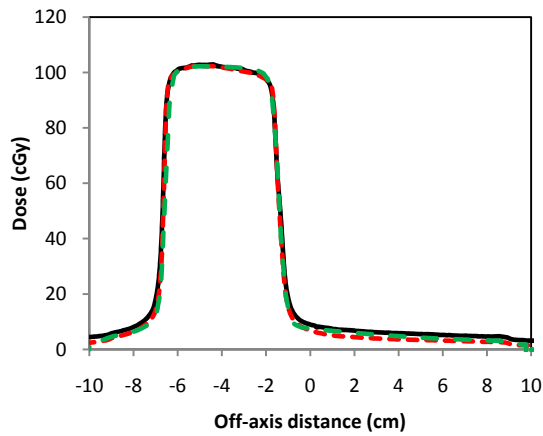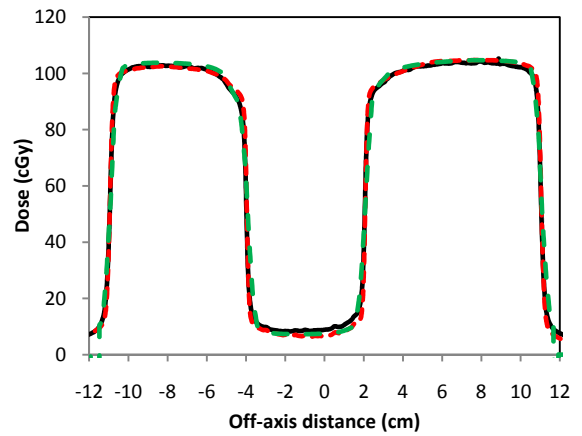
(b) Profiles at x=0 for oval shape

(c) Profiles at y=0 for C shape

(d) Profiles at x=0 for C shape
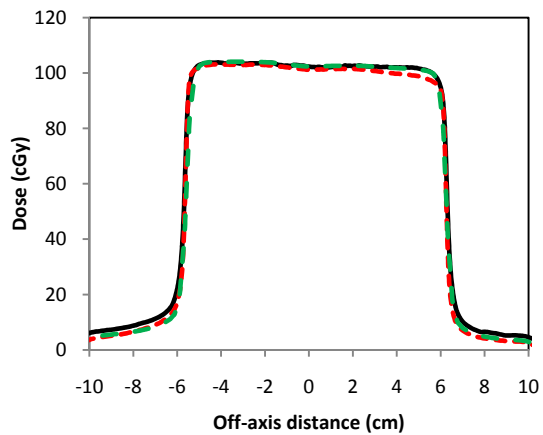
(e) Profiles at y=0 for squiggle shape
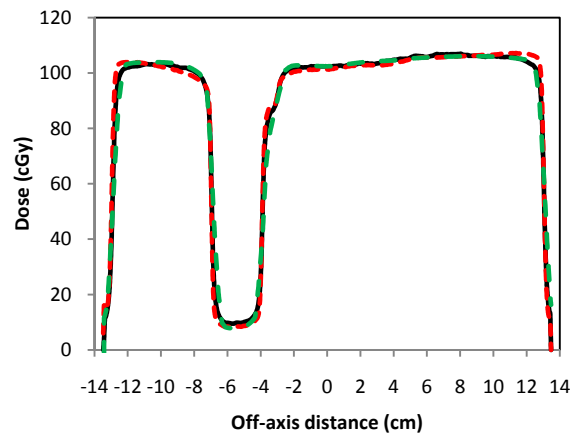
(f) Profiles at x=0 for squiggle shape

Figure IV.29. Cross-plane (a,c,e) and in-plane (b,d,f) profiles along the central axis for oval (a-b), C (c-d) and squiggle shapes (e-f) for film, EPID and CVSP calculations.
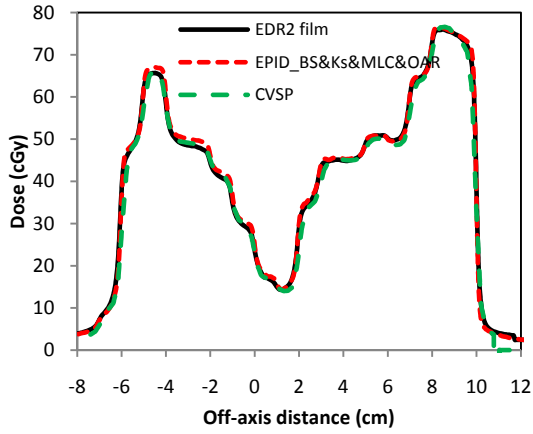
(a) Profiles at y=-4.5
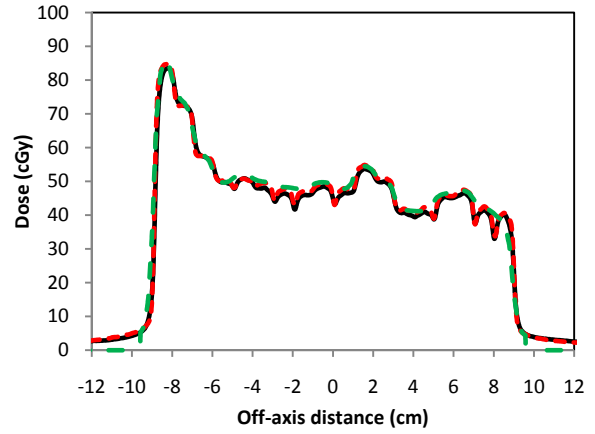
(b) Profiles at x=-2.5
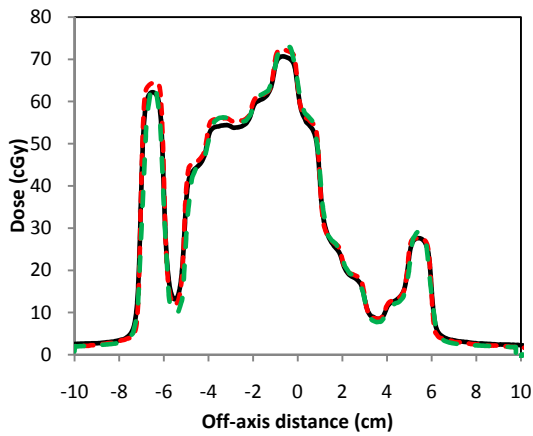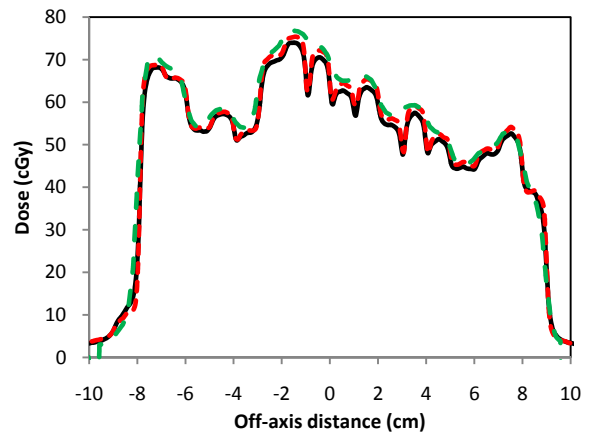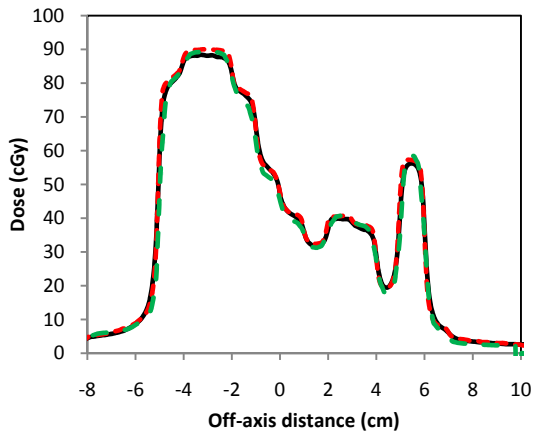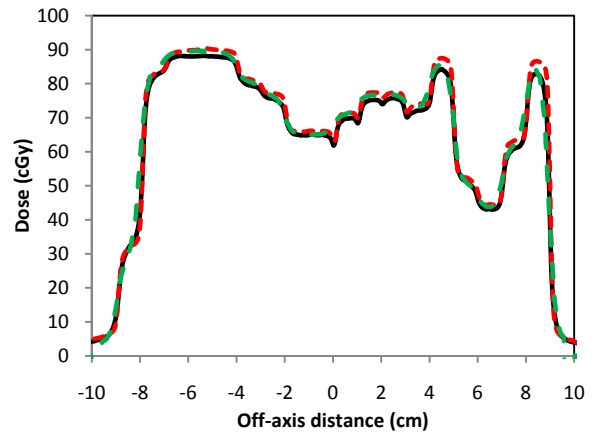
(c) Profiles at y=-0.5

(d) Profiles at x=-0.5

(e) Profiles at y= 4.5
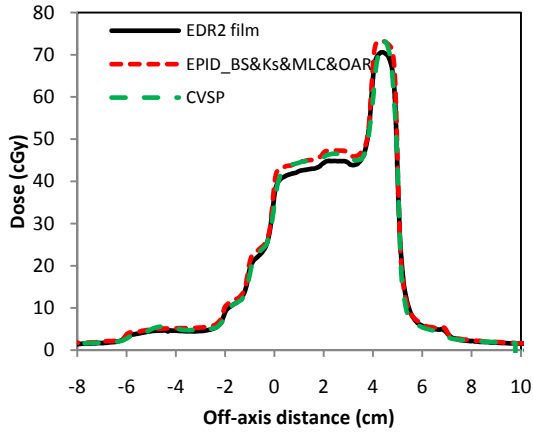
(f) Profiles at x= -1.5
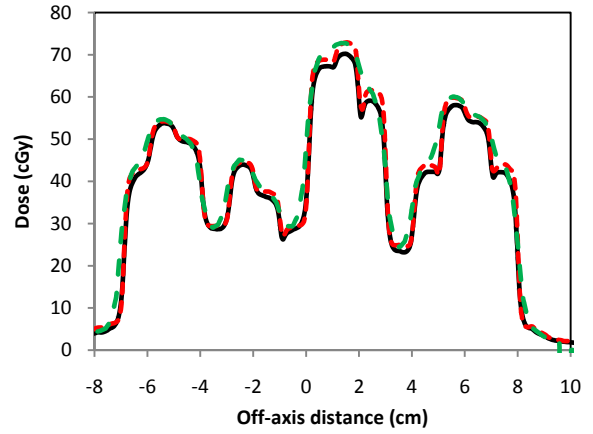
(g) Profiles at y=1.5
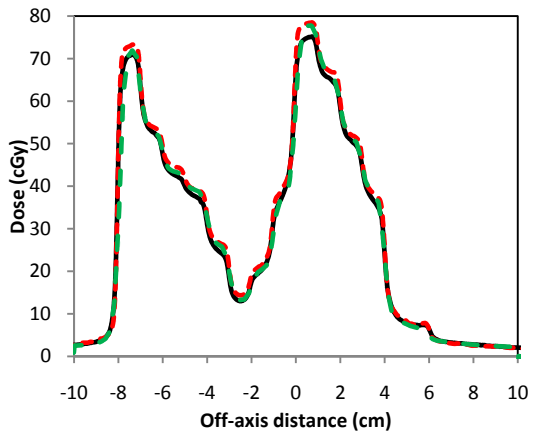
(h) Profiles at x=4.5
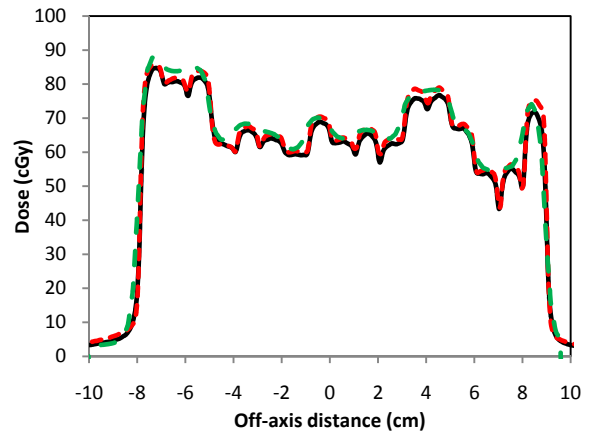
(i) Profiles at y=1.5

(j) Profiles at x=1.5

Figure IV.30. Cross-plane (a,c,e,g,i) and in-plane (b,d,f,h,j) profiles along the central axis for IMRT fields: LPO (a-b), LLAT (c-d), AP (e-f), RLAT (g-h) and RPO (i-j) for film, EPID and CVSP calculations.

Table IV.5. The γ (2%/2 mm and 3%/3 mm) and C (2%/1 mm and 5%/1 mm) indices to quantify the discrepancy between CVSP calculations and EPID data for IMRT fields for EPID raw data (no correction), EPID with the backscatter correction (BS), EPID with the backscatter, kernel and off-axis corrections (BS+Ks+OAR), and EPID with the backscatter, kernel, MLC and off-axis corrections (BS+Ks+MLC+OAR).

Field	Segments	Correction	r		C	
			2%/2 mm	3%/3 mm	2%/1 mm	5%/1 mm
LPO	132+190	No	88.6%	98.4%	94.1%	99.4%
		BS	90.4%	98.8%	96.7%	99.7%
		BS+Ks+OAR	92.8%	98.8%	97.3%	99.7%
		BS+Ks+MLC+OAR	90.8%	98.8%	96.5%	99.8%
LLAT	192	No	85.2%	96.8%	89.1%	96.6%
		BS	85.2%	96.7%	89.7%	97.1%
		BS+Ks+OAR	86.4%	98.1%	90.6%	97.1%
		BS+Ks+MLC+OAR	89.7%	98.7%	92.6%	97.6%
AP	183+101	No	87.7%	98.1%	92.0%	98.7%
		BS	89.7%	98.5%	95.1%	99.2%
		BS+Ks+OAR	90.2%	98.5%	94.6%	98.8%
		BS+Ks+MLC+OAR	91.7%	98.5%	95.7%	99.2%
RLAT	152	No	89.3%	98.7%	92.3%	98.1%
		BS	89.2%	98.8%	93.0%	98.7%
		BS+Ks+OAR	89.1%	98.4%	92.2%	98.4%
		BS+Ks+MLC+OAR	90.9%	98.9%	93.8%	98.6%
RPO	237	No	86.3%	97.5%	89.7%	97.3%
		BS	86.2%	97.5%	90.6%	97.9%
		BS+Ks+OAR	86.0%	97.5%	90.1%	97.6%
		BS+Ks+MLC+OAR	89.0%	98.2%	92.7%	98.1%

IV.D. Discussion

Two approaches have been proposed in the literature for EPID dosimetric verification: (1) calculating predicted EPID responses (arbitrary unit), and (2) converting EPID responses to doses in water (dose unit). While the calibration and correction methods for the approach of predicting EPID responses have been widely investigated, little attention is given to the approach of converting EPID responses to doses in water. An advantage for the approach using the dose unit rather than an arbitrary unit is the capability to directly compare the measured EPID doses with the calculated doses from TPSs.

116

Therefore, this study explored a general calibration method with EPID corrections to convert the EPID responses to doses in water and investigated the influence of these corrections on the accuracy of the EPID response for various radiation fields.

The calibration method proposed in this study accounted for several corrections in EPID dosimetry, including (1) non-uniform backscatter due to the non-uniform geometry in the EPID support structure, (2) kernel-based corrections for the inherent difference between the EPID and water, (3) separation of open field and MLC transmission components by analyzing MLC sequence files, (4) the use of different calibration factors and scatter kernels for open and MLC transmission components, and (5) off-axis correction for the EPID response at off-axis positions for softer beams. This calibration method has two advantages. First, all parameters needed in the calibration method can be acquired from measurements in open and MLC-transmission fields. This does not require prior knowledge of the beam spectrum or detailed understanding in the detector configurations and components for Monte Carlo simulation. This makes the measurement-based approach more straightforward to implement in clinical settings. Second, the EPID responses can be converted to the doses in water at a specific depth (e.g. 0.8 cm in this study), and then the EPID doses can be compared with measurements at the same depth or with the calculations from TPSs for pre-treatment verification. The EPID dose information can be not only used to verify the fluence delivered to patients but also the calculation uncertainty due to incorrect modeling of tongue-and-groove and round-end leaf configuration in the TPSs. Since the calibration method and parameters used in EPID dosimetry are different from TPSs, the results in EPID dosimetry can provide an independent check of calculations in TPSs.

In Equation IV.6, several assumptions were made to simplify the equation. First, the transmission fraction acquired from the MLC sequence file was used to separate the

component of the EPID responses from open fields and MLC transmission, rather than to separate the component of fluence from open fields and MLC transmission. Second, the scatter kernel was assumed invariant at off-axis positions although the beam is softer. Third, the off-axis energy dependence correction was included in the calibration factors. The Gaussian correction function was assumed to be the same for open field and MLC transmission components, but the magnitude between open field and MLC transmission was different. Fourth, the scatter kernels and off-axis correction do not consider the difference inside and outside the fields.

Several measurements using the EPID and IC in water were performed to characterize the EPID for dosimetric verification. In assessing the linearity of dose response, the linearity was similar to previous studies.[7, 27] For low MUs, an under-response of the EPID was found and this was attributed to charge trapping within the photodiode layer, which results in a ghosting effect. Due to this fact, the use of EPID for low MUs (< 20 MU) should be avoided. For IMRT fields, the MUs in each segment are usually small. However, for this approach, integrated doses are acquired for an entire field, so the charge trapping effect on IMRT fields would be minimized, unless the total MUs for an entire field are too small.

Regarding the backscatter correction, the needed correction decreases with increasing field size. The magnitude in this study was found comparable to the results reported by Berry *et al*.[19] With respect to scatter kernels in the EPID and water for open fields, the scattering behavior was different. In water, the scatter kernel was wider for higher energy photons. This is likely due to increasing electron range for higher energy photons. When comparing the scattering behavior between the EPID and water, theoretically, the EPID should show a narrower scattering kernel compared to water because of its materials with high Z and high density. However, in our results, the EPID

118

had a wider scattering kernel for 6 MV but a narrower kernel for 16 MV compared to water. A possible explanation for this inconsistency is that there is another scattering effect (different from the dosimetric kernel) in the EPID. Therefore, for the EPID, there is no difference of scattering kernel between 6 and 16 MV photons. The additional scattering effect is likely due to the optical dispersion with the phosphor layer (glare effect). However, the small difference of the EPID response between 6 and 16 MV photons may be coincidental. The scatter kernels in this study were derived from S_p factors based on the assumption of invariant scatter kernels across the entire field. In fact, since the beam is softer off-axis, the scatter behavior may be different off-axis. The assumption may result in incorrect estimation of scatter contributions to the beam center and hide actual scattering behavior for the EPID. Therefore, because the scatter kernels in this study are empirically-derived, they may not represent the actual behavior of the EPID response to the low and high energies. Regardless, our results showed that accounting for the difference between the EPID and water for low and high energies can improve the accuracy of converting the EPID responses to doses in water.

Considering the variation of scatter kernels for MLC-transmission fields, the results showed that the water kernel had no significant change in the range of 0 and 5 cm, while the EPID kernel was narrower for MLC-transmission fields than for open fields. Interestingly, the EPID kernel for MLC-transmission fields was close to the water kernels for open and MLC-transmission fields. However, the change of the EPID kernel due to beam hardening for MLC-transmission fields was not consistent with the results for open fields (6 and 16 MV photons). The EPID does not show a difference in scattering for low and high energies but it shows a difference in scattering depending on whether the field is open or MLC-transmission. Therefore, additional investigation such as with MC simulations would be needed. Another possibility of inconsistency between energies and

beam hardening from blocked fields is a large uncertainty of scatter kernel for the MLC-transmission field compared to the open field because of very low signals in MLC-transmission field measurements and the non-uniform data in the entire field (Figure IV.9). Considering the energy dependence of EPID responses at off-axis, this work varied the calibration factors (CF_{op} and CF_{tr}) rather than varying the scatter kernel[10]. Our method showed a similar function. From Figure IV.21, the correction was up to ~7% at 10 cm off-axis.

To validate the proposed calibration method with the acquired parameters, the corrected EPID data were compared with IC and film measurements as well as CVSP calculations for jaw only, MLC-shaped and IMRT fields. In addition to verifying the accuracy of the method and parameters, the influence of various corrections was investigated. For jaw only fields, corrections of backscatter, scatter kernel and off-axis improved the agreement at central axis, off-axis and outside the field. For MLC-shaped fields, the complete corrections showed a significant improvement off-axis. From the comparison between the backscatter correction only and complete corrections, corrections of scatter kernels and off-axis energy dependence were more important for large fields. For IMRT fields, all data without and with corrections agreed with film data. However, the data with corrections still showed a slight improvement from the γ and C indices. In addition, accounting for the MLC transmission effect did not show an improvement in agreement. Based on these results, Equation IV.6 can be simplified to,

$$D_w(x,y) = CF_{op}(x,y) \cdot R_{op}(x,y) \otimes^{-1} K_{E_{op}}(x,y) \otimes K_{w_{op}}(x,y) \quad \textbf{(Equation IV.13)}$$

Our results indicated that the proposed calibration method and parameters can accurately convert the EPID responses to doses in water for jaw only, MLC-shaped and IMRT fields. This work developed a technique to use the EPID as a water-equivalent

dosimeter for pre-treatment verification. For IMRT fields, our current results showed that the raw EPID data without any corrections may be accurate enough, but it is difficult to conclude due to limited number of fields. This good agreement in raw data may be due to extremely non-uniform intensity for head-and-neck fields. Future work can investigate a range of treatment field types such as fields with less modulation and fewer segments, e.g. the IMRT fields for prostate treatment, and extend this method for dose conversions at other depths and for transit dosimetry.

IV.E. Conclusion

In this study, the general calibration method with corrections associated with the EPID was developed and verified for jaw only, MLC-shaped and IMRT fields. The method converted the EPID responses to doses in water through two sets of parameters for open ($\{CF_{op}(0,0), K_{Eop}, K_{wop}\}$) and MLC-transmission fields ($\{CF_{tr}(0,0), K_{Etr}, K_{wtr}\}$) and the off-axis correction matrix. For jaw only and MLC-shaped fields, the calibration method improved the agreement to within 1.4% of film data. For IMRT fields, the EPID data agreed with the film data for both uncorrected and corrected EPID data. Comparing the influence of EPID corrections on the accuracy of dosimetry, the kernel and off-axis corrections for the difference between the EPID and water was more significant, while the MLC transmission correction had less influence for the studied IMRT fields. The generality and accuracy of the proposed method were validated. This work showed the possibility of using the EPID as a water-equivalent dosimeter to verify both the fluence delivered by the machine and the calculation uncertainties in TPSs.

References

1. L. E. Antonuk, Y. El-Mohri, W. Huang, K. W. Jee, J. H. Siewerdsen, M. Maolinbay, V. E. Scarpine, H. Sandler and J. Yorkston, "Initial performance evaluation of an indirect-detection,

active matrix flat-panel imager (AMFPI) prototype for megavoltage imaging," Int J Radiat Oncol Biol Phys 42, 437-454 (1998).

2. Y. El-Mohri, L. E. Antonuk, J. Yorkston, K. W. Jee, M. Maolinbay, K. L. Lam and J. H. Siewerdsen, "Relative dosimetry using active matrix flat-panel imager (AMFPI) technology," Med Phys 26, 1530-1541 (1999).

3. C. Kirkby and R. Sloboda, "Consequences of the spectral response of an a-Si EPID and implications for dosimetric calibration," Med Phys 32, 2649-2658 (2005).

4. B. M. McCurdy, K. Luchka and S. Pistorius, "Dosimetric investigation and portal dose image prediction using an amorphous silicon electronic portal imaging device," Med Phys 28, 911-924 (2001).

5. P. B. Greer, "Correction of pixel sensitivity variation and off-axis response for amorphous silicon EPID dosimetry," Med Phys 32, 3558-3568 (2005).

6. J. Chen, C. F. Chuang, O. Morin, M. Aubin and J. Pouliot, "Calibration of an amorphous-silicon flat panel portal imager for exit-beam dosimetry," Med Phys 33, 584-594 (2006).

7. A. Van Esch, T. Depuydt and D. P. Huyskens, "The use of an aSi-based EPID for routine absolute dosimetric pre-treatment verification of dynamic IMRT fields," Radiother Oncol 71, 223-234 (2004).

8. C. Kirkby and R. Sloboda, "Comprehensive Monte Carlo calculation of the point spread function for a commercial a-Si EPID," Med Phys 32, 1115-1127 (2005).

9. L. Ko, J. O. Kim and J. V. Siebers, "Investigation of the optimal backscatter for an aSi electronic portal imaging device," Phys Med Biol 49, 1723-1738 (2004).

10. W. Li, J. V. Siebers and J. A. Moore, "Using fluence separation to account for energy spectra dependence in computing dosimetric a-Si EPID images for IMRT fields," Med Phys 33, 4468-4480 (2006).

11. R. Mohan, C. Chui and L. Lidofsky, "Energy and angular distributions of photons from medical linear accelerators," Med Phys 12, 592-597 (1985).

12. P. B. Greer, P. Vial, L. Oliver and C. Baldock, "Experimental investigation of the response of an amorphous silicon EPID to intensity modulated radiotherapy beams," Med Phys 34, 4389-4398 (2007).

13. P. Vial, P. B. Greer, P. Hunt, L. Oliver and C. Baldock, "The impact of MLC transmitted radiation on EPID dosimetry for dynamic MLC beams," Med Phys 35, 1267-1277 (2008).

14. J. Chang, G. S. Mageras, C. C. Ling and W. Lutz, "An iterative EPID calibration procedure for dosimetric verification that considers the EPID scattering factor," Med Phys 28, 2247-2257 (2001).

15. B. M. McCurdy and S. Pistorius, "A two-step algorithm for predicting portal dose images in arbitrary detectors," Med Phys 27, 2109-2116 (2000).

16. B. Warkentin, S. Steciw, S. Rathee and B. G. Fallone, "Dosimetric IMRT verification with a flat-panel EPID," Med Phys 30, 3143-3155 (2003).

17. P. B. Greer, P. Cadman, C. Lee and K. Bzdusek, "An energy fluence-convolution model for amorphous silicon EPID dose prediction," Med Phys 36, 547-555 (2009).

18. P. Rowshanfarzad, B. M. McCurdy, M. Sabet, C. Lee, D. J. O'Connor and P. B. Greer, "Measurement and modeling of the effect of support arm backscatter on dosimetry with a varian EPID," Med Phys 37, 2269-2278 (2010).

19. S. L. Berry, C. S. Polvorosa and C. S. Wuu, "A field size specific backscatter correction algorithm for accurate EPID dosimetry," Med Phys 37, 2425-2434 (2010).

20. J. V. Siebers, J. O. Kim, L. Ko, P. J. Keall and R. Mohan, "Monte Carlo computation of dosimetric amorphous silicon electronic portal images," Med Phys 31, 2135-2146 (2004).

21. S. Wang, J. K. Gardner, J. J. Gordon, W. Li, L. Clews, P. B. Greer and J. V. Siebers, "Monte Carlo-based adaptive EPID dose kernel accounting for different field size responses of imagers," Med Phys 36, 3582-3595 (2009).

22. P. Storchi and E. Woudstra, "Calculation of the absorbed dose distribution due to irregularly shaped photon beams using pencil beam kernels derived form basic beam data," Phys Med Biol 41, 637-656 (1996).

23. B. Fraass, K. Doppke, M. Hunt, G. Kutcher, G. Starkschall, R. Stern and J. Van Dyke, "American Association of Physicists in Medicine Radiation Therapy Committee Task Group 53: quality assurance for clinical radiotherapy treatment planning," Med Phys 25, 1773-1829 (1998).

24. Y. Chen, J. M. Moran, D. A. Roberts, Y. El-Mohri, L. E. Antonuk and B. A. Fraass, "Performance of a direct-detection active matrix flat panel dosimeter (AMFPD) for IMRT measurements," Med Phys 34, 4911-4922 (2007).

25. J. M. Moran, J. Radawski and B. A. Fraass, "A dose gradient analysis tool for IMRT QA," J Appl Clin Med Phys 6, 62-73 (2005).

26. D. A. Low, W. B. Harms, S. Mutic and J. A. Purdy, "A technique for the quantitative evaluation of dose distributions," Med Phys 25, 656-661 (1998).

27. L. N. McDermott, S. M. Nijsten, J. J. Sonke, M. Partridge, M. van Herk and B. J. Mijnheer, "Comparison of ghosting effects for three commercial a-Si EPIDs," Med Phys 33, 2448-2451 (2006).

CHAPTER V

APPLICATION OF EPID DOSIMETRY FOR PRE-TREATMENT DOSE VERIFICATION

In Chapter IV, a general calibration method was presented for the EPID as a water-equivalent dosimeter. It was tested for jaw only, MLC-shaped and IMRT fields. However, the calibration method was limited to the dose conversion at 8 mm depth in water, which has limitations, especially because of inaccuracies in dose calculations due to the variation in near-surface dose as a function of the collimation. Therefore, this chapter investigates the possibility to use the calibration method for the dose conversion at any specific depth in water.

V.A. Introduction

In Chapter IV, it was shown that the EPID can be used as a water-equivalent dosimeter for dosimetric verification. A general calibration method which converts the EPID response into dose at 8 mm depth in water was generally validated for clinically-relevant fields. However, the dose conversion at 8 mm depth limits the application of this technique. In clinics, dose verification for pretreatment quality assurance (QA) is usually performed at depths beyond the buildup region, e.g. at 5 or 10 cm. This ensures that the dose measurements and calculations are in regions of electronic equilibrium, where the data are more reliable. Therefore, the EPID technique at 8 mm depth needs to be generalized. To address this issue, this study investigates extending the method proposed in Chapter IV to other depths, and focuses on 6 MV photon beams**.**

V.B. Methods and materials

V.B.1. Equipment and calibration

All measurements were performed with a dose rate of 600 MU/min, jaw only field (MLC parked), 0° collimator angle, and photon energies of 6 MV (and 16 MV for scatter kernels) using a Varian 21EX accelerator (Varian Medical Systems, Palo Alto, CA) equipped with a 120-leaf Millennium multileaf collimator (MLC) and an amorphous silicon EPID (aS500). The accelerator was calibrated with an output of 0.8 cGy/MU at a depth of 10 cm in water for a 10×10 cm^2 field size at 90 cm source-to-surface distance (SSD). The standard calibration of the EPID response followed the vendor's protocols, such as dark field calibration, flood field calibration, beam profile correction and dose normalization (Chapter IV). All EPID images were exported in DICOM format and analyzed using software developed in-house with MATLAB$^®$ (The MathWorks, Inc., Natick, MA). The image processing converted the EPID response to dose in water. Because of the characteristic differences between the EPID and water, additional corrections were applied to the EPID for dosimetric applications. These corrections included (1) non-uniform backscatter from non-uniform geometry in support structures, (2) kernel-based corrections for the inherent difference between the EPID and water, and (3) off-axis correction for EPID over-response off-axis due to softer beams. Based on the results in Chapter IV, the equation used to convert the EPID responses to doses in water can be simplified to:

$$D_w(x,y) = CF(x,y) \cdot R(x,y) \otimes^{-1} K_E(x,y) \otimes K_w(x,y)$$
(Equation V.1)

where *CF (x,y)* is the calibration factor, *R(x,y)* is the EPID response, and K_E and K_w are the dose deposition kernels inside the EPID and water. The parameters (\{*CF*, K_E, K_w\}) must be determined to calculate the dose to water. These parameters depend on the

calibration conditions, e.g. the source-to-detector distance (SDD) and water-equivalent depth.

V.B.2. Application of EPID dosimetry in different conditions

Figure V.1 shows a diagram outlining the conversion of the EPID response to dose at a reference depth (d_{ref}) in water, e.g. 5 or 10 cm. The procedure includes (1) applying an
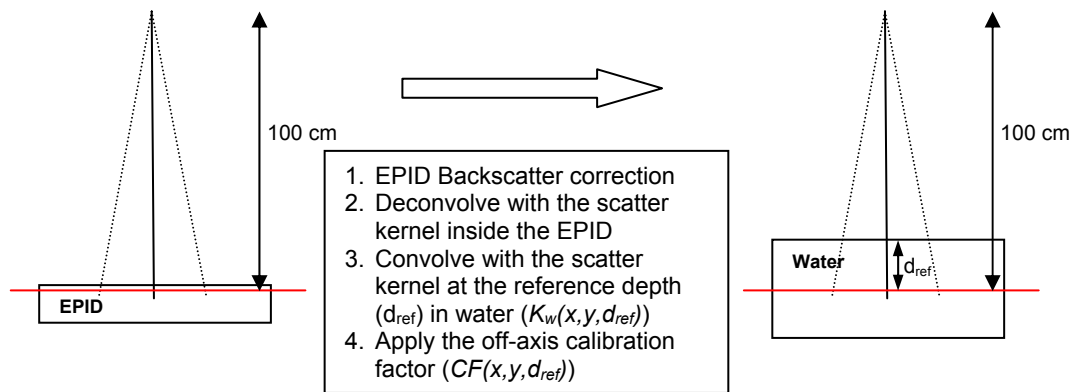
Figure V.1. A diagram outlining the conversion of the EPID response to dose in water at a specific depth at 100 cm SDD.

EPID backscatter correction matrix depending on the field size, (2) deconvolving with the scatter kernel for the EPID, (3) convolving with the scatter kernel for water, which depends on the reference depth in water, e.g. 0.8 cm in Chapter IV or 5 or 10 cm in this chapter, and (4) applying an off-axis correction matrix, which also depends on the reference depth in water. Since the backscatter correction and scatter kernel for the EPID are independent of the reference depth in water, these two parameters are the same as those in Chapter IV. This chapter addresses parameters depending on the reference depth in water, i.e. scatter kernels ($K_w(x,y,d_{ref})$) and off-axis calibration factors ($CF(x,y,d_{ref})$).

V.B.3. Scatter kernels and off-axis correction factors in water

The collimator scatter (S_c) at 100 cm SDD for field sizes from 3 × 3 - 20 × 20 cm^2 was measured using an ion chamber (IC) in a mini-phantom. For water, the S_{cp} factors at 100 cm SDD were acquired from an IC in water at various depths (0.8, 5, 6 and 10 cm for 6 MV, and for 0.8, 1, 5 and 10 cm for 16 MV) for field sizes from 3 × 3 - 20 × 20 cm^2. The depths of 6 cm for 6 MV and 1 cm for 16 MV were chosen to understand scattering behavior in water as a function of depth. These S_c data acquired with a mini-phantom and S_{cp} data in water were obtained from the commissioning database for those energies. The phantom scatter (S_p) in water was then calculated as a function of field size by dividing the S_{cp} factor by the S_c factor. These S_p factors were used to derive the scatter kernels in water (K_w) using the method proposed by Storchi *et al* [1].

In order to obtain off-axis calibration factors, the EPID responses (after the scatter kernel correction) for a 20 x 20 cm^2 field size were compared with IC measurements in water at 0.8, 5 and 10 cm for 6 MV photons. Then the correction matrix was determined for each depth and was applied to EPID data.

V.B.4. Experimental verification for jaw only, MLC-shaped and IMRT fields

To verify the dosimetric accuracy of the EPID, corrected EPID doses were compared with IC measurements in water and film measurements in Solid Water (40 x 40 x 20 cm^2) for 6 MV photon beams. Film measurements were performed at 0.8, 5 and 10 cm depths using Kodak EDR films (Carestream Health, Inc., Rochester, NY) for selected jaw only (10x10 cm^2 field size), MLC-shaped (C-shape) and an example IMRT field (RPO) (Figure IV.10(b) and IV.11(e)). Films were placed at 100 cm SDD. A calibration curve was acquired with a dose range from 0 to 400 cGy. All films were developed using a Kodak X-OMAT 3000RA Processor (Eastman Kodak, Rochester, NY), digitized with a

VXR-16 Dosimetry PRO^{TM} scanner (VIDAR systems corporation, Herndon, VA) and analyzed using in-house software. The film readout resolution was 0.179 × 0.179 mm^2.

V.B.5. EPID doses vs. calculations for jaw only, MLC-shaped and IMRT fields

The EPID doses at 0.8, 5 and 10 cm depths were also compared with calculated doses using the convolution/superposition (CVSP) algorithm implemented in the University of Michigan treatment planning system (UMPlan) for jaw only, MLC-shaped and IMRT fields for 6 MV photon beams. These fields were the same as those used in Chapter IV (Figure IV.10 and IV.11). The only difference is the geometry used in the calculations, with all geometries having a backscatter thickness larger than 10 cm. Dose calculations were performed in a manually-created (uniform density) geometry with a density of 1 g/cm^3. Detailed information is shown in Table V.1.

Table V.1. Uniform density geometry and dose calculation setup.

	Geometry 1	Geometry 2	Geometry 3
Depth in water (cm)	0.8	5	10
SSD (cm)	99.2	95	90
Manual phantom dimension (cm^3)	30 x 30 x 10.8	30 x 30 x 20	30 x 30 x 20

V.C. Results

V.C.1. Scatter kernels and off-axis correction factors in water

Figure V.2 shows the S$_p$ factors as a function of field size for the EPID and water at various depths for 6 and 16 MV photon beams. Figure V.3 shows the scatter kernels vs. off-axis distance for the EPID and water at various depths for both energies. From these two figures, it can be seen that although the water-equivalent thickness in the front of photodiode surface for the EPID is close to 8 mm, the scatter behavior differs from that

for water at 8 mm depth. This is because the EPID is constructed of materials with high atomic number (Z) and high density. Therefore, the electron range in the EPID is less than that in water (at 8 mm depth).
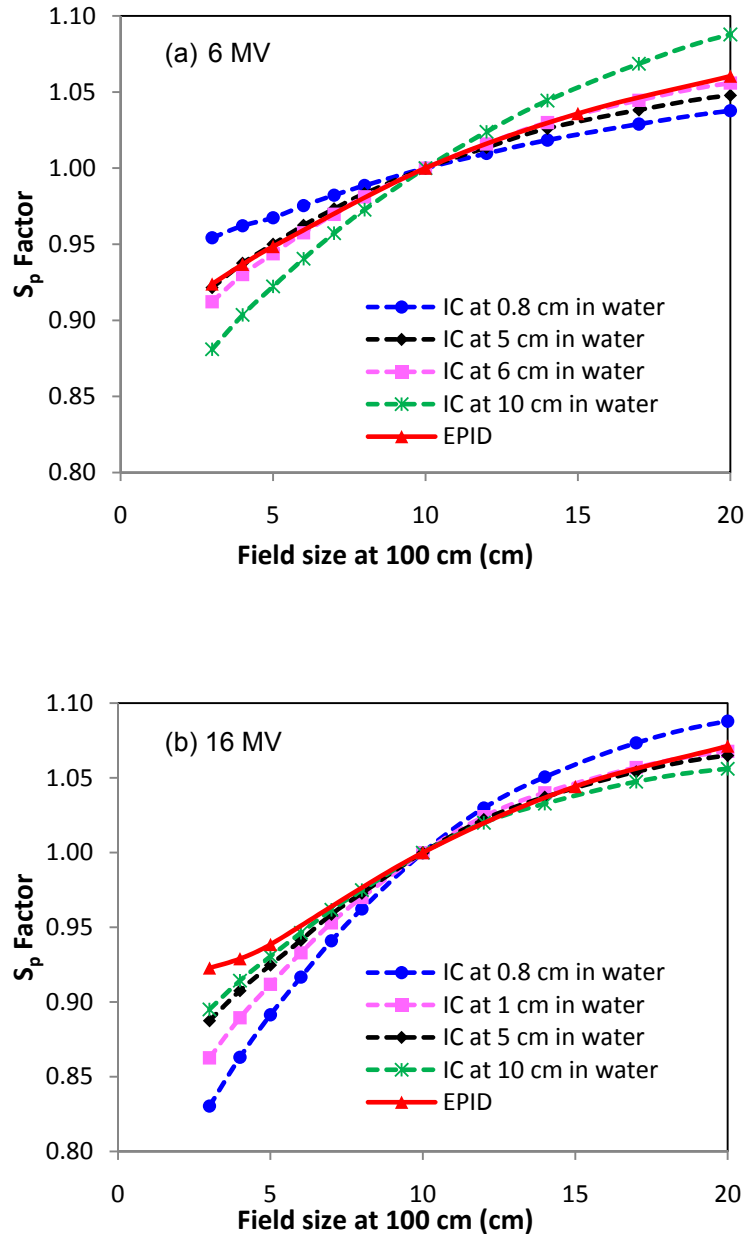
Figure V.2. S_p factors as a function of field size at 100 cm SDD for the EPID and water at (a) 0.8, 5, 6 and 10 cm for 6 MV photons and (b) 0.8, 1, 5 and 10 cm for 16 MV photons.
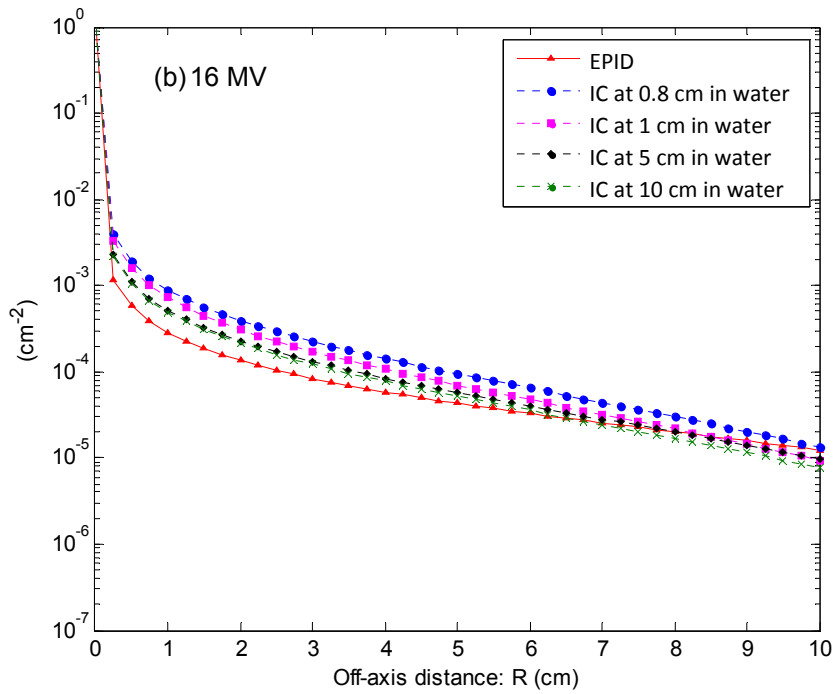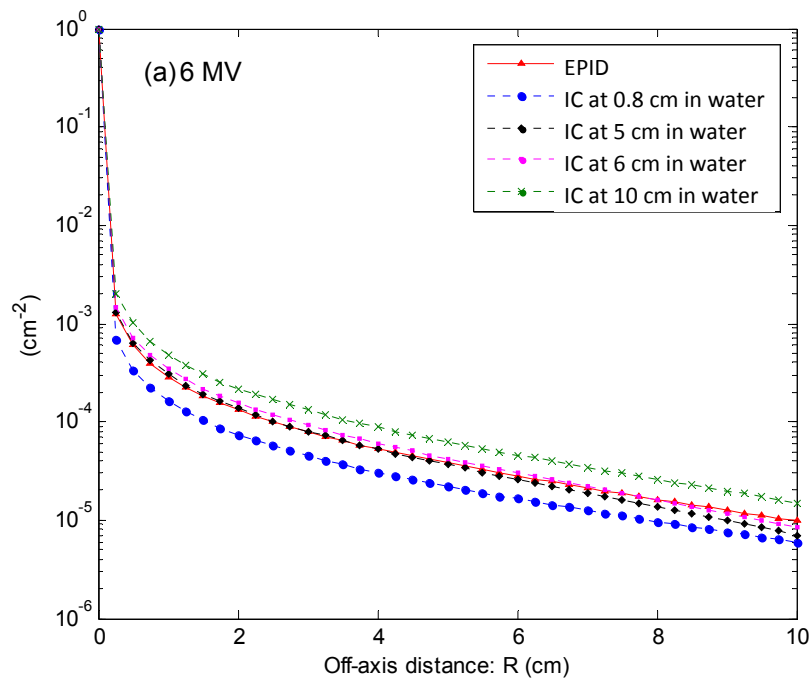
Figure V.3. Scatter kernels at 100 cm SDD for the EPID and IC in water at (a) 0.8, 5, 6 and 10 cm for 6 MV photons and (b) 0.8, 1, 5 and 10 cm for 16 MV photons.

Interestingly, the scatter behavior of the EPID is similar to that of water at 5 to 6 cm for 6 MV and 5 to 10 cm for 16 MV. This is because the scatter behavior in water varies with depth. When the depth increases, more low-energy photons are created and spread out (i.e. not in a forward direction). Therefore, the width of the scatter kernel increases with increasing depth. At a particular depth, the width of the scatter kernel will start to decrease (more in a forward direction) because of the absorption of low-energy photons and the effect of beam hardening. The point spread function in the axial view would be shaped similar to a water-drop. For 6 MV photons, the width of the scatter kernel in water increases with increasing depth (from 0.8 cm to 10 cm), which is similar to what is expected. However, the width of scatter kernel decreases with increasing depth for 16 MV. The regions at the shallow depths (i.e. 0.8 and 1 cm) are in the buildup region, which includes primary photons, and low-energy scatter photons as well as electron contamination from the machine head. A possible explanation for the behavior at 16 MV at 0.8 and 1 cm depth is that the absorption of low-energy scattering photons increases with increasing depth in the buildup region; therefore, the width of the scatter kernel decreases with increasing depth. However, it is challenging to explain the scatter behavior for the results at the deeper depths (i.e. 5 and 10 cm), without studying the scatter shapes in the axial view.

The scatter kernel of the EPID has two components: a dosimetric scatter term and a detector-glare term. There is no significant difference in the kernel when comparing 6 MV and 16 MV data for the EPID. In addition, the electron range is small for the EPID because of its high density. These results imply that the detector-glare term may be the main component in the scatter function of the EPID, resulting in less dependence on the energy. For water, the scatter function is only due to the dosimetric scatter term. Basically, the scattering behaviors in the EPID and water are due to

different factors. However, at certain depths, the EPID has a similar scatter behavior to water. This is attributed to the variation of scatter behavior as a function of depth in water, which has been explained previously.

Figure V.4 shows the off-axis correction factors for converting the EPID response to dose in water at various depths. The correction factors are normalized to the center value for each curve. The calibration factor at the center ($CF(0,0)$) depends on depth, and the values were determined to be 1.014, 0.989 and 0.826 at 0.8, 5 and 10 cm depths, respectively. The smaller $CF(0,0)$ values at 5 and 10 cm depths are because the dose decreases with increasing depth. When the EPID is calibrated at a shallow depth, a lower $CF(0,0)$ value is needed at deeper depths. On the other hand, because the dose profile varies with depth, the off-axis correction factors vary with depth.
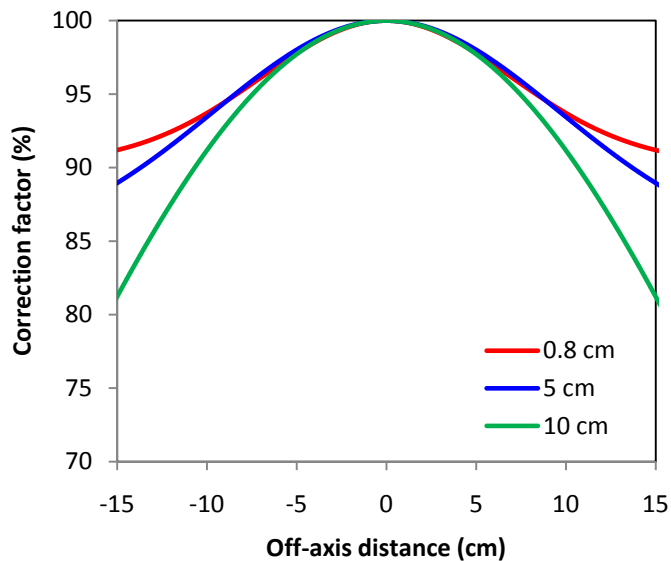
Figure V.4. Corrections as a function of distance from the central axis for 6 MV photons. The data shown in the figure are normalized to the central axis values, $CF(0,0,d_{ref})$, which are 1.014, 0.989 and 0.826 at 0.8, 5 and 10 cm depths, respectively.

V.C.2. Experimental verification for jaw only, MLC-shaped and IMRT fields

By applying individual parameters (i.e. scatter kernel and off-axis corrections) at different depths, the EPID response can be converted into dose at any depth in water. To verify the accuracy of parameters and the calibration method, the corrected EPID doses were compared with IC measurements and film measurements at 0.8, 5 and 10 cm depths. Table V.2 shows the comparison between the IC measurements in water and the corrected EPID doses at the central axis. The difference was within 0.4% for studied conditions. Figure V.5 compares the in-plane and cross-plane profiles for selected fields between the film and EPID data. Overall, the EPID data agreed well with the film data with an average difference within 0.8% except for one field (Table V.3). The discrepancies can be found at the field edge, in low dose regions and off-axis (Figure V.5).

Table V.2. Comparison of central axis doses between IC measurements in water and the corrected EPID doses at various depths.

Field size (cm^2)	Depth=0.8 cm			Depth=5 cm			Depth=10 cm		
	IC	EPID	Diff	IC	EPID	Diff	IC	EPID	Diff
3 × 3	0.898	0.899	0.1%	0.867	0.869	0.2%	0.829	0.828	-0.1%
4 × 4	0.918	0.918	0.1%	0.894	0.894	-0.1%	0.862	0.859	-0.3%
5 × 5	0.934	0.935	0.2%	0.917	0.916	-0.1%	0.890	0.887	-0.3%
10 × 10	1.000	1.000	0.0%	1.000	1.000	0.0%	1.000	1.000	0.0%
15 × 15	1.039	1.038	-0.1%	1.047	1.048	0.1%	1.070	1.073	0.3%
20 × 20	1.064	1.062	-0.2%	1.074	1.075	0.1%	1.115	1.120	0.4%

(a) Profiles at x=0 for 10x10 cm^2

(b) Profiles at x=0 for C-shape

(c) Profiles at y=1.5 for IMRT-RPO field

(d) Profiles at x=1.5 for IMRT-RPO field
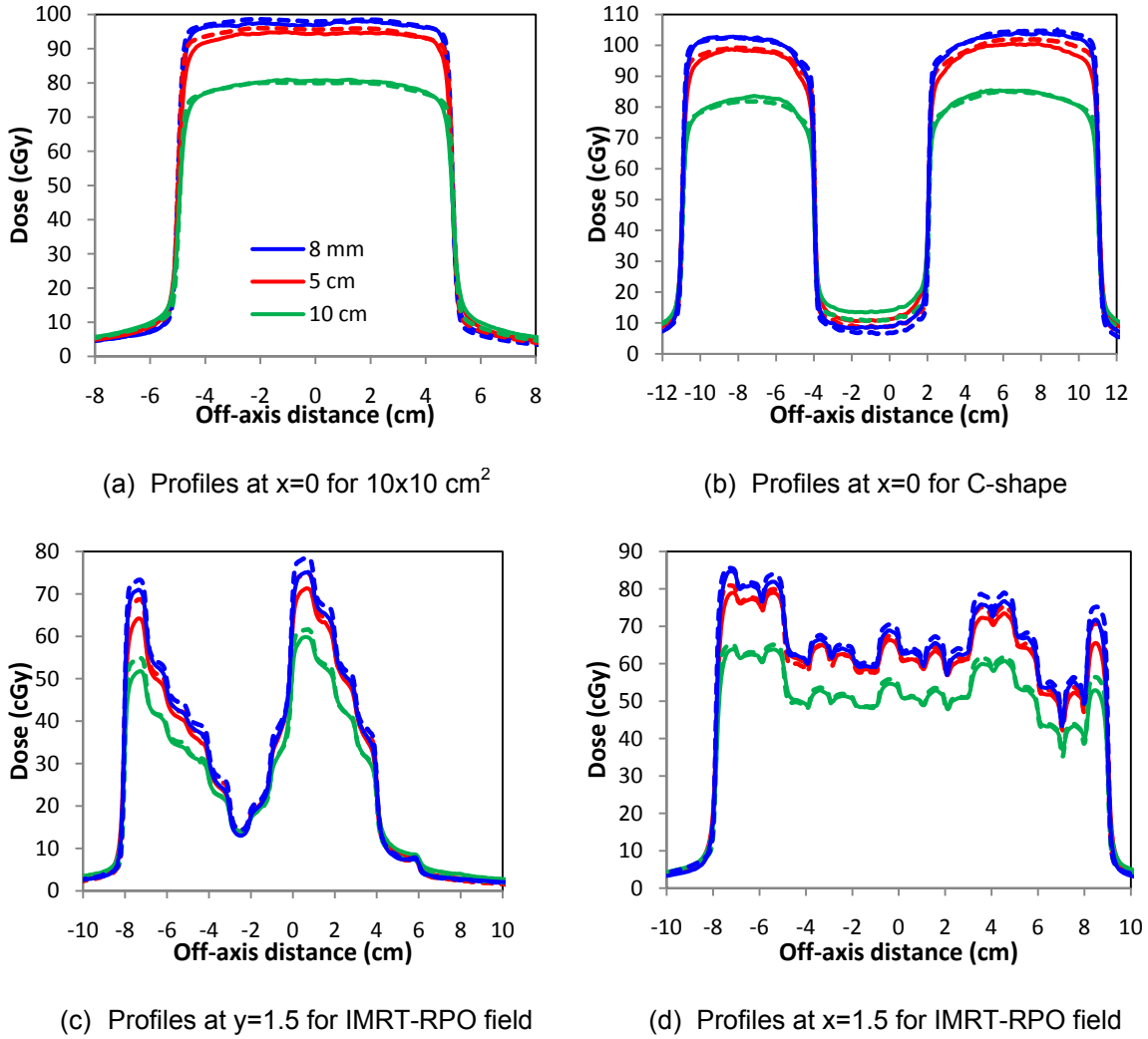
Figure V.5. Profile comparison between the film data (solid lines) and EPID data (dash lines) at 0.8, 5 and 10 cm depths for (a) in-plane profile for 10 × 10 cm^2 field, (b) in-plane profile for C-shape field, and (c) cross-plane and (d) in-plane profiles for IMRT-RPO field.

Table V.3. Differences (average and one standard deviation) between the film and EPID data relative to maximum film doses for region of interest (ROI) > 10% maximum film dose.

Field	Depth = 0.8 cm	Depth = 5 cm	Depth = 10 cm
10 × 10 cm^2	0.36% ± 2.30%	0.73% ± 2.96%	-0.75% ± 2.65%
C-shape	-0.57% ± 2.41%	-0.26% ± 3.35%	-2.36% ± 2.58%
IMRT-RPO	0.28% ± 1.80%	0.42% ± 2.97%	-0.41% ± 2.70%

V.C.3. EPID doses vs. calculations for jaw only, MLC-shaped and IMRT fields

In addition to the film data comparisons, the corrected EPID doses were compared with CVSP calculations at 0.8, 5 and 10 cm depths for all studied fields used in Chapter IV (Figure IV.10 and IV.11). Figure V.6 shows the comparison between the EPID doses and CVSP calculations at 0.8, 5 and 10 cm depths for 3 × 3, 5 × 5, 10 × 10, and 15 × 15 cm^2 field sizes. Figure V.7 and V.8 show the comparison between the EPID doses and CVSP calculations at 0.8, 5 and 10 cm depths for three MLC-shaped fields. Figure V.9 and V.10 show the comparison between the EPID doses and CVSP calculations at 0.8, 5 and 10 cm depths for five IMRT fields. Table V.4 shows the γ and C indices at 0.8, 5 and 10 cm depths for five IMRT fields to quantify the differences between the EPID doses and CVSP calculations. All data showed that EPID data agreed with CVSP calculations within the field at the three depths evaluated. There were disagreements primarily in the penumbra region where the EPID data showed a sharper penumbra than the CVSP data. This can be partly attributed to the calculation grid size in the calculation algorithm. Based on the data in Section V.C.2 and V.C.3, the calibration method with the depth-dependent parameters can accurately convert the EPID responses into doses in water at any specific depth.
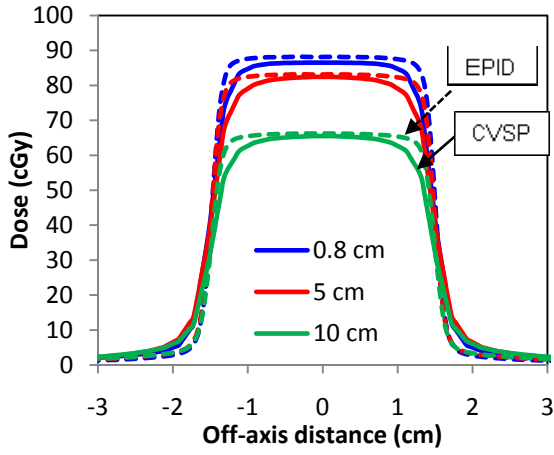
(a) Profiles at y=0 for 3x3 cm^2
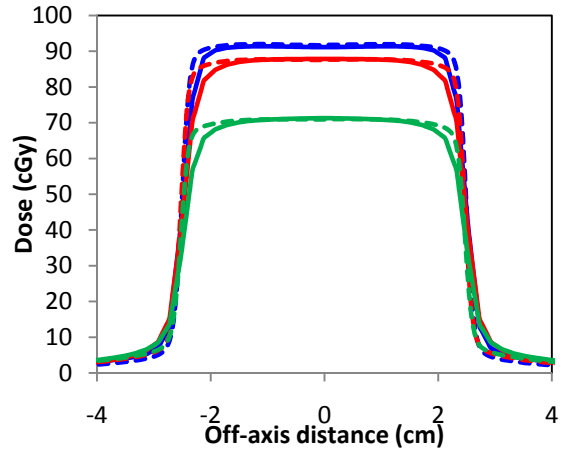
(b) Profiles at y=0 for 5x5 cm^2
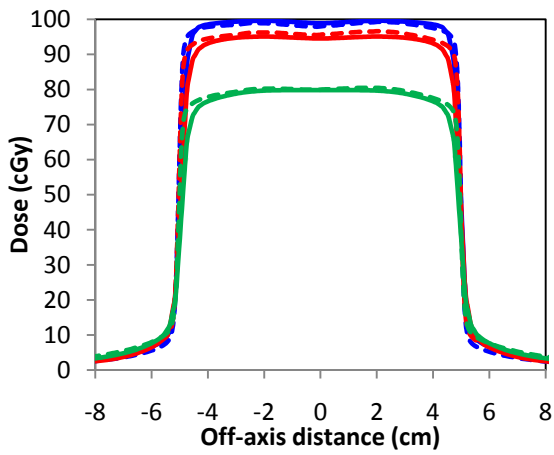
(c) Profiles at y=0 for 10x10 cm^2
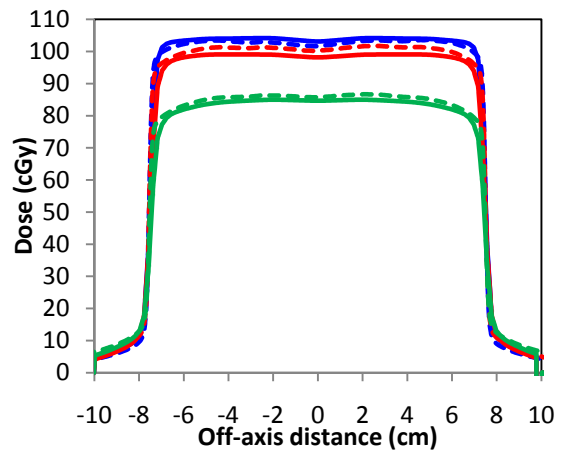
(d) Profiles at y=0 for 15x15 cm^2

Figure V.6. Cross-plane profiles along the central axis at 0.8, 5 and 10 cm depths for (a) 3 × 3, (b) 5 × 5, (c) 10 × 10 and (d) 15 × 15 cm^2 field sizes for CVSP calculations (solid lines) and corrected EPID doses (dash lines).
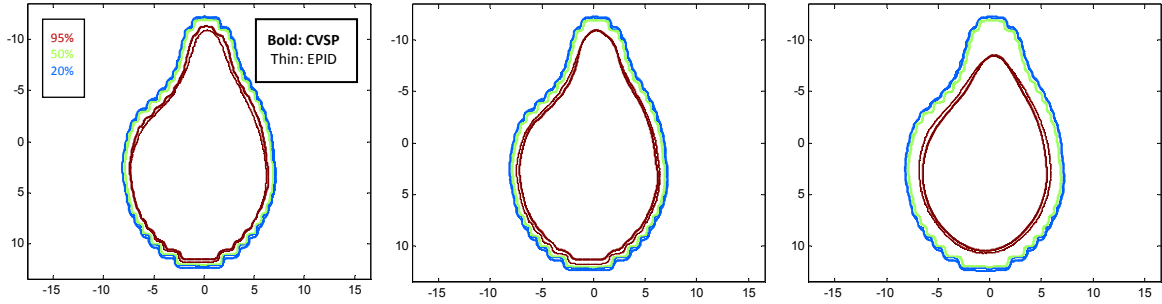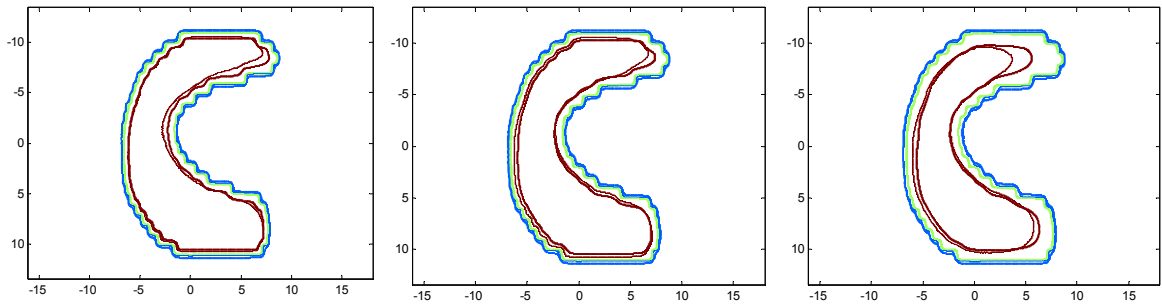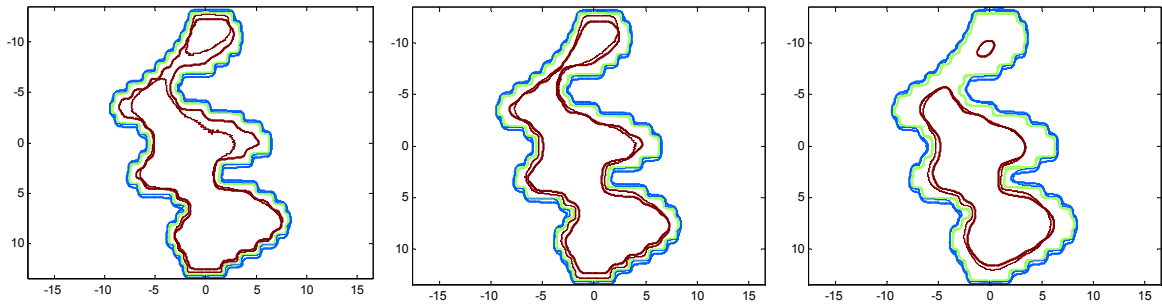
Figure V.7. Dose contours between EPID (thin lines) and CVSP (thick lines) results at 0.8, 5 and 10 cm depths for MLC-shaped fields: oval (a-c), C (d-f) and squiggle (g-i).
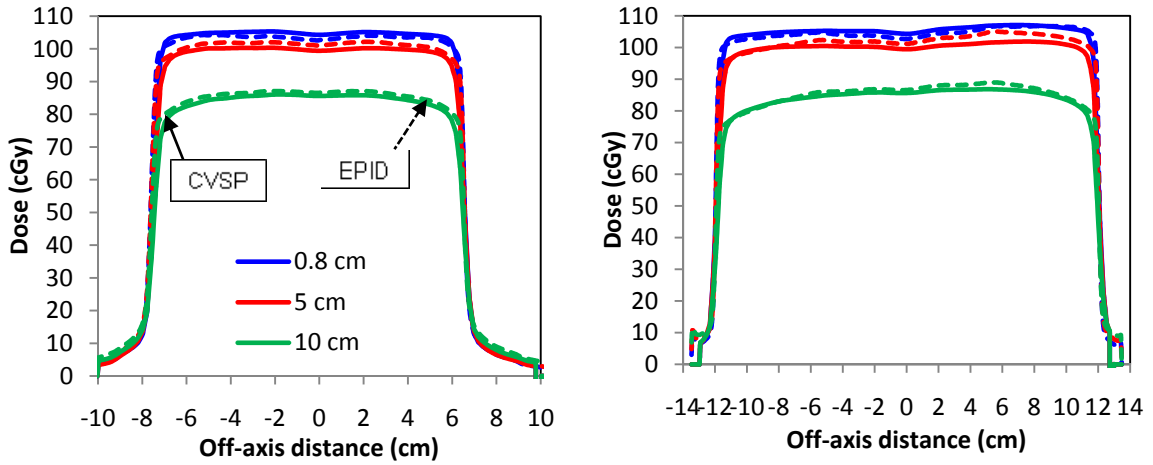
(a) Profiles at y=0 for oval shape

(b) Profiles at x=0 for oval shape
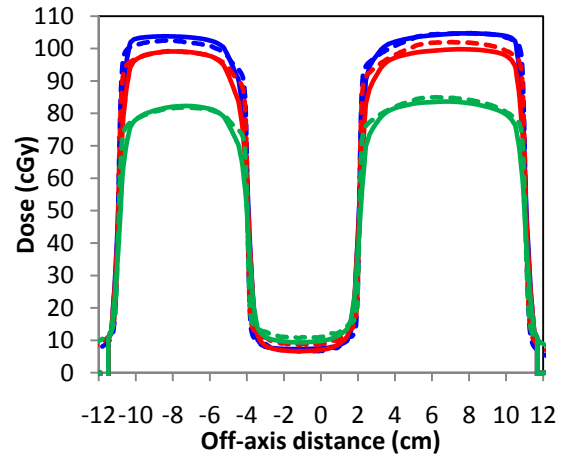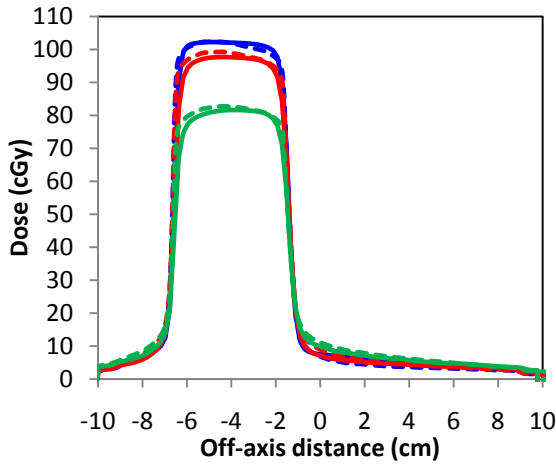
(c) Profiles at y=0 for C shape

(d) Profiles at x=0 for C shape
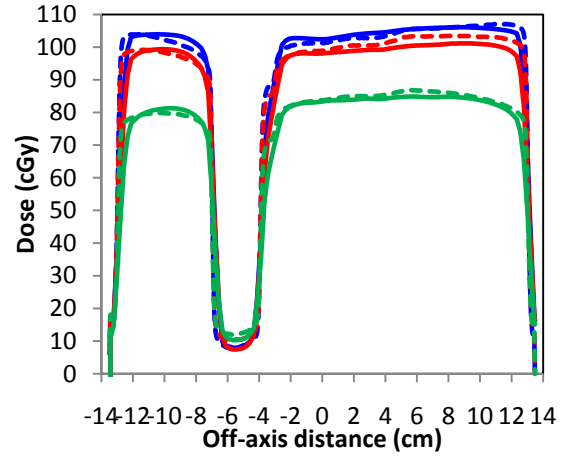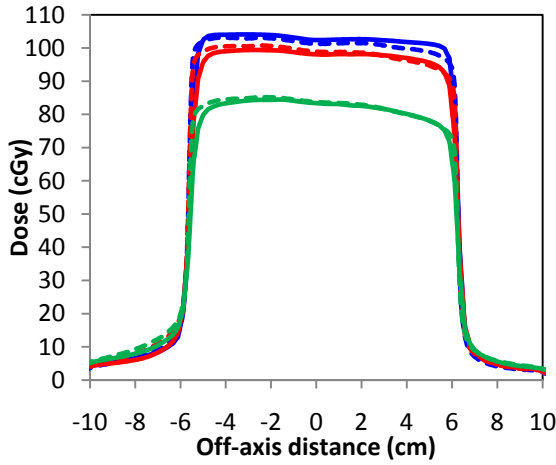
(e) Profiles at y=0 for squiggle shape

(f) Profiles at x=0 for squiggle shape

Figure V.8. Cross-plane (a,c,e) and in-plane (b,d,f) profiles along the central axis at 0.8, 5 and 10 cm depths for oval, C and squiggle shapes for CVSP (solid lines) and EPID data (dash lines).
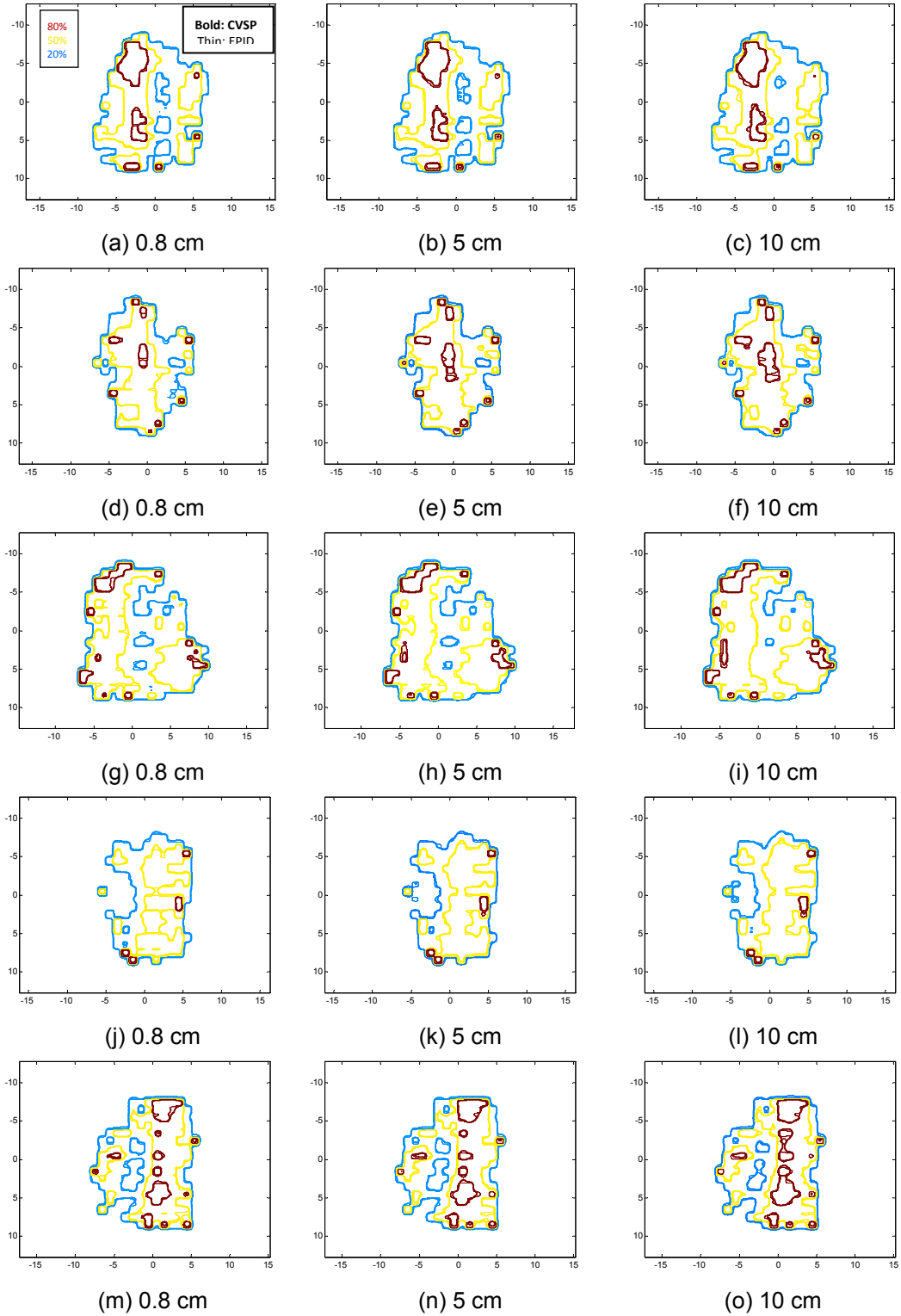
Figure V.9. Dose contours at 0.8, 5 and 10 cm depths between EPID (thin lines) and CVSP (**thick** lines) results for IMRT fields: LPO (a-c), LLAT (d-f), AP (g-i), RLAT (j-l) and RPO (m-o).
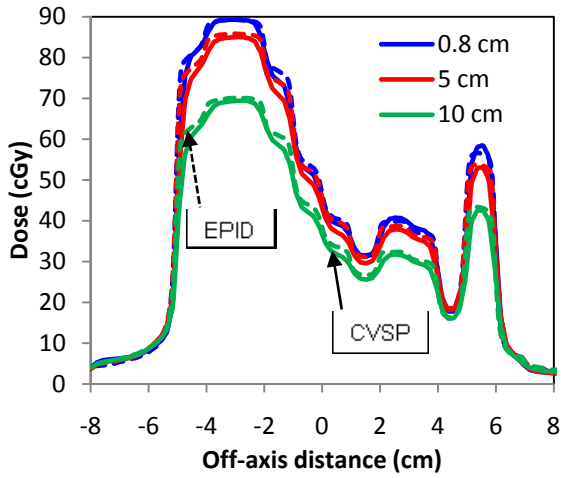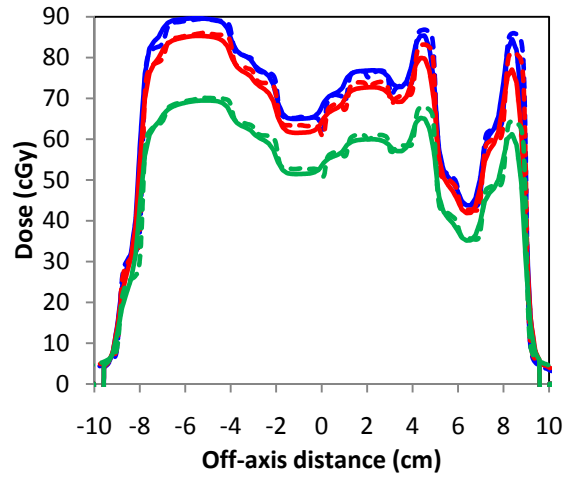
(a) Profiles at y=-4.5
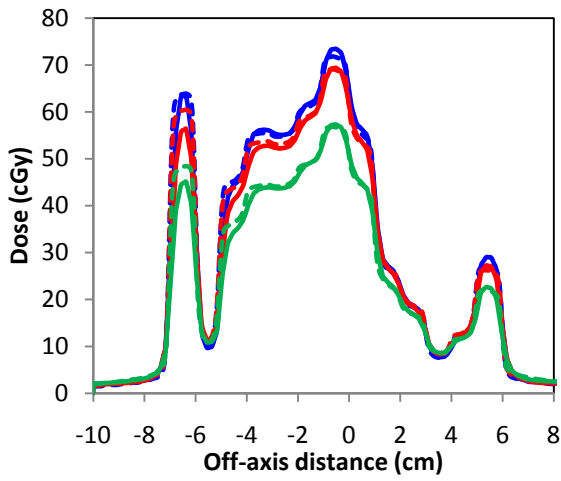
(b) Profiles at x=-2.5
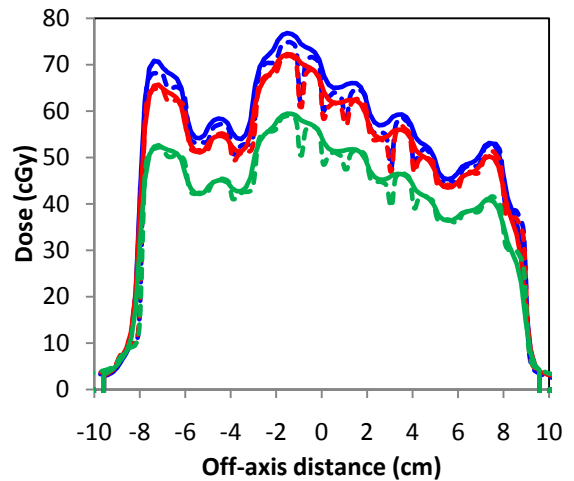
(c) Profiles at y=-0.5
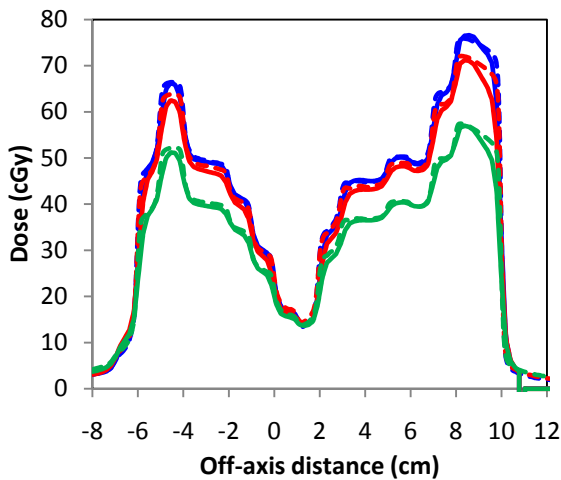
(d) Profiles at x=-0.5
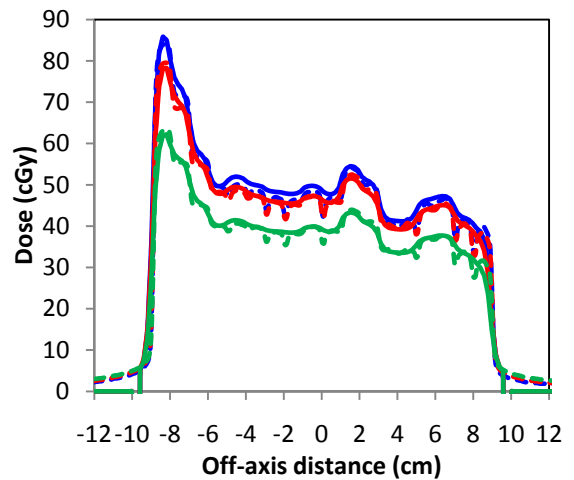
(e) Profiles at y= 4.5
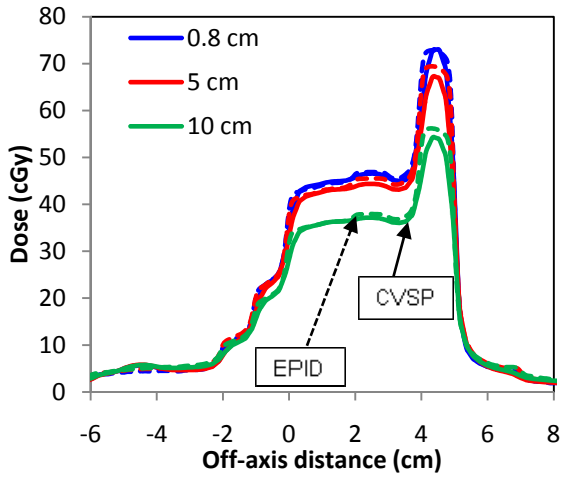
(f) Profiles at x= -1.5
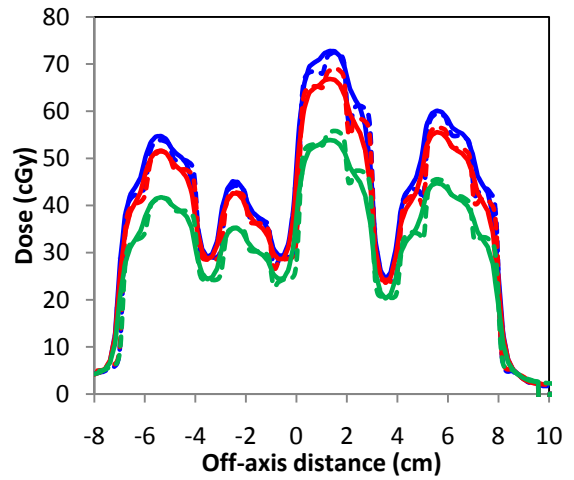
(g) Profiles at y=1.5
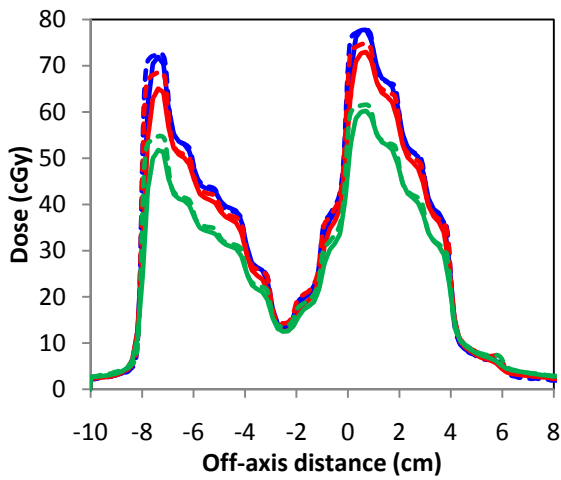
(h) Profiles at x=4.5
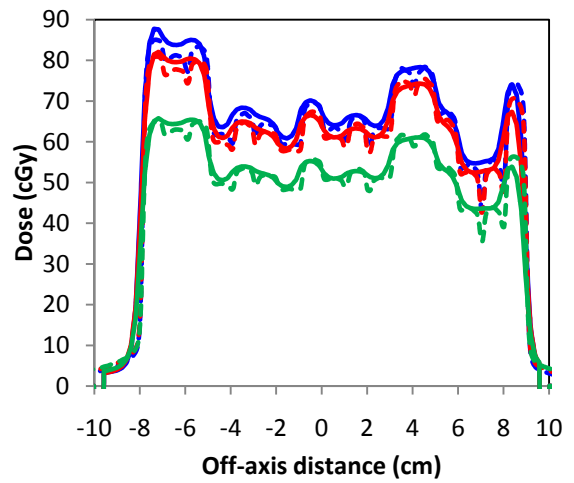
(i) Profiles at y=1.5

(j) Profiles at x=1.5

Figure V.10. Cross-plane (a,c,e,g,i) and in-plane (b,d,f,h,j) profiles along the central axis at 0.8, 5 and 10 cm depths for IMRT fields: LPO (a-c), LLAT (d-f), AP (g-i), RLAT (j-l) and RPO (m-o) for CVSP calculations (solid lines) and EPID data (dash lines).

Table V.4. The γ (2%/2 mm and 3%/3 mm) and C (2%/1 mm and 5%/1 mm) indices to quantify the agreement between CVSP calculations and EPID data for IMRT fields at 0.8 cm, 5 cm and 10 cm depths.

Depth	Field	Segments	r		C	
			2%/2mm	3%/3mm	2%/1mm	5%/1mm
0.8 cm	LPO	132+190	92.8%	98.8%	97.3%	99.7%
	LLAT	192	86.4%	98.1%	90.6%	97.1%
	AP	183+101	90.2%	98.5%	94.6%	98.8%
	RLAT	152	89.1%	98.4%	92.2%	98.4%
	RPO	237	86.0%	97.5%	90.1%	97.6%
5 cm	LPO	132+190	85.3%	98.2%	91.7%	99.3%
	LLAT	192	88.0%	98.3%	91.2%	97.6%
	AP	183+101	88.2%	98.1%	93.2%	98.8%
	RLAT	152	88.8%	98.5%	92.8%	98.2%
	RPO	237	86.8%	98.1%	91.5%	97.9%
10 cm	LPO	132+190	87.6%	98.5%	93.5%	99.5%
	LLAT	192	88.9%	98.6%	91.6%	97.7%
	AP	183+101	89.5%	98.3%	94.0%	99.0%
	RLAT	152	89.8%	98.6%	93.0%	98.3%
	RPO	237	88.1%	98.4%	92.3%	98.2%

V. D. Discussion

Chapter IV showed that the use of the EPID as a water-equivalent dosimeter is possible and the response can be accurately converted to dose at 0.8 cm depth in water for clinically-relevant fields. This chapter aims to validate the EPID calibration method to convert the EPID response to dose at any depth in water, making the method more applicable to clinical pre-treatment verification. The main parameters relevant to the calibration depth in water are the scatter kernels in water (K_w) and off-axis correction factors ($CF(x,y)$). These two parameters vary with depth in water and must be acquired for individual conditions in order to accurately convert the EPID response to dose in water. The first parameter, i.e. the scatter kernel, was derived from the S_p factor as a function of field size. Results showed that for 6 MV photons, the scattering behavior in

the EPID is similar to that at 5 or 6 cm depth in water. Our finding was similar to the results of Lee *et al*[3]. Based on this finding, the calibration method can be simplified by ignoring the scatter kernel correction when the EPID response is converted to dose-to-water at 5 cm depth. In addition, the use of a normalization factor and diagonal profile at 5 cm depth (refer to Chapter IV.B.2) in the EPID calibration removes the need for the off-axis correction, and only the backscatter correction is needed (Figure IV.3). This approach may make EPID dosimetry easier to implement in clinics for pre-treatment dose verification. The accuracy of this simplified approach was not studied here.

The accuracy of the parameters and calibration method was validated with IC and film measurements at 5 and 10 cm depths for jaw only, MLC-shaped and IMRT fields. The comparison between the EPID doses and CVSP calculations was also reported. The EPID dose agreed with both measurements and calculations at the depths studied. These results indicated that the proposed calibration method can be used to convert the EPID response to dose at any depth in water. The calibration method has been validated generally at depths and field shapes that are considered to be clinically relevant. Future work could investigate an improvement to the calibration method with an emphasis on the agreement close to the field edge, MLC-transmission region, and penumbra region, and to efficiently implement the EPID dosimetry in clinics for dose verification.

V. E. Conclusion

This study extended the EPID calibration method proposed in Chapter IV and converted the EPID dose to depths beyond the buildup region. Its accuracy was validated for doses at a range of depths, such as 5 and 10 cm depth, for jaw only, MLC-shaped and IMRT fields. The accuracy at 5 and 10 cm depth was comparable to that at 0.8 cm depth when

compared with IC and film measurements as well as calculations. Using an individual set of parameters, i.e. the scatter kernel and off-axis correction factors, the EPID responses can be converted to any depth in water. The generality of the EPID calibration method has been verified at depths for clinically-relevant conditions in this study.

References

1. P. Storchi and E. Woudstra, "Calculation of the absorbed dose distribution due to irregularly shaped photon beams using pencil beam kernels derived from basic beam data," Phys Med Biol 41, 637-656 (1996).

2. A. Van Esch, T. Depuydt and D. P. Huyskens, "The use of an aSi-based EPID for routine absolute dosimetric pre-treatment verification of dynamic IMRT fields," Radiother Oncol 71, 223-234 (2004).

3. C. Lee, F. Menk, P. Cadman and P. B. Greer, "A simple approach to using an amorphous silicon EPID to verify IMRT planar dose maps," Med Phys 36, 984-992 (2009).

CHAPTER VI

EVALUATION OF EPID ACCURACY AT THE DETECTOR LEVEL IN TRANSIT DOSIMETRY

In Chapter IV, a general calibration method was explored for the EPID as a water-equivalent dosimeter, and its accuracy has been validated for non-transmission measurements (i.e. without any phantom in the beam). This chapter extends the calibration method for transmission measurements (i.e. with a phantom in the beam). The accuracy of the EPID for transit dosimetry is evaluated for homogeneous and heterogeneous geometries, so that the EPID transit dosimetry can be employed for dose verification during treatment when a complex patient geometry is involved.

VI.A. Introduction

Both for adaptive radiation therapy and safety concerns, there is renewed interest in a dose verification technique that can be used during treatment to monitor actual doses delivered to patients. Several in-vivo delivered dose verification methods are being investigated, such as monitoring implantable dosimeters inside patients to measure treatment doses[1] and measuring transit doses during beam delivery[2-7]. Due to the invasive method and limited dose information gained with implanted dosimeters, transit dosimetry is an increasingly popular choice, especially with flat-panel detectors with fast acquisition and high resolution. Currently, there are two ways to verify delivered doses to patients using transit dosimetry: (1) dose verification at the detector level[8-11], and (2) two dimensional (2D) or three dimensional (3D) dose reconstruction in patients[12-16]. These

145

techniques involve several steps to make detector corrections and to reconstruct the delivered dose. The complexity of these dose reconstruction methods may limit their applications for dose verification in clinics, and their accuracy requires further investigation. Both methods of transit dosimetry provide necessary dose information during beam delivery (e.g. errors in machine malfunction, data transfer and patient-specific uncertainties). In addition, dose reconstruction inside patients can detect errors due to calculation uncertainties if an independent dose calculation algorithm is used for dose reconstruction. The preference for one method or the other may depend on the treatment technique and the purpose of the collected dose information, e.g. for a dose compensation in adaptive radiotherapy or for an error detection to avoid serious errors.

This study uses the method of dose verification at the EPID detector level and evaluates its accuracy for transit dosimetry. The dosimetric accuracy for this method is affected by scatter inside the detector and from the patient. The image signal results from primary photons passing through the patient (without interacting), the scattered radiation from the patient, and scatter within the detector. The primary information to be used to derive actual doses delivered to the patient is from the primary photon interactions, while scattering from the patient or inside the detector deteriorates the image quality and accuracy of transit dosimetry. The magnitude of scattering from the patient varies as a function of field size, patient thickness, and air gap between the patient and detector.[17, 18] To correct the effect of scattering on transmission images, several approaches have been used, including Monte Carlosimulations[19] and analytical methods[20, 21]. For scattering inside the detector, due to its high atomic number (Z) component, the scattering behavior depends on the patient geometry in the beam. Thus, in this study, the influence of scatter from the phantom on accuracy in EPID dosimetry is

quantified to determine the necessary correction factors in order to use the EPID as a water equivalent dosimeter for transit dosimetry.

By using the EPID as a water-equivalent dosimeter, a direct comparison can be made to calculated transit doses, provided that the planning system is able to calculate doses in this geometry. Transit dosimetry using EPIDs is a way to monitor doses actually delivered to patients. It can be used for either fraction-to-fraction comparisons or planning-to-delivery comparisons. To compare measurements from fraction-to-fraction, the measured transmission images can be in arbitrary units as long as they are consistent. However, planning-to-delivery comparisons require that the transmission images and treatment plan information are in the same units. For example, the planning dose can be converted to predicted EPID response or the measured EPID response can be converted to delivered dose. This study uses the EPID as a water-equivalent dosimeter, allowing direct comparison to the calculated transit doses from the planning system. The purposes of this study are to investigate the effect of scatter from the phantom on EPID dosimetry and to evaluate the accuracy of the EPID dosimetry method at the detector level for different phantom geometries.

VI.B. Methods and materials

VI.B.1. Equipment and calibration

All measurements were performed with a dose rate of 600 MU/min, jaw only field (MLC parked), 0° collimator angle, and photon energies of 6 MV using a Varian 21EX accelerator (Varian Medical Systems, Palo Alto, CA) equipped with a 120-leaf Millennium multileaf collimator (MLC) and an amorphous silicon EPID (aS500).All image acquisition, calibration procedures and analysis tools were the same as Chapter IV. The EPID response was converted to dose at 8 mm water-equivalent depth. Additional

corrections were also applied to the EPID response, including (1) non-uniform backscatter from non-uniform geometry in support structures, (2) kernel-based corrections for the inherent difference between the EPID and water, and (3) an off-axis correction for the higher EPID response at off-axis due to softer beams. The equation used to convert the EPID response to dose in water is shown below,

$$D_w(x,y) = CF(x,y) \cdot R(x,y) \otimes^{-1} K_E(x,y) \otimes K_w(x,y)$$ **(Equation VI.1)**

where *CF(x,y)* is the calibration factor, *R(x,y)* is the EPID responses, and K_E and K_w are the dose deposition kernels inside EPID and water. To acquire these parameters, several measurements using the EPID only and ion chambers (ICs) in phantom were performed. All measurements using the EPID were performed at 150 cm source-to-detector distance (SDD). All measurements using ICs in phantom (if applicable) were performed at 8 mm depth and 150 cm SDD. Sections VI.B.1.i to VI.B.1.iv describe the measurements without any phantom in the beam to characterize and correct the EPID at 150 cm SDD for dosimetric purposes with an emphasis on 6 MV photon beams (Figure VI.1(a)). The details of how these measurement data are used to derive calibration parameters have been described in Chapter IV.

VI.B.1.i. Dose response linearity

To check the linearity of the EPID response, MUs ranging from 5 to 600 were delivered with a 10 × 10 cm^2 field size for both energies (6 and 16 MV). The average pixel response was determined over ~0.6 cm^2 (10 × 10 pixels) region of interest (ROI) at the field center.

VI.B.1.ii. Non-uniform backscatter correction

To correct for the backscatter artifact, the method by Berry *et al*[22] was implemented. To use their method, EPID images for field sizes of 2 × 2, 3 × 3, 4 × 4, 5 × 5, 10 × 10 and 15 × 15 cm^2 were measured and analyzed for 6 MV photon beams.

VI.B.1.iii. Scatter kernels in EPID and water

The collimator scatter (S_c) for field sizes from 3 × 3 - 15× 15 cm^{2}was measured using an IC10 ion chamber (Scanditronix Wellhöfer North America, Bartlett, TN) in a CIRS mini-phantom (4 cm in diameter, Computerized Imaging Reference System, Inc., Norfolk, VA) with 200 MUs. For the field size factors (S_{cp}) in water, IC measurements (A12 Exradin Farmer-Type Chamber with an Inovision Therapy Dosimeter Model 35040) were performed at 8 mm depth in water for the same range of field sizes. For determination of the S_{cp} in the EPID, the data were acquired for the same field sizes with 300 MUs. The phantom scatter (S_p) in the EPID and water as a function of field size was then calculated by dividing the S_{cp} factor by the S_c factor. These S_p factors were used to derive the scatter kernels for the EPID (K_E) and water (K_w) using the method proposed by Storchi *et al*[23].

VI.B.1.iv. Off-axis correction

In order to determine the calibration factors at off-axis, the EPID response (after the scatter kernel correction) for a 20 x 20 cm^2 field size were compared with IC measurements in water. Then the correction matrix was determined and applied to the EPID data.

VI.B.2. EPID transmission images for homogeneous geometries: scatter effect as a function of phantom thickness and air gap

In Section VI.B.1, the calibration procedure was performed and calibration parameters were acquired for the situation without any phantom in the beam (i.e. non-transmission images). This section investigates the scatter effect in the situation with the phantom placed in the beam as a function of phantom thickness and air gap (transmission images).As described in the introduction, when there is a phantom or patient in the beam (for a transmission condition), the scatter from the phantom or patient affects the responses and scattering behavior in the EPID, which is different from the result when no phantom or patient is in the beam (for a non-transmission condition). In this situation, the accuracy of EPID dosimetry is questionable and will depend on the complexity of the patient geometry.

First, S_c factors were measured using an IC in the mini-phantom and S_{cp} factors were measured using the EPID and an IC at 8 mm depth in water. The S_{cp} factors of field sizes from 3 × 3 - 15 × 15 cm^2 for phantom thicknesses of 10 and 20 cm (Figure VI.1(b) and (c))and air gaps of ~30, 40 and 50 cm between the phantom bottom surface and EPID (Figure VI.2) were measured with 300 MUs. The phantom materials were Solid Water (SW) phantom blocks (Gammex RMI, Middleton, WI) with lateral dimension of 30 × 30 cm^2 and a density of 1.04 g/cm^3. The effect of air gap on the EPID response (30, 40 and 50 cm) was investigated using the geometry in FigureVI.1(c) over a range of SSDs from 80 to 100 cm (Figure VI.2). Figure VI.3 shows an example of the S_{cp} measurement setup with the EPID and an IC in water when a phantom is in the beam. The S_c factors were measured for field sizes from 3 × 3 - 15 × 15 cm^2 in the same geometries as the S_{cp} measurements (Figure VI.1 and VI.2), but with 200 MUs using an IC10 in a mini-phantom. The S_c factors represent scatter from the phantom to the EPID excluding the detector scatter component, and therefore they were used to derive the ratio of phantom scatter to primary photons which arrive at the EPID. Then, S_c and S_{cp}

factors were used to calculate S_p factors, which were used to derive scatter kernels in the EPID as a function of air gap and phantom thickness.
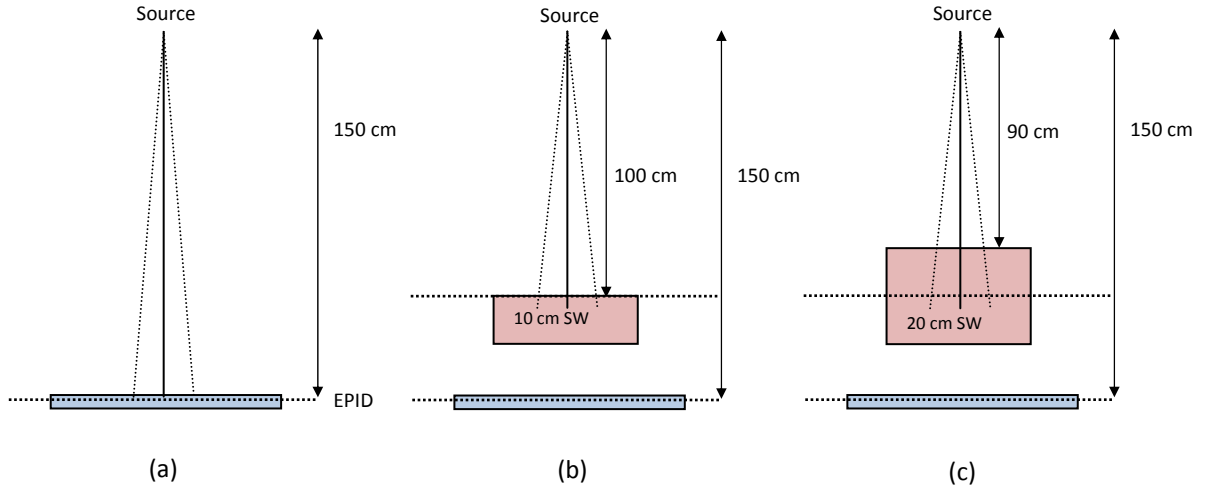
Figure VI.1. Geometric description of (a) no phantom in place (non-transmission data), (b) 30 × 30 × 10 cm^3 SW phantom in place (transmission data) and (c) 30 × 30 × 20 cm^3 SW phantom in place (transmission data).
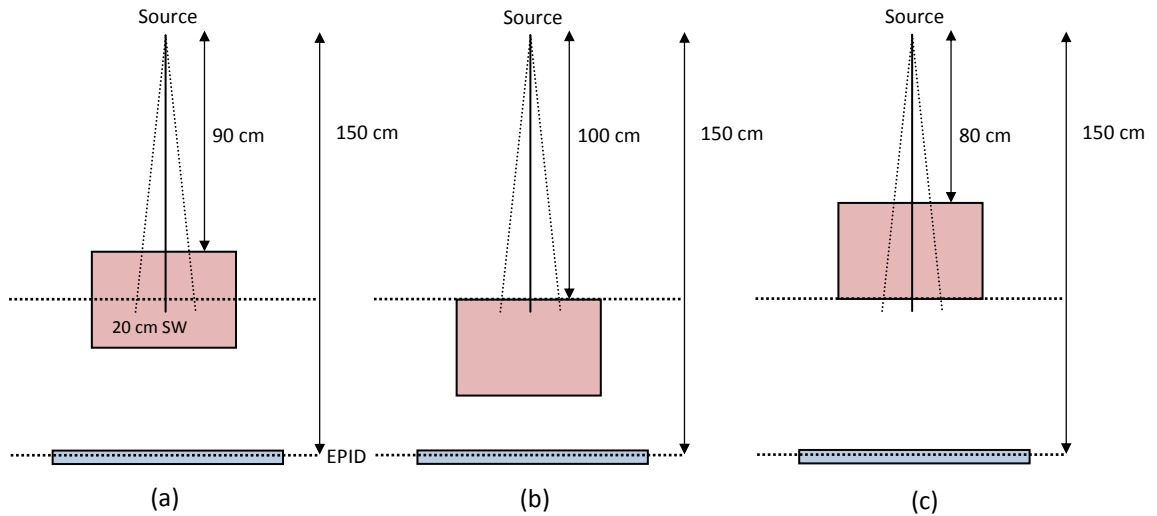
Figure VI.2. Geometric description of 30 × 30 × 20 cm^3 SW phantom in place (transmission data) with air gap of (a) 40 cm, (b) 30 cm and (c) 50 cm from the phantom bottom surface to the detector.
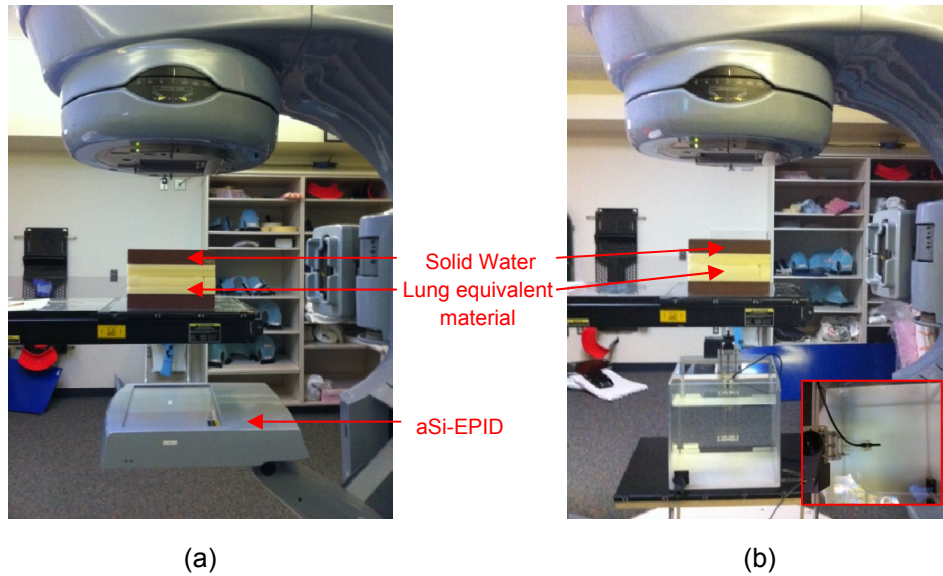
Figure VI.3. An example of measurement setup for (a) the EPID and (b) IC measurements at 8 mm depth in water for transmission measurements.

VI.B.3. EPID transmission measurements for heterogeneous geometries

Section VI.B.2 investigates the effect of scatter on the response in the EPID and water for homogeneous phantom geometries, and the derived kernels can be used for the EPID in transit dosimetry applications. This section investigates the accuracy of transit dosimetry when the scatter kernels derived from homogeneous geometries (Section VI.B.2) are applied to heterogeneous geometries, which is relevant to the clinical situation, particularly for treatments involving lung.

Two heterogeneous geometries were investigated in this study: simple homogeneous lung and tumor-in-lung geometries (Figure VI.4 and VI.5). The phantom materials included SW phantom blocks and lung-equivalent phantom blocks (Gammex RMI, Middleton, WI) with a density of 0.30 g/cm^3. The total dimension of simple lung and tumor-in-lung geometries was 30 × 30 × 20 cm^3. For tumor-in-lung geometry, a small

lung tumor with dimensions of 4 × 3 ×3 cm^3 was embedded in the lung phantom. For these two geometries, the field sizes of 4 × 4, 5 × 5 and 10 × 10 cm^2 with 600 MUs were used.
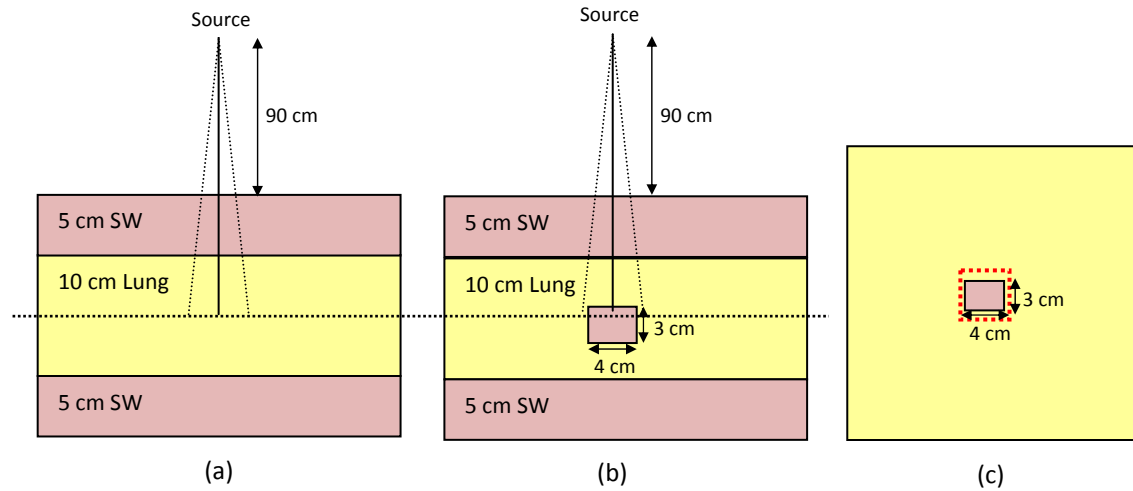
Figure VI.4. Geometric description of (a) simple lung and (b) lung tumor geometry in the axial view, and (c) lung tumor geometry in beam's eye view (BEV). The dimension of both geometries is 30 × 30 × 20 cm^3. The dimension of SW block used to simulate a small lung tumor is 4 × 3 ×3 cm^3. The isocenter is at the middle plane of lung or at 1 cm depth in the simulated tumor (when present). The planned field size (dotted line in (c)) is 5 × 5 cm^2 in order to cover the simulated tumor.
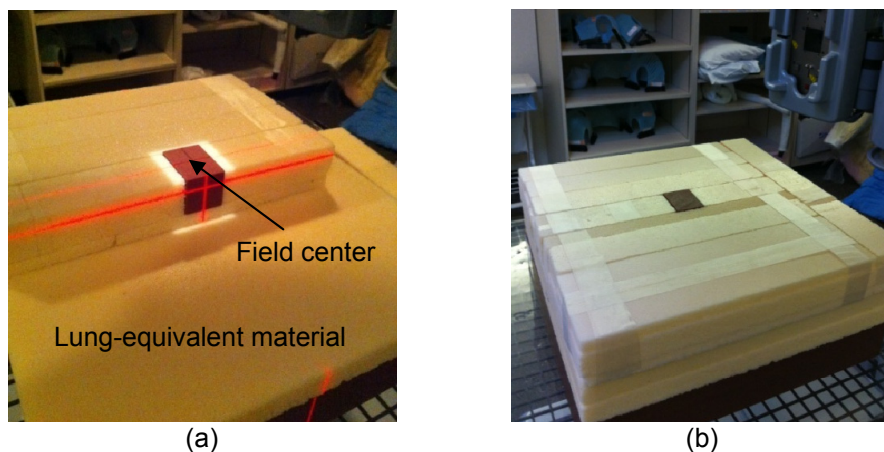
Figure VI.5. Tumor-in-lung geometry (Figure VI.4 (b-c)) in the measurements: (a) isocenter position and (b) tumor embedded in the lung-equivalent medium.

VI.B.4. Experimental verification with an IC and film measurements for non-transmission and transmission measurements

To verify the EPID accuracy for non-transmission and transmission conditions, corrected EPID doses were compared with IC measurements in water and film measurements in SW (40 x 40 x 20 cm^3). In addition to the IC measurements described in Section VI.B.2, the doses at 8 mm depth in water were also measured for the heterogeneous geometries shown in Figure VI.4 for 4 x 4, 5 x 5 and 10 x 10 cm^2 field sizes. Film measurements were performed using Kodak EDR film (Carestream Health, Inc., Rochester, NY) for a 10 x 10 cm^2 field size. The 2D doses were measured for non-transmission and transmission with homogeneous and heterogeneous geometries. The transmission measurements were performed with a 40 cm air gap between the bottom of the phantom and the film. A film calibration curve was acquired with a dose range from 0 to 400 cGy. All films were developed using a Kodak X-OMAT 3000RA Processor (Eastman Kodak, Rochester, NY), digitized with a VXR-16 Dosimetry PRO^{TM} scanner (VIDAR systems corporation, Herndon, VA) and analyzed using in-house software. The film resolution was 0.179 × 0.179 mm^2.

VI.C. Results

VI.C.1. Characterization of EPID non-transmission images

VI.C.1.i. Dose response linearity

Figure VI.6 shows the linearity for 6 and 16 MV photons. The linearity was good for MUs greater than100 MUs. The linearity was worse for smaller MU, with a 12% reduction for 5 MU.
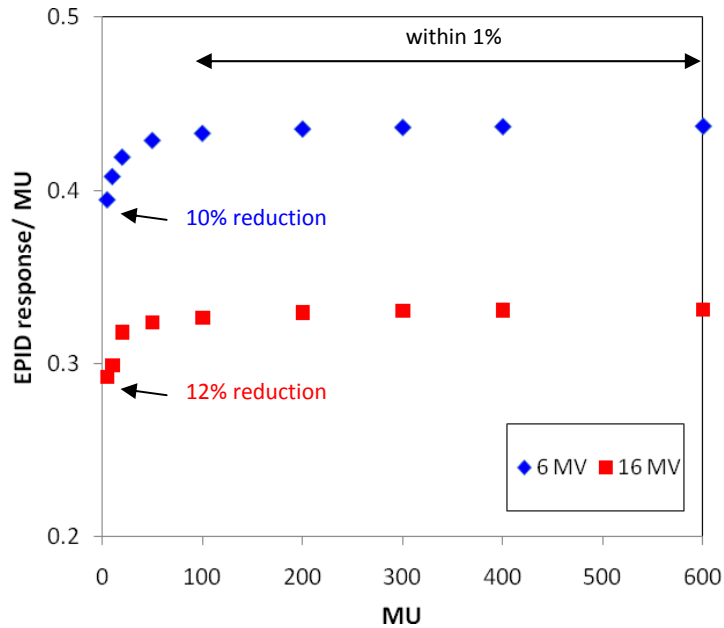
Figure VI.6. EPID response linearity (response per MU vs. MU) at SDD of 150 cm for 6 and 16 MV photon beams.

VI.C.1.ii. Non-uniform backscatter correction

Figure VI.7 shows the corrections vs. distance from the EPID center as a function of field size (defined at 100 cm) for 6 MV photons. The slope of the correction equation depends on field size (Figure VI.8). Therefore, for pixels from the center to the target side, the corrections (Cor_{BS}) as a percentage for 6 MV can be acquired using Equation VI.2.

$$Cor_{BS}(Y_{Jaw}, d) = 100 - 2.8625 \cdot e^{-0.2405 \cdot Y_{Jaw}} \cdot d \qquad \textbf{(Equation VI.2)}$$

where Y_{Jaw} and d represent jaw sizes in in-plane direction and distances from the center to the target side, respectively. For pixels from the center to the gun side, no correction is needed. The EPID raw data are then multiplied by an individual correction matrix, depending on the in-plane jaw size.
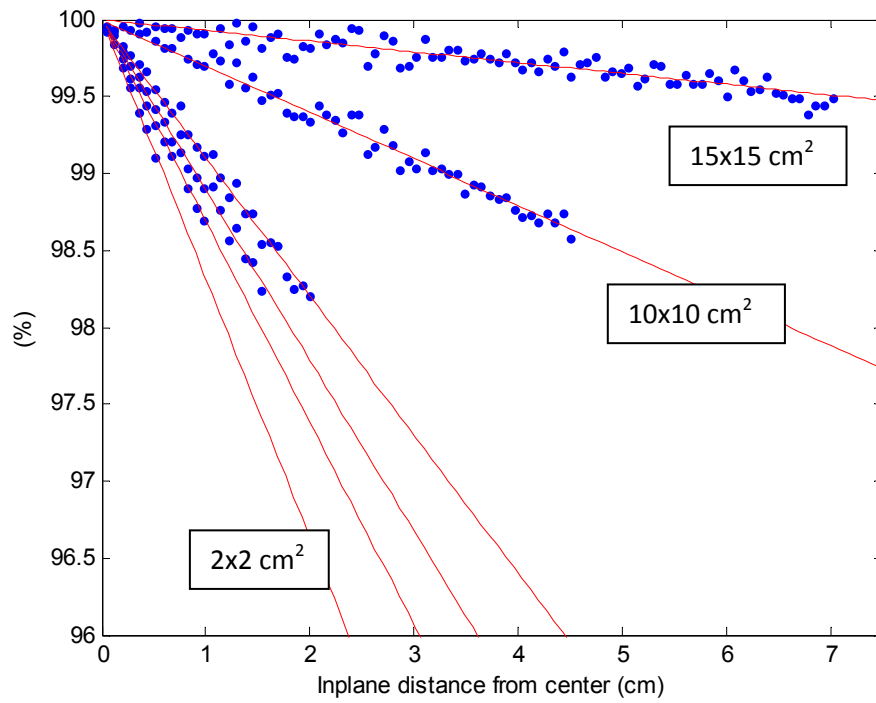
Figure VI.7. Corrections vs. distance from the EPID center at 150 cm SDD for 6 MV photons as a function of field size. The slope of correction equations decreases with increasing field size.

$$y = -2.8625e^{-0.2405x}$$
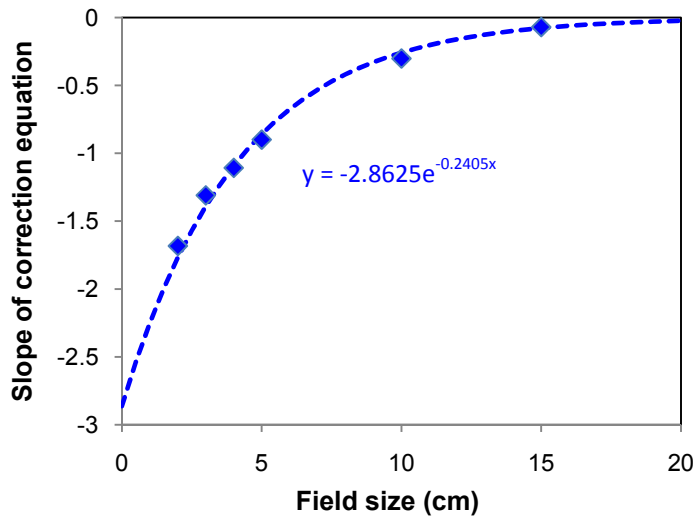
Figure VI.8. The slope of correction equations at 150 cm SDD for 6 MV photons as a function of field size.

VI.C.1.iii. Scatter kernels in EPID and water

The S_p value as a function of field size was used to derive the scatter kernels in the EPID and water (Figure VI.9). The EPID scatter kernel was different from the water kernel, similar to the finding in Figure IV.16.
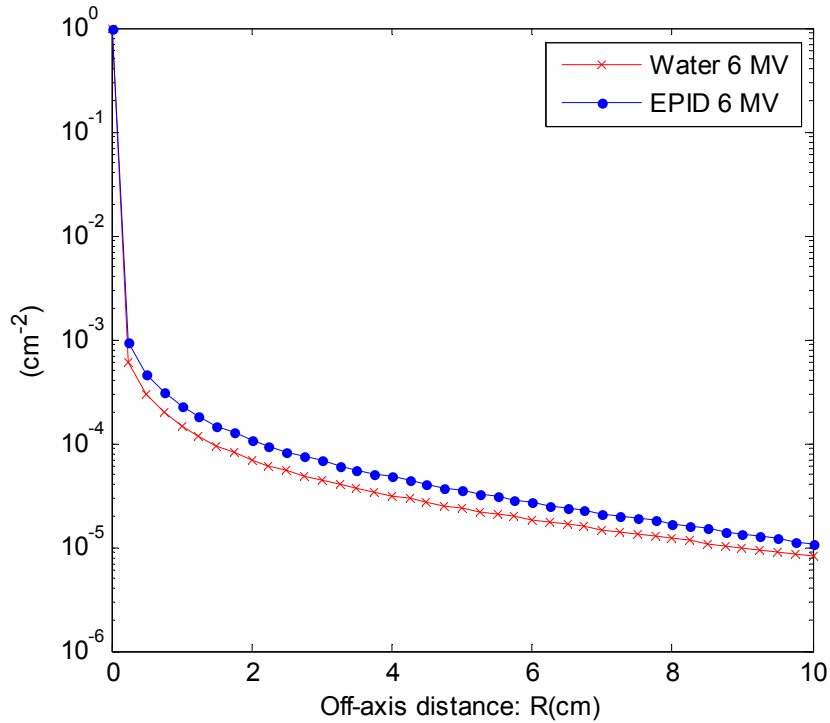
Figure VI.9. Scatter kernels of EPID and water at 150 cm SDD for 6 MV photon beams. The bin size to acquire the kernels is 0.25 cm (see Chapter IV). The data shown here are normalized to the value at R = 0 cm for the individual curve.

VI.C.1.iv. Off-axis correction

Figure VI.10 shows the off-axis correction factor as a function of off-axis distance. The correction factor was ~3% at 15 cm off-axis. The magnitude at 150 cm SDD was smaller than that at 100 cm SDD (Figure IV.21).
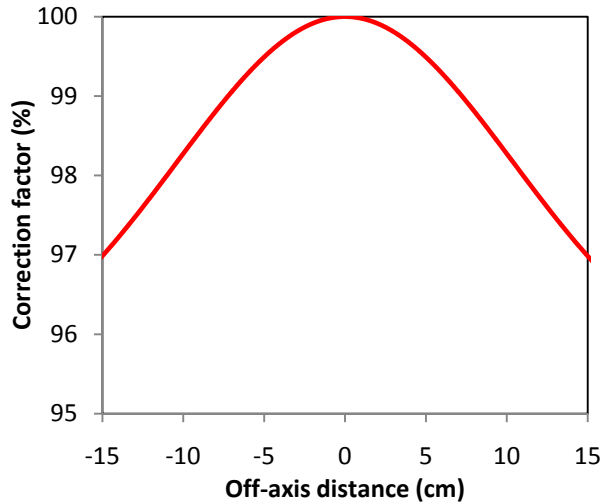
Figure VI.10. Off-axis correction factor as a function of off-axis distance for 6 MV photons.

VI.C.2. EPID transmission images for homogeneous geometries: phantom scatter effect as a function of phantom thickness and air gap

Section VI.C.1 showed the parameters related to the EPID calibration without any phantom in the beam. When there is a phantom (or patient in the clinical situation) in the beam, the energy spectrum exiting the phantom is different from that without phantom in the beam (i.e. non-transmission images). The parameters derived in the previous section may not be valid for transmission images. Therefore, in this section, S_{cp}, S_c and S_p were acquired for various phantom thicknesses and air gaps between the phantom and detector to understand how the phantom scatter changes the responses in water and EPID.

Figure VI.11 shows the relative dose as a function of phantom thickness and air gap measured using the EPID and the IC in water. Because of beam attenuation, the relative dose decreases with increasing phantom thickness, and the curve should be similar to the exponential function. When the field size increases, the scatter from the phantom and from inside the media (i.e. EPID and water) increases. Therefore, the

relative dose increases with increasing field size. This increase is more significant for the water medium than for the EPID. Regarding the air gap effect, the relative dose decreases with increasing air gap from the phantom to the detector plane. This is due to increased scatter from the phantom arriving at the detector for smaller distances of air gap. In addition, the air gap plays an important role for large fields, especially for water. For a 30 cm air gap, the increase in relative dose in water ranged from 1.4% (2×2 cm^2, not shown) to 12.8% (15×15 cm^2), while the increase in relative dose in the EPID ranged from 0.3% (2×2 cm^2, not shown) to 10.5% (15×15 cm^2).This result indicates that the EPID and water responses have a different dependence on phantom thickness and air gap and corrections are needed to convert the EPID response to dose in water for different conditions.
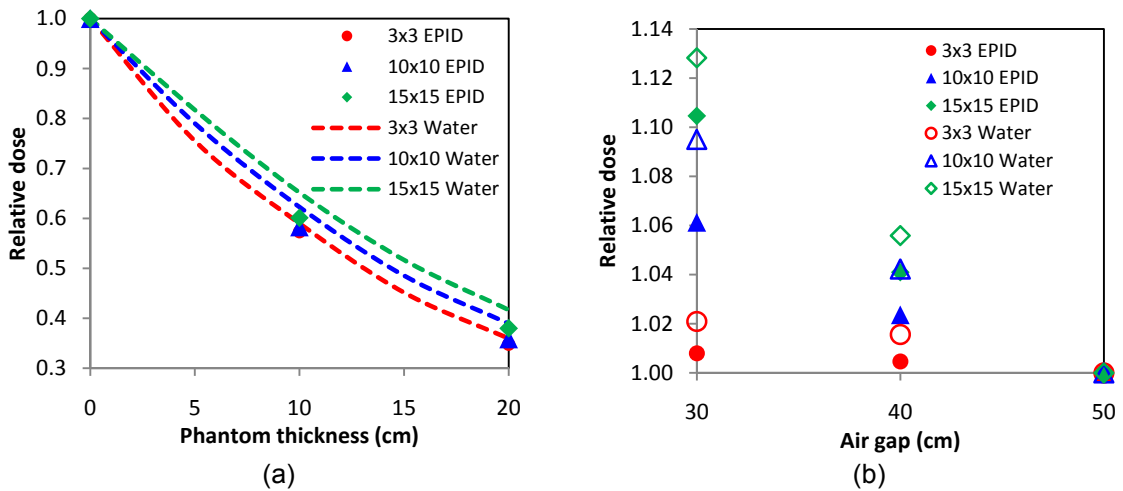
Figure VI.11. Relative doses in the EPID and water as a function of (a) phantom thickness (cm) and (b) air gap (cm) for 3×3, 10×10 and 15×15 cm^2 field sizes for 6 MV photons.

Figure VI.12 shows the S_c factor as a function of field size for various phantom thicknesses and air gap. These factors were acquired using the IC in a mini-phantom, and used to quantify the scatter from the collimator (no phantom) and scatter from the phantom in the beam. This factor represents the scatter arriving to the measurement
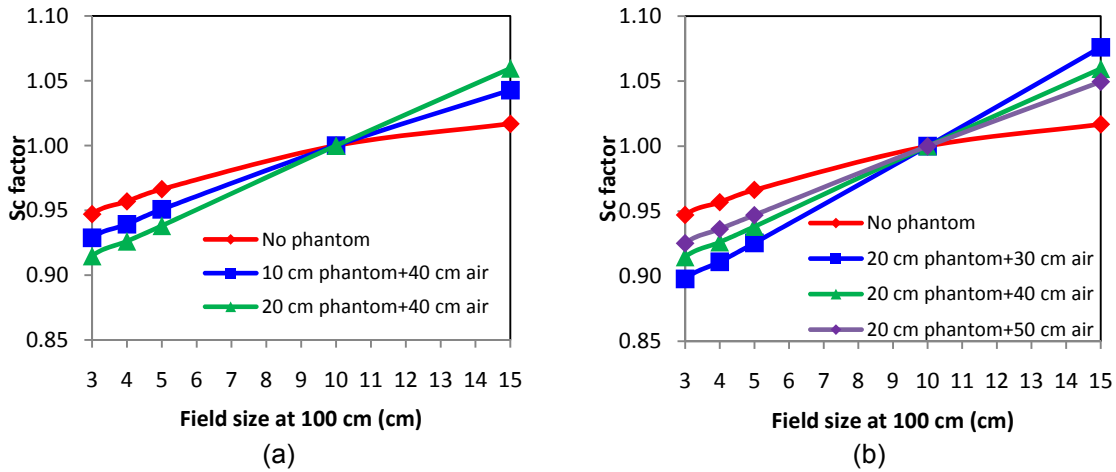
Figure VI.12. S_c factors as a function of field size for (a) various phantom thicknesses and (b) various distances in air gap.

point as a function of the field size and is the same for the EPID and water. The slope of S_c as a function of field size increases with increasing phantom thicknesses and decreasing air gap (Figure VI.12). These data are normalized to a 10 x 10 cm^2 field size for each measurement condition, making it difficult to understand the scatter variation. Therefore, we extrapolated the S_c factor to the zero field size ($S_c(0)$). Theoretically, the $S_c(0)$ represents the doses from primary fluence only, excluding the scatter from the collimator or scatter from the phantom. Here, we define the scatter-to-primary ratio (SPR) as shown in the following equation,

$$SPR(X) = \frac{Scatter + Primary}{Primary} - 1 = \frac{Sc(X)}{Sc(0)} - 1 \qquad \textbf{(Equation VI.3)}$$

where *X* represents the field size (cm). Figure VI.13 shows the SPR as a function of phantom thickness and air gap. The SPR increases with increasing field size and phantom thickness, and decreasing air gap. The SPR for large field sizes depends significantly on the phantom thickness and air gap. The SPR increases from 11.3% (without the phantom) to 20.8% (with the phantom of 20 cm) for 15 x 15 cm^2 field size, while increasing slightly for 3 x 3 cm^2 field size (from 3.6% to 4.3%). When the air gap

decreases from 50 cm to 30 cm, the SPR increases from 3.8% to 5.0% and from 17.7% to 25.8% for 3 x 3 and 15 x 15 cm^2 field sizes, respectively.
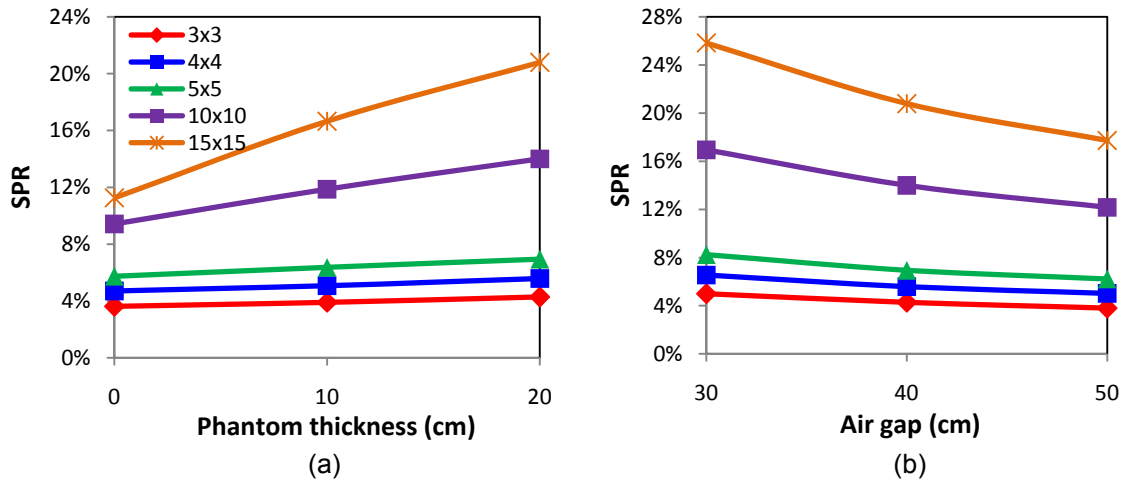
Figure VI.13. SPR as a function of (a) phantom thickness with 40 cm air gap (if available) and (b) air gap with 20 cm phantom thickness for various field sizes.

Figure VI.14 shows S$_p$ factors in the EPID and water for various geometries. Comparing Figure VI.14 (a-d), the phantom thickness and air gap affected the scatter behavior in water, while they did not significantly affect the behavior in the EPID. Therefore, the S$_p$ difference between the EPID and water depends on the field size, phantom thickness and air gap (Figure VI.14 (e-f)). This result shows that the scatter kernel for the EPID (K_E in Equation VI.1) is slightly different for non-transmission and transmission images. However, the scatter kernel for water (K_w in Equation VI.1) is significantly different for non-transmission and transmission images (Figure VI.15). Since this study aims to convert the EPID response to dose in water for transit dosimetry, geometry-specific water kernels will be needed to achieve good accuracy. This work investigated a limited range of phantom thicknesses and air gaps. Additional work could include study of more geometries, including sloped surfaces.

161
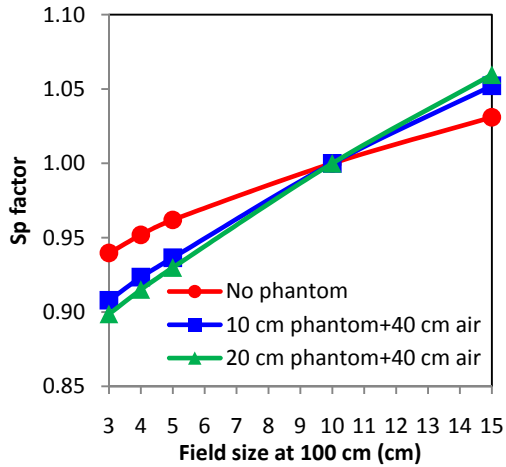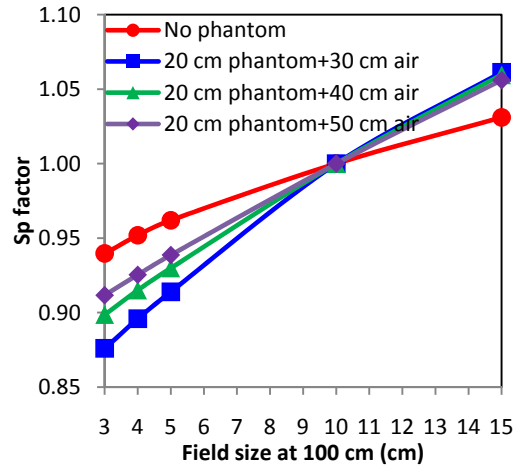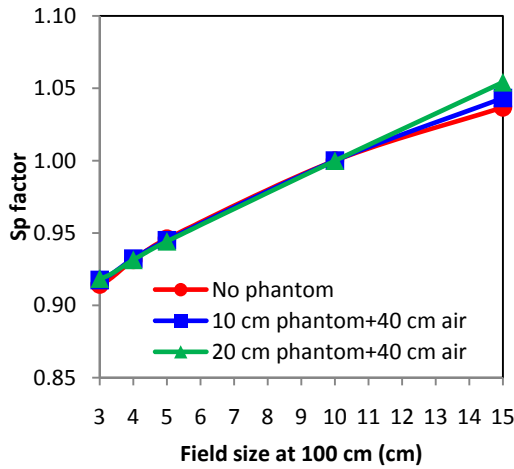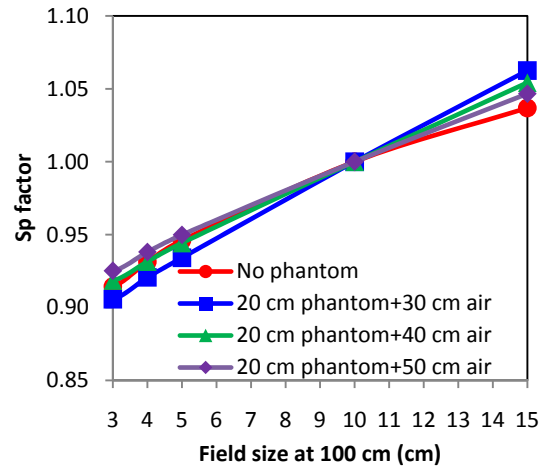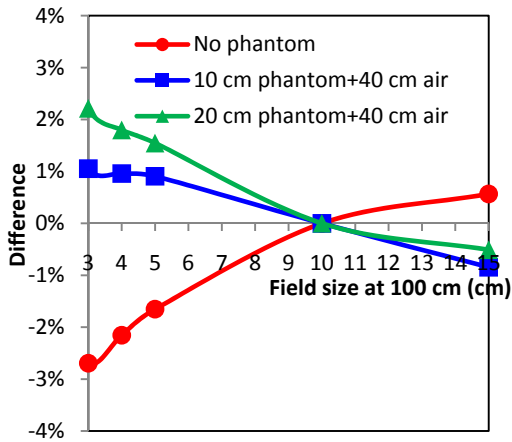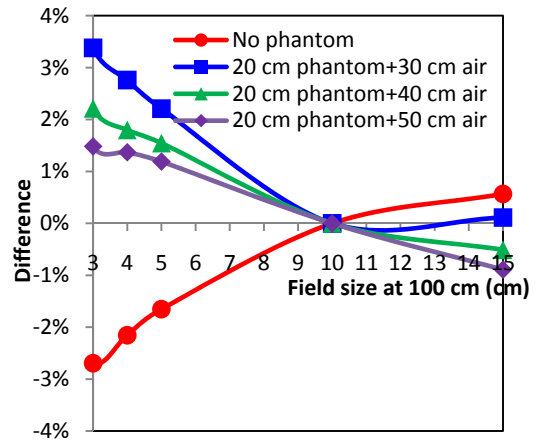
Figure VI.14. S_p factors inside water (a-b) and inside the EPID (c-d) as a function of phantom thickness and air gap, and the difference relative to water data (e-f).
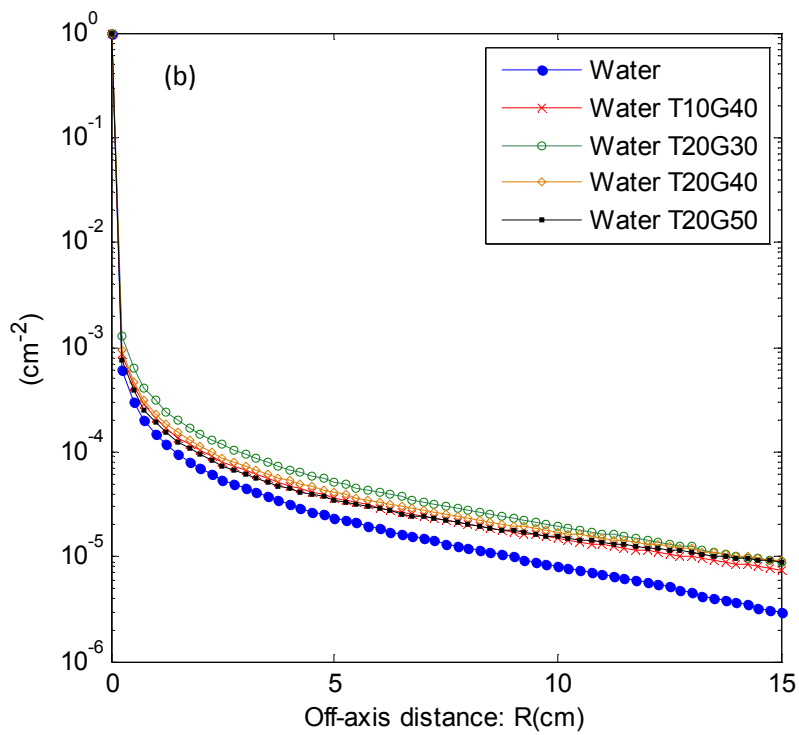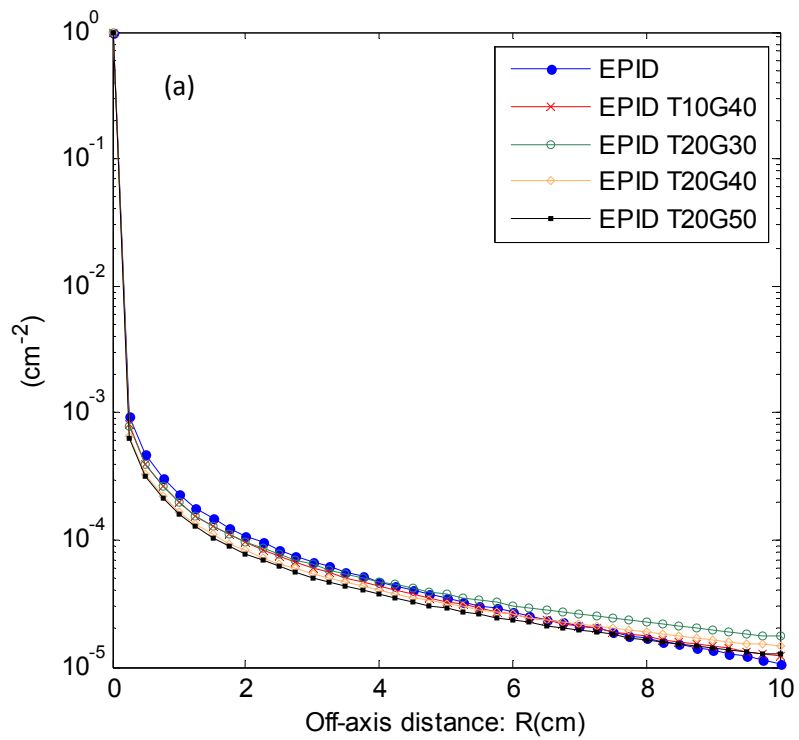
Figure VI.15. Scatter kernels inside (a) the EPID and (b) water as a function of phantom thicknesses (T) and air gap (G).

In Figure VI.11, the response relationship between the EPID and water varied with phantom thickness and air gap. This result indicates that the calibration factor (*CF(0,0)*) in Equation VI.1 is not constant and its magnitude depends on the phantom thickness and air gap. In the EPID calibration for non-transmission images, the *CF(0,0)* equals to 1, i.e. for 10 x 10 cm^2 field size, the EPID response is the same as the dose at 8 mm depth in water. To acquire the *CF(0,0)* for different conditions, the EPID response was compared with the dose at 8 mm depth in water for the studied phantom thicknesses and air gaps. The *CF(0,0)* for various conditions were shown in Table VI.1.

Table VI.1. *CF(0,0)* values for non-transmission and transmission images for various phantom thicknesses and air gap (1% in one standard deviation (1σ)).

Type	Non-transmission	Transmission	Transmission	Transmission	Transmission
Thickness (cm)	0	10	20	20	20
Air gap (cm)	0	40	30	40	50
CF(0,0)	1.000	1.069	1.100	1.086	1.066

The *CF(0,0)* increases with increasing phantom thicknesses and decreasing air gap. The difference was up to 10%. When there is a phantom present, the EPID is affected by beam hardening and phantom scatter effects, leading to an incorrect conversion of the response to dose in water if the *CF(0,0)* for non-transmission images is used. A *CF(0,0)* larger than 1 corrects for the beam hardening effect, while smaller than 1 corrects for the beam softening effect. The phantom thicknesses and air gaps evaluated was not exhaustive in this study, but may be sufficiently accurate for transit dosimetry. A more thorough investigation of *CF(0,0)* for more geometries can be done in a future study. With additional measurements, an equation of *CF(0,0)* as a function of phantom thicknesses and air gap could be derived. Currently, we used a simple linear

interpolation to get the *CF(0,0)* for an individual phantom thickness and air gap. Regarding the off-axis correction for transmission images, we assumed that the shape is the same for transmission images (i.e. Figure VI.10).

In summary, for non-transmission images, the *CF (0,0)* equals 1 and the off-axis correction factor is shown in Figure VI.10. The parameters of K_E and K_w kernels are shown in Figure VI.9. For transmission images, the *CF(0,0)* is calculated using Table VI.1 for various phantom thicknesses and air gap, and the off-axis correction factor is the same as that used for non-transmission images. The parameters K_E and K_w depend on the phantom thickness and air gap and the kernels shown in Figure VI.15 were used. For the geometries not included in the figure, the scatter kernels for a similar phantom thickness and air gap were chosen. This choice should not significantly affect the accuracy of transit dosimetry because the scatter behavior does not vary significantly for the phantom thickness of 10 and 20 cm, and the air gap of 30-50 cm (Figure VI.15). However, it does depend on whether or not the phantom is present.

VI.C.3. EPID dose accuracy for non-transmission and transmission images

For transmission images with heterogeneous geometries (Figure VI.4), the water-equivalent thicknesses of the heterogeneous phantoms were 12.5 and 14.75 cm for the simple lung and lung tumor geometries, respectively. Therefore, interpolating the data in Table VI.1, the *CF(0,0)* values were 1.073 and 1.077 for simple lung and lung tumor geometries. The scatter kernel used for both geometries was the same as that for homogeneous geometry with a 10 cm thickness (Figure VI.1(b)).

Corrected EPID responses (converted to doses in water) for homogeneous and heterogeneous geometries are shown in Table VI.2 and are also compared with IC measurements in water. The results were normalized to the non-transmission data for

the 10 x 10 cm^2 field size for each individual dataset. For homogeneous geometries, the corrected EPID responses agreed with IC measurements within 0.3% for field sizes from 3×3 to 15×15 cm^2. For a 2×2 cm^2 field, the agreement was 1.8%. This disagreement was attributed to measurement error because of the large cavity of the IC used to measure doses in small fields. Small field dosimetry is a challenging issue, which was described in the beginning of this dissertation. For heterogeneous geometries, the agreement was within 3.5% for studied field sizes. The disagreement was greater with decreasing field size. The larger difference for the 10 x 10 cm^2 field size for heterogeneous geometries (up to ~2%) compared to homogeneous geometries is due to using a less accurate *CF(0,0)* to correct the EPID responses. The *CF(0,0)* in heterogeneous geometries was derived from Table VI.1 using linear interpolation. The error can be reduced by acquiring a relationship of *CF(0,0)* as a function of phantom thickness. Regarding the increasing differences for smaller field sizes, this is attributed to the use of an approximate scatter kernel (the kernel for 10 cm phantom thickness).

In addition to the comparison to IC measurements, the corrected EPID doses were compared to film measurements for non-transmission and transmission conditions with homogeneous and heterogeneous phantom geometries. Figure VI.16 shows the cross-plane or in-plane profiles across the center for a 10x10 cm^2 field size. Generally, the corrected EPID doses agreed with film measurements for all studied geometries. The main discrepancy was found off-axis for a 20 cm thick homogeneous phantom (Figure VI.16(c)). This is attributed to the less accurate off-axis correction for the large phantom thickness. This study assumed that the needed off-axis correction is independent of phantom thickness and air gap. Based on this result, using different off-axis correction factors for various geometries could improve the off-axis accuracy of EPID doses for transit dosimetry, especially when large thicknesses of the phantom (or

patient) are involved. Regardless of the off-axis discrepancy, the average difference

(ROI > 10% maximum film dose) was within 1.3% for all studied geometries (Table VI.3).

Table VI.2. Comparisons between the IC in water and EPID at the central axis and 150 cm SDD. Doses were normalized to non-transmission 10x10 cm^2 field size for each individual detector.

Geometry	Field size(cm^2)	IC in water	EPID	Difference
Non-transmission	2 × 2	0.851	0.866	1.8%
	3 × 3	0.890	0.889	-0.1%
	4 × 4	0.911	0.910	-0.1%
	5 × 5	0.930	0.929	-0.1%
	10 × 10	**1.000**	**1.000**	**0.0%**
	15 × 15	1.048	1.047	-0.1%
Transmission 10 cm SW 40 cm air gap	2 × 2	0.500	0.507	1.4%
	3 × 3	0.525	0.525	-0.1%
	4 × 4	0.540	0.540	0.0%
	5 × 5	0.555	0.555	0.0%
	10 × 10	0.623	0.623	0.0%
	15 × 15	0.683	0.683	0.0%
Transmission 20 cm SW 30 cm air gap	2 × 2	0.305	0.308	1.3%
	3 × 3	0.322	0.321	-0.1%
	4 × 4	0.334	0.334	0.0%
	5 × 5	0.346	0.346	0.1%
	10 × 10	0.409	0.408	-0.3%
	15 × 15	0.467	0.467	0.1%
Transmission 20 cm SW 40 cm air gap	2 × 2	0.304	0.309	1.4%
	3 × 3	0.320	0.320	-0.1%
	4 × 4	0.330	0.330	-0.1%
	5 × 5	0.339	0.340	0.1%
	10 × 10	0.389	0.389	0.0%
	15 × 15	0.437	0.437	0.1%
Transmission 20 cm SW 50 cm air gap	2 × 2	0.300	0.305	1.5%
	3 × 3	0.315	0.314	-0.2%
	4 × 4	0.324	0.323	-0.1%
	5 × 5	0.332	0.332	0.1%
	10 × 10	0.373	0.373	0.0%
	15 × 15	0.414	0.414	-0.1%
Transmission 10 cm SW+10 cm Lung 40 cm air gap	4 × 4	0.460	0.469	2.0%
	5 × 5	0.473	0.482	1.9%
	10 × 10	0.536	0.540	0.8%
Transmission Lung tumor geometry 40 cm air gap	4 × 4	0.409	0.423	3.4%
	5 × 5	0.421	0.435	3.2%
	10 × 10	0.483	0.492	1.9%
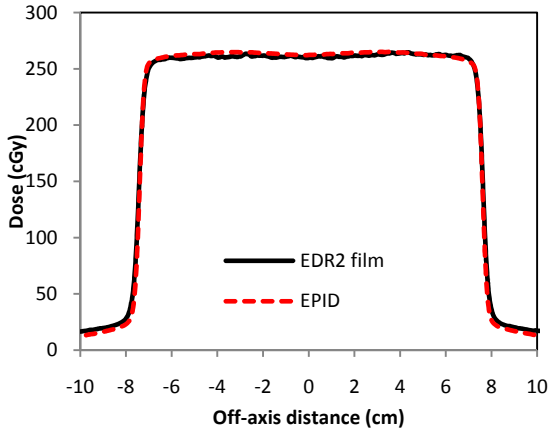
(a) Profiles at y=0 for non-transmission
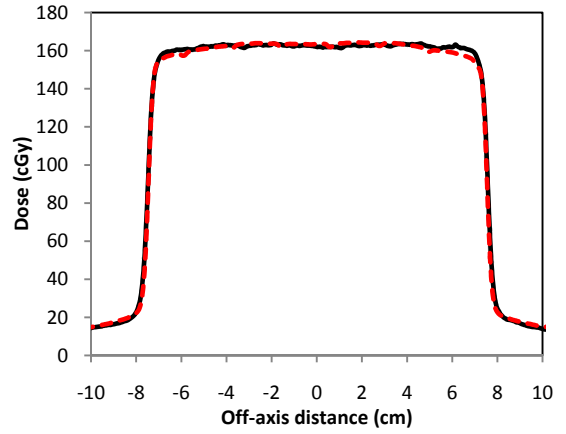
(b) Profiles at y=0 for transmission (10 cm SW)
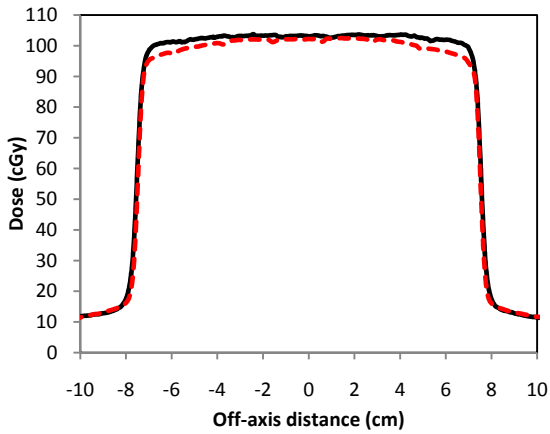
(c) Profiles at y=0 for transmission (20 cm SW)
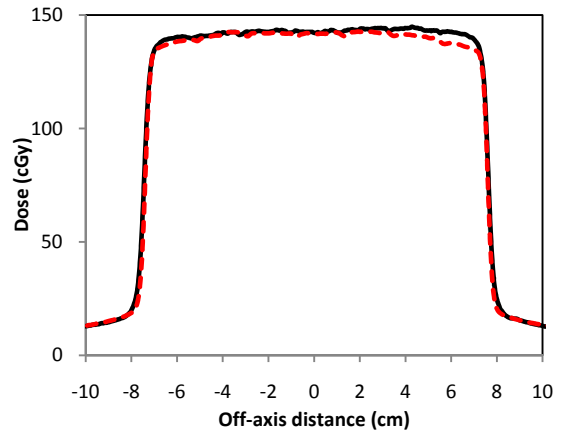
(d) Profiles at y=0 for transmission (SW & Lung)
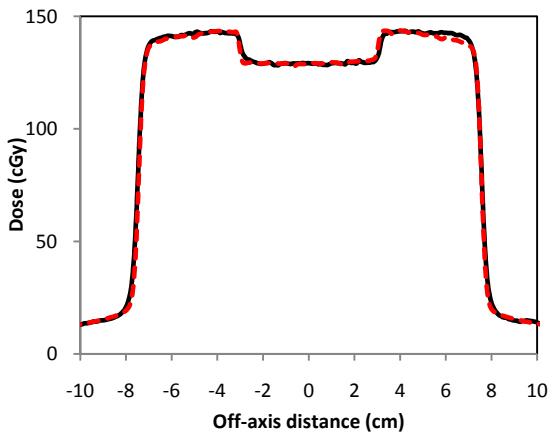
(e) Profiles at y=0 for transmission (Lung tumor)
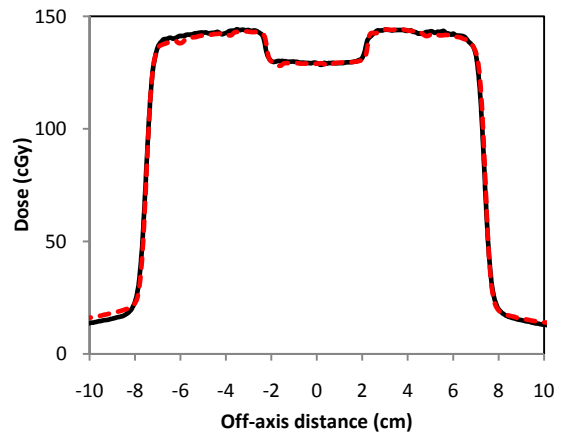
(f) Profiles at x=0 for transmission (Lung tumor)

Figure VI.16. Film vs. EPID data with 600 MUs: cross-plane (a-e) and in-plane (f) profiles for (a) non-transmission, (b) transmission with 10 cm SW, (c) transmission with 20 cm SW, (d) transmission with 10 cm SW & 10 cm lung, and (e-f) transmission with lung tumor geometry.

Table VI.3. Differences (average and 1σ) between the film and EPID data relative to maximum film doses for ROI > 10% maximum film dose.

Geometry	Relative difference to maximum dose
Non-transmission	-0.24% ± 1.76%
Transmission: 10 cm SW	-0.79% ± 1.55%
Transmission: 20 cm SW	-1.21% ± 1.92%
Transmission: 10 cm SW + 10 cm Lung	-1.14% ± 1.65%
Transmission: Lung tumor	-0.97% ± 1.70%

VI.D. Discussion

It will be a critical improvement to patient care to implement delivered dose verification techniques in radiotherapy to monitor actual doses delivered to patients. Among these techniques, transit dosimetry using EPIDs shows several advantages, including a real-time display of 2D information. This study evaluated the accuracy of an EPID as a water-equivalent dosimeter for transit dosimetry. The conversion of EPID response to dose in water has the advantage of allowing a direct comparison to calculated transit doses from a treatment planning system. Comparisons between measured and calculated transit doses provide information about deviations between delivered and planned doses. To convert EPID response into dose in water, corrections are needed for backscatter, scatter kernels and the off-axis energy dependence. These corrections have been discussed in Chapter IV for non-transmission measurements with the EPID position at 100 cm SDD. In this chapter, we extended the calibration method for non-transmission measurements to transmission measurements with the EPID position at 150 cm SDD. In addition, the accuracy of EPID dosimetry was investigated as a function of phantom geometries, such as homogeneous and heterogeneous geometries.

For non-transmission measurements at 150 cm SDD, the dose response linearity, backscatter correction factors as a function of field size and off-axis distance, scatter kernels in the EPID and water, and off-axis correction factors were determined. The linearity, backscatter correction factors, and scatter kernels for 150 cm SDD were similar to the results for 100 cm SDD. However, the correction factor at 15 cm from the central axis was ~97% (Figure VI.10) and ~91% (Figure IV.21) for 150 cm SDD and 100 cm SDD, respectively. This is because at the large SDD, the energy fluence across the detector varies slightly as a function of off-axis distance. The needed off-axis correction is smaller for the larger distance.

Regarding the transmission measurements, the effect of scatter from the phantom as a function of phantom thickness and air gap was investigated. The scatter effect on the responses in the EPID and water was different. The responses in water strongly depend on the phantom thickness and air gap. This dependence varies with field size. However, for the EPID, the response as a function of phantom thickness is nearly independent of field size (Figure VI.11(a)). In addition, the EPID response as a function of air gap varies with field size but the magnitude is smaller for the EPID than for water. The reason for the difference between the EPID and water responses is that the EPID is constructed of high Z and high density materials, and its response is different from water (low Z and low density). The protective cover and copper layer of the EPID may remove some low-energy scatter radiations from the phantom, resulting in less dependence of the response on the phantom thickness and air gap compared to water. When comparing the scatter kernels between the EPID and water, there was little variation in the scatter kernels of the EPID, while there was large variation in the scatter kernels for water without and with a phantom in the beam. Another possible explanation for this difference is that the scattering behavior in the EPID has less dependence on

energy (which can be seen in Figure IV.16) compared to water. This is likely because the main component in the scatter kernel is the detector-glare effect rather than the dosimetric scatter effect. Although the scattering kernel has less dependence on phantom thickness and air gap, the different response between the EPID and water as a function of phantom thickness and air gap still needs to be considered when using the EPID as a water-equivalent dosimeter. In this study, we acquired scatter kernels and calibration factors ($CF(0,0)$) as a function of phantom thickness and air gap for the EPID and water. These parameters were used to convert the EPID responses to doses in water for transit dosimetry. Current results showed that the accuracy of EPID dosimetry is within 3.5% for studied geometries and field sizes, and indicated that the EPID could be used as a water-equivalent dosimeter for transit dosimetry for heterogeneous geometries. Future work can verify this approach on a complex chest phantom geometry for application to patient measurements.

VI.E. Conclusion

This study investigated the accuracy of the EPID as a water-equivalent dosimeter for transit dosimetry for both homogeneous and heterogeneous geometries. The results showed that the EPID behaves differently from water as a function of phantom thickness and air gap. As a result, parameters, such as scatter kernels and calibration factors, will need to be determined for different geometries in order to improve the accuracy of conversion of EPID responses to doses in water. In this study, the accuracy of EPID transit dosimetry has been validated to be within 3.5% for a range of field sizes and various phantom geometries. The use of the EPID as a water-equivalent dosimeter will allow the direct comparison between measured transit doses and planned transit doses to quantify the delivered dose errors.

References

1. G. P. Beyer, C. W. Scarantino, B. R. Prestidge, A. G. Sadeghi, M. S. Anscher, M. Miften, T. B. Carrea, M. Sims and R. D. Black, "Technical evaluation of radiation dose delivered in prostate cancer patients as measured by an implantable MOSFET dosimeter," Int J Radiat Oncol Biol Phys **69**, 925-935 (2007).

2. W. van Elmpt, S. Petit, D. De Ruysscher, P. Lambin and A. Dekker, "3D dose delivery verification using repeated cone-beam imaging and EPID dosimetry for stereotactic body radiotherapy of non-small cell lung cancer," Radiother Oncol **94**, 188-194.

3. L. N. McDermott, M. Wendling, J. Nijkamp, A. Mans, J. J. Sonke, B. J. Mijnheer and M. van Herk, "3D in vivo dose verification of entire hypo-fractionated IMRT treatments using an EPID and cone-beam CT," Radiother Oncol **86**, 35-42 (2008).

4. S. M. Nijsten, W. J. van Elmpt, B. J. Mijnheer, A. W. Minken, L. C. Persoon, P. Lambin and A. L. Dekker, "Prediction of DVH parameter changes due to setup errors for breast cancer treatment based on 2D portal dosimetry," Med Phys **36**, 83-94 (2009).

5. A. Mans, M. Wendling, L. N. McDermott, J. J. Sonke, R. Tielenburg, R. Vijlbrief, B. Mijnheer, M. van Herk and J. C. Stroom, "Catching errors with in vivo EPID dosimetry," Med Phys **37**, 2638-2644 (2010).

6. S. M. Nijsten, B. J. Mijnheer, A. L. Dekker, P. Lambin and A. W. Minken, "Routine individualised patient dosimetry using electronic portal imaging devices," Radiother Oncol **83**, 65-75 (2007).

7. K. L. Pasma, M. Kroonwijk, S. Quint, A. G. Visser and B. J. Heijmen, "Transit dosimetry with an electronic portal imaging device (EPID) for 115 prostate cancer patients," Int J Radiat Oncol Biol Phys **45**, 1297-1303 (1999).

8. K. L. Pasma, B. J. Heijmen, M. Kroonwijk and A. G. Visser, "Portal dose image (PDI) prediction for dosimetric treatment verification in radiotherapy. I. An algorithm for open beams," Med Phys **25**, 830-840 (1998).

9. K. L. Pasma, S. C. Vieira and B. J. Heijmen, "Portal dose image prediction for dosimetric treatment verification in radiotherapy. II. An algorithm for wedged beams," Med Phys **29**, 925-931 (2002).

10. W. J. van Elmpt, S. M. Nijsten, B. J. Mijnheer and A. W. Minken, "Experimental verification of a portal dose prediction model," Med Phys **32**, 2805-2818 (2005).

11. T. R. McNutt, T. R. Mackie, P. Reckwerdt, N. Papanikolaou and B. R. Paliwal, "Calculation of portal dose using the convolution/superposition method," Med Phys **23**, 527-535 (1996).

12. R. Boellaard, M. Essers, M. van Herk and B. J. Mijnheer, "New method to obtain the midplane dose using portal in vivo dosimetry," Int J Radiat Oncol Biol Phys **41**, 465-474 (1998).

13. R. Boellaard, M. van Herk, H. Uiterwaal and B. Mijnheer, "Two-dimensional exit dosimetry using a liquid-filled electronic portal imaging device and a convolution model," Radiother Oncol **44**, 149-157 (1997).

14. M. Wendling, R. J. Louwe, L. N. McDermott, J. J. Sonke, M. van Herk and B. J. Mijnheer, "Accurate two-dimensional IMRT verification using a back-projection EPID dosimetry method," Med Phys **33**, 259-273 (2006).

15. L. N. McDermott, M. Wendling, B. van Asselen, J. Stroom, J. J. Sonke, M. van Herk and B. J. Mijnheer, "Clinical experience with EPID dosimetry for prostate IMRT pre-treatment dose verification," Med Phys **33**, 3921-3930 (2006).

16. L. N. McDermott, M. Wendling, J. J. Sonke, M. van Herk and B. J. Mijnheer, "Replacing pretreatment verification with in vivo EPID dosimetry for prostate IMRT," Int J Radiat Oncol Biol Phys **67**, 1568-1577 (2007).

17. D. A. Jaffray, J. J. Battista, A. Fenster and P. Munro, "X-ray scatter in megavoltage transmission radiography: physical characteristics and influence on image quality," Med Phys **21**, 45-60 (1994).

18. B. M. McCurdy and S. Pistorius, "Photon scatter in portal images: physical characteristics of pencil beam kernels generated using the EGS Monte Carlo code," Med Phys **27**, 312-320 (2000).

19. W. Swindell and P. M. Evans, "Scattered radiation in portal images: a Monte Carlo simulation and a simple physical model," Med Phys **23**, 63-73 (1996).

20. S. R. Ozard and E. E. Grein, "Analytical calculation of the portal scatter to primary dose ratio: an EGS4 Monte Carlo and experimental validation at large air gaps," Phys Med Biol **46**, 1719-1736 (2001).

21. L. Spies and T. Bortfeld, "Analytical scatter kernels for portal imaging at 6 MV," Med Phys **28**, 553-559 (2001).

22. S. L. Berry, C. S. Polvorosa and C. S. Wuu, "A field size specific backscatter correction algorithm for accurate EPID dosimetry," Med Phys **37**, 2425-2434 (2010).

23. P. Storchi and E. Woudstra, "Calculation of the absorbed dose distribution due to irregularly shaped photon beams using pencil beam kernels derived from basic beam data," Phys Med Biol **41**, 637-656 (1996).

CHAPTER VII

EVALUATION OF THE FEASIBILITY OF TRANSIT DOSIMETRY IN ERROR DETECTION FOR PULMONARY STEREOTACTIC BODY RADIOTHERAPY (SBRT)

In Chapter VI, the accuracy of the EPID for transit dosimetry has been verified as a function of geometry. This chapter explores the sensitivity of EPID transit dosimetry as a function of test delivery errors, such as field size, output and patient setup variations, and discusses the possibility of using transit dosimetry for on-line error detection.

VII.A. Introduction

As treatment techniques become more complex, the need for accurate delivered dose verification becomes more important. Dosimetric verification, particularly in-vivo, has been historically regarded as cumbersome to implement. However, with the recent developments in the field of electronic portal device dosimetry, in-vivo dose verification during beam delivery is becoming feasible. The most common type of electronic portal imaging devices (EPIDs) today is the amorphous silicon electronic portal imaging device (a-Si EPID). For dosimetric verification, the EPID can be used to measure transmission images (known as exit or transit dosimetry) during beam delivery. The transmission images are affected by the beam delivery and patient-specific variations. This information can be used to understand the actual doses delivered to patients, and the patient setup or treatment plans may be reviewed and modified when the measured doses are significantly different from the expected doses. To interpret the transmission data, two approaches have been investigated. In the first approach, the doses can be

directly verified at the level of EPIDs.[1-4] For example, Van Elmpt et al[3] adapted the portal

dose prediction model proposed by Pasma et al.[1] This model used pencil beam scatter

kernels and was based on a portal dose image without the patient in the beam in

combination with the radiological thickness of the patient to calculate the portal dose

image behind the patient. Then the calculated portal dose image can be compared with

the measured portal dose to verify actual doses delivered to the patient. In the second

approach, the two-dimensional (2D) and three-dimensional (3D) doses can be

reconstructed in each patient.[5-11] The dose reconstruction procedure involves converting

the EPID response to dose, correcting for the scatter inside the EPID and from the

patient, deriving the entrance energy fluence using attenuation information from planned

CT images or CBCT images during treatment, and then reconstructing the dose inside

the patient.

Hypo-fractionated stereotactic body radiotherapy (SBRT) delivers a higher dose

per fraction and a smaller number of fractions compared to conventional fractionation

treatment regimens. Due to these characteristics, it is very important to ensure the

correct doses are delivered to patients receiving SBRT. With SBRT, an image-guidance

system is used to verify the target setup for the patient before treatment. With careful

setup, treatment discrepancies can be greatly reduced. However, to avoid unpredictable

errors during irradiation, such as machine malfunction or patient movement, the dose

verification technique must be implemented during treatment. This verification can serve

to detect errors during treatment and for the more complex application to reconstruct

patient dose.

This study is designed to investigate the capability of transit dosimetry for error

detection for lung SBRT. If transit dose information is used to detect errors and to trigger

a review of the treatment, 2D information at the detector level during treatment would

likely be sufficient. While a patient dose reconstruction method is very useful, it may not be able to provide a sufficiently quick review, i.e. on-line treatment verification. Instead, dose reconstruction can be a next step when the discrepancy between expected and delivered doses at the detector level is found to exceed acceptable criteria. An acceptance and rejection criteria on the 2D dose discrepancy can be determined based on the influence of the discrepancy on in-vivo dose distributions and possible clinical outcome. Usually, quantification analyses include calculating dose differences, distance-to-agreement (DTA) or gamma values between delivered and planned dose maps. The accuracy and sensitivity of transit dosimetry for different types of delivery errors may affect the determination of these criteria to trigger a plan review for clinical use.

In Chapter VI, the accuracy of the EPID for transit dosimetry has been verified for homogeneous and heterogeneous geometries, within 4%. Therefore, this study investigates the sensitivity of transit dosimetry to delivery errors in a phantom geometry. This study provides information which may be used to determine acceptance and rejection criteria for transit dosimetry when using it in error detection mode and indicates the next steps in research before this method can be implemented in clinics.

VII.B. Methods and materials

VII.B.1. Equipment and calibration

All measurements were performed with a dose rate of 600 MU/min, jaw only field (MLC parked), 0° collimator angle, and photon energies of 6 MV using a Varian 21EX accelerator equipped with a 120-leaf Millennium multileaf collimator (MLC) and an amorphous silicon EPID (aS500).All image acquisition, calibration procedures and analysis tools were the same as Chapter IV.

VII.B.2. Transmission dose measurements for test delivery errors

The three geometries used in this study included homogeneous Solid Water (SW), simple lung, and tumor-in-lung geometries (Figure VII.1). The phantom materials included Solid Water phantom blocks (Gammex RMI, Middleton, WI) with a density of 1.04 g/cm^{3}and lung-equivalent phantom blocks (Gammex RMI, Middleton, WI) with a density of 0.30 g/cm^3. The total dimensions of all phantom geometries were 30 × 30 × 20 cm^3 (Figure VII.1). The beam isocenter was at the mid-plane of the phantom geometry; therefore, the source-to-surface distance (SSD) was 90 cm. The simple lung geometry included a 5 cm SW slab, 10 cm of lung slabs, and a 5 cm SW slab. The tumor-in-lung geometry included a 5 cm SW slab, a small lung tumor with dimension of 4 × 3 × 3 cm^3 embedded in the 10 cm of lung slabs, and a 5 cm SW slab. The simulated tumor position was at depths from 9 to 12 cm. The EPID position was at 150 cm SDD, and was used to measure transmission doses.

Transmission measurements for homogeneous SW and simple lung geometries (Figure VII.1(a) and (b)) were used to compare with calculated transit doses (which will be described in Section VII.B.5). The data for these two geometries have been acquired in Chapter VI, so this chapter used the same dataset. The detailed irradiation parameters are described in Table VII.1. For transmission measurements in the tumor-in-lung geometry, the investigation included beam delivery and patient-specific variations to represent possible delivery errors (Table VII.1). For patient-specific variations (i.e. setup error), five different shifts were measured for the tumor-in-lung geometry: ((0,0), (0,0.2), (0,0.5), (1,0), (2,0) in (AP,LAT)) where the units are in centimeters. The AP and LAT represent anterior-posterior and left-right directions, respectively (Table VII.1). For example, the shift of (0,0.2) represents that the phantom is shifted 0.2 cm toward the

right side while the shift of (1,0) represents that the phantom is shifted 1 cm anterior (Figure VII.1 (c)).
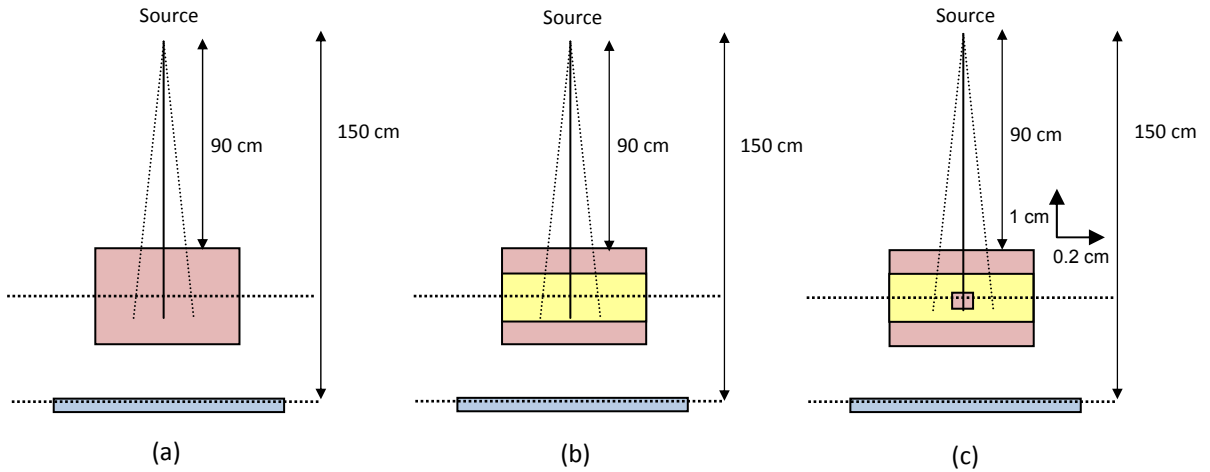
Figure VII.1. Geometric description of (a) SW phantom, (b) simple lung, and (c) lung tumor geometry in the axial view. The total dimension of all phantoms is 30 × 30 × 20 cm^3. The lung thickness in (b) and (c) is 10 cm. The solid water block used to simulate a small lung tumor in (c) is 4(L) × 3(W) × 3(H) cm^3. The isocenter is at 10 cm depth in the phantom.

Table VII.1. Beam delivery and patient-specific variations used in this study.

Geometry	Beam parameters		Setup error	
	Field size (cm^2)	MU	AP (cm)	LAT (cm)
Solid Water	5 × 5, 10 × 10	300	None	None
Lung	5 × 5, 10 × 10	600	None	None
Tumor-in-lung	4 × 4, 5 × 5, 6 × 6, 10 × 10	570, 600, 630, 660	0, 1, 2	0, 0.2, 0.5

VII.B.3. Analysis of transmission images

The measured transmission images were corrected for non-uniform backscatter and the EPID response was converted to dose at 8 mm water-equivalent depth (as described in Chapter VI). The corrected EPID doses for each condition were compared with the reference transmission doses. In this study, the field size of 5x5 cm^2 and setup error of 0 mm was considered as a reference (planned condition). The 2D dose difference maps, profiles and dose differences at the detector center were evaluated.

VII.B.4. Doses at the isocenter (mid-plane in the phantom) as a function of delivery errors

In addition to the transmission measurements for various delivery errors, the dose variations at the isocenter (in phantom or patient in clinical situation) were investigated. By comparing the variation of in-phantom and transit doses as a function of delivery errors, the correlation between the variation of in-phantom and transit doses may be established. Since the DPM Monte Carlo method has been validated as a function of heterogeneous geometries (Chapter III), the in-phantom doses at isocenter were calculated using DPM for all studied delivery errors described in Table VII.1. The details of simulated geometry, dimension and density for DPM calculations are shown in Table VII.2. The density of 0.25 g/cm^3 for the lung phantom was used for simulation based on

Table VII.2. Simulated geometry, dimension and density used in the DPM calculations.

Geometry	Medium	Dimension (cm^3)	Density (g/cm^3)
Homogeneous SW	SW	30x30x20	1
	Air	30x30x39.2	0.0012
	Detector	30x30x10.8	1
Simple lung	SW (I)	30x30x5	1
	Lung	30x30x10	0.25
	SW (II)	30x30x5	1
	Air	30x30x39.2	0.0012
	Detector	30x30x10.8	1
Lung tumor	SW (I)	30x30x5	1
	Lung	30x30x10	0.25
	Simulated Tumor	4x3x3	1
	SW (II)	30x30x5	1
	Air	30x30x39.2	0.0012
	Detector	30x30x10.8	1

the average density (density range from 0.2 to 0.3 g/cm^3) of the lung-equivalent media on the CT images. The calculation voxel size was 1.2 × 2.7(depth) × 1.2 mm^3. The

number of histories was 5×10^{11}. Then, the doses at the isocenter were extracted for comparison.

VII.B.5. Preliminary study of transit dose calculations using the DPM Monte Carlo method

The advantage of converting the EPID response to dose in water is the ability to compare with calculated doses from treatment planning systems (TPSs), and this comparison can provide information on patient dose accuracy. This study also performed a preliminary investigation of calculation accuracy for transit doses using DPM.DPM Monte Carlo was used rather than convolution/superposition (CVSP) algorithm because the Monte Carlo method should provide more accurate results in the presence of the air gap between the phantom and the detector and because the current CVSP algorithm is not implemented and commissioned for use at a large distance (i.e.150 cm). Based on test calculations using DPM and CVSP at 150 cm, DPM was selected for transit dose calculations with various geometries presented in Table VII.2. The simulated air gap and detector with the density and geometry is described in Table VII.2. The calculated transit doses were compared with the measured transit doses for these geometries.

VII.C. Results

VII.C.1. Sensitivity of transit dosimetry on delivery errors

Figure VII.2 shows the dose difference between the delivered transit doses and the expected (reference) transit doses. Figure VII.3 shows the cross-plane dose profile comparisons crossing the detector center as a function of output, field size, and setup error in the RL and AP directions. Tables VII.3 and VII.4 present the dose difference relative to the expected transit dose at the detector center for various errors. The

reference condition was the 5 × 5 cm^2 field size and 600 MU with no shift in the tumor position. Output and field size variations can be easily identified with the transit dose comparison (Figures VII.2(a-b) and VII.3(a-b)). The dose differences at the detector center were up to 10% and 13% for a 10% output variation and four times larger field size, respectively (Table VII.3 and Table VII.4).The setup variation can be detected from dose difference maps (Figure VII.2(c-d)) and profile comparisons (Figure VII.3(c-d)), but the difference is small, up to 1% and 0.3% for a 5 mm shift in the RL direction and a 2 cm shift in the AP direction, respectively (Table VII.3 and Table VII.4). For the shift in the RL direction (perpendicular to the beam axis), the main dose difference appears near the field edge which is close to the interface between the simulated tumor and lung. This difference may not be easily seen for a geometry with a similar density (i.e. treatments outside the lung). However, because the tumor is embedded in the low-density lung tissue, the difference may be able to be distinguished near the field edge or at the interface between high and low density tissues. For the shift in the AP direction (parallel to the beam axis), the magnitude of the dose difference is very small. Such a small difference will be hidden in clinical situations at this angle due to the complicated geometry inside the human body. Therefore, the transit dose is less sensitive to the setup error parallel to the beam axis than perpendicular to the beam axis.

FS05MU630-FS05MU600 (ROI> 0% Dmax)
Difference: 0.67 +/- 1.58 cGy

FS06MU600-FS05MU600 (ROI> 0% Dmax)
Difference: 6.19 +/- 18.53 cGy

(a) Output variation (5%)

(b) Field size variation (44%)

FS05MU600RL2mm-FS05MU600 (ROI> 0% Dmax)
Difference: -0.07 +/- 0.80 cGy

FS05MU600AP1cm-FS05MU600 (ROI> 0% Dmax)
Difference: -0.08 +/- 0.19 cGy

(c) RL setup error (2 mm)

(d) AP setup error (1 cm)
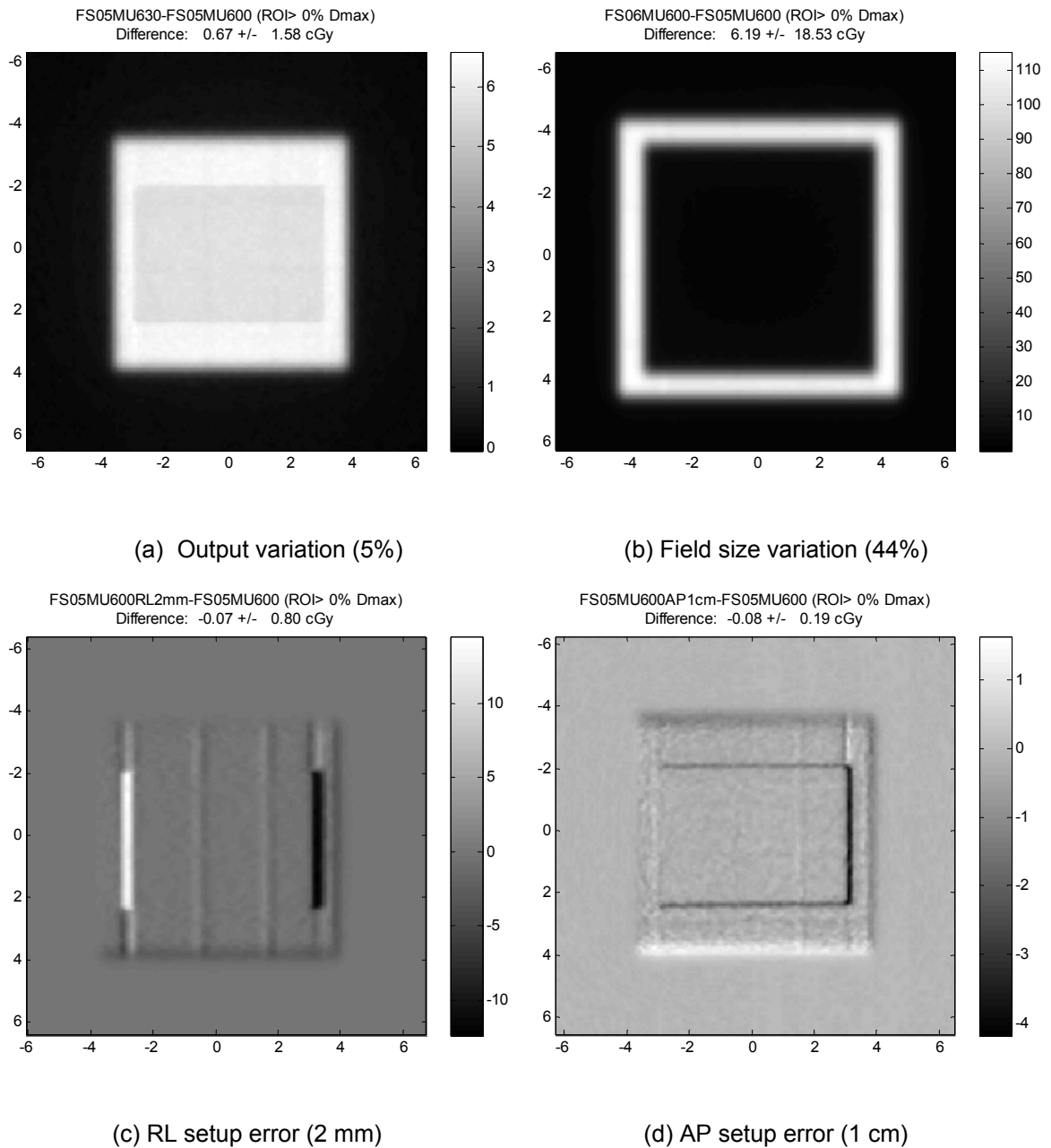
Figure VII.2. Corrected EPID transit images: 2D dose difference maps between expected (reference) transit images and delivered transit images for (a) 5% output variation, (b) 44% field size variation (changes from 5x5 to 6x6 cm^2), (c) 2 mm setup error in RL direction (tumor shifts toward the right side), and (d) 1 cm setup error in AP direction (phantom shifts anteriorly).
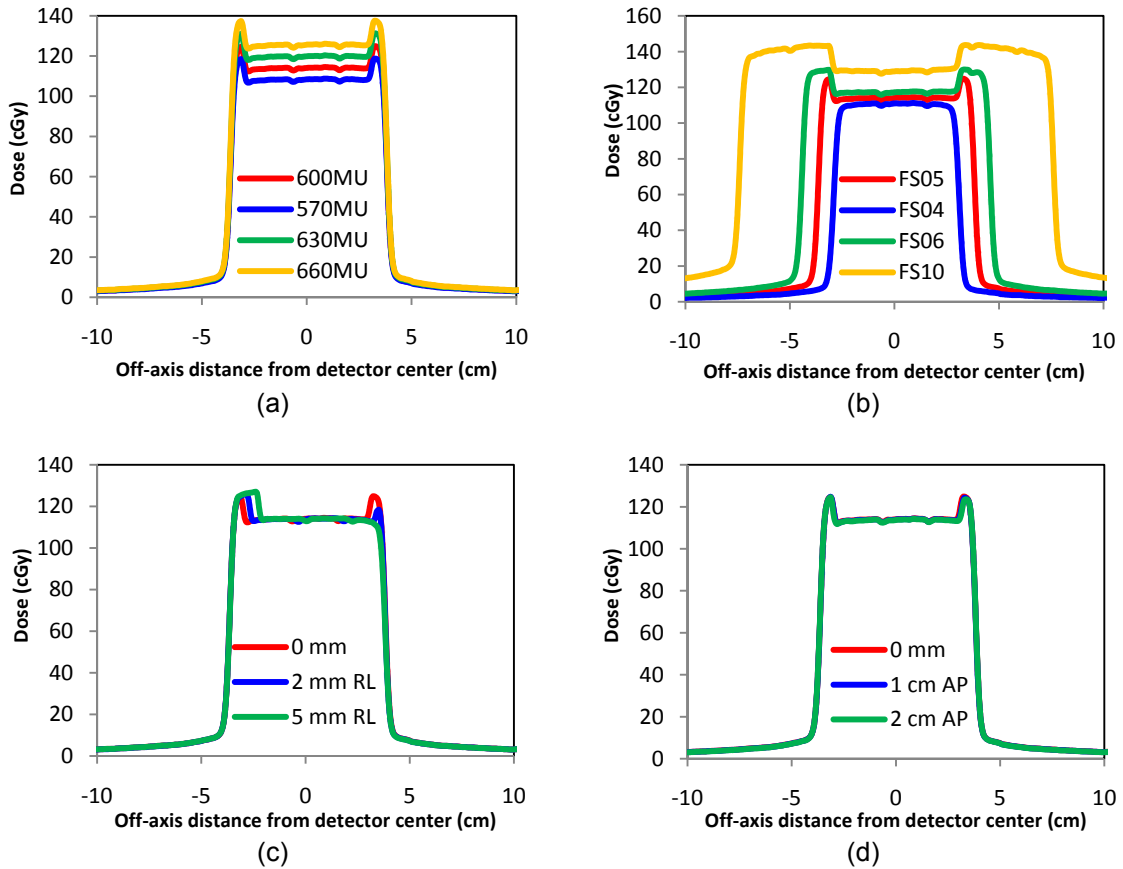
Figure VII.3. Corrected EPID transit images: one dimensional (1D) dose profiles as a function of delivery errors for (a) output variation, (b) field size variation, (c) setup error in the RL direction, and (d) setup error in the AP direction.

Table VII.3. Corrected EPID doses: the dose variation at the detector center as a function of field size and setup errors.

	0 mm	2 mm RL	5 mm RL	1 cm AP	2 cm AP
FS04	-2.7%	-3.1%	-3.7%	-2.9%	-3.0%
FS05	**0.0%**	-0.3%	-1.0%	-0.1%	-0.3%
FS06	2.7%	2.5%	1.8%	2.6%	2.4%
FS10	13.0%	12.7%	12.0%	12.7%	12.3%

Table VII.4. Corrected EPID doses: the dose variation at the detector center as a function of output and setup errors.

	0 mm	2 mm RL	5 mm RL	1 cm AP	2 cm AP
570 MU	-4.9%	-5.2%	-5.9%	-5.1%	-5.3%
600 MU	**0.0%**	-0.3%	-1.0%	-0.1%	-0.3%
630 MU	5.1%	4.7%	4.0%	4.9%	4.8%
660 MU	10.1%	9.8%	9.0%	9.9%	9.8%

VII.C.2. Variation of isocenter doses as a function of delivery error and its correlation with the variation of transit doses

Table VII.5 shows in-phantom dose variation at the isocenter as a function of field size and setup error. It can be found that for the studied geometry, small magnitudes of setup errors in the direction perpendicular to the beam axis had less impact on the in-phantom dose variation. The magnitude of setup errors for the direction parallel to the beam axis had a significant impact on in-phantom dose variation. However, the results may depend on the phantom geometry.

Table VII.5. In-phantom doses: the dose variation at the isocenter as a function of field size and setup errors

	0 mm	2 mm RL	5 mm RL	1 cm AP	2 cm AP
FS04	-2.4%	-2.3%	-2.4%	-5.7%	-10.6%
FS05	**0.0%**	-0.2%	0.0%	-3.6%	-8.3%
FS06	2.0%	1.9%	1.8%	-1.6%	-6.3%
FS10	8.1%	8.0%	8.0%	4.4%	-0.1%

While the magnitude of setup errors for the direction parallel to the beam axis affected the doses at the isocenter, it had little impact on transit doses at the detector center (Tables VII.3 and VII.4). The correlation between in-phantom dose variation at the isocenter and transit dose variation at the detector center depends on the type of delivery errors. For example, the 5% output variation leads to 5% dose variation for both in-phantom and transit doses (not shown); the four times field size variation leads to 8.1% and 13% increases for in-phantom and transit doses, respectively; the 5 mm setup error in the direction perpendicular to the beam axis results in 0% and 1% (nearly no change) variation for in-phantom and transit doses; the 2 cm setup error in the direction parallel to the beam axis results in 8.3% and 0.3% variation for in-phantom and transit

doses. Figure VII.4 shows the correlation of dose variations at the center between in-phantom and transit doses as a function of field size and setup errors (data from Tables VII.3 and VII.5). Based on this figure, there exists a relationship between in-phantom and transit dose variations which depends on the type of the delivery error. For example, the beam delivery variation changes the slope of the relationship while the setup variation changes the intercept. Therefore, the relationship between in-phantom and transit dose variations can be described by the following equation,

$$\delta_{iso} = a(\delta_d - b) + c \hspace{3cm} \textbf{(Equation VII.1)}$$

where δ_{iso} and δ_d represent the dose variations at the isocenter and at the EPID center, respectively; the parameters (a,b,c) depend on the type of delivery errors. The parameter a depends on the type of beam delivery errors, e.g. output or field size variation, and the parameters b and c depend on the movement direction of the setup error, e.g. setup error perpendicular (parameter b) and parallel (parameter c) to the beam axis. For the geometry used in this study, the parameter a was 1 and 0.649 for output and field size variations, respectively. It should be noted that this simplified equation was derived based on the geometry used in this study. It may depend on the complexity of the geometry and treatment plan. Further study must be done for complex geometries. Generally, from the current results, a correlation of dose variation between in-phantom and transit doses may be established. For clinical applications, this relationship can be used to derive the dose variation inside the patient (from transit doses) as an index to estimate how accurately doses are delivered to patients and used to determine the acceptance or rejection criteria based on the transit dose variations. Since this correlation depends on the type of delivery errors, the individual criteria for different types of errors may be needed.
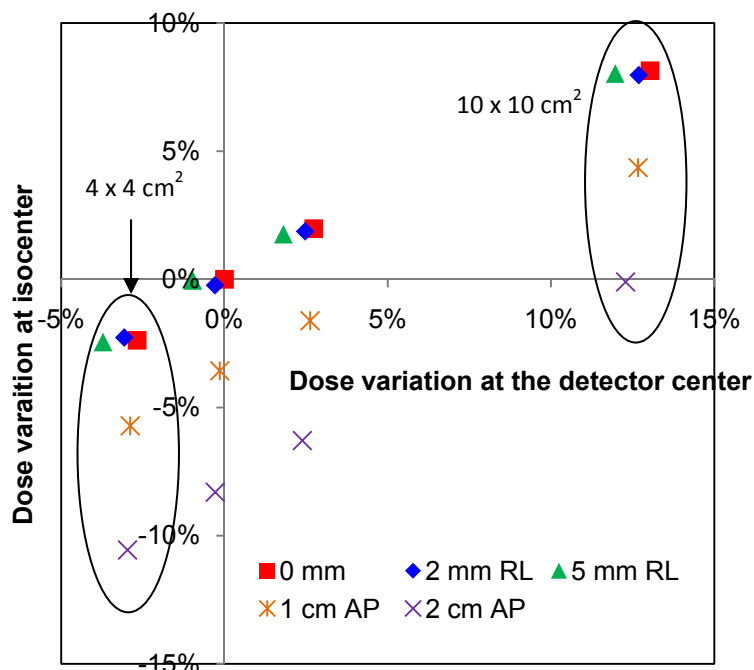
Figure VII.4. The correlation between dose variations at isocenter and dose variations at the detector center for field size variations (4x4, 5x5, 6x6 and 10x10 cm^2) and setup errors in RL (2 and 5 mm) and AP directions (1 and 2 cm). The isocenter (at 100 cm) and detector center (at 150 cm) were along the beam axis.

VII.C.3. Preliminary study of transit dose calculations using the DPM Monte Carlo method

This study also tested the capability of the DPM to calculate transit doses with different

geometries in the beam, and verified its accuracy with ion chamber (IC) measurements

as a function of field size and geometry (Table VII.6) as well as film measurements for a

10 x 10 cm^2 field size as a function of geometry (Figure VII.5). The EPID agreed with IC

measurements, within 3.5%. The large difference for small field sizes for the EPID data

was due to the error of calibration factors and scatter kernels, which has been explained

in Section VI.C.3. However, DPM showed a difference up to 8% for the studied fields

and geometries which increases with decreasing field size. This may be due to a number

of factors such as the approximation of the phantom geometry and density used for modeling (e.g. limited dimension of air gap and ignoring the scatter from the couch in the treatment room) as well as the voxel size used in the calculations (e.g. the density and calculation voxel sizes). The approximation of the phantom geometry and density used for modeling may result in an inaccurate simulation of the scatter from the phantom in the beam and air gap as a function of field size.

Regarding the off-axis dose comparison for film and EPID measurements as well as DPM calculations (Figure VII.5), DPM agreed with the film and EPID measurements for the 10x10 cm^2 field size as a function of geometry, with an average difference of 2%. Similar to the results in Table VII.6, the DPM calculation showed a larger discrepancy for 5x5 cm^2 field size (an average difference of 3%). Particularly close to the tumor edge, the DPM calculations did not show the same dose behavior as the EPID measurements. This may be due to a limited voxel size in the calculation, either the density or simulation voxel size. However, based on current results, DPM shows a potential for transit dose calculations, which can be used to compare with measured transit doses for a planning-to-delivery comparison.

Table VII.6. Comparisons between the IC in water, EPID and DPM calculations at 150 cm SDD. Doses were normalized to transmission data with 20 cm SW for 10x10 cm^2 field size for individual detector.

Geometry	Field size (cm^2)	IC in water	EPID	Diff	DPM	Diff
Transmission	4x4	0.848	0.847	-0.1%	0.880	3.9%
20 cm SW	5x5	0.872	0.873	0.1%	0.900	3.2%
40 cm air gap	**10x10**	**1.000**	**1.000**	**0.0%**	**1.000**	**0.0%**
Transmission	4x4	1.182	1.206	2.0%	1.269	7.3%
10 cm SW+10 cm Lung	5x5	1.215	1.238	1.9%	1.292	6.3%
40 cm air gap	10x10	1.377	1.388	0.8%	1.413	2.6%
Transmission	4x4	1.050	1.086	3.4%	1.133	7.9%
Lung tumor geometry	5x5	1.082	1.117	3.2%	1.158	7.0%
40 cm air gap	10x10	1.241	1.264	1.9%	1.280	3.2%
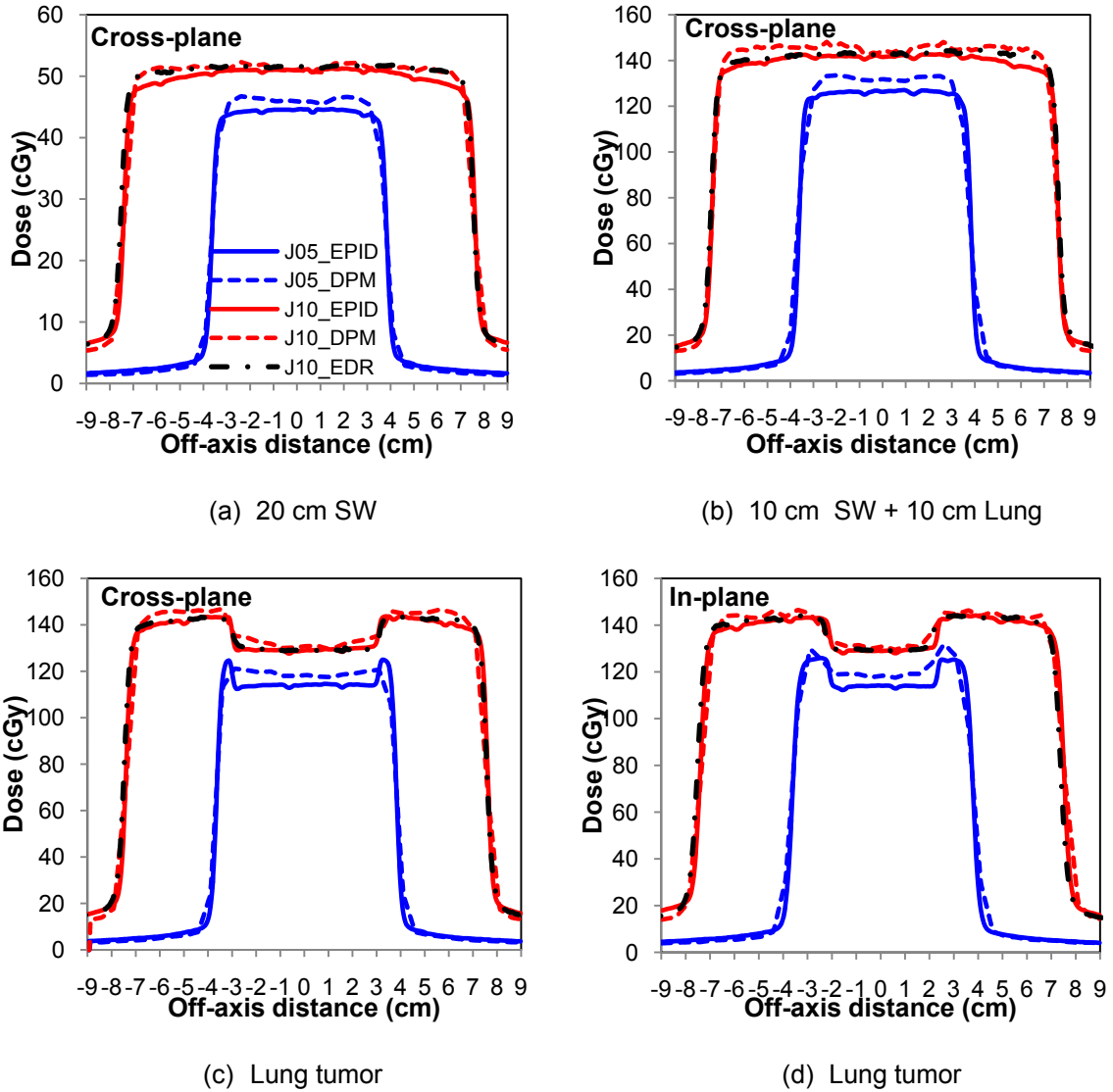
Figure VII.5. Cross-plane (a-c) and in-plane (d) profiles between EPID doses and DPM calculations at 150 cm SDD for 5x5 and 10x10 cm^2 field sizes with (a) 20 cm SW (300 MUs), (b) 10 cm SW and 10 cm lung (600 MUs), and (c-d) lung tumor geometries (600 MUs) in the beam. The EDR film data for the 10x10 cm^2 field size for various geometries are also shown for comparison. Figure VII.1 shows the detailed geometry descriptions.

VII.D. Discussion

This study investigates the performance of transit dosimetry during treatment. Most studies focused on back-projecting doses inside the phantom or patient using the transit images acquired for each beam. This method involves several corrections, including the

conversion of EPID response to dose, the correction of scatter inside the EPID and from the patient, the derivation of the entrance energy fluence using attenuation information from planned CT images or CBCT images during treatment, and then dose reconstruction inside the patient. The complexity of dose reconstruction makes it difficult to use transit dosimetry in this way for on-line verification. On-line verification or real-time monitoring can be valuable for advanced radiotherapy. Current radiotherapy imaging and delivery techniques have been greatly improved to provide more precise treatments, resulting in significant benefit to patients. However, techniques are needed to verify that the delivery is reliable and safe. Although errors in radiation oncology can be reduced, they cannot be eliminated because the treatment process is complex, hardware and software technology can malfunction, communications can be misunderstood, and especially, because humans are involved. Therefore, treatment approaches must be fault-tolerant and they must be designed to catch and correct errors before they can harm the patients.[12]On-line verification of the delivered dose can have a significant impact in improving advance radiotherapy, e.g. catching errors as soon as practical. Especially for techniques delivering large doses per fraction, incorrect delivery of dose to patients cannot be tolerated even if caught after one or two fractions. To avoid this situation, real-time monitoring to catch unpredicted errors is important. Therefore, this study evaluated the feasibility of transit dosimetry in error detection with an emphasis on lung SBRT.

In this study, several possible errors were tested, including beam delivery errors in the output and field size, and setup errors in the direction parallel and perpendicular to the beam axis. EPID transmission images were measured for various conditions and were converted into doses-in-water. The corrected EPID data included corrections for backscatter, scatter kernels and the off-axis energy dependence for the EPID raw data.

The corrected EPID data can be used for planning-to-delivery comparisons. Current results showed that corrected data are capable of error detection during treatment. The information gained from 2D dose difference maps, profile comparisons and dose differences at the detector center can be used to understand the quality of doses delivered to patients during the treatment. The expected transit doses (reference doses) can be derived from either the EPID images acquired in the first fraction (for fraction-to-fraction comparison) or the calculated transit doses from the TPS if the system is capable of accurate dose calculation at the EPID location (for planning-to-delivery comparisons). Transit doses acquired during treatment can provide a real-time check for delivered doses.

Our results showed that beam delivery errors (e.g. beam output and field size errors) lead to more significant delivered dose errors compared to patient-specific errors (e.g. setup error). The beam delivery errors can be easily found from the transmission image comparison. The 2D dose difference map can be used to understand what type of errors occurs during the beam delivery. Transit dosimetry is more sensitive to setup error in the direction perpendicular to the beam axis than the direction parallel to the beam axis. However, since treatments are delivered from multiple beam angles, an error in the direction parallel to the beam axis for one beam will be distinguished from transit images of other beams. Individual institutions can set their criteria to stop the beam if the field size or output error is unacceptable. This could then trigger are view of the plan and acquisition of images using the cone-beam CT (CBCT) attached to the linear accelerator or conventional CT if the patient-specific error is unacceptable.

In addition to monitoring delivered dose errors to patients during the treatment, the quantification of dose errors is valuable. The actual doses delivered to patients can be related to evaluation of treatment outcomes. Based on the results in this study, we

propose an empirical equation to estimate the error of delivered doses for all fractions by acquiring the transmission images using the EPID during the treatment for individual fields (or beam). The equations are shown as below,

$$\Delta D = \frac{1}{n} \sum_{i=1}^{n} \sum_{j=1}^{m} R(g_j, \varepsilon_j) \cdot w_j \cdot \delta_{ij}$$ **(Equation VII.2)**

$$\sum_{j=1}^{m} w_j = 1$$ **(Equation VII.3)**

$$\delta_{ij} = (MTD_{ij} - PTD_j)/PTD_j$$ **(Equation VII.4)**

where ΔD = the dose error relative to the cumulative prescribed dose (for all fractions) at the isocenter inside patients

n = the total number of treatment fractions (with constant dose per fraction)

m = the total number of beams

$R(g_j, \varepsilon_j)$= the correlation factor between the variation of doses at the beam isocenter and the variation of doses at the EPID detector center in transit dosimetry.

w = the weight that each individual beam contributes to the doses at the beam isocenter. The sum of all beam weights is equal to 1.

δ = the dose error relative to the expected dose at the EPID detector center in transit dosimetry for each individual beam and each fraction

MTD = the measured transit doses for individual beam and fraction

PTD =the planned transit doses for individual beam.

Note that the parameter $R(g_j, \varepsilon_j)$ depends on the type of errors (ε_j) and the geometry (g_j), e.g. the pathlength (x_j) from the isocenter to the exit point in the patient's geometry along the beam axis for each individual beam (Figure VII.6). The variation in the pathlength results in a fluence variation due to the beam attenuation and scatter variation arriving at

the detector, changing the relationship between dose variations at the isocenter and dose variations at the detector center. This correlation factor may be able to be acquired as a function of pathlength, and an empirical equation may be derived.

The above equations are proposed for the situation when the isocenter is inside the tumor and the isocenter and EPID center are along the beam axis. However, for clinical situations, the isocenter may be not inside the tumor. In these situations, the dose error at the isocenter (ΔD) can be adapted to the dose error at the tumor center.
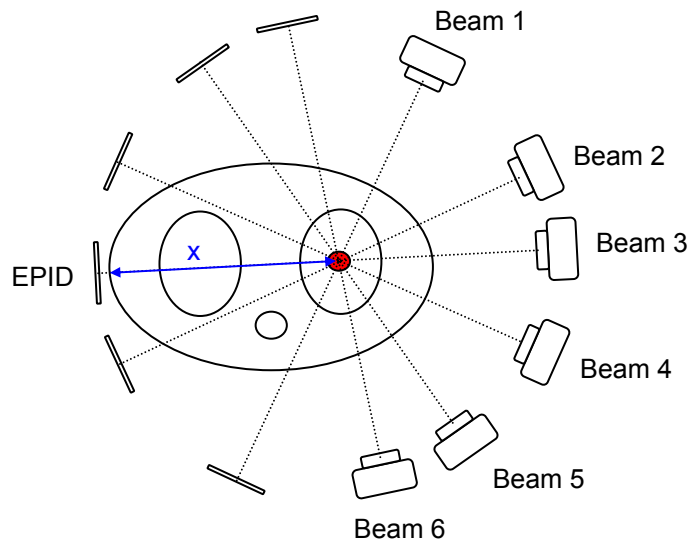
Figure VII.6. An illustration showing geometry where the EPID can be used to measure the transmission images during beam delivery for individual beams. This figure is presented only as an example. Under clinical conditions, the number of beams could be greater than six for SBRT plans. This example geometry shows the lung, spine and a lung tumor. The beam isocenter may be inside the tumor or at another reference position.

The 2D transit images acquired during treatment can provide valuable information related to the beam delivery and patient-specific parameters. These images can be used to monitor the doses delivered to patients in real-time, and if robust criteria are set, appropriate actions can be defined for the treatment therapists to take right

away if the transmission images are significantly different from the expected images. The purpose of this method for 2D transit doses is to catch errors on-line during the treatment and to trigger the review of the case if necessary without needing to wait for off-line dose reconstruction. Implementation of transit dosimetry for error detection can be beneficial for improving patient safety, and ensuring that the planned doses are precisely delivered to patients.

The use of transit dosimetry for delivered dose verification is not only useful for hypo-fractionated SBRT techniques, but also for standard fractionation schemes using any technique. The delivered dose for standard fractionation regimens(180-200 cGy per fraction) is much lower than for hypo-fractionation regimens. Due to the lower doses, the charge trapping effect in the EPID will be significant, leading to signal loss. The rate of signal loss may be almost constant for similar doses. For a fraction-to-fraction comparison, its influence may be ignored. However, for planning-to-delivery comparison, the correction of signal loss for low dose delivery should be performed; otherwise, the delivered dose may be under-estimated and lead to an over-estimation of the error in delivered doses.

Future work could evaluate if TPSs are capable of calculating transit doses accurately for the planning-to-delivery comparison method. Our preliminary study implied that it is possible to use a calculation algorithm implemented in a TPS to accurately calculate transit doses for comparison with measured transit doses for a planning-to-delivery comparison. The main issue affecting the accuracy of calculated transit doses may be the scatter dependence on the phantom or patient geometry as a function of field size and air gap. For model-based calculation algorithms, different sets of beam parameters may be needed for the standard treatment distance (90 to 110 cm from the source) and the EPID position (from 140 to 160 cm from the source).Future work could

also investigate the correlation factor R (Equation VII.2) as a function of error type and pathlength from the isocenter to the exit point, and investigate the sensitivity of transit dosimetry and accuracy of the proposed equations (Equation VII.2) for a full SBRT delivery on different phantoms such as a chest phantom (Figure VII.7).Finally, future work can include implementation of transit dosimetry in a clinical environment for real-time error detection.

Ion chamber holder   Lung-equivalent material

(a)   (b)

(c)   (d)
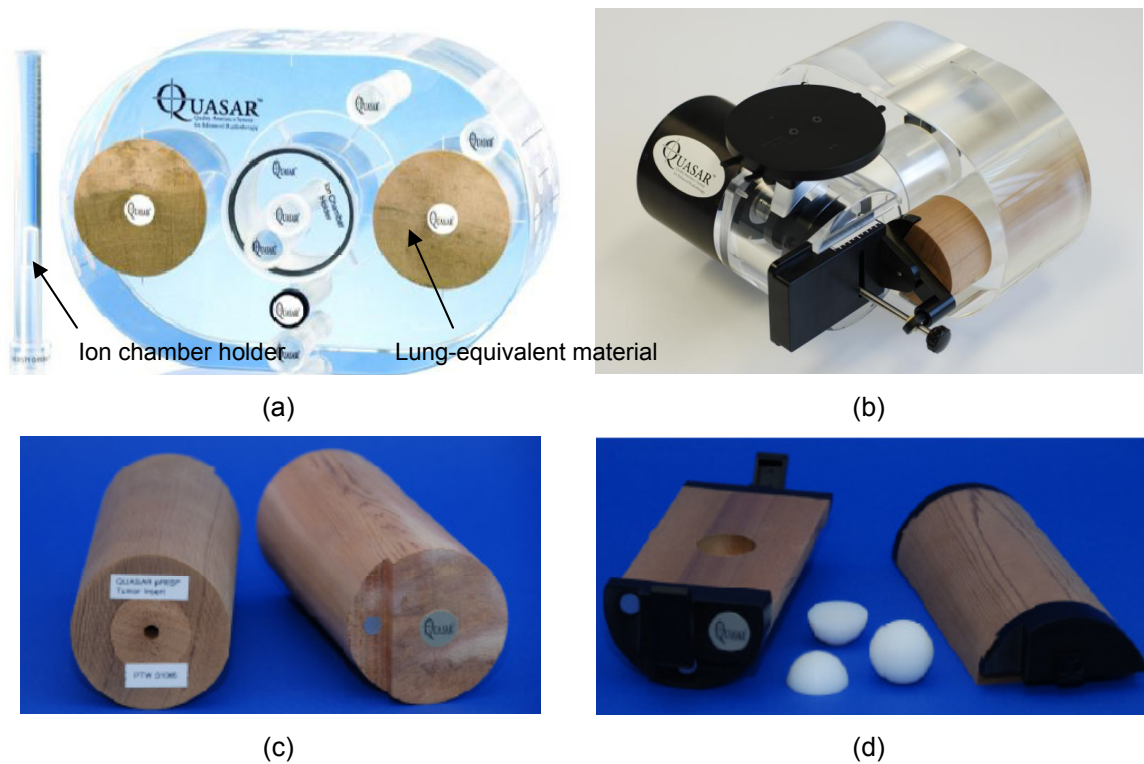
Figure VII.7. An example of a chest phantom (QUASAR[TM]) with a simulated lung tumor and motion equipment from Modus Medical Devices Inc. (London, Ontario, Canada). (a) Multi-Purpose Body Phantom with an IC holder, (b) Multi-Purpose Body Phantom with respiratory motion rotation stage, (c) Cedar insert with solid tumor for IC dosimetry, and (d) Cedar lung tumor insert for Gafchromic[TM] film dosimetry.

VII.E. Conclusion

This study showed that 2D transit dosimetry is sensitive to beam delivery variations and setup errors. Although it is not sensitive to the setup error in the direction parallel to the

beam axis, this error can be detected by measurements of other beams. In addition, the

correlation between in-vivo and transit dose variations may be able to be established

and used to estimate in-vivo dose errors as well as to determine the acceptance or

rejection criteria for the difference between the expected and delivered transit doses.

Our results indicate that individual criteria for the difference in transit doses may be

needed for different types of errors, since different types of errors result in a different

relationship between in-vivo and transit dose variations. Acquiring the transit doses for

each beam provides information about how the doses were delivered. Real-time error

detection is possible by comparing the transit doses fraction by fraction. Then immediate

action can be taken on-line before the errors adversely impact the patient.

References

1. K. L. Pasma, B. J. Heijmen, M. Kroonwijk and A. G. Visser, "Portal dose image (PDI) prediction for dosimetric treatment verification in radiotherapy. I. An algorithm for open beams," Med Phys 25, 830-840 (1998).

2. K. L. Pasma, S. C. Vieira and B. J. Heijmen, "Portal dose image prediction for dosimetric treatment verification in radiotherapy. II. An algorithm for wedged beams," Med Phys 29, 925-931 (2002).

3. W. J. van Elmpt, S. M. Nijsten, B. J. Mijnheer and A. W. Minken, "Experimental verification of a portal dose prediction model," Med Phys 32, 2805-2818 (2005).

4. T. R. McNutt, T. R. Mackie, P. Reckwerdt, N. Papanikolaou and B. R. Paliwal, "Calculation of portal dose using the convolution/superposition method," Med Phys 23, 527-535 (1996).

5. R. Boellaard, M. Essers, M. van Herk and B. J. Mijnheer, "New method to obtain the midplane dose using portal in vivo dosimetry," Int J Radiat Oncol Biol Phys 41, 465-474 (1998).

6. R. Boellaard, M. van Herk and B. J. Mijnheer, "A convolution model to convert transmission dose images to exit dose distributions," Med Phys 24, 189-199 (1997).

7. R. Boellaard, M. van Herk, H. Uiterwaal and B. Mijnheer, "Two-dimensional exit dosimetry using a liquid-filled electronic portal imaging device and a convolution model," Radiother Oncol 44, 149-157 (1997).

8. R. Boellaard, M. van Herk, H. Uiterwaal and B. Mijnheer, "First clinical tests using a liquid-filled electronic portal imaging device and a convolution model for the verification of the midplane dose," Radiother Oncol 47, 303-312 (1998).

9. M. Wendling, R. J. Louwe, L. N. McDermott, J. J. Sonke, M. van Herk and B. J. Mijnheer, "Accurate two-dimensional IMRT verification using a back-projection EPID dosimetry method," Med Phys 33, 259-273 (2006).

10. L. N. McDermott, M. Wendling, B. van Asselen, J. Stroom, J. J. Sonke, M. van Herk and B. J. Mijnheer, "Clinical experience with EPID dosimetry for prostate IMRT pre-treatment dose verification," Med Phys 33, 3921-3930 (2006).

11. L. N. McDermott, M. Wendling, J. J. Sonke, M. van Herk and B. J. Mijnheer, "Replacing pretreatment verification with in vivo EPID dosimetry for prostate IMRT," Int J Radiat Oncol Biol Phys 67, 1568-1577 (2007).

12. W. R. Hendee and M. G. Herman, "Improving patient safety in radiation oncology," Med Phys 38, 78-82 (2011).

CHAPTER VIII

SUMMARY

Over the last ten years, radiotherapy planning and delivery techniques have been greatly improved allowing for more precise treatments which can benefit patients. However, there are safety considerations, since the treatment processes are complex, hardware and software technology can malfunction, and communications can be misunderstood, especially when humans are involved. Due to these factors, we must realize that errors in radiotherapy can be reduced but cannot be completely eliminated. However, aided by on-line delivered dose verification techniques, the occurrence of severe treatment errors can be greatly reduced or possibly avoided. In particular, ensuring precise treatment is extremely important for hypo-fractionation treatment regimens with a larger dose per fraction and fewer fractions compared to standard fractionation regimens. One hypo-fractionated treatment technique is pulmonary stereotactic body radiotherapy (SBRT). This type of treatment suffers from several challenges, such as calculation uncertainty of heterogeneous geometries (with low-and-high density media) and organ motion due to breathing. Therefore, this dissertation has focused on certain issues that are important for lung SBRT treatments. These issues included the validation of calculation accuracy for various heterogeneous geometries and the development of techniques utilizing an electronic portal imaging device (EPID) for pre-treatment and treatment dosimetric verification.

Chapter I has provided an overview of issues in advanced radiotherapy, such as challenges in targeting for patients and concerns with respect to dosimetric accuracies. This chapter discussed the current state of radiotherapy, how delivery errors can affect treatment outcomes, the types of delivery errors, and several approaches to verifying doses delivered to patients.

Chapter II has reviewed the literature relevant to issues in lung SBRT treatments. The first issue addressed was the challenge of measurements and calculations in electron disequilibrium conditions. This disequilibrium mainly exists in the region close to field edges. The influence of the lateral disequilibrium is great when a small beam size or a high energy is used, and the situation is worse for low-density tissues in the patient geometry. By reviewing the literature, an appropriate detector and methodology was selected in this dissertation. The second issue discussed was the influence of organ motion due to breathing. The third issue addressed was related to the possibility of using an EPID for pre-treatment and treatment verification. The characteristics of the most common type of EPIDs (indirect amorphous-silicon EPIDs) mounted on linear accelerators were discussed. In addition, several approaches of using EPIDs for pre-treatment and treatment verification were reviewed. The chapter closed with a discussion of research gaps in solving these issues.

Chapter III investigated dose distributions for lung tumor geometries for a 6 MV photon beam. To address the measurement challenges in the disequilibrium region, Gafchromic™ EBT film was chosen to measure multi-planar doses in heterogeneous geometries. The heterogeneous geometries included tumor-in-lung and lung-only geometries with the beam axis (and the tumor) close to and far from the interface. Dose perturbation due to the presence of the film placed parallel to the beam axis in a low-density material was investigated using measurements and DPM Monte Carlo

calculations. The results showed that film perturbation reduced the dose as a function of depth with ~8% reduction beyond 12 cm of lung media. Both measurements and Monte Carlo calculations showed that the perturbation effect was reduced by rotating the gantry by 2°. Good agreement between parallel and perpendicular film results (~2.6%) in this study increases confidence in measured dose accuracy in tumor-in-lung heterogeneous geometries. In addition, multi-planar measurements provide more reliable three-dimensional (3D) dose distributions for understanding dosimetric characteristics of various geometries, and can be used to more thoroughly evaluate the accuracy of calculation algorithms to improve dose calculations for lung SBRT or other techniques involving dose calculations in the lung. The comparison between the measurements and Monte Carlo calculations as a function of heterogeneous geometry was also reported. The DPM Monte Carlo method was found to calculate the doses accurately in various heterogeneous geometries, with a deviation of ~0.5% along the central axis for 4×4 cm^2 field size, and with small deviations in the profile penumbra (up to 1.6 mm difference) and tumor-lung interface regions. These results indicated that DPM can be used as a reference to validate other calculation algorithms or to evaluate the doses delivered to patients for lung treatment.

Chapter IV has characterized a commercial amorphous silicon EPID (aS500) mounted on a Varian linear accelerator for dosimetric verification. A general calibration method for EPID dosimetry was explored. The calibration method accounted for several corrections in EPID dosimetry, including (1) non-uniform backscatter due to the non-uniform geometry in the EPID support structure, (2) kernel-based corrections for the inherent difference between the EPID and water, (3) separation of open field and MLC transmission components by analyzing MLC sequence files, (4) the use of different calibration factors and scatter kernels for open and MLC transmission components, and

(5) an off-axis correction for the EPID response at off-axis positions for softer beams. The calibration method converted the EPID response to dose-to-water. This approach provides dose information which can be directly compared with the calculations from treatment planning systems (TPSs), rather than the arbitrary unit information which can only be used to verify the fluence. In order to validate the proposed calibration method, the EPID responses were converted to doses-in-water at 8 mm, and were compared with film measurements and convolution/superposition (CVSP) calculations for jaw only (MLC parked), MLC-shaped and non-uniform intensity (IMRT) fields. The corrected EPID doses agreed with ion chamber and film measurements as well as CVSP calculations for all fields studied. The results have shown the possibility of using an indirect a-Si EPID as a water-equivalent dosimeter for pre-treatment and treatment dose verification.

Chapter V has evaluated the accuracy of the calibration method proposed in Chapter IV to convert the EPID response to dose at any specific depth in water for pre-treatment dose verification. In the clinical environment, dose verification in a phantom before treatment (i.e. pre-treatment verification) is usually performed at a deeper depth, e.g. 5 or 10 cm, since dose measurements and calculations in the buildup region have a larger uncertainty than at deeper depths. However, the calibration method in Chapter IV was only validated at 8 mm depth (in the buildup region for 6 MV photons). To develop a more-clinically relevant calibration method, it was extended for dose conversion at depths deeper than 8 mm. To do that, individual off-axis correction factors and scatter kernels were acquired at 5 and 10 cm depths in water. These parameters were used to convert the EPID response to dose at 5 and 10 cm depths. To validate the accuracy of the correction, the corrected EPID responses were compared with film measurements and CVSP calculations for jaw only, MLC-shaped and IMRT fields. Evaluating the different techniques at 0.8, 5, and 10 cm depths, the results were comparable between

the EPID method, ion chamber and film measurements, and CVSP calculations. Using individual sets of parameters, i.e. scatter kernels and off-axis correction factor, the EPID response can be converted to dose at any depth in water. The generality of the EPID calibration method has been verified at depths for clinically-relevant conditions in this chapter.

Chapter VI has evaluated the accuracy of EPID transit dosimetry at the detector plane. The calibration method proposed in Chapter IV has been validated for pre-treatment verification (without any phantom or patient in the beam). This chapter extended the method for transit dosimetry, i.e. dose verification for patients under treatment. The transit doses can be used for dose reconstruction inside patients or for direct verification at the detector plane. Since the dose reconstruction involves several complex procedures, the accuracy and limitation will need further exploration. Transit dosimetry for on-line or real-time dose verification must be simple and fast. For the purpose of error detection, the two-dimensional (2D) dose information at the detector plane may be sufficient. Therefore, this chapter focused on the approach of dose verification at the EPID detector level. One challenge for EPID transit dosimetry is the influence of the scatter inside the detector or from the patient on dosimetric accuracy. This influence depends on each patient's anatomy. Therefore, this chapter investigated the effect of scatter from the phantom on the EPID dosimetry, and evaluated the accuracy of EPID dosimetry at the detector level as a function of phantom geometries, including homogeneous and heterogeneous geometries. The parameters of the calibration method (from Chapter IV) were acquired for transit dosimetry, and its accuracy was validated with film and ion chamber measurements. The results showed that the EPID behaves differently from water as a function of phantom thickness and air gap. These results indicated that individual parameters, such as scatter kernels and

calibration factors, will be needed for different patient geometries in order to improve the accuracy of using the EPID as a water-equivalent dosimeter. The accuracy of EPID transit dosimetry was validated within 3.5% for a range of field sizes and various phantom geometries. The use of the EPID as a water-equivalent dosimeter will allow direct comparison between measured transit doses and planned transit doses (for TPSs capable of calculating transit dose) in order to quantify the delivered dose errors.

In Chapter VII, the sensitivity of transit dosimetry in error detection for lung SBRT has been evaluated with an emphasis on on-line treatment verification, e.g. catching errors during delivery. Especially for techniques with large doses delivered per fraction, it cannot be tolerated for incorrect doses to be delivered to patients and only caught after one or two fractions. To avoid this situation, a real-time monitor to catch unpredicted errors is more important. If transit dose information is used to detect errors and trigger a review for treatment, 2D information at the detector level during treatment would be sufficient. Delivered dose reconstruction inside the patient is very useful; however, it may not be able to provide the immediate feedback that is possible with on-line treatment verification. Instead, dose reconstruction can be a next step when the discrepancy between expected and delivered doses at the detector level is found to exceed acceptable criteria. Therefore, this chapter investigated the sensitivity of the technique by testing several possible errors, including beam delivery errors in the output and field size, and setup errors in the direction parallel and perpendicular to the beam axis. The results showed that corrected EPID doses (using the method and parameters from Chapter VI) are capable of detecting errors during treatment. Information such as the 2D dose difference map, profile comparison and dose difference at the detector center can be used to evaluate the accuracy of doses delivered to patients during the treatment. In this chapter, the possibility of using TPSs to calculate transit doses has been discussed

by comparing them with the measured transit doses. In addition, considerations for the implementation of transit dosimetry in a clinical environment for SBRT treatment have been discussed.

Future studies can investigate the dosimetric accuracy using an anthropomorphic phantom with a full SBRT delivery, develop improvements of the accuracy of the calibration method as a function of patient geometry for transit dosimetry, and investigate how to implement transit dosimetry in clinics (e.g. individual use or in conjunction with image-guidance systems) to verify delivered doses to patients or for error detection. In addition, the influence of organ motion on transit dosimetry would need further exploration.

Although radiotherapy employs many complex procedures and quality assurance techniques, errors cannot be completely eliminated. However, by thoroughly evaluating calculation algorithms and improving their calculation accuracy in challenging conditions, the delivered dose uncertainty caused by calculation algorithms can be reduced. Using pre-treatment quality assurance, the delivered dose uncertainty caused by a machine malfunction or error in data transfer can be reduced. Finally, implementation of transit dosimetry for on-line error detection will detect unpredicted errors and greatly reduce or avoid the occurrence of serious errors which are harmful to patients' treatment outcome or lives. This dissertation work has provided a methodology to evaluate calculation algorithms, and evaluated EPID dosimetry for pre-treatment and treatment verification, which will be beneficial to improving the safety of patients treated with radiotherapy.